UDC 62

MACHINERY & ENERGETICS

Publisher:
National University of Life and Environmental Sciences of Ukraine

Year of foundation: 2010
Frequency of issue: Four times per year

Recommended for printing and distribution
via the Internet by the Academic Council
of National University of Life and Environmental Sciences of Ukraine
(Minutes No. 14 of May 21, 2026)

State Registration:
Media identifier R30-02298.
Decision of the National Council
of Television and Radio Broadcasting of Ukraine
No. 1795, Minutes No. 31, dated 21.12.2023.

The journal is included in the list of Professional Scientific Publications of Ukraine
Category "B". Branch of sciences – Technical.
Specialties: 0715 – Mechanics and Metal Trades, 0716 – Motor Vehicles, Ships and Aircraft,
0713 – Electricity and Energy, 0714 – Electronics and Automation
(Order of the Ministry of Education and Science of Ukraine of December 23, 2025, No. 1693)

The journal is presented international scientometric databases, repositories
and scientific systems:
Google Scholar, Professional Publications of Ukraine, Vernadsky National Library of Ukraine,
BASE, J-Gate, Dimensions, Cambridge University Library, Leipzig University Library,
European University Institute, SOLO - Search Oxford Libraries Online, University of Hull Library,
University of Oslo Library, EBSCO, UCSB Library, Ulrichsweb Global Serials Directory,
OUCI (Open Ukrainian Citation Index), WorldCat, Litmaps, CABI

Editors office address:
National University of Life and Environmental Sciences of Ukraine
03041, 15 Heroiv Oborony, Kyiv, Ukraine
Tel.: +38(044)-258-42-63
E-mail: me@technicalscience.com.ua
https://technicalscience.com.ua/en

УДК 62

ТЕХНІКА ТА ЕНЕРГЕТИКА

Видавець:
Національний університет біоресурсів і природокористування України

Рік заснування: 2010
Періодичність випуску: 4 рази на рік

Рекомендовано до друку та поширення
через мережу Інтернет Вченою радою
Національного університету біоресурсів і природокористування України
(протокол № 14 від 21 травня 2026 р.)

Державна реєстрація:
Ідентифікатор медіа R30-02298.
Рішення Національної ради України
з питань телебачення і радіомовлення
№ 1795, протокол № 31 від 21.12.2023 р.

Журнал входить до переліку наукових фахових видань України

Категорія «Б». Галузь наук – Технічні.
Спеціальності: 131 – «Прикладна механіка», 133 – «Галузеве машинобудування»,
141 – «Електроенергетика, електротехніка та електромеханіка»,
174 – «Автоматизація, комп'ютерно-інтегровані технології та робототехніка»
(Наказ Міністерства освіти і науки України від 23 грудня 2025 року № 1693)

Журнал представлено у міжнародних наукометричних базах даних,
репозитаріях та пошукових системах:
Google Scholar, Фахові видання України, Національна бібліотека України імені
В. І. Вернадського, BASE, J-Gate, Dimensions, Cambridge University Library,
Leipzig University Library, European University Institute, SOLO - Search Oxford Libraries Online,
University of Hull Library, University of Oslo Library, EBSCO, UCSB Library, Ulrichsweb Global
Serials Directory, OUCI (Open Ukrainian Citation Index), WorldCat, Litmaps, CABI

Адреса редакції:
Національний університет біоресурсів і природокористування України
03041, вул. Героїв Оборони, 15, м. Київ, Україна
Тел.: +38(044)-258-42-63
E-mail: me@technicalscience.com.ua
https://technicalscience.com.ua/uk

Редакційна колегія

CONTENTS

V. Duhanets, O. Hovorov, V. Pukas
Analysis and optimisation of internal combustion engine cooling systems
to improve thermal efficiency and operational reliability 7

Kh.A. Hossain, M.J. Mia, M.F. Hossen, M.M. Rahman
Design and modification of a combined grass cutting and grinding machine 22

T. Bilas, V. Yaras
Economic efficiency of the Net Billing model for solar power plants
in the private sector of Ukraine (using houses of 120-200 m^2 as an example) 39

V. Naumenko, L. Chervinsky
Analysis of the influence of the geometry of the working zone
on the distribution of the electric field in powder coating systems 50

O. Hanpantsurova, O. Hubarev, K. Bielikov, A. Murashchenko, O. Levchenko
Synthesis and decomposition of a mechatronic system
with hydro-pneumatic automation devices 65

O. Velhas
Methodological approach to the performance indicators
of functional elements in the smart technical diagnostic system for combine harvesters 78

O. Shvydun
Intelligent system of operating parameters
for monitoring the technical condition of combine harvesters 88

R. Shatrov
Analytical structural and energy model of agrotronics
for combine harvesting of grain crops 98

M. Umanskyi
Agricultural drone routing based on the artificial bee colony algorithm 108

V. Hrytsiuk
Analytical assessment of the use of plant material shredder 121

ЗМІСТ

В. Дуганець, О. Говоров, В. Пукас
Аналіз та оптимізація систем охолодження двигунів внутрішнього згоряння
для підвищення теплової ефективності та надійності роботи двигуна 7

Х. А. Хоссейн, М. Дж. Мія, М. Ф. Хоссен, М. М. Рахман
Конструкція та модифікація комбінованої траворізально-подрібнювальної машини 22

Т. Білас, В. Ярас
Економічна ефективність моделі Net Billing для сонячних електростанцій
у приватному секторі України (на прикладі будинків 120-200 м²) 39

В. Науменко, Л. Червінський
Аналіз впливу геометрії робочої зони на розподіл електричного поля
в системах порошкового фарбування 50

О. Ганпанцурова, О. Губарев, К. Бєліков, А. Муращенко, О. Левченко
Синтез та декомпозиція мехатронної системи
з гідропневматичними пристроями автоматизації 65

О. Вельгас
Методологічність показників функціональних елементів
Smart системи технічного діагностування зернозбиральних комбайнів 78

О. Швидун
Інтелектуальна система експлуатаційних параметрів контролю
технічного стану зернозбиральних комбайнів 88

Р. Шатров
Аналітична структурно-енергетична модель агротроніки
комбайнового збирання зернового збіжжя 98

М. Уманський
Маршрутизація агродронів на основі ройового інтелекту бджолиної колонії 108

В. Грицюк
Аналітичність машиновикористання подрібнювача рослинних матеріалів 121

Machinery & Energetics
Vol. 17, No. 2. 2026

Journal homepage:
https://technicalscience.com.ua/en

UDC 631.362:004.94
DOI: 10.31548/machinery/2.2026.1

ISSN 2663-1334
e-ISSN 2663-1342

Viktor Duhanets*
Doctor of Pedagogical Sciences, Professor
Higher Educational Institution "Podillia State University"
32316, 12 Shevchenko Str., Kamianets-Podilskyi, Ukraine
https://orcid.org/0000-0002-3383-5907

Oleksandr Hovorov
PhD in Technical Sciences, Senior Researcher
Higher Educational Institution "Podillia State University"
32316, 12 Shevchenko Str., Kamianets-Podilskyi, Ukraine
https://orcid.org/0000-0002-1645-1725

Vitaliy Pukas
PhD in Technical Sciences, Associate Professor
Higher Educational Institution "Podillia State University"
32316, 12 Shevchenko Str., Kamianets-Podilskyi, Ukraine
https://orcid.org/0000-0002-0083-7359

Analysis and optimisation of internal combustion engine cooling systems to improve thermal efficiency and operational reliability

Abstract. The study aimed to quantitatively evaluate and optimise the operation of internal combustion engine cooling systems with a view to improving their thermal efficiency and reliability. The methodology combined engine bench tests with measurements of temperature, coolant and fuel flow rates, heat flux calculations with uncertainty assessment following guidance on the expression of measurement uncertainty, computational fluid dynamics in a coupled "fluid-solid" formulation, analysis of the stress-strain state of the cylinder head, and investigation of the transient warm-up regime from 20 to 90°C. The study established that the modernised configurations ensured a 10-17% increase in heat flux under maximum load conditions, a 5-6% and 10-12% reduction in peak temperatures in critical pre-chamber zones, and an 18-22% and 30-35% reduction in internal temperature gradients. This was accompanied by a reduction in equivalent stresses of 18-22% and an increase in the safety factor from 1.45 to 1.87 in the most efficient configuration. In transient mode, the system with an electric drive pump reduced the time to reach operating temperature by 9-12% and reduced integral fuel consumption by 10-12%, whilst the split-loop configuration provided a stable reduction in these figures of 6-8% and 5-7% respectively. An analysis of specific fuel consumption during braking in standard steady-state conditions revealed no statistically significant deterioration in fuel economy for the upgraded systems. The integrated ranking showed that a system with separate circuits provides a balanced combination of reduced of maximum temperature, minimised temperature gradients and increased safety margin without compromising fuel efficiency, whilst an electric drive pump is appropriate for minimising warm-up time and fuel consumption during cold starts. The practical significance of the study is determined by the development of quantitatively substantiated criteria for selecting cooling system configurations and coolant flow control strategies for engineering departments to improve thermal reliability and durability of engines

Keywords: local temperature gradients; thermal stress state; equivalent stresses; safety factor; transient heating regime; integral fuel consumption

Article's History: Received: 12.01.2026; Revised: 09.04.2026; Accepted: 21.05.2026; Published: 29.05.2026.

Suggested Citation:
Duhanets, V., Hovorov, & Pukas, V. (2026). Analysis and optimisation of internal combustion engine cooling systems to improve thermal efficiency and operational reliability. *Machinery & Energetics,* 17(2), 7-21. doi: 10.31548/machinery/2.2026.1.

*Corresponding author (duhanetsviktor@hotmail.com)

INTRODUCTION

Improvements in the thermal efficiency and reliability of modern internal combustion engines depend directly on the cooling system's ability to consistently maintain optimal temperatures across a wide range of loads and operating speeds. Overheating of critical areas of the combustion chamber, cylinder head and cylinder block accelerates wear, increases the risk of knocking and failures, whilst excessive cooling increases losses and reduces fuel efficiency. Therefore, the cooling system is regarded not merely as an auxiliary heat dissipation circuit, but as a controlled thermal subsystem module that directly influences the engine's performance and efficiency indicators, enabling a simultaneous improvement in both engine efficiency and service life.

W. Li *et al.* (2020) established, using numerical modelling of cavitation in the pump of an internal combustion engine (ICE) cooling system, that the reliability of predicting cavitation characteristics is determined by the accuracy of the cavitation model and the adequacy of the simulation of the formation and development of vapour cavities in the flow path. It is shown that cavitation not only limits the hydraulic efficiency of the pump but also reduces the reliability of the cooling system due to pressure pulsations, noise and accelerated wear of working surfaces. The optimisation of the heat transfer circuit using Computational Fluid Dynamics (CFD) methods is demonstrated in the study by S. Qin *et al.* (2022), where, using the example of a diesel engine water jacket, a causal relationship was established between the channel configuration, flow structure and the formation of the wall temperature field. It is shown that a reduction in local temperature peaks is achieved by controlling the hydrodynamics within the jacket, whereas simply increasing the coolant flow rate does not guarantee a proportional improvement in heat dissipation.

In parallel with design solutions, the role of active thermal control has been strengthened: M. Turabimana *et al.* (2023) proposed an active cooling system with a thermostat based on a shape-memory alloy, which implements adaptive control through controlled changes in the circuit's flow capacity. It has been demonstrated that replacing passive thermostating with an active approach improves the accuracy of temperature maintenance during transient conditions and simultaneously reduces the risk of overheating and losses due to overcooling. Research by D. di Battista *et al.* (2026), conducted under real-world driving conditions, showed that the coolant control strategy determines the thermal state of the engine during operational dynamics. It was established that controlling the temperature and flow rate of the coolant affects not only the intensity of warm-up and total heat losses, but also actual emission figures, transforming the cooling system into a tool for simultaneously managing efficiency and environmental parameters.

A. Sheikhi *et al.* (2026) formulated thermal management of a heavy-duty six-cylinder diesel engine as a multi-physical problem involving the interaction of combustion, coolant flow and the stress-strain state of components within a coupled Computational Fluid Dynamics – Finite Element Analysis (CFD/FEA) approach. It was demonstrated that local peaks in temperature and stress were determined not only by the flow rate and geometry of the channels, but also by the spatio-temporal distribution of heat release, which made such modelling the basis for flow redistribution and design solutions in critical zones. I. Gritsuk *et al.* (2024) proposed an adapted model for ensuring the thermal readiness of a vehicle, in which fuel flow and emission parameters are considered as integral markers of the engine's thermal state. It has been demonstrated that linking control algorithms to routinely measured operational thermal indicators (in particular, fuel consumption and emission parameters) enables the formulation of rational decisions for warm-up modes and transient processes without the need for highly detailed real-time numerical models.

D.S. Pohorletsky *et al.* (2023) examined the reliability of heat-loaded components in low-speed marine internal combustion engines in relation to low-temperature corrosion, which occurs when specific surface temperature conditions combine with the condensation of aggressive components in the peri-cylinder zone. The study demonstrated that the cooling system acts as a thermochemical regulator: temperature shifts within critical ranges can both minimise the conditions for the condensation of acidic compounds and intensify corrosion processes. The operational aspect of the internal combustion engine cooling system reliability is detailed in terms of the properties of the coolant (antifreeze). In the study by M. Nahliuk *et al.* (2023), a statistically significant correlation was established between antifreeze quality indicators and their electrical conductivity. The possibility of using electrical conductivity as an operational indicator of coolant degradation has been substantiated, which can be used for adjustment of replacement intervals and the reduction of risks of corrosive and electrochemical damage to cooling system components.

Further developments in this applied field are outlined in the work by V.I. Kholdenko (2025), which systematises methods for diagnosing cooling system pumps, with a focus on sensor-based and vibration monitoring. It is shown that the transition to preventive maintenance ensures the stability of coolant flow, maintains the specified heat balance and prevents local overheating. V.V. Pylyov *et al.* (2024) refined the empirical model of the boundary conditions for heat transfer in the piston of a high-speed diesel engine based on experimental data and approximations for identifying temperatures in control zones. It is shown that the reproduction of the mode-dependent temperature field ensures sufficient engineering accuracy in the estimation of thermal stress without increasing computational complexity.

Despite the substantial research devoted to optimisation of pump, water jacket and thermal management strategies, there is a lack of a formalised integrated approach that would simultaneously account for temperature non-uniformity in critical zones, heat dissipation intensity, fuel efficiency during transient conditions, and the thermomechanical reliability of engine components. In this regard, the study aimed to improve the thermal efficiency and operational reliability of ICEs by developing an integrated methodology for evaluating and optimising the design and control parameters of the cooling system. To achieve this objective, the following tasks were defined: to identify critical zones of ICE and develop a system of quantitative indicators of temperature non-uniformity; to assess the influence of the cooling system configuration and coolant circulation modes on heat dissipation intensity, temperature gradients and the associated stress state of engine components, with the determination of the safety factor; to develop an integrated criterion for optimising the ICE cooling system configuration, incorporating transient warm-up, fuel consumption and thermomechanical reliability indicators.

MATERIALS AND METHODS

The study was conducted between February and October 2025 under laboratory and engine test bench conditions, which enabled the reproduction of steady-state and transient thermal regimes characteristic of the operation of modern petrol internal combustion engines. The subject of the study was a 1.6-litre four-cylinder in-line engine with a closed-loop liquid cooling system and an electronically controlled thermostat. Three cooling system configurations were compared: the standard base system with a mechanical pump (S1), a system with an electric variable-displacement pump (S2), and a configuration with separate cooling circuits for the cylinder block and cylinder head (S3), in which the flow was split after the pump into two parallel branches, "block" and "cylinder head", with the standard internal bypass between the circuits shut off and a fixed flow balance established during bench setup. Comparability of the thermal load between S1-S3 was ensured by identical operating modes in terms of rotational speed and load, as well as by monitoring the effective power at control points following ISO 15550:2016 (2016).

A 50/50 water-glycol solution containing G12++ class corrosion inhibitors was used as the coolant; to improve the accuracy of the heat balance, the density $\rho(T)$ and specific heat capacity $c_p(T)$ were determined experimentally in the range 20-110°C and used as temperature-dependent input data in the heat transfer calculations. Temperatures were monitored using type K thermocouples with an error of ±0.5°C in accordance with IEC 60584-1:2013 (2013), and the coolant flow rate was monitored using an electromagnetic flow meter with an accuracy class of no worse than ±1.0%.

Signals were recorded using a multi-channel data acquisition system. Thermal imaging of the external surfaces of the cylinder block and cylinder head (temperature sensitivity 0.04°C) was used as an auxiliary means of detecting areas of local overheating and cooling anomalies; quantitative comparisons were made solely based on thermocouple data at critical control points. Additionally, fuel consumption was recorded at stationary points and during warm-up, followed by calculation of brake-specific fuel consumption (BSFC) and integral fuel consumption until operating temperature was reached. To ensure comparability between S1-S3, all series were conducted under identical external conditions and using the same operating algorithms for the test bench's auxiliary systems; in particular, the air temperature at the radiator inlet and the fan/airflow control mode were kept constant (fixed control signal and stabilisation within the test bench tolerances) to minimise unintended effects on the coolant outlet temperature.

The study was conducted in four interrelated stages. In the first stage, the intensity of heat removal via the cooling system under steady-state conditions was assessed based on measured parameters of the coolant flow. The heat flux through the cooling circuit was calculated using equation (1):

$$\dot{Q}_{cool} = \dot{m} \times c_p \times (T_{out} - T_{in}), \qquad (1)$$

where $\dot{Q}_{cool}$ – the heat flux transferred to the coolant circuit (partial heat balance of the cooling circuit); $\dot{m}$ – mass flow rate of the coolant; c_p – specific heat capacity; T_{in} and T_{out} – inlet and outlet temperatures of the engine.

The tests were conducted at speeds of 1,500, 2,500 and 3,500 rpm under loads of 25%, 50% and 75% of the rated load, whilst maintaining the temperature difference (T_{out} – T_{in}) within the range of 8-15°C, as is typical for operating conditions. Recording for each "mode-configuration" pair was performed after reaching quasi-steady state, which was determined by the stabilisation of the temperatures T_{in} and T_{out} and the coolant flow rate: for at least 120 s, the change in T_{in} and T_{out} did not exceed 0.2°C/min, and the change in flow rate did not exceed 1% (provided that n and the load remained constant within the bench tolerances). Reproducibility was verified by repeated runs at the reference point of 2,500 rpm and 50% load ($n = 2$) following an identical warm-up and stabilisation protocol, whilst the transient warm-up regime was repeated for each configuration S1-S3 ($n = 2$). The uncertainty of $\dot{Q}_{cool}$ was estimated by propagating the measurement errors $\dot{m}$, T_{in}, T_{out} and the uncertainty $c_p(T)$ following JCGM 100:2008 (2008) approach, and the difference between configurations was interpreted as practically significant if it exceeded the total estimated uncertainty of the corresponding parameters.

In the second stage, a CFD analysis of the flow and heat transfer within the cooling jacket was performed in a coupled "fluid-solid" configuration using ANSYS Fluent 2024 R1 (Ansys, Inc., 2024, USA) based on CAD geometry, solving the Navier-Stokes equations for incompressible turbulent flow using the k-ω SST model and the heat transfer equations (Menter, 1994). For configurations S1-S3, the temperature and velocity fields and local heat transfer coefficients were determined at flow rates of 40, 60 and 80 L/min and T_{in} = 85-95°C. The boundary conditions for T_{in} and flow rate were set within these ranges in accordance with the measured bench test values for each mode; in particular, for the 3,500 rpm and 75% load mode, the CFD analysis was performed for a T_{in}/flow rate combination corresponding to the bench test parameters of this mode. The computational mesh comprised 3.2-4.5 million elements, and mesh independence was accepted based on a criterion of peak temperature variation <1.5% relative to the base mesh. Validation of the CFD model was performed by comparing the calculated metal temperatures at control points on the cylinder head with experimental readings from *K*-type thermocouples at these same points; the temperatures T_{in} and T_{out} were used as input boundary conditions but were not included in the validation criterion.

Comparisons were conducted for the maximum thermal load condition at 3,500 rpm and 75% load, and additionally for the reference condition at 2,500 rpm and 50% load, which corresponded to the bench test repeatability reference point. In total, six reference points were compared, located in critical zones of the pre-chamber region (valve clearance, exhaust port area) and on the periphery of the cylinder head to assess temperature gradients; a relative deviation between calculation and measurement within 3-5% at each point was considered acceptable. CFD was used as an explanatory tool to interpret the differences between S1-S3, focusing on areas of insufficient flow and local temperature maxima. Due to the lack of replicates for most stationary points, statistical tests were not applied, and comparisons were performed using deterministic metrics, considering the specified measurement instrument errors. The key indicators were T_{max} in critical zones, distributions of heat transfer coefficients, and the identification of areas with insufficient flow as indicators of overheating risk, consistent with experimental temperature trends at control points.

In the third stage, the effect of temperature fields on reliability was assessed via the thermal stress state of the cylinder head in ANSYS Mechanical 2024 R1 (Ansys, Inc., 2024, USA), using the metal temperature fields obtained in the CFD stage in a coupled formulation as boundary conditions. The thermal load from engine operation was applied implicitly via this spatial temperature distribution for the relevant operating modes, without additionally imposing heat fluxes in the strength analysis. The material was modelled as AlSi7Mg, and the parameters $E = 70$ GPa and $\alpha = 22 \times 10^{-6}$ 1/K were specified according to technical tabulated data (Primary Foundry Alloys, n.d.). The calculation was performed in a linearly elastic formulation as a comparative indicator of the influence of cooling configurations without life (cyclic) prediction. Mises equivalent stresses σ_{vM} were calculated, and the safety factor was determined using the accepted reference value $\sigma_{0.2} \approx 240$ MPa, and the threshold $n \geq 1.5$ was applied as an engineering criterion for ranking configurations and localising potentially critical zones.

In the fourth stage, the engine warm-up transient response from 20°C to 90°C was investigated. Warm-up was performed according to a reproducible bench test protocol with a fixed speed of 2,000 rpm and a load of 25% of the rated load (the same for all S1-S3 series) under constant radiator cooling conditions; The initial state was defined as a stabilised coolant temperature of 20 ± 2°C. The time to reach 90°C was determined based on the coolant temperature and control points; additionally, the integral fuel consumption up to 90°C was calculated to establish a quantitative relationship between the cooling strategy and warm-up efficiency. For S2, the electric pump control was varied using a discrete set of at least three performance scenarios depending on the coolant temperature, which were defined as step laws with temperature thresholds and fixed levels of the electric pump control signal (as a percentage of the maximum): (i) "minimum start" – 30% at T < 60°C, 60% at 60-80°C and 100% at T ⩾ 80°C; (ii) "moderate start" – 50% at T < 60°C, 75% at 60-80°C and 100% at T ⩾ 80°C; (iii) "smooth transition" – 40% at T < 50°C, 60% at 50-70°C, 80% at 70-85°C and 100% at T ⩾ 85°C, with switching upon reaching thresholds and a hysteresis of 2°C to prevent frequent switching. For temperature-controlled systems, the effect of thermostat settings was additionally analysed by varying the target opening temperature within the range of 88-92°C and the hysteresis within the range of 3-5°C within the bench-test configuration, and assessing their impact on the heating rate and the amplitude of temperature fluctuations after reaching steady state.

Optimisation involved selecting the best configuration and control settings from among the tested options based on a set of criteria, which simultaneously required a targeted reduction in peak temperature in critical zones by 8-12%, a reduction in temperature gradients by at least 10%, and an improvement in warm-up characteristics (time and/or integral fuel consumption up to 90°C) without compromising power output and without increasing BSFC in the reference steady-state modes relative to S1. The final selection of the "optimal" solution was recorded only when the advantage according to the criteria exceeded the estimated uncertainty of the measurements of heat flux and temperature parameters.

RESULTS

Comparative assessment of heat dissipation under steady-state conditions

An assessment of the heat dissipation rate through the cooling circuit under steady-state conditions in the range of 1,500-3,500 rpm at 25-75% load revealed systematic and reproducible differences between configurations S1-S3, manifested both in the absolute values of the heat flux and in scaling with increasing rotational speed and load. Determination of the heat flux $\dot{Q}_{cool}$ in accordance with formula (1) confirmed a regular increase in heat dissipation intensity with an increase in the engine's thermal load and was used for a quantitative assessment of the impact of design changes to the cooling system. The study established that the upgraded configurations demonstrate a more pronounced response of heat dissipation to increased load compared to the base system. The summarised values of $\dot{Q}_{cool}$, obtained based on the measured parameters of the coolant mass flow rate and the temperature difference at the engine inlet and outlet, are given in Table 1.

Table 1. The value of the cooling heat flux $\dot{Q}_{cool}$ for configurations S1-S3 at speeds of 1,500-3,500 rpm under 25-75% load

n, RPM	Load, %	$\dot{Q}_{cool}$ S1, kW	$\dot{Q}_{cool}$ S2, kW	$\dot{Q}_{cool}$ S3, kW	ΔS2-S1, %	ΔS3-S1, %	U($\dot{Q}_{cool}$), kW
1,500	25	18.0	18.7	19.3	3.9	7.2	±0.5
1,500	50	24.0	25.7	26.4	7.1	10.0	±0.7
1,500	75	31.0	34.1	35.3	10.0	13.9	±0.9
2,500	25	22.0	23.1	23.8	5.0	8.2	±0.7
2,500	50	30.0	32.7	33.6	9.0	12.0	±0.9
2,500	75	40.0	44.8	46.0	12.0	15.0	±1.2
3,500	25	26.0	27.6	28.3	6.2	8.8	±0.8
3,500	50	36.0	40.0	41.0	11.1	13.9	±1.1
3,500	75	48.0	54.2	56.2	12.9	17.1	±1.4

Note: $U(\dot{Q}_{cool})$ is presented as the total estimated standard uncertainty (~3% of the S1 value in the corresponding mode). In all modes, at 50-75% load, the difference between S1 and S2/S3 exceeds the uncertainty limit, confirming the practical significance of the observed differences

Source: compiled by the authors based on JCGM 100:2008 (2008), IEC 60584-1:2013 (2013)

As shown in Table 1, for all configurations, an increase in $\dot{Q}_{cool}$ is observed as the load increases at a fixed rotational speed. Within each mode, an increase in load from 25% to 75% is accompanied by an increase in heat flux of approximately 1.7-2 times (depending on the configuration), which corresponds to an increase in indicated power and total heat release in the cylinders. At the same time, the nature and magnitude of the increase in $\dot{Q}_{cool}$ vary between configurations, indicating differences in heat dissipation efficiency and the cooling system's sensitivity to changes in thermal load. At 75% load during the transition from 1,500 to 3,500 rpm, the increase in $\dot{Q}_{cool}$ was 17 kW for S1, 20.1 kW for S2 and 20.9 kW for S3, reflecting the varying intensity of heat dissipation scaling with increasing steady-state thermal load. At the highest load point of 3,500 rpm and 75% load, S3 demonstrated the greatest deviation from the baseline configuration: the difference relative to S1 was 8.2 kW (17.1%), whilst for S2 it was 6.2 kW (12.9%); in the 50-75% load range, these differences exceeded the total estimated measurement uncertainty, confirming their reproducibility. Analysis of the temperature difference ($T_{out} - T_{in}$) as an indicator of the circuit's thermal load showed that the highest ΔT values were recorded in S1 under high-load conditions (13-15°C), whereas for S2 and S3 under the same conditions, ΔT is lower, by 0.8-1.2°C and 1.5-2.0°C, respectively. A combination of a lower ΔT with an increase in coolant flow rate corresponds to an increase in total heat removal and reflects a change in the heat transfer conditions within the circuit. The minimum difference between S2 and S3 is characteristic of low-load conditions, whereas at high-load points, the dominance of S3 increases, which is consistent with the effect of separating the block and head circuits on targeted cooling supply to areas of increased heat generation compared to a scenario where modernisation is achieved solely through a controlled electric pump. Analysis of repeat measurements at the reference point of 2,500 rpm and 50% load demonstrated reproducibility of results within 2-3%, confirming the stability of the data obtained. The deviations between repeated runs for each configuration did not exceed the total estimated uncertainty; therefore, the average values are representative for comparative analysis.

Overall, the study established that upgrading the cooling system affects not only the absolute values of the heat flux but also the nature of its scaling with increasing load and rotational speed. The S2 configuration ensures a steady increase in $\dot{Q}_{cool}$ across the entire operating range without signs of saturation at high speeds, whereas S3 demonstrates the maximum increase in heat dissipation precisely under conditions of increased thermal load. The difference between S1 and S3 under high-speed and high-load conditions exceeds the estimated measurement uncertainty, rendering it engineering significant.

Temperature distribution and thermal stress state of the cylinder head

The transition from an integrated quantitative assessment of heat dissipation to a spatial analysis of the temperature distribution revealed that the differences between configurations S1-S3 are distinctly local in nature and are caused by the non-uniformity of the flow around individual zones of the cooling jacket. The analysis was performed for the 3,500 rpm mode at 75% load, for which the CFD interpretation was formulated under boundary conditions of T_{in} = 85-95 °C and coolant flow rates of 40/60/80 L/min, which were consistent with the measured bench test parameters corresponding to the maximum $\dot{Q}_{cool}$ values established in steady-state tests. The study determined that it is precisely under increased thermal load that the design features of the cooling systems become most pronounced. A comparison of temperature fields showed that the formation of local maxima is determined by a combination of heat release intensity in the pre-chamber zone and the spatial structure of the coolant velocity field. For the base configuration S1, the highest temperature gradients were found in the inter-valve outlet zone, whereas in S2 and S3, a partial or significant reduction was observed. The identified differences are consistent with the difference in the magnitude of the total heat flux and confirm the systematic influence of the hydrodynamic organisation of the flow on the thermal state of critical components. To interpret the causes of the identified differences between the configurations, a CFD analysis of the temperature fields in the cooling jacket was performed (Fig. 1).

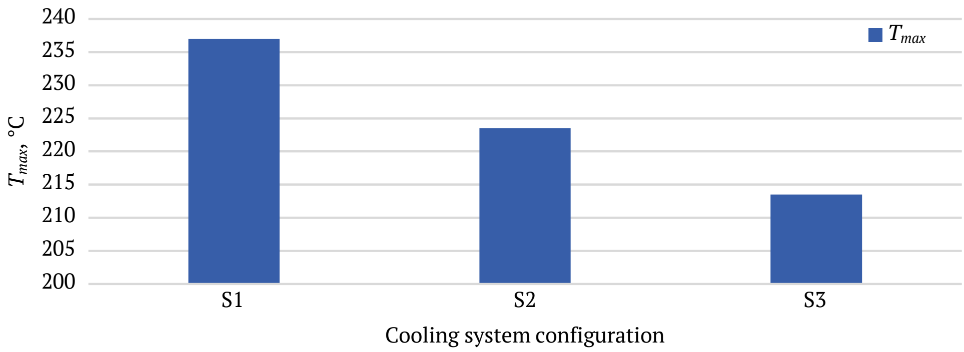

Figure 1. T_{max} in the critical area of the cylinder head for configurations S1-S3
Note: sidebars on the columns indicate the minimum and maximum T_{max} values recorded within the relevant series of calculations
Source: compiled by the authors based on F.R. Menter (1994), IEC 60584-1:2013 (2013)

Following Figure 1, in configuration S1, a local temperature maximum forms in the area between the exhaust valves of the first and second cylinders. The peak temperature T_{max} in this region was 236-238°C, which is 18-22°C higher than the average temperature across the cylinder head. Spatial analysis revealed a region of reduced coolant velocity in this zone, accompanied by a local decrease in the heat transfer coefficient and the formation of a superheated region. In the S2 configuration, the maximum temperature in the corresponding zone decreased to 222-225°C, corresponding to a reduction of 5-6% compared to S1. Comparison with the steady-state heat balance showed that the increase in coolant flow rate ensured intensified heat removal from the pre-chamber region. At the same time, the temperature distribution remained partially non-uniform: local peaks persisted near the walls of the water jacket, indicating that the hydrodynamic restrictions had not been fully eliminated. The most uniform temperature distribution was recorded in the S3 configuration. T_{max} in the critical zone did not exceed 212-215°C, corresponding to a reduction of approximately 9-11% compared to S1. At the same time, the internal temperature gradients between the pre-chamber and peripheral zones within a single cylinder decreased from 28-30°C for S1 to 18-20°C for S3, i.e. by approximately 30-35%. The separation of the cooling circuits ensured that most of the coolant flow was directed towards areas of intense heat generation and minimised parasitic flow, which stabilised temperature distribution and reduced localised peak loads.

Analysis of heat transfer coefficient *h* fields showed that in S1, the minimum values were localised at the rear of the cylinder head and in the area where the jacket channels converge, where *h* fell to 2,400-2,600 W/(m²·K), which is 18-20% lower than the average value across the surface. In S2, the minimum values increased to 2,700-2,900 W/(m²·K), whilst the area of their localisation decreased. For S3, an increase in the minimum local values to 3,100-3,300 W/(m²·K) was observed, along with the virtual absence of stagnant zones in the pre-chamber region. A comparison of the velocity fields confirmed that in S1, regions with reduced turbulent intensity formed, which limited convective heat transfer. In S2, the intensification of circulation increased local velocities, although geometrically induced recirculation zones were partially retained. In S3, the redistribution of flows smoothed the velocity profile and increased the average heat transfer coefficient in the zone of maximum thermal load by 12-15% compared to S1.

A comparison of the CFD results with experimental data from control points demonstrated a high degree of agreement: the calculated temperatures differed from the measured values by no more than 3-4%. The location of T_{max} coincided with the points of elevated temperature recorded by thermocouples in the exhaust port area, confirming the adequacy of the model. Analysis of temperature gradients within the cylinder head revealed that in S1, the difference between the maximum and minimum temperatures within a single cylinder reached 28-30°C. In S2, this figure decreased to 22-24°C, and in S3, to 18-20°C. The study established that the reduction in internal temperature gradients is directly linked to an increase in heat transfer uniformity. Thus, the CFD analysis showed that differences in total heat dissipation have a clear spatial basis. In S1, localised areas of insufficient flow cause the formation of peak temperatures and elevated gradients. In S2, intensified circulation reduces T_{max} but does not eliminate hydrodynamic limitations. In S3, the separation of the circuits ensures the most uniform temperature distribution and an increase in local heat transfer coefficients. The decrease in T_{max} in this configuration is consistent with the increase in $\dot{Q}_{cool}$ and is accompanied by a reduction in temperature gradients, which forms the basis for a further assessment of the thermal stress state.

The analysis of the thermal stress state revealed that the spatial distribution of equivalent stresses according to von Mises showed a clear correlation between the location of temperature maxima and the magnitude of temperature gradients in the near-chamber zones. The study established that the determining factor in the formation of local thermal stresses is precisely the amplitude of the temperature gradients, whilst the absolute level of the average temperature has a secondary influence. A comparison of the temperature and stress fields confirmed the coincidence of σ_{vM} concentration zones with areas of increased thermal heterogeneity, which attests to a cause-and-effect relationship between the nature of heat transfer and the stress state of the structural element. The results obtained showed that the non-uniformity of the temperature field determines the intensity of the thermomechanical load in critical zones of the cylinder head, primarily in the inter-valve space and in the area of the exhaust valve seats. To quantitatively illustrate the influence of temperature fields on the stress state, the distribution of equivalent stresses σ_{vM} is shown in Figure 2.

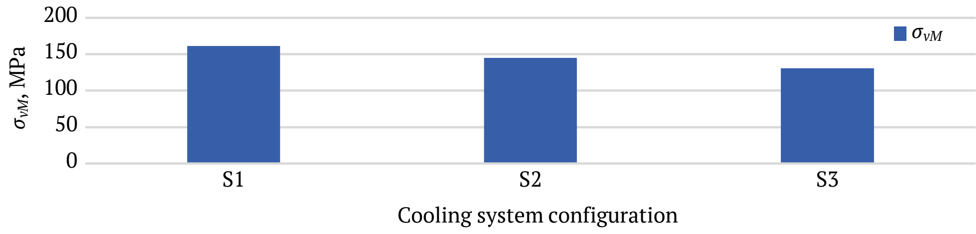

Figure 2. Maximum equivalent stresses σ_{vM} in the critical zones of the cylinder head for configurations S1-S3
Note: calculated for an operating speed of 3,500 rpm and a load of 75%. The bars represent the average values of the maximum equivalent stresses σ_{vM} in the critical zones; side-bars represent the min-max range corresponding to the minimum and maximum values of σ_{vM} recorded in the respective series
Source: compiled by the authors based on F.R. Menter (1994), Primary Foundry Alloys (n.d.)

As shown in Figure 2, in the base configuration S1, the maximum equivalent stresses were concentrated in the area between the exhaust valve seats of the first and second cylinders, as well as in the bridges between the combustion chambers. At 3,500 rpm under 75% load, the σ_{vM} values reached 158-165 MPa (average 161.5 MPa), and spatial comparison confirmed that these regions coincided with the zones of elevated temperature gradients identified in the previous stage, indicating that the formation of the stress state was thermally induced. In the S2 configuration, the maximum values of σ_{vM} decreased to 142-148 MPa (average 145.0 MPa), corresponding to a reduction of 8-10% compared to S1; at the same time, the levelling of the temperature field and the decrease in T_{max} were accompanied by a reduction in the amplitude of local deformations. The nature of stress localisation in S2 generally remained in the pre-chamber region, but the area of the high-stress zone decreased by approximately 12-15%, indicating a reduction in the degree of localisation of the thermally stressed state. The lowest values of σ_{vM} were found for the S3 configuration: in the critical zones, they did not exceed 128-134 MPa (average 131.0 MPa), which is 18-22% lower than for S1; the stress distribution became more uniform, and the peak values lost the form of sharply pronounced local concentrations. Thus, the separation of the cooling circuits ensured not only a reduction in T_{max}, but also a quantitatively confirmed decrease in equivalent stresses in the cylinder head.

The structural reliability assessment showed that for S1, under maximum thermal load conditions, the safety factor decreased to $n = 1.45\text{-}1.52$, whilst in certain sections of the crossbeams it approached the threshold value of $n \geqslant 1.5$, indicating that these areas are particularly sensitive to thermal cycling. In S2, the safety factor increased to 1.62-1.69 in the most heavily loaded sections, ensuring consistent compliance with the criterion throughout the entire volume of the cylinder head. The most favourable indicators were observed in S3: n ranged from 1.78 to 1.87 in critical zones and exceeded the threshold value by a significant margin in all investigated conditions. Analysis of the stress distribution across the thickness of the block head confirmed that in S1, temperature gradients created a combination of tensile stresses in the near-surface layers and compressive stresses deeper within the material; the difference between them exceeded 60 MPa. In S2, this difference decreased to 45-50 MPa, and in S3 to 35-40 MPa, which is consistent with the levelling of the temperature field and the reduction of internal thermomechanical gradients. Thus, the results of the thermal stress analysis confirmed a clear cause-and-effect relationship between the cooling system architecture, the nature of the temperature field, and the level of thermal stresses in the cylinder head. The reduction in T_{max} and temperature gradients in the S3 configuration was accompanied by a significant decrease in σ_{vM} and an increase in the safety factor, confirming its superiority in terms of durability and thermal reliability compared to S1 and S2.

Analysis of the transient warm-up regime

An analysis of the transient warm-up behaviour, conducted under reproducible bench test conditions with an initial coolant temperature of 20 ± 2°C, revealed significant differences in the dynamics of the engine reaching its operating temperature for configurations S1-S3. The time taken to reach operating temperature was determined by the average coolant temperature in the main circuit reaching 90°C. The study established that the cooling system architecture directly influences the duration of the transient process and the intensity of the initial heating, which is reflected both in the time taken to reach 90°C and in the nature of the temperature curve. The dynamics of engine warm-up from 20 to 90°C for configurations S1-S3 are shown in Figure 3.

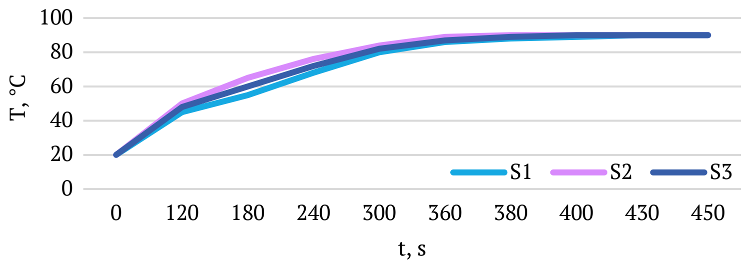

Figure 3. Coolant temperature curves for configurations S1-S3
Source: compiled by the authors based on JCGM 100:2008 (2008), IEC 60584-1:2013 (2013)

The data shown in Figure 3 demonstrates that the use of a variable-capacity electric pump resulted in a faster reach of the operating temperature range compared to the baseline configuration. For S1, the time taken to reach 90°C averaged 420-435 s, whereas for S2 this figure fell to 370-385 s, representing a reduction of 9-12%. Configuration S3 demonstrated an intermediate result – 395-405 s, corresponding to a 6-8% reduction in warm-up time relative to S1. The reduction in warm-up time achieved in S2 and S3 exceeds the limits of the total estimated measurement uncertainty, confirming the engineering significance of the effect. Analysis of the temperature curves showed that in S1, the heating process is nearly linear until the thermostat opens, after which the rate of temperature rise decreases due to the connection of the main circuit and the activation of circulation through the radiator. In the S2 configuration, a more intense initial rise in temperature was observed, which correlates with a reduction in the electric pump's performance during the cold start phase. The restriction of coolant flow in the first few minutes of operation was accompanied by a reduction in heat dissipation and an acceleration in reaching the operating temperature range without exceeding permissible values. For S3, the warm-up behaviour remained stable and controlled: the initial phase was more intense than in S1, but less pronounced compared to S2, reflecting the effect of circuit separation under constant circulation parameters.

The total fuel consumption up to 90°C showed a clear correlation with the duration of the warm-up. For S1, this figure was 0.082-0.086 kg of fuel, whilst for S2 it decreased to 0.073-0.076 kg, corresponding to a saving of 10-12%. In the S3 configuration, the integral consumption was 0.078-0.080 kg, i.e., a reduction of 5-7% compared to the base system. The comparison showed that the fuel savings achieved exceed the limits of experimental uncertainty and are statistically significant.

It has been established that reducing the duration of engine operation in the rich-mixture mode directly reduces the total fuel consumption during the transition phase. Further analysis of electric pump control scenarios in S2 showed that using a minimum flow rate until 60°C is reached, followed by a stepwise increase in coolant flow, resulted in the shortest warm-up time – approximately 370 s. When a smooth linear dependence of flow rate on temperature was applied, the warm-up time increased by 4-6%, but the amplitude of temperature fluctuations after the thermostat opened decreased. The comparison confirmed that a discrete strategy with clearly defined temperature thresholds provides better fuel efficiency without adversely affecting thermal stability. Analysis of steady-state conditions after warm-up completion revealed no increase in BSFC for S2 and S3 relative to S1. At 2,500 rpm under 50% load, the difference in BSFC between S1 and S2 did not exceed 1.5%, which is within the experimental uncertainty. Thus, accelerated warm-up is not accompanied by a deterioration in fuel efficiency under steady-state conditions.

Temperature fluctuations after reaching 90°C were considered as an indicator of the stability of thermal regulation. In S1, the amplitude of the fluctuations was 6-8°C, whereas in S2, under the optimal control algorithm, it decreased to 4-5°C. In S3, the amplitude was 5-6°C. It was established that adaptive control of coolant flow rate contributes to increased thermal stability after reaching operating temperature. Thus, the results of the transient analysis showed that configuration S2 provides the shortest warm-up time and minimum integral fuel consumption without compromising BSFC performance in steady-state conditions. Configuration S3 demonstrates a moderate reduction in warm-up time and fuel consumption, whilst simultaneously improving temperature uniformity and reducing the thermal stresses identified previously. The data obtained confirmed that optimising the cooling system can simultaneously improve the engine's thermal reliability and fuel efficiency, and that adaptive control of the electric pump's performance is an effective tool for reducing fuel consumption in cold start conditions without adversely affecting steady-state operating characteristics.

Integral ranking and selection of the optimal configuration

A comprehensive analysis of the results from all stages of the study has shown that the differences between configurations S1-S3 are systematic in nature and manifest simultaneously in terms of heat dissipation, temperature uniformity, thermal stress, and fuel efficiency during transient operation. The generalisation was conducted by directly comparing quantitative indicators with the accepted optimisation criteria without introducing additional empirical coefficients or new input data. For a comprehensive assessment of the efficiency of the configurations under study, a generalised matrix of optimisation criteria was formed, in which, for each variant S1-S3, the achieved level of reduction in peak temperatures, internal temperature gradients, equivalent stresses, as well as indicators of transient and steady-state fuel efficiency are shown (Table 2).

Table 2. Comparative matrix of optimisation criteria for S1-S3

Criteria	S1	S2	S3
Reduction in T_{max} relative to S1	-	5-6%	10-12%
Reduction in temperature gradients	-	18-22%	30-35%
Maximum σ_{vM}, MPa	158-165	142-148	128-134
Safety factor n	1.45-1.52	1.62-1.69	1.78-1.87
Reduced warm-up time	-	9-12%	6-8%
Reduction in overall fuel consumption	-	10-12%	5-7%
Changes in BSFC under steady-state conditions	-	⩽1.5%	⩽1.5%
Excess of the effect over the estimated measurement uncertainty ($\dot{Q}_{cool}$, T_{max}, ΔT)	-	confirmed	confirmed

Source: compiled by the authors based on F.R. Menter (1994), JCGM 100:2008 (2008)

Analysis of the data in Table 2 showed that the base configuration S1, under maximum thermal load conditions, is characterised by peak temperatures and stresses that locally approach the threshold conditions for long-term reliability. The safety factor n for S1 decreased to 1.45-1.52, i.e., in certain inter-valve zones it reached the minimum permissible level of 1.5. A comparison with the results of the spatial temperature analysis confirmed that the key cause of critical stresses is precisely temperature inhomogeneity and high internal gradients, rather than merely the absolute level of the metal's average temperature. Regarding the criterion of reducing T_{max} by 8-12%, it was found that configuration S2 reduced the peak temperature in critical zones by only 5-6%, i.e., it did not reach the specified range, although it demonstrated a noticeable improvement compared to S1. In contrast, configuration S3 demonstrated a reduction in T_{max} of 10-12%, which fully meets the specified limit and ensures a significant "reduction" in peak temperatures from potentially dangerous levels. This indicates that it is the structural modernisation of the cooling system (separation of the block and head circuits) that has a decisive influence on maximum temperatures in the areas of greatest thermal load. Concerning the criterion of reducing temperature gradients by at least 10%, it was found that the S2 configuration reduced internal temperature gradients by approximately 18-22% compared to S1; that is, the result exceeded the minimum acceptable level and indicates a noticeable smoothing of the difference between the near-surface and deeper layers. In configuration S3, an even more significant reduction in temperature gradients of 30-35% was recorded, indicating a qualitatively different degree of thermal field equalisation. The consistency of this effect with the results of the CFD analysis confirmed that the separation of the cooling circuits provides a structural, rather than a local compensatory, reduction in thermal heterogeneity, which is of fundamental importance for the durability of the cylinder head.

An assessment of the thermal stress state showed that the maximum values of σ_{vM} decreased from 158-165 MPa in S1 to 142-148 MPa in S2 and to 128-134 MPa in S3; that is, the total reduction for S3 was approximately 18-22% compared with the base configuration. This was directly reflected in an increase in the safety factor to 1.78-1.87 in S3. The study established that for this configuration, the criterion $n \geqslant 1.5$ was met with a significant margin in all modes considered, whereas in S2 the value $n = 1.62$-1.69 ensured reliable compliance with the threshold, but with a narrower "safety margin". Thus, in terms of long-term strength and resistance to thermal cycling loads, S3 has the most favourable margin, whilst S2 remains a compromise between improved warm-up and reduced stresses. Transient analysis showed that the shortest warm-up time was achieved by the S2 configuration: the reduction was 9-12% compared to S1, with a corresponding decrease in total fuel consumption of 10-12%. For S3, the warm-up time was reduced by 6-8%, and the integral fuel consumption by 5-7%, which also exceeds the limits of experimental uncertainty. The comparison confirmed that the effects of both upgraded configurations in transient mode are engineering-significant and provide real fuel savings in cold start mode. However, the analysis of steady-state conditions revealed no deterioration in BSFC for S2 and S3: the differences did not exceed 1.5% and fell within the experimental margin of error, determining a trade-off of the "faster warm-up – poorer efficiency" type at the reference steady-state points.

A comprehensive comparison based on uncertainty analysis showed that, for the key criteria – reduction of T_{max}, reduction of σ_{vM} and reduction of warm-up time – the advantage of S2 and S3 over S1 exceeds the limits of the total measurement uncertainty by a factor of 2-3, confirming the reliability and practical significance of the established differences. At the same time, the integrated ranking revealed different "specialisations" of the upgrades: configuration S2 demonstrated the greatest effect in terms of transient thermal and fuel efficiency, whilst S3 provided the best balance between reducing peak temperatures, minimising temperature gradients and increasing the safety factor without any deterioration in steady-state fuel economy. Thus, the results of the integrated ranking showed that the S3 configuration is the most balanced engineering-determined solution among the options studied, as it is the only one that fully meets the criteria for reducing T_{max} (8-12%) and decreasing temperature gradients (by at least 10%, with an actual reduction of 30-35%) whilst providing an increased safety margin ($n \geqslant 1.5$ with a substantial reserve) and no deterioration in BSFC under steady-state conditions. The comparison confirmed that the advantages of S3 are quantitatively proven and exceed the total measurement uncertainty, which justifies recommending this particular configuration as optimal in terms of improving thermal efficiency, durability and engine reliability.

DISCUSSION

The results of thermal modelling and experimental measurements showed that the architecture of the cooling system determined not only the overall level of heat dissipation, but also the spatial structure of the temperature field and the associated thermal stress state of the cylinder head. The increase in $\dot{Q}_{cool}$ in configurations S2 and S3, the reduction in T_{max} in critical inter-valve zones to 222-225°C and 212-215°C, respectively, as well as the reduction in internal temperature gradients to 18-20°C for S3 is consistent with the concept of nodal thermal modelling proposed by D. Chalet *et al.* (2017), according to which local overheating of cylinder head components arises due to the uneven distribution of heat fluxes between functional nodes and the restriction of convective heat transfer in individual channels. The study demonstrated that optimising coolant circulation trajectories and redistributing flows between subsystems makes it possible to simultaneously reduce peak temperatures and equalise the thermal field. This mechanism was replicated for S3, where the separation of the block and head circuits ensured an increase in the minimum local heat transfer coefficients and a reduction in stagnant flow zones. The identified relationship between the magnitude of temperature gradients and the level of equivalent stresses σ_{vM} confirmed the decisive role of spatial heterogeneity in heating, rather than just the absolute temperature of the metal.

The CFD results for S3 demonstrated an increase in the minimum local heat transfer coefficients and the virtual elimination of stagnation and recirculation zones in the pre-chamber region, indicating a change in the coolant flow path as the mechanism for reducing temperature peaks. This interpretation is consistent with the findings of L. Tan *et al.* (2023), who attributed the reduction in local overheating to the shortening of inefficient hydrodynamic paths and the redistribution of flow between branches. In terms of the causal chain, the effect was described as "modification of channel geometry → smoothing of the velocity profile → increase in local h → reduction in temperature gradients", which explained the simultaneous reduction in T_{max} and smoothing of the temperature profile in S3. Furthermore, H. Salehi *et al.* (2023) demonstrated experimentally and numerically that passive flow control in cooling channels reduces the proportion of recirculation zones, increases the intensity of local convection, and lowers peak metal temperatures. The S3 data obtained in the present study reproduced this mechanism and indicated the priority of structural improvement of the circulation path over simply increasing the flow rate. Therefore, the CFD/FEA structural block is consistent with the coupled heat transfer approach and can be reduced to a single mechanism: reorganising the flow in the cooling jacket increases the local h and eliminates stagnation and recirculation zones, which reduces T_{max}, stabilises the temperature field (reducing gradients), and, as a result, reduces σ_{vM} whilst increasing the safety margin. A. Pandey *et al.* (2024) demonstrated that "hot spots" were caused by the combined effect of convection within the channels, thermal conductivity in the metal and adjacent circuits; consequently, hydrodynamic changes were systematically translated into the stress state. Following the same line of reasoning, L. Yang *et al.* (2024) established those geometric modifications which smooth the velocity field and eliminate recirculation and stagnation reduce local overheating, corresponding to the S3 configuration with a sustained reduction in peak temperatures, temperature gradients and σ_{vM} in the context of an increase in $\dot{Q}_{cool}$.

Transient warm-up analysis showed that S2 reduced the time taken to reach 90°C by 9-12% and lowered the total fuel consumption by 10-12%. Similarly to R. Bakatwar *et al.* (2018), limiting coolant flow at start-up reduces heat loss during the "cold" phase and accelerates entry into the operating temperature window. The temperature-threshold strategy for controlling the electric pump was interpreted within this same causal framework: reducing output to 60°C ensured heat accumulation in the early phase without exceeding permissible limits. Once the thermostat opened, the key factor was not so much the absolute temperature as the stability of the operating mode, and the reduction in the amplitude of fluctuations to 4-5°C in S2 was consistent with the findings of H. Savaripour *et al.* (2022) for a thermostat with map-based control, where temperature-dependent flow control reduced overshoot during the transition to steady-state conditions. A pattern emerged: adaptive control simultaneously reduced warm-up time and stabilised the temperature field without compromising steady-state fuel efficiency (BSFC did not rise beyond the uncertainty limit), whereas integral ranking revealed different "specialisations" of the upgrades: S2 maximised the gain in the transient phase, whilst S3 ensured a deeper structural reduction in T_{max} and gradients with a direct transition to a less thermally stressed state. The trends obtained supported the interpretation of the cooling system as a controlled loop in transient modes. S.-J. Jeong *et al.* (2024) demonstrated that the switching speed of the controlled elements and the flow control algorithm altered the shape of the temperature curve; consequently, the control system itself determined both the heating rate and the amplitude of oscillations once steady-state conditions were reached.

Following the same logic, the results of S2 correlated with the predictive control approach proposed by A. Kaleli (2020), where the predictive adjustment of the coolant flow rate accelerated warm-up and suppressed oscillations through a feedforward action; in the case under consideration, this principle was implemented through a threshold restriction on circulation in the early phase, followed by a controlled increase. In contrast, the advantage of S3 under heavy loads is consistent with the load- and speed-sensitive cooling map approach proposed by A. Naderi *et al.* (2021). In their study, optimal thermal behaviour was achieved not by a constant increase in flow rate, but by its targeted adaptation to the thermal load. In the presented study, the separation of circuits in S3 ensured that cooling resources were prioritised for areas of maximum heat dissipation; consequently, the effect naturally intensified with increasing load and manifested as a more significant reduction in T_{max} and temperature gradients than in S2.

The accelerated warm-up and temperature stabilisation were not accompanied by a deterioration in BSFC at steady-state points (differences ⩽1.5% within the margin of uncertainty). B. Lu *et al.* (2023) emphasised the need to maintain a stable temperature "window" under non-design conditions to prevent efficiency losses during integration with waste heat recovery circuits. In this context, the reduction in the amplitude of temperature fluctuations in configurations S2 and S3 after reaching the operating level was interpreted as the establishment of a controlled temperature regime, compatible with the subsequent expansion of energy integration. Such stabilisation of the temperature profile after reaching the operating level was consistent with approaches to predictive model control in vehicle thermal management tasks, where the regulation of coolant flow was considered as a tool for simultaneously minimising heat losses during the warm-up phase and adhering to constraints regarding temperature stability and the risk of local overheating in transition zones. In the study by P. Lu *et al.* (2019), Model Predictive Control (MPC) was described as an approach to coordinating heat transfer between the under-bonnet space and thermal subsystems, within which flow control performed an energy-oriented function without losing stabilisation capability. In this causal framework, the S2 effect was interpreted as a controlled change in the effective "thermal resistance" during the warm-up phase (restriction of circulation followed by a controlled increase), whilst the reduction in oscillation amplitude after reaching the operating temperature reflected the absence of overshoot and compliance with temperature limits.

The results regarding temperature stabilisation after reaching steady state correlated with approaches involving integrated valve modules and multi-channel flow control. L. Pimpinella *et al.* (2021) demonstrated that such modules provided more accurate flow distribution between branches, improving the stability of the cooler temperature and reducing overshoot. In the case under consideration, a similar effect was achieved through the electric pump control algorithm and the split-loop architecture, i.e., through controlled flow redistribution, which reduced thermal mode fluctuations. This is consistent with the review by H. Liu *et al.* (2021), which highlighted the shift from passive temperature maintenance to active thermal management using controlled pumps, thermostats and mode-dependent maps. Within this framework, the results obtained demonstrated the functional differentiation of the upgrades: S2 provides the best warm-up performance and fuel economy in cold mode, whilst S3 produces a more uniform temperature field and minimal thermal stresses, which explains its advantage in terms of durability. Further development of this approach was linked to hybrid "simulation + machine learning" solutions. Y. Zou *et al.* (2025) demonstrated the possibility of predicting the performance of electric fans and electric pumps based on a combination of modelling and machine learning, which created the possibility of more precise control under variable operating conditions. In the context of the results obtained, this is relevant as the performance of S2 in cold mode remained sensitive to the parameterisation of the control algorithm, and improving the accuracy of the prediction made it possible to maintain the fuel efficiency whilst ensuring temperature stability.

From an energy efficiency perspective, the findings are consistent with the approach of minimising the parasitic power of the cooling system. P.H.A. Brayner *et al.* (2024) demonstrated that reducing the power consumption of the pump or fan drive can improve fuel economy without compromising the engine's thermal performance. The observed fuel savings in transient mode for S2 were explained precisely by this mechanism: a reduction in the electric pump's output during a cold start reduced the energy costs of circulation and limited heat dissipation, thereby shortening the duration of the cold phase. At the same time, the absence of noticeable changes in BSFC at steady-state points confirmed that the effect of minimising parasitic power was primarily evident in dynamic modes.

This interpretation was supported by models of bypass circulation circuits. R.I.A. Jalal *et al.* (2021) demonstrated that a bypass electric water pump reduced warm-up time by limiting heat dissipation in the "large" circuit during the early stages and concentrating heat to accelerate warm-up. Although in S2 this effect was achieved through variable capacity, the underlying mechanism remained similar – controlled circulation restriction reduced heat loss and shortened the duration of the cold phase. In this same context, G. Kaltakkıran (2021) emphasised that during warm-up, the cooling strategy determined the distribution of energy between useful work, metal heating and losses to the environment. The practical significance of this effect is also confirmed by the results of M. di Bartolomeo *et al.* (2023), which show that the electric pump delivered measurable fuel savings and CO_2 reductions provided that control was coordinated with the engine's thermal requirements across the various phases of the cycle. The bench test results demonstrated a similar pattern: savings were achieved by shortening the cold phase, whilst a stable temperature window was maintained at steady-state points without any deterioration in BSFC. To extend the observed effects to a wider operating range, a coordinated description of heat transfer and hydraulic losses is required, as these components determine the limits of further parametric optimisation. The study by A. Jafari *et al.* (2022) demonstrates that the error in predicting the performance of a cooling system is determined by the degree of consistency between the heat transfer and pressure loss models, which influence temperature stability and the energy consumption of the circulation. In this context, the results obtained were interpreted as a consequence of the control and architecture under fixed radiator characteristics and hydraulic resistances, which imposed constraints on the subsequent tuning of parameters and determined the conditions for reproducibility across a wider range of operating modes.

An analysis of the experimental data and numerical simulations showed that combining structural optimisation of the cooling circuit with adaptive flow control created a unified circuit of thermo-hydrodynamic and thermomechanical processes, within which T_{max}, internal temperature gradients and σ_{vM} were reduced, whilst the safety margin increased, whilst fuel savings during warm-up were achieved without compromising BSFC at steady-state points. This reflected the integration of duct geometry, mode-dependent control and energy coordination within a single engineering loop of the engine cooling system's operation.

CONCLUSIONS

This study conducted a comprehensive assessment of the impact of the cooling system architecture on the thermal efficiency, thermal stress conditions and fuel economy of a petrol internal combustion engine under steady-state and transient conditions. The study demonstrated that the modernisation of the standard S1 system using a variable-capacity electric pump (S2) and the separation of the block and head cooling circuits (S3) results in systemic differences that manifest themselves consistently in terms of heat dissipation, temperature fields, stresses and warm-up dynamics. In steady-state conditions, an increase in the heat flux $\dot{Q}_{cool}$ for S2 and S3 of 10-17% relative to S1 has been established in zones of maximum thermal load, accompanied by a reduction in ΔT between the inlet and outlet under constant external conditions, i.e., an intensification of convective heat transfer without circuit overload.

CFD analysis confirmed that the reduction in peak temperatures in the pre-chamber zones is 5-6% for S2 and 10-12% for S3, whilst internal temperature gradients decrease by approximately 18-22% and 30-35% respectively, reflecting a transition from localised overheated regions in S1 to a more uniform temperature field in S3. This correlates directly with a decrease in equivalent stresses σ_{vM} from 158-165 to 128-134 MPa and an increase in the safety factor n from 1.45-1.52 to 1.78-1.87, meaning that in the S3 configuration, the criterion $n \geqslant 1.5$ is met with a significant margin for all analysed modes. In the transient warm-up mode, it was found that the S2 variant reduces the time to reach 90°C by 9-12% and decreases the integral fuel consumption by 10-12% compared to S1, whilst S3 provides a moderate, but reproducible reduction in these indicators of 6-8% and 5-7% respectively, whilst simultaneously improving temperature uniformity. Analysis of BSFC in control steady-state modes showed that accelerated warm-up and modernisation of the cooling system are not accompanied by a statistically significant deterioration in fuel efficiency: the differences do not exceed the limits of experimental uncertainty. Integral ranking accounting for uncertainty confirmed that the S2 configuration is the most effective in terms of minimising warm-up time and fuel consumption in cold-start mode, whereas configuration S3 provides the best balance between reducing T_{max}, minimising temperature gradients, reducing σ_{vM} and establishing an increased safety margin without compromising fuel efficiency.

The results obtained provide a sound basis for recommending S3 as the optimal engineering solution for improving the thermal reliability and durability of internal combustion engines, whilst S2 should be considered a targeted option for applications where reducing warm-up time and emissions during the cold start phase is a priority. Further research should analyse long-term cyclic operation of the upgraded systems, adapting the pump control algorithms to different load profiles, and scaling the proposed solutions to other engine types and displacement volumes.

ACKNOWLEDGEMENTS

None.

FUNDING

None.

CONFLICT OF INTEREST

None.

REFERENES

[1] Bakatwar, R., Nesamani, K., Bhargava, A., & Jain, R. (2018). Performance analysis & optimization of engine cooling system by using electronically controlled thermostat for improving thermal efficiency. *SAE Technical Paper*. doi: 10.4271/2018-01-0053.

[2] Brayner, P.H.A., da Costa, J.Â.P., Ochoa, A.A.V., Urbano, J.J., Leite, G.N.P., & Michima, P.S.A. (2024). Analysis and optimization of the fuel consumption of an internal combustion vehicle by minimizing the parasitic power in the cooling system. *Processes*, 12(2), article number 321. doi: 10.3390/pr12020321.

[3] Chalet, D., Lesage, M., Cormerais, M., & Marimbordes, T. (2017). Nodal modelling for advanced thermal-management of internal combustion engine. *Applied Energy,* 190, 99-113. doi: 10.1016/j.apenergy.2016.12.104.

[4] Di Bartolomeo, M., Di Battista, D., & Cipollone, R. (2023). Experimentally based methodology to evaluate fuel saving and CO_2 reduction of electrical engine cooling pump during real driving. *SAE International Journal of Engines,* 16(5), 693-708. doi: 10.4271/03-16-05-0041.

[5] Di Battista, D., di Bartolomeo, M., & Cipollone, R. (2026). The performance of engine coolant control strategies on real driving emissions. *Applied Thermal Engineering*, 289(1), article number 129753. doi: 10.1016/j.applthermaleng.2026.129753.

[6] Gritsuk, I., Pohorletskyi, D., Bulgakov, M., Khudiakov, I., Volodarets, M., Smyrnov, O., Korohodskyi, V., Symonenko, R., Holovashchenko, O., & Hrytsuk, V. (2024). Development of an approach to the construction of an adapted model for ensuring the thermal readiness processes of a vehicle based on fuel consumption and exhaust gas emissions. *Eastern-European Journal of Enterprise Technologies*, 6(4(132)), 26-45. doi: 10.15587/1729-4061.2024.316922.

[7] IEC 60584-1:2013. (2013). *Thermocouples – part 1: EMF specifications and tolerances*. Retrieved from https://webstore.iec.ch/en/publication/2521.

[8] ISO 15550:2016. (2016). *Internal combustion engines – determination and method for the measurement of engine power – general requirements*. Retrieved from https://www.iso.org/standard/70030.html.

[9] Jafari, A., Sadeghianjahromi, A., & Wang, C.-C. (2022). Experimental and numerical investigation of brazed plate heat exchangers – a new approach. *Applied Thermal Engineering,* 200, article number 117694. doi: 10.1016/j.applthermaleng.2021.117694.

[10] Jalal, R.I.A., Yusoff, M.A.M., Hasan, H.M.A., & Yahya, M.N. (2021). Simulation of bypass electric water pump to reduce the engine warm-up time. *Journal of Mechanical Engineering Science,* 15(3), 8241-8252. doi: 10.15282/jmes.15.3.2021.03.0647.

[11] JCGM 100:2008. (2008). *Evaluation of measurement data – guide to the expression of uncertainty in measurement.* Retrieved from https://www.bipm.org/documents/20126/2071204/JCGM_100_2008_E.pdf.

[12] Jeong, S.-J., Kang, J.-H., Moon, S.-J., & Lee, G.-S. (2024). Transient and dynamic simulation of the fluid flow through five-way electric coolant control valve of a 100 kW fuel cell vehicle by CFD with moving grid technique. *Actuators*, 13(3), article number 110. doi: 10.3390/act13030110.

[13] Kaleli, A. (2020). Development of the predictive based control of an autonomous engine cooling system for variable engine operating conditions in SI engines: Design, modeling and real-time application. *Control Engineering Practice,* 100, article number 104424. doi: 10.1016/j.conengprac.2020.104424.

[14] Kaltakkıran, G. (2021). A study on the effects of coolant strategy on the instantaneous energy balance during the warm-up period in a spark ignition engine. *International Journal of Innovative Research and Reviews,* 5(2), 1-8.

[15] Kholdenko, V.I. (2025). Analysis of existing methods for diagnostic of ship pumps. *Visnyk of Kherson National Technical University*, 1(2(93)), 280-286. doi: 10.35546/kntu2078-4481.2025.2.1.36.

[16] Li, W., Li, E., Shi, W., Li, W., & Xu, X. (2020). Numerical simulation of cavitation performance in engine cooling water pump based on a corrected cavitation model. *Processes,* 8(3), article number 278. doi: 10.3390/pr8030278.

[17] Liu, H., Wen, M., Yang, H., Yue, Z., & Yao, M. (2021). A review of thermal management system and control strategy for automotive engines. *Journal of Energy Engineering,* 147(2). doi: 10.1061/(ASCE)EY.1943-7897.0000743.

[18] Lu, B., Zhang, Z., Cai, J., Wang, W., Ju, X., Xu, Y., Lu, X., Tian, H., Shi, L., & Shu, G. (2023). Integrating engine thermal management into waste heat recovery under steady-state design and dynamic off-design conditions. *Energy,* 272, article number 127145. doi: 10.1016/j.energy.2023.127145.

[19] Lu, P., Gao, Q., Lv, L., Xue, X., & Wang, Y. (2019). Numerical calculation method of model predictive control for integrated vehicle thermal management based on underhood coupling thermal transmission. *Energies*, 12(2), article number 259. doi: 10.3390/en12020259.

[20] Menter, F.R. (1994). Two-equation eddy-viscosity turbulence models for engineering applications. *AIAA Journal,* 32(8), 1598-1605. doi: 10.2514/3.12149.

[21] Naderi, A., Qasemian, A., Shojaeefard, M.H., Samiezadeh, S., Younesi, M., Sohani, A., & Hoseinzadeh, S. (2021). A smart load-speed sensitive cooling map to have a high-performance thermal management system in an internal combustion engine. *Energy,* 229, article number 120667. doi: 10.1016/j.energy.2021.120667.

[22] Nahliuk, M., Pavlenko, V., Kuzhel, V., & Chernenko, P. (2023). Quality indicators of antifreeze and their correlation with electrical conductivity during the intercity buses operation. *Journal of Mechanical Engineering and Transport*, 17(1), 108-113. doi: 10.31649/2413-4503-2023-17-1-108-113.

[23] Pandey, A., Schlautman, J., Liu, Z., Dhar, S., & Yashwanth, B.L. (2024). Conjugate heat transfer analysis of an i-4 engine including pistons, liners, block, heads, water cooling jacket, and oil cooling jets. *SAE Technical Paper*. doi: 10.4271/2024-01-2696.

[24] Pimpinella, L., Mikuláš, O., Ko, M.S., Bae, I.H., Herceg, M., Pekař, J., Kim, Y.K., & Jung, Y.H. (2021). Advanced coolant temperature control study with integrated thermal management system valve. *IFAC-PapersOnLine,* 54(6), 200-205. doi: 10.1016/j.ifacol.2021.08.545.

[25] Pohorletsky, D.S., Gritsuk, I.V., Khudiakov, I.V., Chernenko, V.V., & Polishuk, A.V. (2023). Features of low-temperature corrosion protection of cylinder sleeves of ship low-speed engines. *Reporter of the Priazovskyi State Technical University. Section: Technical Sciences*, 46, 122-130. doi: 10.31498/2225-6733.46.2023.288181.

[26] Primary Foundry Alloys. (n.d.). *Technical data sheet: AlSi7Mg0.3*. Retrieved from https://cdn.thomasnet.com/ccp/00176659/102129.pdf.

[27] Pylyov, V.V., Linkov, O.Y., & Marchenko, A.P. (2024). Refining the empirical model of the heat transfer boundary conditions of the piston of a high-speed diesel engine. *Internal Combustion Engines,* 2, 3-11. doi: 10.20998/0419-8719.2024.2.01.

[28] Qin, S., Xie, C., Li, S., Yang, Q., Chen, J., & Sun, K. (2022). CFD analysis and optimization of a diesel engine cooling water jacket. *Fluid Dynamics & Materials Processing*, 18(3), 647-659. doi: 10.32604/fdmp.2022.017519.

[29] Salehi, H., Savaripour, H., Bidhendi, H.M.M., Farhani, F., & Rosen, M.A. (2023). Experimental and simulation study of an automobile cooling system: Performance improvement using passive flow control. *International Communications in Heat and Mass Transfer,* 149, article number 107168. doi: 10.1016/j.icheatmasstransfer.2023.107168.

[30] Savaripour, H., Hosseini, S.A., Nasrollahnezhad, S., Jahangiri, A., & Rosen, M.A. (2022). Investigation of engine's thermal management based on the characteristics of a map-controlled thermostat. *International Communications in Heat and Mass Transfer,* 135, article number 106156. doi: 10.1016/j.icheatmasstransfer.2022.106156.

[31] Sheikhi, A., Saray, R.K., Ghazani, A.S., Geimechi, A., & Lashkarpour, S.M. (2026). Thermal management and optimization of a 6-cylinder heavy-duty diesel engine: A two-way coupled CFD, FEA and combustion numerical study. *Fuel*, 405(C), article number 136634. doi: 10.1016/j.fuel.2025.136634.

[32] Tan, L., Yuan, Y., & Huang, C. (2023). CFD modelling on flow field characteristics of engine cooling water jacket and its cooling performance improvement based on coolant transport path analysis method. *Proceedings of the Institution of Mechanical Engineers, Part A: Journal of Power and Energy*, 237(2), 385-401. doi: 10.1177/09576509221116503.

[33] Turabimana, M., Sohn, J.W., & Choi, S.-B. (2023). A novel active cooling system for internal combustion engine using shape memory alloy based thermostat. *Sensors*, 23(8), article number 3972. doi: 10.3390/s23083972.

[34] Yang, L., Lu, G., & Wang, T. (2024). Structure improvement of two-cylinder engine cooling water jacket based on flow field simulation. *Sustainability*, 16(24), article number 11092. doi: 10.3390/su162411092.

[35] Zou, Y., Li, R., Pan, H., Sun, X., & Fu, J. (2025). Performance prediction of electronic fan and water pump of engine cooling system based on joint simulation and machine learning. *Scientific Reports,* 15, article number 15672. doi: 10.1038/s41598-025-00313-x.

Віктор Дуганець

Доктор педагогічних наук, професор
Заклад вищої освіти «Подільський державний університет»
32316, вул. Шевченка, 12, м. Кам'янець-Подільський, Україна
https://orcid.org/0000-0002-3383-5907

Олександр Говоров

Кандидат технічних наук, старший науковий співробітник
Заклад вищої освіти «Подільський державний університет»
32316, вул. Шевченка, 12, м. Кам'янець-Подільський, Україна
https://orcid.org/0000-0002-1645-1725

Віталій Пукас

Кандидат технічних наук, доцент
Заклад вищої освіти «Подільський державний університет»
32316, вул. Шевченка, 12, м. Кам'янець-Подільський, Україна
https://orcid.org/0000-0002-0083-7359

Аналіз та оптимізація систем охолодження двигунів внутрішнього згоряння для підвищення теплової ефективності та надійності роботи двигуна

Анотація. Метою дослідження було кількісно оцінити та оптимізувати роботу систем охолодження двигуна внутрішнього згоряння з огляду на підвищення його теплової ефективності та надійності. Методологія поєднувала моторно-стендові випробування з вимірюванням температур, витрати охолоджувальної рідини та палива, розрахунок теплового потоку з оцінкою невизначеності відповідно до керівництва з вираження невизначеності вимірювань, обчислювальну гідродинаміку у спряженій постановці «рідина – тверде тіло», аналіз напружено-деформованого стану головки блока та дослідження перехідного режиму прогріву від 20 до 90°C. Установлено, що модернізовані конфігурації забезпечили зростання теплового потоку за умов максимального навантаження на 10-17 %, зниження пікових температур у критичних прикамерних зонах на 5-6 % і 10-12 %, а також зменшення внутрішніх температурних градієнтів на 18-22 % і 30-35 %. Це супроводжувалося зниженням еквівалентних напружень на 18-22 % та підвищенням коефіцієнта запасу міцності з 1,45 до 1,87 у найбільш ефективній конфігурації. У перехідному режимі система з електроприводним насосом скорочувала час досягнення робочої температури на 9-12 % і зменшувала інтегральну витрату палива на 10-12 %, тоді як конфігурація з розділеними контурами забезпечувала стабільне зниження цих показників на 6-8 % і 5-7 %, відповідно. Аналіз гальмової питомої витрати палива в контрольних стаціонарних режимах не виявив статистично значущого погіршення паливної економічності для модернізованих систем. Інтегральне ранжування показало, що система з розділеними контурами забезпечує збалансоване поєднання зниження максимальної температури, мінімізації температурних градієнтів і підвищення запасу міцності без компромісів щодо паливної ефективності, тоді як електроприводна помпа є доцільною для мінімізації тривалості прогріву та витрати палива під час холодного запуску. Практична значущість дослідження полягає у формуванні кількісно обґрунтованих критеріїв вибору конфігурації системи охолодження та стратегій керування витратою теплоносія для інженерних підрозділів з метою підвищення теплової надійності й довговічності двигунів

Ключові слова: локальні температурні градієнти; термонапружений стан; еквівалентні напруження; коефіцієнт запасу міцності; перехідний режим прогріву; інтегральна витрата палива

Machinery & Energetics
Vol. 17, No. 2. 2026

Journal homepage:
https://technicalscience.com.ua/en

UDC 631.527:631.8:621.9
DOI: 10.31548/machinery/2.2026.2

ISSN 2663-1334
e-ISSN 2663-1342

Khandakar Akhter Hossain
Vice Chancellor
Bangladesh Maritime University
1216, Plot No. 14/06-14/23, Pallabi, Mirpur-12, Dhaka, Bangladesh
https://orcid.org/0009-0008-3080-2270

Md. Jobayer Mia*
Lecturer
Bangladesh Maritime University
1216, Plot No. 14/06-14/23, Pallabi, Mirpur-12, Dhaka, Bangladesh
https://orcid.org/0000-0003-0630-004X

Mohammad Farhad Hossen
Additional Registrar
Bangladesh Maritime University
1216, Plot No. 14/06-14/23, Pallabi, Mirpur-12, Dhaka, Bangladesh
https://orcid.org/0009-0005-6734-7505

Md. Masudur Rahman
Postgraduate Student
Bangladesh Maritime University
1216, Plot No. 14/06-14/23, Pallabi, Mirpur-12, Dhaka, Bangladesh
https://orcid.org/0009-0004-1215-2586

Design and modification of a combined grass cutting and grinding machine

Abstract. Efficient preparation of livestock feed remains a major challenge for small and medium farmers in Bangladesh, where manual fodder cutting, and separate grinding processes require considerable time, labour, and cost. Rising feed prices and limited access to affordable mechanised equipment make the development of locally manufacturable multipurpose machinery highly relevant for the agricultural sector. This article aimed to design, fabricate, and evaluate a combined grass-cutting and grinding machine suitable for practical use in Bangladesh. The study used field visits, focus group discussions, Computer-aided design-based modelling, prototype fabrication, and performance testing to assess the machine's design, operation, and user suitability. The developed machine integrated grass cutting and grain grinding in a single compact system powered by a 3 HP electric motor. Unlike many conventional machines that depend on belt-pulley arrangements, the proposed design uses a spur gear transmission system to improve durability, stability, and power transfer. The gear arrangement provided a final reduction ratio of 0.846, producing a driven shaft speed of approximately 1,015-1,523 rpm and a blade tip speed of about 15.9-23.9 m/s. Trials with fresh grass, straw, and lentils showed that the machine could process 180-200 kg/hr of grass, 150-170 kg/hr of straw, and 50-60 kg/hr of lentils into fine powder. The chopped output was uniform, feeding was smooth, and the protective casing helped improve operational safety. The design also supported blade sharpening, local fabrication, and lower maintenance requirements. The results can be applied in small-scale livestock farming, feed preparation centres, and rural machinery workshops to reduce labour, improve feed processing efficiency, and support agricultural mechanisation

Keywords: grass cutter; grinder; agriculture; agricultural machinery; feed preparation

Article's History: Received: 19.01.2026; Revised: 14.04.2026; Accepted: 21.05.2026; Published: 29.05.2026.

Suggested Citation:
Hossain, K.A., Mia, M.J., Hossen, M.F., & Rahman, M.M. (2026). Design and modification of a combined grass cutting and grinding machine. *Machinery & Energetics,* 17(2), 22-38. doi: 10.31548/machinery/2.2026.2.

*Corresponding author (jobayer.naoe@bmu.edu.bd)

INTRODUCTION

Agriculture remains one of the most important sectors of Bangladesh's economy because it supports food security, rural employment, poverty reduction, agro-based industry, and livestock production. Although the relative share of agriculture in national gross domestic product has gradually declined with industrialisation, the sector still contributes substantially to the economy; existing studies report agriculture's contribution at about 13.61% of national gross domestic product (GDP) while earlier sectoral estimates reported nearly 20% of GDP and around 50% of national employment, according to A. Ghimire *et al*. (2021). The rice subsector is particularly important, contributing more than 70% of agricultural GDP, while Bangladesh produces about 37 million tons of rice annually, representing approximately 6.3% of global rice production (Rayhan *et al*., 2023).

Beyond crops, fisheries and livestock also play major roles in rural livelihoods and nutrition; fish production, as noted by M.M. Shamsuzzaman *et al*. (2020), increased from 17.81 lakh metric tons in 2000-2001 to 41.34 lakh metric tons in 2016-2017, showing the growing economic relevance of fisheries in Bangladesh. Similarly, K. Moller *et al*. (2023) pointed out that livestock and aquaculture are closely linked with farm household income, protein supply, and integrated rural production systems, but they face challenges related to climate change, feed availability, disease management, and market access. At the same time, Bangladesh's agricultural production system is highly vulnerable to climate variability, land pressure, labour shortages, and environmental degradation, making improved farm mechanisation and efficient feed-preparation technologies increasingly important (Rahman *et al*., 2021; Chowdhury *et al*., 2022; Jamal *et al*., 2023). Therefore, the development of locally manufacturable, low-cost, and multipurpose agricultural machines, such as combined grass-cutting and grinding equipment, is highly relevant for improving livestock feed preparation, reducing manual labour, and supporting sustainable agricultural mechanisation in Bangladesh.

Several researchers have worked to enhance the design, implement improvements, and increase the efficiency of grass-cutting machines. J. Sinha & A. Kumar (2021) studied the ergonomic and mechanical efficacy of manual chaff cutters used in animal farming, emphasising reduced power consumption during fodder cutting. The study indicated that a three-blade cutter with a smaller feeding area used less energy and was more comfortable to use. This research enhances the design of fodder cutters, increasing their energy efficiency and user comfort. Nevertheless, greater research is required to investigate alternative materials and evaluate the long-term health effects of these alterations. D. Yallappa *et al*. (2024) introduced the design and development of a versatile chaff-cutting machine intended to address the challenges of cutting both dry and wet chaff for animal feeding. The machine was designed to process various types of fodder, including sugarcane waste and other green resources. This concept simplified traditional machinery and gave farmers a simple, portable option. More enhancements could be made to make the machine more useful for different types of fodder and to look into more environmentally friendly energy sources.

N.S. Navgale *et al*. (2023) showed the design and adaptation of a chaff cutter and coconut dehusking machine that operates with a single engine for both tasks. The proposed method was cheaper and required less space because it combined the two units into a single unit. The machine had a 1 HP electric motor, making these jobs much easier for anyone to do. The study laid out a precise plan for building a multitasking machine from mild steel and shows how useful it is for small-scale farmers in rural areas, especially those who have both cattle and coconut trees. P. Jayendra & G.Y. Suresh (2020) examined the design and development of a chaff-cutter machine intended to enhance efficiency and reduce manual labour for farmers. The machine was made to cut several kinds of fodder, such as dry grass, wheat stalks, and maize straw, into smaller pieces so that animals could consume them more easily. The new design was smaller, cheaper, and used less energy than standard chaff cutters. E. Rajkumar *et al*. (2020) investigated chaff-cutter-related injuries in rural India and proposed safety measures to mitigate them. The investigation led to the creation of three interventions: a serrated roller to serve as a warning sign, a blade guard to keep hands away from cutting blades, and a flywheel lock to stop the machine from being used while it isn't working. It was observed that these measures helped prevent people from getting hurt without affecting the machine's performance. Farmers liked that these safety features were added to old chaff cutters.

Although several researchers have worked on the development of grass-cutting machines, there are still gaps in the literature regarding a multipurpose machine. The current study proposed a gear-based modification of a multipurpose grass cutting cum grinding machine suitable for rural, semi-urban, and urban farmers of Bangladesh. This study aimed to develop a machine that will be cost-effective, easy to use, locally manufacturable, more durable, easy to maintain, low-cost, and readily available for the farmers of Bangladesh.

MATERIALS AND METHODS

Research design and overall methodological approach. This study followed a design-fabrication-testing methodology to develop and evaluate a combined grass-cutting and grinding machine suitable for small- and medium-scale livestock farmers in Bangladesh. The methodology consisted of five sequential stages: field investigation, user requirement identification, engineering design and calculation, prototype fabrication, and performance testing. The machine was designed to integrate three major functional units: a feeding unit, a cutting and grinding unit, and a power transmission unit. A 3-horsepower electric motor was used as the prime mover, and power was transmitted to the cutting and grinding shaft through a spur gear train. Computer-aided design modelling was performed using AutoCAD and SOLIDWORKS before fabrication to ensure proper dimensional arrangement, component fitting, and safe enclosure of rotating parts. Figure 1 shows the methodology used in the current research.

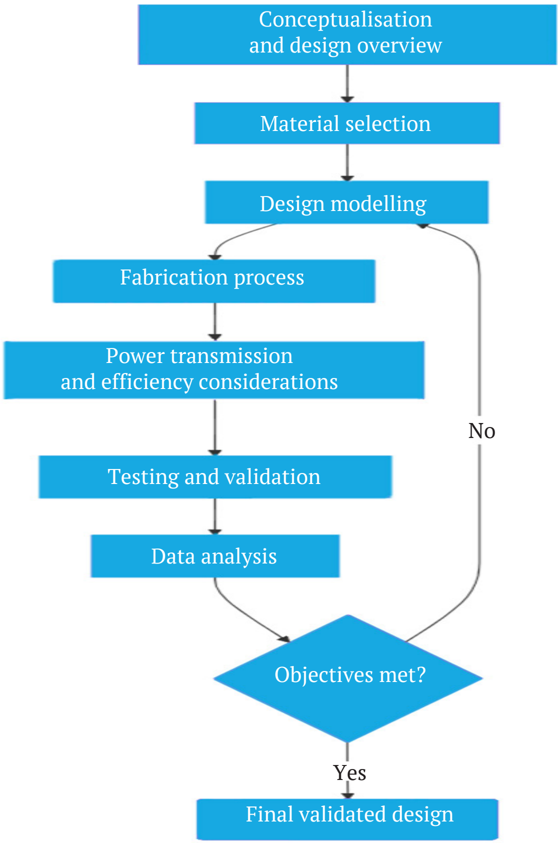

Figure 1. Methodology of research

Source: compiled by authors

Field visit. Field visits were made to Nawabpur and Dholaikhal, Dhaka, Bangladesh's largest engineering marketplaces and fabrication areas, to gather real-world information on current grass-cutting machines, available mechanical parts, fabrication techniques, and maintenance practices. Using a structured observation checklist, the observations were written down in a systematic way. The checklist had information about the type of machine, the size of the motor, the arrangement of the blades, the feeding system, the way power is transmitted, the arrangement of the shaft and bearing, the design of the casing, the safety features, the availability of parts, the ease of repair, and the most typical difficulties that mechanics and users have with the machine. The study team also talked to people at local machine shops and fabrication workshops to find out what kinds of motors, gears, shafts, bearings, blades, sheet metal, and structural elements were available. Measurements of relevant machine parts were taken where possible, and component specifications were compared with locally available alternatives. The collected information was organised into a design requirement sheet and used to determine the major mechanical features of the proposed machine, including motor power, transmission system, blade material, casing arrangement, and fabrication feasibility. This process helped ensure that the proposed design could be manufactured using locally available materials and workshop facilities.

Focus group discussion (FGD). FGDs were conducted in Savar, Sadarpur in Faridpur, and Mithapukur in Rangpur, Bangladesh, with 120 purposively selected participants. The study involving human participants was carried out in accordance with the ethical standards outlined in the Declaration of Helsinki (1964), ensuring voluntary participation, informed consent, and the protection of participants' confidentiality and well-being. The participants included small and medium farmers, livestock feed users, machine operators, and local mechanics. The discussions focused on current fodder preparation practices, labour demand, manual cutting problems, grinding needs, safety, maintenance, repairability, and expected machine performance. The responses were coded into major user requirement categories. Since participants could mention more than one issue, the percentages represent multiple-response frequencies. The frequencies were obtained through manual coding of repeated responses across the three FGD locations. The most frequently reported requirement was reducing manual labour and processing time, mentioned by 98 participants or 81.7%. This was followed by the need for a combined grass-cutting and grinding machine, reported by 91 participants or 75.8%. Safety during operation was mentioned by 84 participants or 70.0%, while durability and low maintenance were mentioned by 78 participants or 65.0%. Local repairability was reported by 72 participants or 60.0%, easy operation by 69 participants or 57.5%, preferred fodder size by 62 participants or 51.7%, and adequate processing capacity by 56 participants or 46.7% (Table 1).

Table 1. Translation of FGD findings into engineering design decisions

User requirement	Frequency, n = 120	Percentage, %	Design decision
Reduce labour and time	98	81.7	Motor-driven cutting and grinding system
Combine cutting and grinding	91	75.8	Integrated grass-cutting and grain-grinding unit
Improve operator safety	84	70.0	Protective casing and enclosed rotating parts
Ensure durability and low maintenance	78	65.0	Spur gear transmission instead of belt-pulley system
Allow local repair	72	60.0	Use of standard gears, shafts, bearings, and sheet metal
Make operation simple	69	57.5	Separate feed inlets and clear discharge outlets
Produce suitable chopped fodder size	62	51.7	Blade arrangement targeting 2-5 cm chopped output
Ensure practical capacity	56	46.7	Selection of 3 HP motor and gear-driven shaft

Source: compiled by authors

These findings were directly translated into the engineering design of the machine. The strong demand for reduced labour and time led to the selection of a motor-driven system. The need for both fodder cutting and feed grinding resulted in an integrated cutting-grinding chamber. Safety concerns were addressed through a protective casing, enclosed rotating parts, and separate feeding and discharge paths. Similarly, the demand for durability and easier maintenance led to the use of spur gear transmission instead of a belt-pulley system. Local repairability was considered by using standard components that can be sourced and serviced in local workshops. Thus, the FGD findings provided a clear user-centred basis for the final machine design.

Engineering calculation methodology. Engineering calculations were performed to determine gear geometry, gear ratio, driven shaft speed, blade tip speed, angular velocity, torque transmission, and theoretical power transmission. These calculations were used to verify whether the selected motor, gear train, shaft arrangement, and blade system were suitable for the required cutting and grinding operations. The major input parameters used in the calculation were motor power, motor speed, gear teeth number, gear module, blade diameter, driven shaft speed, and processing time. All calculations were performed using standard mechanical design equations. The following assumptions were considered during the calculation: all spur gears had the same module; gear slip was neglected; the intermediate gear acted as an idler gear; the intermediate gear changed the direction of rotation but did not affect the final speed ratio; the motor operated under steady-state conditions; the cutting blade was considered as a rigid rotating circular body; and theoretical power loss due to friction, bearing resistance, and gear tooth wear was neglected.

Gear ratio and shaft speed calculation. For a pair of external spur gears, the speed ratio was calculated using:

$$\frac{N_a}{N_b} = \frac{Z_b}{Z_a}, \tag{1}$$

or,

$$N_b = N_a \times \frac{Z_a}{Z_b}, \tag{2}$$

where N_a is the speed of the driving gear, N_b is the speed of the driven gear, Z_a is the number of teeth on the driving gear, and Z_b is the number of teeth on the driven gear. For the first gear stage, the intermediate gear speed was calculated as:

$$N_2 = N_1 \times \frac{Z_1}{Z_2}, \tag{3}$$

where N_1 is the motor shaft speed, N_2 is the intermediate gear speed, Z_1 is the number of teeth on the drive gear, and Z_2 is the number of teeth on the intermediate gear. For the second gear stage, the driven shaft speed was calculated as:

$$N_3 = N_2 \times \frac{Z_2}{Z_3}, \tag{4}$$

where N_2 is the intermediate gear speed, N_3 is the driven shaft speed, Z_2 is the number of teeth on the intermediate gear, and Z_3 is the number of teeth on the driven gear. Since the intermediate gear acts as an idler gear, the final drive shaft speed can be expressed as:

$$N_3 = N_1 \times \frac{Z_1}{Z_3}, \tag{5}$$

where N_1 is the motor shaft speed, N_3 is the driven shaft speed, Z_3 is the number of teeth on the drive gear, and is the number of teeth on the driven gear. The final transmission ratio was calculated using:

$$i = \frac{Z_1}{Z_3}, \tag{6}$$

where i is the final transmission ratio, Z_1 is the number of teeth on the drive gear, and Z_3 is the number of teeth on the driven gear. Therefore, the driven shaft speed can also be written as:

$$N_3 = iN_1, \tag{7}$$

where N_3 is the driven shaft speed, i is the final transmission ratio, and N_1 is the motor shaft speed.

The angular velocity of the driven shaft was calculated using:

$$\omega = \frac{2\pi N}{60}, \tag{8}$$

where ω is the angular velocity, N is the rotational speed in revolutions per minute, and π is the mathematical constant pi.

The blade tip speed was calculated using:

$$V = \frac{\pi DN}{60}, \tag{9}$$

where V is the blade tip speed, D is the blade diameter, N is the driven shaft speed, and π is the mathematical constant pi. The motor torque was calculated from motor power and rotational speed using:

$$T = \frac{P \times 60}{2\pi N}, \tag{10}$$

where T is the torque, P is the power in watts, N is the rotational speed in revolutions per minute, and π is the mathematical constant pi. When power is expressed in kilowatts, torque can also be calculated using:

$$T = \frac{9{,}550P}{N}, \tag{11}$$

where T is the torque in $N\cdot m$, P is the power in kW, and N is the rotational speed in rpm. For a gear pair, torque changes in proportion to the gear teeth ratio:

$$T_b = T_a \times \frac{Z_b}{Z_a}, \tag{12}$$

where T_a is the torque on the driving gear, T_b is the torque on the driven gear, Z_a is the number of teeth on the driving gear, and Z_b is the number of teeth on the driven gear. For the first gear stage, torque on the intermediate gear was calculated as:

$$T_2 = T_1 \times \frac{Z_2}{Z_1}, \tag{13}$$

where T_1 is the torque on the drive gear, T_2 is the torque on the intermediate gear, Z_1 is the number of teeth on the drive gear, and Z_2 is the number of teeth on the intermediate gear. For the second gear stage, torque on the driven gear was calculated as:

$$T_3 = T_2 \times \frac{Z_3}{Z_2}, \tag{14}$$

where T_2 is the torque on the intermediate gear, T_3 is the torque on the driven gear, is the number of teeth on the intermediate gear, and is the number of teeth on the driven gear. Considering transmission efficiency, the driven shaft torque may be expressed as:

$$T_3 = T_1 \times \frac{Z_3}{Z_1} \times \eta, \tag{15}$$

where T_3 is the driven shaft torque, T_1 is the motor shaft torque, Z_3 is the number of teeth on the driven gear, Z_1 is the number of teeth on the drive gear, and η is the transmission efficiency.

RESULTS AND DISCUSSION

Modelling of the grass cutting machine. The 3D model is developed in SOLIDWORKS. Different parts of the machine are numbered as shown in Figure 2, and their names are listed in Table 2. Figure 2. (a, b) schematic diagram, (c) right side view, and (d) front side view of the model

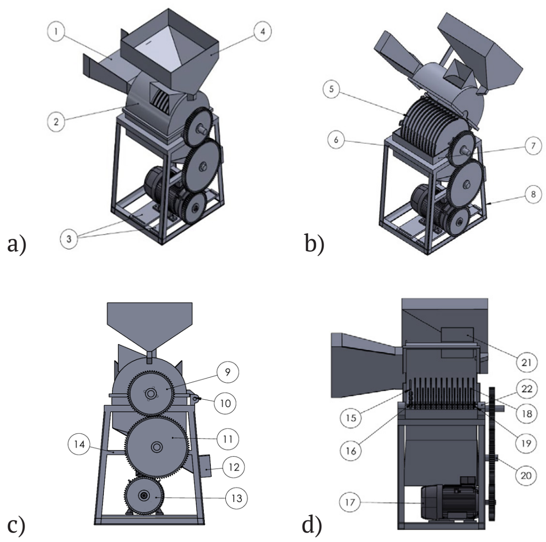

Figure 2. (a, b) schematic diagram, (c) right side view, and (d) front side view of the model
Source: compiled by authors

Table 2. Chaff cutter components

1. Grass feed inlet	12. Outlet 1 (grain powder)
2. Upper casing	13. Drive gear
3. Electric motor base	14. Intermediate gear shaft base
4. Grain inlet hopper	15. Grass cutter blade
5. Circular Blade	16. Cutter blade nut and bolt
6. Base	17. Electric motor
7. Lower casing	18. Grinder hammer
8. Frame	19. Grinder hammer holder
9. Cutter Roller Gear (Driven Gear)	20. Intermediate gear shaft
10. Casing Hinge	21. Outlet 2 (dry fodder)
11. Intermediate gear	22. Bearing house and bearing

Source: compiled by authors

Each component was modelled in 2D using AutoCAD for better understanding (Fig. 3). Details of each part are described as follows. *Grass cutter blade and grinder hammer holder*. This part is a combination of a grass cutting blade, a grass cutting blade holder, nuts and bolts, and a grinder hammer holder shaft. First, on top of the blade holder, grass-cutting blades are placed with nuts and bolts. In the centre, the main shaft is located, and the grinder hammer shaft is arrayed around the main shaft at an equal distance. At the end of the hammer shaft, bolts are used to secure the whole set.

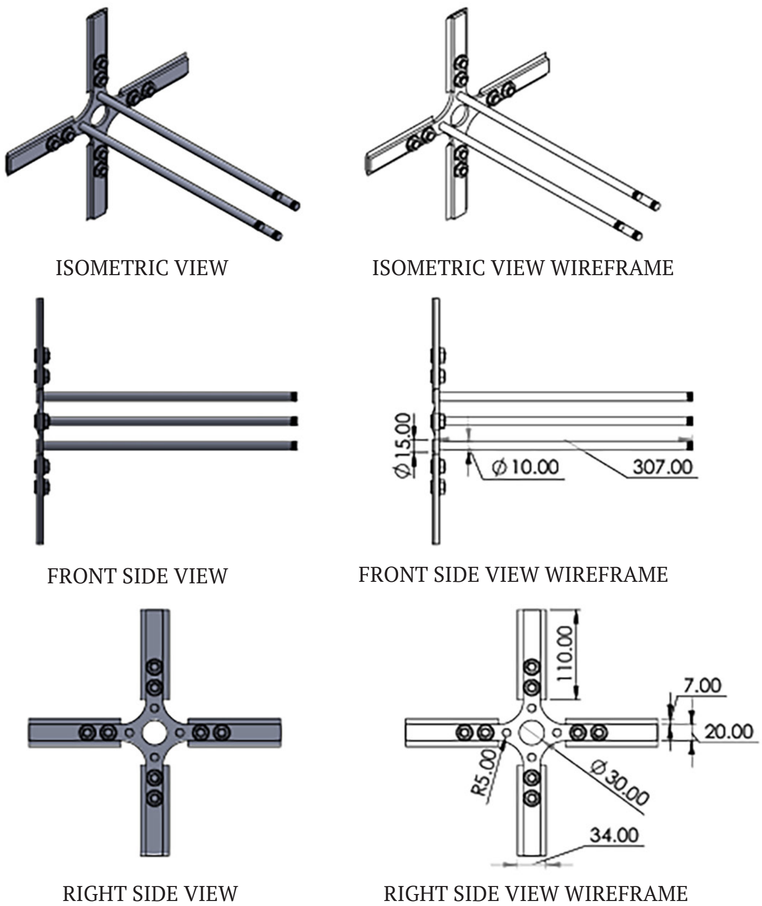

Figure 3. Grass cutting blades and grinder hammer set

Source: compiled by authors

Grass cutting blade holder. To secure cutting blades, this part is used, along with nuts and bolts to hold the blades in place (Fig. 4). These blades can be removed from the holder for sharpening using the nuts and bolts. Including that the main shaft and grinder hammer shaft are attached to this part.

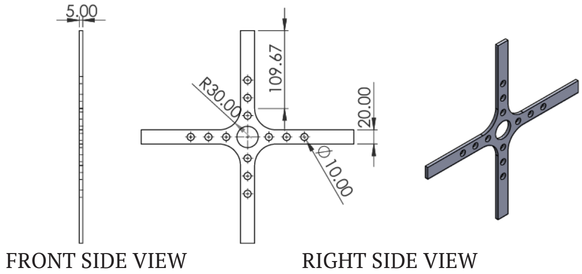

Figure 4. Grass cutting blade holder

Source: compiled by authors

Grass cutting blade. The grass-cutting blade (Fig. 5) performs the primary chopping of fresh grass and straw. Its functional role is to convert long fodder into smaller pieces suitable for livestock feeding and mixing. The blade also affects feeding resistance, cut length, power requirement, and output uniformity. The blade diameter used in the machine is 300 mm. The driven shaft speed is approximately 1015-1523 rpm, producing a blade tip speed of about 15.9-23.9 m/s. The blade material is high-carbon steel.

High-carbon steel was selected because the blade is exposed to repeated impact, abrasive contact with grass/straw, and edge wear. This material provides better hardness and edge retention than ordinary mild steel. The removable bolted arrangement was selected so that the blades can be sharpened or replaced without replacing the complete blade holder. The blade interacts with the grass feed inlet, blade holder, main shaft, bearing housing, and outlet for chopped grass. Its alignment and balance are critical because imbalance can increase vibration and bearing load.

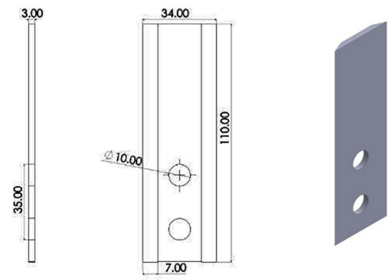

Figure 5. Grass cutting blades

Source: compiled by authors

*Blades holding nuts & bolts***.** These nuts & bolts (Fig. 6) are used to hold the cutting blade with the holder in place.

Circular blade. The circular blade (Fig. 7) assists in cutting and grinding, especially for grain or harder feed materials. Its role is to create additional shearing and size-reduction action inside the processing chamber. It improves the machine's multifunctionality by allowing the same shaft assembly to support both fodder cutting and grain grinding. Key design parameters include diameter, thickness, tooth or edge geometry, material, mounting diameter, and clearance from the casing. High-carbon steel is justified because grinding and cutting create abrasive wear. A circular blade is preferred because it provides continuous rotational cutting action and distributes cutting load around the blade circumference. It interacts with the main shaft, grinder hammer, grain hopper, casing, and powder outlet.

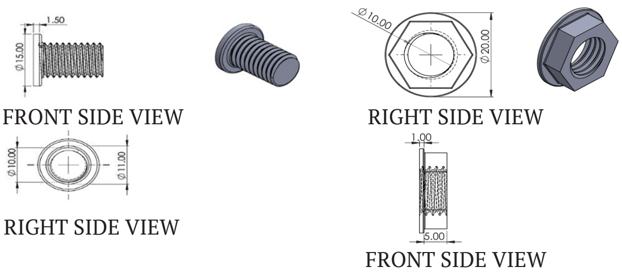

Figure 6. Nuts and bolts of the machine

Source: compiled by authors

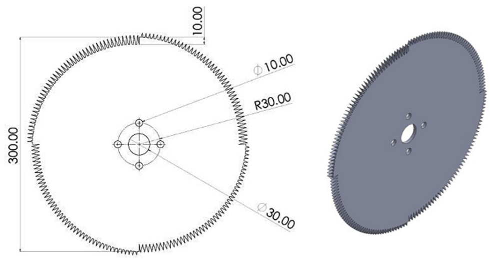

Figure 7. Circular blades used in the machine

Source: compiled by authors

Bearing house and bearing. This part (Fig. 8) holds the main shaft, grass-cutting blades, circular blades, and grinder hammers. It also helps to rotate all the cutting parts together with the driven gear. It is the most important component that transfers the power from the gear to the cutting parts and holds all the parts in place.

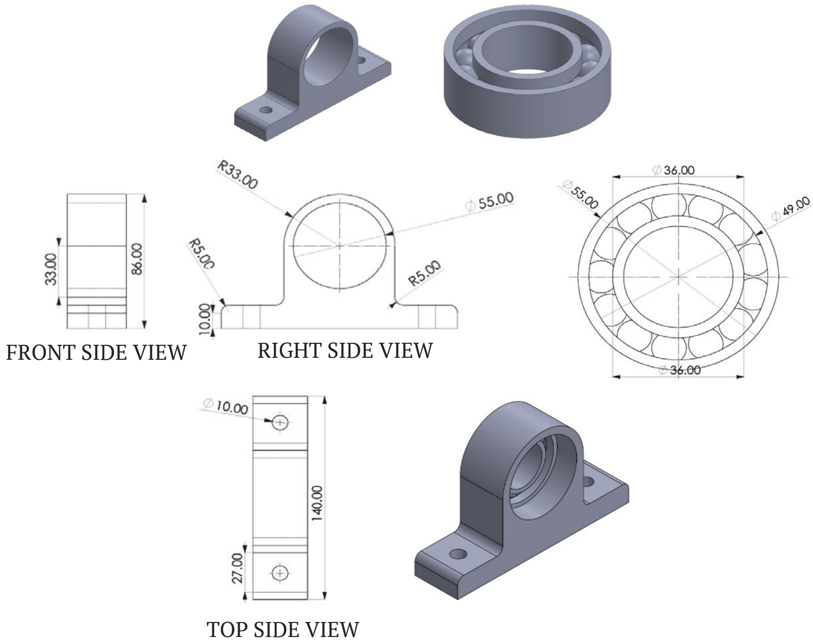

Figure 8. Bearing housing and bearing

Source: compiled by authors

Grain inlet hopper. This part (Fig. 9) is made of a thin metal sheet that holds and circulates grain at a specific speed into the grinding or cutting chamber. Generally, gravity is used to send the grain into the grinding chamber.

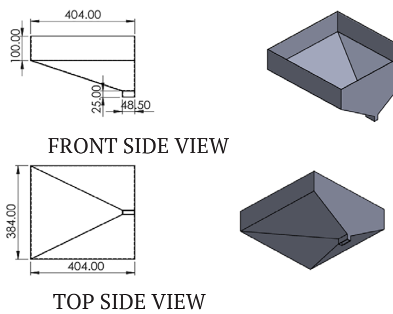

Figure 9. Grain inlet hopper

Source: compiled by authors

The top casing and the feed inlet. It prevents the spread of feeding materials outside and protects people from injury from the rotating parts. The feed inlet, as well as the grain inlet hopper, is attached to it (Fig. 10).

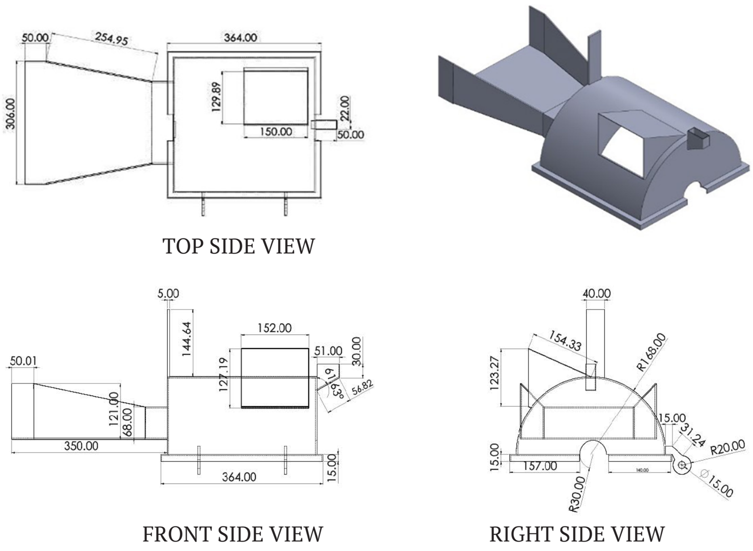

Figure 10. Top casing & feed inlet

Source: compiled by authors

Base, frame and motor base. Basically, this part holds all other parts in place in an order and also provides the necessary support for the cutting and grinding process (Fig. 11).

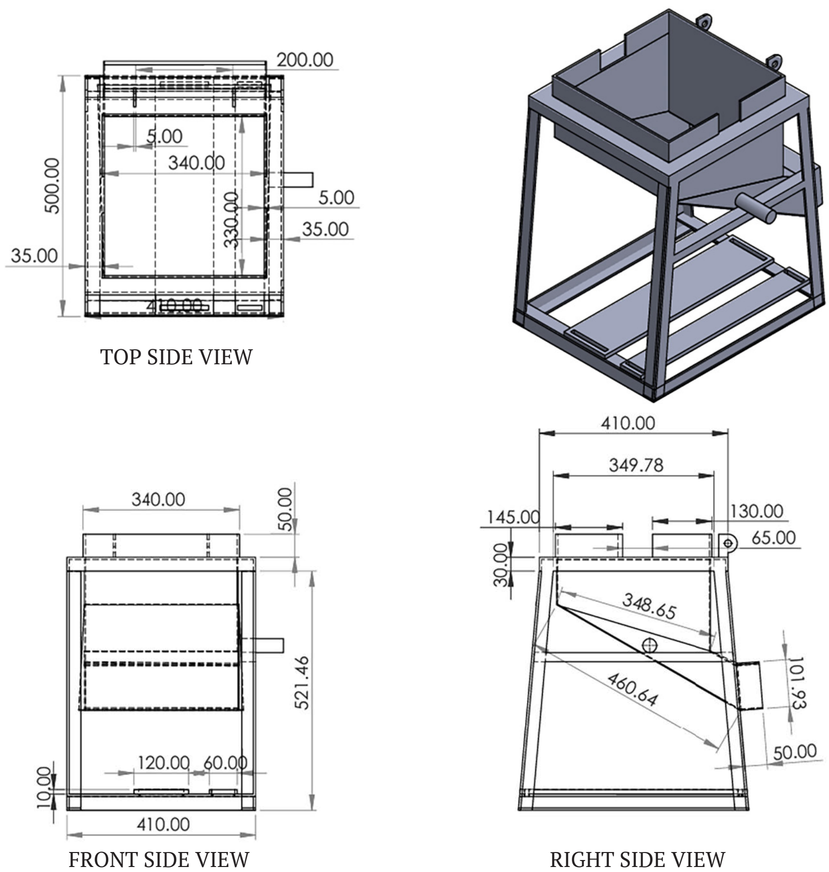

Figure 11. Frame and base

Source: compiled by authors

Power transmission. In this chaff cutter, there are 3 spur gears that transmit the power needed for cutting and grinding grass & grain (Table 3). There is a drive gear attached directly to the motor, then the intermediate gear, which is attached to a shaft that runs to the frame. After that, there is a driven gear directly connected to the main shaft. These gears mesh with each other to form a gear train.

Table 3. Specification of the gear

Gear	Teeth Z	Pitch dia d = mZ (mm)	Outside dia / Addendum dia d + 2 m (mm)	Clearance = 0.157 m (mm)	Dedendum = m + clearance (mm)	Dedendum circle / Root dia d – 2b (mm)
Driven gear (3)	65	208	214.4	0.502	3.702	200.6
Intermediate gear (2)	90	288	294.4	0.502	3.702	280.6
Drive gear (1)	55	176	182.4	0.502	3.702	168.6

Source: compiled by authors

Gear ratio:
Stage 1:

$$N_2 = N_1 \times \frac{55}{90};$$

stage 2:

$$N_{driven} = N_2 \times \frac{90}{65}.$$

Combine:

$$N_{driven} = N_{motor} \times \frac{55}{65} = N_{motor} \times 0.846.$$

Final reduction ratio: 0.846.

Required RPM from the motor. In this chaff cutter machine, a 3 hp electric motor is used. The motor's rpm can be regulated from 1,200 to 1,800 rpm using an inverter.

Shaft rpm at 1,200 rpm motor:
N_{driven} = 0.846 × 1,200 = 1,015 rpm.
At 1,800 rpm motor:

$$N_{driven} = 0.846 \times 1{,}800 = 1{,}523\ RPM.$$

Shaft speed ranges from 1015 to 1523 rpm.

Blade tip speed:
Blade diameter is 300 mm, thus the tip speed will be $V = \pi DN/60$.
At 1,015 RPM:
V = 15.9 m/s. At 1,523 RPM:

$$V = 23.9\ \text{m/s}.$$

Blade tip speed range:

$$15.9 - 23.9\ \text{m/s}.$$

This is ideal for efficient cutting.
Torque at driven gear:

Motor power = 3 HP = 2,238 W
Gear train:
Motor → 55T → 90T (intermediate) → 65T (driven).

Overall ratio:
$N_{driven} = N_{motor} \times \frac{55}{65} = 0.846 N_{motor}$.

Case 1: At 1,200 RPM Motor

Torque at Motor Shaft (55T Gear)
Formula:
$T = \frac{9{,}550P}{N} T_{motor} = \frac{9{,}550 \times 2.238}{1200} T_{motor} = 17.8\ Nm$ Torque on 55T gear = 17.8 Nm

Torque on 90T Intermediate Gear
Torque increases proportional to gear ratio:
$T_{90} = T_{55} \times \frac{90}{55} = 17.8 \times 1.636 = 29.1 Nm$ Torque on 90T gear = 29.1 Nm.

Torque on 65T Driven Gear
Second stage:
$T_{65} = T_{90} \times \frac{65}{90} = 29.1 \times 0.722 = 21.0 Nm$ Torque on 65T gear (Drum shaft) = 21 Nm.

Case 2: At 1,800 RPM Motor
Motor Torque (55T):
$T = \frac{9{,}550 \times 2.238}{1{,}800} T = 11.9\ Nm$ Torque on 55T = 11.9 Nm

Torque on 90T Gear
$T_{90} = 11.9 \times 1.636 = 19.5\ Nm$ Torque on 65T Gear (Driven):

$$T_{65} = 19.5 \times 0.722 = 14.1\ Nm.$$

The final torque summary is shown in Table 4.

Key attributes of the designed model are summarised in Table 5.

Table 4. Final torque summary

Gear	Teeth	Torque at 1,200 rpm	Torque at 1,800 rpm
Motor gear	55	17.8 Nm	11.9 Nm
Intermediate gear	90	29.1 Nm	19.5 Nm
Driven gear	65	21.0 Nm	14.1 Nm

Source: compiled by authors

Table 5. Summary of the key attributes

Attribute	Value (from report)	Notes / derived value
Primary functions	Chaff/grass cutting (wet + dry) + grain grinding	Multipurpose intent is explicit.
Motor power	3 hp	The report uses 3 HP ≈ 2.24 kW.
Motor speed control	1,200-1,800 rpm via "inverter"	Variable speed is a key differentiator.
Transmission	Spur gears (drive, idler, driven)	Tooth counts: drive 55T, idler 90T, driven 65T.
Reduction ratio	0.846 (final reduction ratio)	Used to compute driven shaft speed.
Driven shaft speed	~1,015-1,523 rpm	Derived: 0.846 × 1,200 = 1,015 rpm; 0.846 × 1,800 ≈ 1,523 rpm.
Blade diameter	300 mm (0.30 m)	Used for tip-speed estimate.
Tip speed (derived)	~15.9-23.9 m/s	Derived: $V = \pi DN/60$, D = 0.30 m, N = 1,015 – 1,523 rpm.
Reported torque (driven gear)	~21.0 Nm @ 1,200 rpm motor; ~14.1 Nm @ 1,800 rpm motor	Values appear in the report's computed table.
Blade material	High carbon steel (for grass blade and circular blade)	Durability-positive.

Source: compiled by authors

Manufacturing. The production stage confirmed that it was possible to turn the CAD-based design into a working prototype. The main result of the fabrication was that the proposed integrated layout, which included the feeding unit, cutting and grinding chamber, spur gear transmission, motor base, frame, bearing support, and protective casing, could be put together without changing how the designed model worked. But the final prototype was afflicted by a number of production limitations. Standard sizing for shafts, bearings, sheet metal, and gears meant that during fabrication, only small changes needed to be made to the mounting positions and casing clearances. These changes didn't change how the machine worked; they merely made sure that the motor gear, intermediate gear, and driving gear were all in the right place.

Keeping the gear meshing and shaft alignment correct was the most important manufacturing problem. Because the machine has a spur gear transmission system instead of a belt-pulley system, slight mistakes in positioning could make vibrations, noise, and tooth wear worse. To lower this danger, the motor base and intermediate gear shaft support were changed during assembly to keep the 55-tooth drive gear, 90-tooth intermediate gear, and 65-tooth driven gear in stable contact with each other. The made-up gear configuration kept the planned transmission function and supported the calculated driven shaft speed range of about 1,015-1,523 rpm.

There was also an important result that had to do with the cutting and grinding chamber. The shell had to be close enough to the 300 mm rotating blade to keep materials from moving around inside the chamber, but it also had to be far enough away to let the blade move freely. To avoid blade contact, vibration, and material leakage, the space between the blade path and the casing was verified during fabrication. Using high-carbon steel for the cutting and circular blades made the prototype more resistant to wear, which is significant because these parts will be hit and scraped by grass, straw, and grains again and over again. The bolted blade configuration also made it easier to keep up with because the blades can be taken off for sharpening or replacement.

The built frame and base were strong enough to hold the motor, gear train, casing, and rotating assembly. Any little differences between the model and the built structure were mostly due to cutting, welding, and bending sheet metal by hand. Before the final assembly, local grinding, slot correction, and re-alignment were used to fix these differences. The protective case also made the created prototype safer by covering the revolving cutting and grinding parts. In general, the manufacturing stage showed that the design can be made with workshop tools that are available in the area. However, it also showed that gear alignment, shaft concentricity, blade clearance, and casing rigidity are the most important factors for keeping performance, durability, and safe operation. The manufacturing process is demostrated on Figure 12.

Figure 12. Illustration of the manufacturing process

Source: taken by authors

Manufactured model. The manufactured prototype confirmed that the designed system could integrate grass cutting and grain grinding within one machine structure. The completed model included the grass feed inlet, grain inlet hopper, cutting blade, circular blade, grinder hammer, frame, motor base, bearing housing, protective casing, and spur gear transmission system. The 3 HP motor and gear train produced an estimated driven shaft speed of approximately 1,015-1,523 rpm, with a blade tip speed of about 15.9-23.9 m/s and driven gear torque of about 21.0 $N \cdot m$ at 1,200 rpm and 14.1 $N \cdot m$ at 1,800 rpm. These calculated values indicate that the fabricated power transmission system was suitable for rotating the combined cutting and grinding assembly under the selected operating range.

The performance of the manufactured model was verified through trial operation using fresh grass, straw, and lentils. As shown in Table 5, the machine processed fresh grass at 180-200 kg/hr and produced chopped material of 2-5 cm. For straw, the measured throughput was 150-170 kg/hr with a similar cut size of 2-5 cm, although the feeding rate was slightly lower because of the drier material condition. In the grinding test, lentils were processed at 50-60 kg/hr and produced fine particles below 2 mm. The trial observations also showed smooth feeding and uniform chopping for fresh grass, consistent cutting for straw, and uniform grinding without clogging for lentils. These results provide direct evidence that the manufactured prototype can process both fodder and grain-type material under the tested conditions.

The safety features of the manufactured model were evaluated through design verification and operational observation during the trial. The cutting and grinding elements were enclosed by a protective casing, and separate feeding and discharge paths were provided for grass, grain powder, and chopped material. During the test operation, the casing prevented direct exposure to the rotating blade and hammer assembly, while the outlets allowed processed material to leave the chamber without manual contact with the cutting zone. However, no quantitative safety test, such as failure rate measurement, operator risk scoring, vibration level, noise level, or long-duration reliability testing, was conducted. Therefore, the result should be interpreted as validation of incorporated safety features during prototype operation, not as a full safety certification. Further testing is required to measure energy consumption, vibration, noise, blade wear, and long-term failure rate under continuous operating conditions. The final manufacture of the machine is presented on Figure 13.

Figure 13. Final manufacture of a multipurpose grass cutting machine
Source: taken by authors

Trial of the machine. The test findings showed that the prototype that was made could chop fodder and grind grain in the conditions that were evaluated. Three materials were tested: lentils, fresh grass, and straw. Table 5 shows the results in terms of throughput, output size, and operational observations. The machine had the highest throughput for fresh grass, which was between 180 and 200 kg/hr. The chopped output size was around 2-5 cm, which means that the cutting mechanism made fodder that was about the same size, which is good for making feed for animals. During the fresh grass testing, the feed entrance, blade configuration, and discharge path were all in the right places for soft green fodder, which meant that feeding went smoothly.

The throughput for straw dropped to 150-170 kg/hr, but the cut size stayed the same at about 2-5 cm. The reduced throughput compared to fresh grass is because straw is drier and stiffer, which makes it harder to chop and less smooth to feed. But the output stayed the same, which means that the cutting blade and rotating shaft assembly could handle dry food without too much trouble. The machine-made fine particles smaller than 2 mm and processed 50 to 60 kilogram of lentils per hour. This result proves that the prototype can grind things up and that the hammer and circular blade configuration can turn grain-type materials into powder. During the lentil trial, there were no clogs, which means that the grain inlet, grinding chamber, and powder output all worked well together under the specified environment.

Overall, the trial results, shown on Figure 14, reveal that the machine cut fresh grass better than straw in terms of throughput. The grinding operation had a lower throughput since it needed to reduce the size of the particles more finely. The test also showed that one prototype could use the same motor-driven system to treat both long, fibrous feed and grain-like material. The testing did not, however, contain any quantitative measurements of energy use, vibration, noise level, blade wear, or failure rate over a long period of time. So, the results should be seen as early prototype validation rather than full performance certification.

Figure 14. Illustration of the input and output of the feed

Source: taken by authors

The results demonstrate that the machine worked differently based on the type of input material and the sort of processing operation that was needed. Fresh grass had the highest throughput of all the materials evaluated, ranging from 180 to 200 kg/hr. This means that the cutting device worked best while it was cutting soft, wet feed. The fresh grass came out in pieces that were 2 to 5 cm long, which showed that the blade arrangement could make chopped fodder that was quite uniform and good for feeding livestock. The throughput for straw dropped to 150-170 kg/hr, but the output size stayed in the same 2-5 cm range. The average throughput for straw was around 16% lower than that of fresh grass. The drier and stiffer structure of straw makes it harder to cut and slows down the feeding of materials. This is why the amount of straw has gone decreased. But the machine nevertheless made cuts of the same size, which means that the cutting blade and shaft assembly could handle both green and dry feed materials in the conditions that were tested.

The grinding test with lentils had a reduced throughput of 50-60 kg/hr and a particle size of less than 2 mm. This decreased capacity is predicted because grinding needs to break things down into smaller pieces than just chopping. You simply need to chop grass and straw into little pieces, but you need to break lentils into small pieces, which means the circular blade and grinder hammer need to touch them more. The fact that there was no clogging during the lentil trial shows that the grain input, grinding chamber, and powder exit were set up correctly for the material that was tested. In general, Table 5 shows that the prototype can do more than one thing. The machine was able to cut more fodder than it could grind grain, but it was still able to do both jobs. The results also show that the same motor-driven system may handle materials with varying textures and processing needs. The table, on the other hand, just shows throughput, output size, and basic operating observations. For a more thorough performance assessment, subsequent testing must encompass energy consumption, cutting efficiency, grinding efficiency, vibration, noise level, blade wear, and long-term operational stability. So, the results in Table 6 should be seen as a first step in proving that the prototype works, not as a full test of its long-term engineering reliability.

Table 6. Summary of the trial results

Material	Throughput (kg/hr)	Cut/Particle Size	Observations
Fresh Grass	180-200	2-5 cm	Smooth feeding, uniform chopping
Straw	150-170	2-5 cm	Slightly slower due to dryness; consistent cut
Lentils	50-60	Fine powder (< 2 mm)	Uniform grinding; no clogging

Source: compiled by authors

The results of the present study demonstrate that the developed combined grass-cutting and grinding machine can perform two feed-preparation operations within a single mechanical system. The prototype successfully processed fresh grass, straw, and lentils, producing a throughput of 180-200 kg/hr for fresh grass, 150-170 kg/hr for straw, and 50-60 kg/hr for lentil grinding. The results also showed that the machine produced relatively uniform chopped material of 2-5 cm and fine ground particles below 2 mm for lentils. These findings indicate that the proposed machine is suitable for handling both soft green fodder and comparatively dry or hard feed materials. The use of a 3 HP electric motor, spur gear transmission, removable cutting blades, grinder hammers, and protective casing contributed to the stable operation of the system.

The findings of this study are partly consistent with the work of J. Sinha & A. Kumar (2021), who examined the ergonomic and mechanical performance of fodder cutters by changing the number of blades and feeding throat geometry. They showed that blade arrangement and feeding design strongly influence cutting efficiency and user comfort. The present study also confirms the importance of blade arrangement and feeding stability, as smooth feeding was observed during the trial with fresh grass. However, J. Sinha & A. Kumar mainly focused on ergonomic improvement of manual fodder cutters, whereas the present study developed a powered multipurpose machine that integrates both cutting and grinding operations. N. Sankpal *et al*. (2017) worked on the design and modification of chaff cutter machines to improve cutting efficiency and reduce manual effort. Their study emphasized machine modification for better usability, which is also reflected in the current design. The common point between their work and the present study is the intention to reduce labour and improve fodder-cutting performance. However, the present study differs by introducing a gear-based transmission system and an additional grinding function, while N. Sankpal *et al*. mainly focused on chaff-cutting improvement.

A. Kumar *et al*. (2013), M. Yadaw (2015) and M. Hammad (2019) designed and modelled a portable and safe chaff cutter machine, giving importance to compactness and operator safety. The present study supports this safety-oriented approach by including a protective casing around the cutting and grinding parts. Both studies recognise that exposed rotating components create operational risk. However, Hammad's work was mainly centred on portability and safe cutting, while the present research extends the design concept by combining grass cutting and grain grinding in one machine. S.M.S. Kumar *et al*. (2025) developed a chaff cutter using an AISI-1019 blade and focused on blade strength, cutting ability, and fabrication. Their work is related to the present study because blade durability is also an important design consideration here. In this research, high-carbon steel was selected for the grass-cutting and circular blades to improve wear resistance and service life. The difference is that S.M.S. Kumar *et al*. concentrated more on blade material and cutting structure, whereas the present study considered the whole machine system, including power transmission, grinding mechanism, casing, and local manufacturability. M.P. Patil *et al*. (2019) designed a flexible chaff-cutting machine capable of handling different types of fodder materials. Their work is comparable with the present study because both machines aim to process more than one type of agricultural material. The trial results of the present prototype with fresh grass and straw show that it can handle materials of different texture and moisture condition. However, M.P. Patil *et al*. focused mainly on flexibility in cutting, while the present study adds a grinding unit, making the machine more multifunctional for feed preparation.

D. Yallappa *et al*. (2024) evaluated a power-operated chaff cutter for selected fodder crops and considered performance parameters such as cutting efficiency and throughput. Their study is closely related to the present research because both works tested machine performance using fodder materials. The present machine showed a throughput of 180-200 kg/hr for fresh grass and 150-170 kg/hr for straw, which indicates practical applicability for small- and medium-scale farms. However, D. Yallappa *et al*. focused on performance evaluation of a chaff cutter, whereas the present study includes design, modelling, fabrication, and performance testing of a combined cutting and grinding machine. N.S. Navgale *et al*. (2023) developed a modified machine that combined chaff cutting and coconut dehusking using a single motor. Their work demonstrated that multiple agricultural operations can be integrated into one compact system. The present research follows a similar multifunctional design philosophy, but the functional combination is different. Instead of combining cutting with dehusking, this study combines grass cutting with grain grinding, which is more directly related to livestock feed preparation. Therefore, the present machine addresses a different user requirement and is more suitable for farmers who need both chopped fodder and ground feed ingredients. D.V. Nimbalkar (2018) and D.V. Nimabalkar *et al*. (2018) designed a low-cost lightweight chaff cutter cum grinder for small-scale farmers. Their work is one of the closest to the present study because both machines combine cutting and grinding functions. The common finding is that a combined machine can reduce the need for separate equipment and simplify feed preparation. However, the present study differs by using a spur gear transmission system instead of depending mainly on conventional belt-pulley arrangements. This gear-based design is expected to provide better durability, more stable power transmission, and reduced maintenance requirements.

Overall, comparison with previous studies shows that many researchers have addressed individual aspects of fodder-processing machinery, such as ergonomics, blade design, portability, safety, flexibility, and cutting performance. The present study contributes by integrating these concerns into a single locally manufacturable machine with both grass-cutting and grinding capacity. Its main technical distinction is the use of a gear-based power transmission system with a 3 HP motor, which produced a driven shaft speed range of approximately 1,015-1,523 rpm and supported effective cutting and grinding operation. The study also demonstrates that practical design decisions based on field visits, user feedback, component availability, and engineering calculation can lead to a machine suitable for local agricultural conditions. However, further testing with a wider range of fodder crops, longer operating periods, power consumption measurement, noise assessment, and blade wear analysis would be necessary to validate long-term reliability and commercial readiness.

CONCLUSIONS

The purpose of this study was achieved through the design, fabrication, and preliminary testing of a combined grass-cutting and grinding machine for livestock feed preparation. The developed prototype successfully integrated two major feed-processing operations- fodder cutting and grain grinding, within a single motor-driven mechanical system. The use of a 3 HP electric motor, spur gear power transmission, cutting blades, grinder hammers, separate feeding paths, and protective casing demonstrated that the proposed design can operate as a practical multipurpose machine under the tested conditions.

The review of relevant literature showed that previous studies mainly focused on individual aspects of chaff cutter development, such as ergonomic improvement, blade configuration, portability, safety, low-cost fabrication, and performance evaluation. However, limited attention was given to an integrated machine capable of both grass cutting and grain grinding with a durable gear-based transmission system. The concept of a combined feed-preparation machine is important because grass cutting and grinding are related but mechanically different processes: cutting requires controlled shearing of fibrous material, while grinding requires impact and repeated size reduction of harder feed materials. This study addressed both functions through a combined cutting and grinding chamber.

The results of prototype testing confirmed the functional performance of the machine. The machine processed fresh grass at 180-200 kg/hr with an output size of 2-5 cm, straw at 150-170 kg/hr with a similar cut size, and lentils at 50-60 kg/hr with particle size below 2 mm. These results indicate that the machine performed better for soft green fodder than for dry straw, while the grinding operation naturally produced lower throughput because finer size reduction was required. The protective casing, enclosed rotating assembly, and separate outlets also contributed to safer operation during the trial.

The novelty and practical value of this work lie in the development of a locally manufacturable combined machine using spur gear transmission instead of a conventional belt-pulley system. This design can reduce the need for separate cutting and grinding machines and may support small and medium-scale livestock farmers in feed preparation. Further research should include long-duration performance testing, measurement of energy consumption, vibration, noise level, blade wear, gear wear, and failure rate. Future studies should also test the machine with different fodder crops and grain types, optimise blade and hammer geometry, and conduct a detailed safety and reliability assessment before commercial production.

ACKNOWLEDGEMENTS

The authors acknowledge Bangladesh Maritime University for institutional and financial support.

FUNDING

This research was funded by the Postgraduate Research Management and Technology Transfer Centre (PRMTTC) of Bangladesh Maritime University. The authors would like to express their sincere gratitude to Bangladesh Maritime University and the University Grants Commission (UGC) for their financial support and assistance in conducting this research.

CONFLICT OF INTEREST

None.

REFERENCES

[1] Chowdhury, S., Khan, S., Sarker, M.F.H., Islam, M.K., Tamal, M.A., & Khan, N.A. (2022). Does agricultural ecology cause environmental degradation? Empirical evidence from Bangladesh. *Heliyon*, 8(6), article number e09750. doi: 10.1016/j.heliyon.2022.e09750.

[2] Ghimire, A., Lin, F., & Zhuang, P. (2021). The impacts of agricultural trade on economic growth and environmental pollution: Evidence from Bangladesh using ARDL in the presence of structural breaks. *Sustainability*, 13(15), article number 8336. doi: 10.3390/su13158336.

[3] Hammad, M. (2019). *Design and modelling of portable & safe chaff cutter machine* (Doctoral thesis, University of Engineering and Technology, Lahore, Pakistan).

[4] Jamal, M.R., Kristiansen, P., Kabir, M.J., & Lobry de Bruyn, L. (2023). Challenges and adaptations for resilient rice production under changing environments in Bangladesh. *Land*, 12(6), article number 1217. doi: 10.3390/land12061217.

[5] Jayendra, P., & Suresh, G.Y. (2020). Design and modification of chaff cutter. *International Journal for Scientific Research & Development*, 8(2), 421-425.

[6] Kumar, A., Singh, J.K., & Singh, C. (2013). Prevention of chaff cutter injuries in rural India. *International Journal of Injury Control and Safety Promotion*, 20(1), 59-67. doi: 10.1080/17457300.2012.674043.

[7] Kumar, S.M.S., Darshan, R., Kalyan, S., Abhishek, M.K., & Prajwal, R. (2025). Design and fabrication of chaff cutter with blade (AISI-1019). *Oeil Research Journal*, 23(6), 61-65.

[8] Moller, K., Eeswaran, R., Nejadhashemi, A.P., & Hernandez-Suarez, J.S. (2023). Livestock and aquaculture farming in Bangladesh: Current and future challenges and opportunities. *Cogent Food & Agriculture*, 9(1), article number 2241274. doi: 10.1080/23311932.2023.2241274.

[9] Navgale, N.S., Bhavesh, T., Ghodake, O., Mahale, A., & Adnak, N. (2023). Design and modification of chaff-cutter. *International Advanced Research Journal in Science, Engineering and Technology*, 10(6), 279-283. doi: 10.17148/IARJSET.2023.10641.

[10] Nimabalkar, D.V., Jadhav, M.L., & More, S.N. (2018). Design of a low-cost light weight chaff cutter cum grinder. *The Andhra Agric*, 65, 36-41.

[11] Nimbalkar, D.V. (2018). Design and development of chaff cutter cum grinder. *International Journal of Agriculture Sciences*, 10(6), 5517-5521.

[12] Patil, M.P., Mali, M.P., Ballal, M.Y., Patil, M.H., & Pawar, M.G. (2019). Design and development flexible chaff cutting machine. *International Journal for Research in Applied Science & Engineering Technology*, 7(6), 2629-2634. doi: 10.22214/ijraset.2019.6446.

[13] Rahman, M.M., Ali, M.R., Oliver, M.M.H., Hanif, M.A., Uddin, M.Z., Tamim-Ul-Hasan, Saha, K.K., Islam, M.H., & Moniruzzaman, M. (2021). Farm mechanization in Bangladesh: A review of the status, roles, policy, and potentials. *Journal of Agriculture and Food Research*, 6, article number 100225. doi: 10.1016/j.jafr.2021.100225.

[14] Rajkumar, E., Pavankumar, P.V., Simha, J.V., & Sai, M.V. (2020). Design and 3D printing of hand operated chaff cutter. *Materials Today: Proceedings*, 22, 2520-2524. doi: 10.1016/j.matpr.2020.03.380.

[15] Rayhan, S.J., Rahman, M.S., & Lyu, K. (2023). The role of rural credit in agricultural technology adoption: The case of Boro rice farming in Bangladesh. *Agriculture*, 13(12), article number 2179. doi: 10.3390/agriculture13122179.

[16] Sankpal, N., Powar, V., Patil, S., Salunke, K., & Pandit, S.V. (2017). Design and modification of chaff cutter machine. *International Journal of Innovative Research in Science, Engineering and Technology*, 6(4), 5675-5683. doi: 10.15680/IJIRSET.2017.0604126.

[17] Shamsuzzaman, M.M., Mozumder, M.M.H., Mitu, S.J., Ahamad, A.F., & Bhyuian, M.S. (2020). The economic contribution of fish and fish trade in Bangladesh. *Aquaculture and Fisheries*, 5(4), 174-181. doi: 10.1016/j.aaf.2020.01.001.

[18] Sinha, J., & Kumar, A. (2021). Ergonomically evaluating and modifying fodder cutter by increasing number of blades and varying throat geometry. *Biological Forum – An International Journal*, 13(2), 110-119.

[19] World Medical Association. (1964). *Declaration of Helsinki*. Retrieved from https://www.wma.net.

[20] Yadaw, M. (2015). *Refinement of manually operated chaff cutter as per ergonomic consideration* (Master's thesis, Indira Gandhi Krishi Vishwavidyalaya, Raipur, India).

[21] Yallappa, D., Shirwal, S., Veerangouda, M., Hirekurubaru, M., Murali, M., Kavan Kumar, V., & Ravi, Y. (2024). Performance evaluation of power operated chaff cutter for selected fodder crops. *Journal of Scientific Research and Reports*, 30(4), 103-114. doi: 10.9734/jsrr/2024/v30i41895.

Кандакар Ахтер Хоссейн
Віце-канцлер
Морський університет Бангладеш
1216, ділянка № 14/06-14/23, Паллабі, Мірпур-12, м. Дакка, Бангладеш
https://orcid.org/0009-0008-3080-2270

Мд Джобаєр Мія
Викладач
Морський університет Бангладеш
1216, ділянка № 14/06-14/23, Паллабі, Мірпур-12, м. Дакка, Бангладеш
https://orcid.org/0000-0003-0630-004X

Мохаммад Фархад Хоссен
Додатковий реєстратор
Морський університет Бангладеш
1216, ділянка № 14/06-14/23, Паллабі, Мірпур-12, м. Дакка, Бангладеш
https://orcid.org/0009-0005-6734-7505

Мд Масудур Рахман
Аспірант
Морський університет Бангладеш
1216, ділянка № 14/06-14/23, Паллабі, Мірпур-12, м. Дакка, Бангладеш
https://orcid.org/0009-0004-1215-2586

Конструкція та модифікація комбінованої траворізально-подрібнювальної машини

Анотація. Ефективне приготування корму для худоби залишається серйозною проблемою для малих та середніх фермерів у Бангладеш, де ручне різання корму та окреме виконання процесів подрібнення характеризуються значними витратами часу, трудових ресурсів і фінансових затрат. Зростання цін на корми та обмежений доступ до доступного механізованого обладнання роблять розробку багатоцільової техніки місцевого виробництва надзвичайно актуальною для сільськогосподарського сектору. Метою цієї статті було спроєктувати, виготовити та оцінити комбіновану машину для скошування та подрібнення трави, придатну для практичного використання в Бангладеш. У дослідженні використовувалися польові виїзди, спілкування з фокус-групою, моделювання на основі автоматизованого проєктування, виготовлення прототипу та випробування продуктивності для оцінки конструкції, експлуатації та придатності машини для користувача. Розроблена машина об'єднує скошування трави та подрібнення зерна в єдиній компактній системі, що живиться від електродвигуна потужністю 3 к.с. На відміну від багатьох традиційних машин, які залежать від ремінно-шківної системи, запропонована конструкція використовує систему передачі з циліндричними зубчастими колесами для підвищення довговічності, стабільності та передачі потужності. Зубчаста конструкція забезпечує кінцеве передавальне число 0,846, що забезпечує швидкість веденого вала приблизно 1015-1523 об/хв та швидкість кінчика леза приблизно 15,9-23,9 м/с. Випробування зі свіжою травою, соломою та сочевицею показали, що машина може переробляти 180-200 кг/год трави, 150-170 кг/год соломи та 50-60 кг/год сочевиці на дрібний порошок. Подрібнений матеріал був рівномірним, подача – плавною, а захисний кожух допоміг підвищити безпеку експлуатації. Конструкція також забезпечує заточування лез, місцеве виробництво та нижчі вимоги до технічного обслуговування. Результати можуть бути застосовані в дрібномасштабному тваринництві, центрах приготування кормів та майстернях сільської техніки для зменшення трудозатрат, підвищення ефективності переробки кормів та підтримки механізації сільського господарства

Ключові слова: газонокосарка; подрібнювач; сільське господарство; сільськогосподарська техніка; приготування кормів

Machinery & Energetics
Vol. 17, No. 2. 2026

Journal homepage:
https://technicalscience.com.ua/en

UDC 621.311.243:621.316.7:338.2
DOI: 10.31548/machinery/2.2026.3

ISSN 2663-1334
e-ISSN 2663-1342

Taras Bilas*

Postgraduate Student
Kyiv National University of Construction and Architecture
03037, 31 Povitrianykh Syl Ave., Kyiv, Ukraine
https://orcid.org/0009-0008-8477-3794

Volodymyr Yaras

PhD in Technical Sciences, Associate Professor
Kyiv National University of Construction and Architecture
03037, 31 Povitrianykh Syl Ave., Kyiv, Ukraine
https://orcid.org/0000-0003-2252-9418

Economic efficiency of the Net Billing model for solar power plants in the private sector of Ukraine (using houses of 120-200 m² as an example)

Abstract. The rapid transformation of the Ukrainian energy sector and the persistent trend towards rising electricity prices for domestic consumers have created an urgent need for homeowners to find ways to achieve energy independence. The purpose of the study was to comprehensively evaluate the economic efficiency of solar systems running the Net Billing model for middle-class households. The study was based on simulation modelling of hourly generation and consumption balances using methods of mathematical analysis and calculation of NPV indicators. The dynamics of return on capital expenditures within three different energy consumption strategies was investigated, which determined the critical impact of the own consumption coefficient on the financial viability of a solar project. A consistent correlation has been identified between profitability and the integration of lithium-iron-phosphate batteries with a capacity of ten kilowatt-hours, which provide an optimal balance between the initial investment and the ability to fully cover evening peak loads in households. It was established that when using active demand management algorithms, the real return period of invested funds was reduced to six whole and nine tenths of a year, which meets the criteria for high investment attractiveness. Technical and economic aspects such as annual physical degradation of photovoltaic panels and operating costs were analysed, which proved the preservation of a positive net present value of the asset throughout the entire twenty-five-year life cycle. It has been concluded that switching to a self-generation system, provided a high SCR level is achieved, provides the homeowner with total savings, and a net financial benefit of over USD 32 thousand. The developed recommendations will become the basis for developers and project companies in the technical substantiation of the construction of autonomous systems in Ukraine

Keywords: prosumerism; energy independence; return on investment; decentralised generation; battery energy storage systems; demand management; photovoltaic systems

INTRODUCTION

As of 2025, the issue of energy independence of private households in Ukraine has become critical due to the need to decentralise the energy system and increase its resistance to external factors. The transformation of the regulatory framework, in particular, the transition from a incentive-based "green" tariff to the Net Billing model, has radically changed the financial logic of investing in renewable energy facilities. For owners of houses with an area of 120-200 m², there is an urgent need to review approaches to choosing equipment capacity and energy consumption algorithms. The importance of investigating this topic was conditioned by the lack of clear application models that

Article's History: Received: 22.12.2025; Revised: 18.03.2026; Accepted: 21.05.2026; Published: 29.05.2026.

Suggested Citation:
Bilas, T., & Yaras, V. (2026). Economic efficiency of the Net Billing model for solar power plants in the private sector of Ukraine (using houses of 120-200 m² as an example). *Machinery & Energetics,* 17(2), 39-49. doi: 10.31548/machinery/2.2026.3.

*Corresponding author (bilas_tm-2024@knuba.edu.ua)

would consider current prices for solar power plant (SPP) components and new rules for interaction with the market. Scientific substantiation of the parameters of such systems determined ways to avoid inefficient distribution of capital in conditions of limited financial resources. The development of accurate economic forecasts for the private housing segment has become a basic condition for further scaling of distributed generation in the country. That is why the study of this issue was identified as a priority area for ensuring the energy sustainability of communities.

The current state of scientific knowledge in the field of decentralised energy is characterised by an active search for optimal models of interaction between prosumers and the general network in the conditions of energy transition. M. Trela & A. Dubel (2022) investigated such an aspect of the topic as the economic efficiency of investment in photovoltaic systems when changing government support mechanisms. Their study concluded that the transition from the Net Metering model to Net Billing in Poland lead to an increase in the payback period of projects, but encourages households to install battery energy storage systems to increase self-consumption.

The issue of integrating prosumers into the structure of smart grids was the focus of O.V. Kyrylenko's research (2022). The researcher pointed out that the development of the Smart Grid concept combined with the active participation of private consumers is critical for ensuring the sustainability of the Ukrainian energy system in the context of military and post-war challenges. These results show that the decentralisation of generation is becoming not only an economic, but also a security factor. In the joint study by S.P. Denysiuk & D.G. Derevianko (2021) analysed the functioning of microgrids and Demand Side Management methods. The researchers concluded that the active involvement of prosumers in load balancing through flexible consumption mechanisms can significantly reduce peak network loads.

P. Benalcazar *et al*. (2025) conducted a comparative analysis of energy surplus compensation models in developing countries. The researchers stressed that the Net Billing model is more financially balanced for distribution system operators, since it considers the market value of electricity in real time, as opposed to quantitative accounting in Net Metering. The economic substantiation of solar stations in the residential sector of Ukraine based on current development scenarios was investigated by T. Kurbatova *et al*. (2024). The researchers found that despite high capital expenditures (CAPEX), the installation of hybrid SPPs remains profitable due to the projected increase in electricity prices for the population and the possibility of selling surpluses through the self-production mechanism. R. Luthander *et al.* (2015) in their paper systematised in detail the technical and economic mechanisms for increasing the level of own solar energy consumption in the residential sector. The researchers concluded that the use of intelligent demand management and local accumulation systems can significantly increase the financial stability of prosumer projects in the context of changing regulatory market models.

J. Fan & H. Zhou (2023) investigated the optimisation aspect of hybrid systems involving PV panels and battery packs. They concluded that the use of intelligent charge/discharge control algorithms can increase the energy independence of households by up to 70-80%. L. Smiech *et al.* (2025) did not address the technical aspects of grid connection; instead, they focused on the socio-economic impact of renewable energy sources on household living standards. It was this optics of the study that determined their conclusions, which consisted in the fact that the development of prosumerism is an effective tool for combating energy poverty and contributes to the decarbonisation of the economy at the level of individual consumers.

U. Pysmenna *et al*. (2023) in their study analysed in detail the current state of the Ukrainian energy market and the barriers that small renewable energy producers face when trying to integrate. The researchers argued that the transformation of market conditions and the transition to new models of interaction requires not only technical re-equipment of microgeneration facilities, but also the creation of clear, transparent institutional rules for stimulating active consumers. Technical aspects of voltage regulation and the use of accumulation systems to stabilise network parameters were considered by M.Z. Zgurovets & M.M. Kulyk (2023). The researchers concluded that the mass installation of inverter systems requires the introduction of automated control systems at the level of local transformer substations. Ensuring the proper quality of electrical energy at the connection points of prosumers is important for optimising the operating modes of distributed microgeneration systems. In particular, the study by V.G. Yagup & K.V. Yagup (2024) proposed a new analytical method for determining the conditions for full reactive power compensation in power supply systems. The researchers proved that mathematically accurate regulation of the power balance allows minimising energy losses in the network, which is critical when designing local generation nodes that work in parallel with a centralised system. M. Kabir *et al*. (2021) focused on the techno-economic analysis of housing systems in different climatic zones. Their results confirmed that the performance of Net Billing models is critically dependent on the difference between the purchase and sale price of energy, which requires careful planning of battery capacity.

The purpose of the study was to determine the parameters of economic efficiency and payback periods of hybrid solar power plants for private homes with an area of 120-200 m² in the context of the transition of the Ukrainian energy market to the Net Billing model. To achieve this goal, the following tasks were defined:

1) hourly profiles of electricity generation and consumption were modelled for the selected type of facilities based on seasonal fluctuations;

2) key financial indicators of the project (NPV, LCOE, DPP) were calculated under various scenarios of state tariff dynamics;

3) practical algorithm for optimising own consumption (SCR) has been developed to increase the return on investment in solar generation.

MATERIALS AND METHODS

The methodology was constructed based on simulation modelling of hourly energy balances and household financial flows over the 25-year project life cycle. To ensure reproducibility of the results, the MS Excel software suite was used with the developed algorithm for calculating the net present value (NPV) and payback period. The PVGIS insolation database (SARAH2) was used to simulate solar generation. In contrast to the simplified average annual methods, the calculation was performed for specific coordinates of the central region of Ukraine (50.45°N, 30.52°E). Simulation parameters included: the installed power of the 10 kW array, the use of Tier-1 monocrystalline modules with an efficiency of more than 21%, an azimuth of 0° (south orientation) and an angle of inclination of 35°. System losses were recorded at 14% to account for cable resistance and degradation of inverter equipment (PVGIS, n.d.). Modelling of the consumption profile was performed for a typical house with an area of 160 m². The annual electricity consumption of 6,500 kWh was justified based on averaged data for households with air conditioning systems and pumping equipment. To construct hourly load profiles, assumptions were made regarding the typical behaviour of a four-person household: the presence of morning (07:00-09:00) and evening (18:00-22:00) peaks in energy consumption, which correlates with studies on the technical and economic prospects of residential systems (Kabir *et al.*, 2021).

Economic parameters were determined based on market indicators as of 2025. Specific CAPEX in the amount of 950 USD/kW were determined based on the results of an analysis of commercial offers of leading installers in Ukraine, including the cost of equipment, logistics, and installation. Annual tariff growth and decarbonisation scenarios were adopted based on forecast models for the development of the electricity sector of Ukraine until 2035 (Sotnyk *et al.*, 2024).

Special attention was paid to the 10 kWh battery energy storage system (BESS) model. The BESS algorithm was based on Self-Consumption Priority, and technical optimisation of DC/AC equipment considered loss minimisation, based on I. Buratynskyi & T. Nechaieva (2022): surplus generation was primarily used to charge batteries, and after reaching 100% charge, it was exported to the network using the Net Billing model. The discharge of the drives was programmed for evening peak periods with a depth-of-discharge (DoD) limit of up to 90% to ensure battery life for 15 years.

To increase scientific reliability, a Sensitivity Analysis of key conclusions before changing the input data was performed. The influence of the variability of tariff growth rates (range 5-20%) and the cost of BESS on the payback period of the project was modelled. Validation of the developed model was carried out by comparing the calculated forecasts with the actual data of the generation of the operating SPP with a capacity of 10 kW in the Kyiv Oblast for 2024, where the root-mean-square deviation was less than 5%. The total generation of the system in the first year of operation was 11,450 kWh. The model (Table 1) considers the linear degradation of photomodules at the level of 0.5% per year, which leads to a decrease in annual output to 10,076 kWh for the 25th year of operation.

Table 1. Output parameters

Object characteristics and source data. A model of a private house corresponding to the characteristics of the middle class in Ukraine has been selected for the calculations	
Total area of the item	160 m² (median value for the range 120-200 m²)
Annual electricity consumption	6,500 kWh (basic level, including operation of air conditioning systems, pumping equipment, and household appliances)
Geographical location	Central region of Ukraine (coordinates for calculating insolation according to PVGIS data)
Discount rate (*r*)	10% (for calculating NPV)
Tariff growth forecast	15% annually
Capital expenditure (CAPEX)	USD 950 per 1 kW of installed capacity (including the cost of battery systems)
Technical parameters of the system. To ensure energy independence and efficient operation within the Net Billing model, a hybrid configuration of a solar power plant has been chosen	
Photovoltaic field (P_{pv})	10 kW (Tier-1 monocrystalline panels with efficiency >2.1%)
Inverter equipment	Hybrid three-phase inverter with a rated power of 10 kW
Battery energy storage system (BESS)	LiFePO4 battery pack with a capacity of 10 kWh
Array orientation	South-facing, with an angle of 35° to the horizon
Power degradation	0.5% per year for the service life (25 years)
Modelling scenarios. Cost-effectiveness of Net Billing is critically dependent on the energy consumption strategy. Study modelled three scenarios	
“Passive” script (Baseline)	Household does not change its consumption habits. Main loads fall on the morning and evening. SCR is minimal (approximately 25-30%)
“Load Shifting” script	Use of Smart Home elements to transfer the operation of energy-intensive appliances (washing machines, boilers, irrigation systems) to peak generation hours (11:00-15:00). Expected SCR – 40-45%

Continued Table 1.

Modelling scenarios. Cost-effectiveness of Net Billing is critically dependent on the energy consumption strategy. Study modelled three scenarios	
BESS optimised script	Integration of algorithms for priority battery charging and discharging during evening consumption peaks. This allows maximising the use of own energy and minimising purchases from the network. Target SCR – 60-70%

Source: developed by the authors

The mathematical model of energy balance has the following form. The dynamics of energy distribution within a household is described by the instantaneous balance equation for each hour t:

$$E_{gen}(t) = E_{sc}(t) + E_{char}(t) + E_{surplus}(t), \quad (1)$$

where: $E_{gen}(t)$ – volume of SPP generation; $E_{sc}(t)$ – volume of instantaneous self-consumption by the house; $E_{char}(t)$ – energy directed to charge the storage device; $E_{surplus}(t)$ – surplus exported to the external network. The efficiency of using own generation was determined by the self consumption ratio (SCR):

$$SCR = \frac{\sum_{t=1}^{8760}(E_{sc}(t)+E_{dis}(t))}{\sum_{t=1}^{8760}E_{gen}(t)}, \quad (2)$$

where $E_{dis}(t)$ – volume (amount) of electrical energy discharged from the battery (BESS) at a particular time t, kWh. Net Billing economic algorithm. Cash credit (C_{nb}) for excess energy transferred to the grid, it is calculated using the equation:

$$C_{nb} = \sum_{i=1}^{n}\left(E_{surplus,i} \times \left(P_{DAM,i} - C_{trans}\right)\right), \quad (3)$$

where: $P_{DAM,\ i}$ – hourly price on the day-ahead market (DAM); C_{trans} – tariff for transmission and distribution services. Financial evaluation criteria. The NPV method was used to determine investment attractiveness:

$$NPV = \sum_{t=1}^{n}\frac{CF_t}{(1+r)^t} - CAPEX. \quad (4)$$

Simple payback period (PBP) is defined as:

$$PBP = \frac{CAPEX}{S_{total} - OPEX}, \quad (5)$$

where S_{total} – annual savings, and OPEX – operating expenses (1% of CAPEX).

RESULTS AND DISCUSSION

Based on simulation modelling of hourly generation profiles for a 10-kilowatt SPP and the energy consumption of a 160 m^2 household, data on the energy balance and financial performance were obtained. The calculations were made considering the annual degradation of the equipment and operating costs for its maintenance. Energy balance accounting for degradation. In the course of the study, the annual generation of a 10 kW SPP was calculated for the entire project life cycle (25 years). To verify the model, absolute output values were set: in the first year of operation, the generation was 11,450 kWh, and in the twenty-fifth year, considering the cumulative effect of degradation, this indicator decreased to 10,076 kWh.

A linear model of productivity reduction of 0.5% per year was selected based on an analysis of the life cycle of photovoltaic systems in the residential sector (Kurbatova *et al.*, 2024), which meets the industry standards of the power conservation guarantee. Degradation was integrated into the hourly model by applying a reduction factor to the baseline generation profile obtained through PVGIS for each subsequent calculation year. Seasonal fluctuations in insolation were considered automatically through the use of historical SARAH2 data series, which helped to maintain a realistic output amplitude in winter and summer periods.

The procedure for obtaining scenario indicators (Table 1) was implemented by iteratively comparing hourly generation values ($E_{\{gen,\ t\}}$) and consumption ($E_{\{load,\ t\}}$). SCR was calculated as the ratio of the integral sum of the combined graphs to the total amount of energy produced for the year. Export volumes were defined as a positive difference between generation and consumption at moments of excess, considered the state of charge of BESS for the corresponding scenario.

The reliability of the simulation was confirmed by comparing the results with empirical monitoring data of real objects. It was found that the root mean square error (RMSE) for the annual figures did not exceed 4.5%. The variability of the results within ±3% was conditioned by possible deviations of meteorological conditions from the average values, which was considered acceptable for strategic financial planning (PVGIS, n.d.). The energy distribution for the three load management scenarios is shown in Table 2.

Table 2. Energy indicators of SPP according to scenarios (1st year of operation)

Indicator	Scenario 1 (Baseline)	Scenario 2 (Load Shifting)	Scenario 3 (BESS Optimised)
Self-consumption ratio (SCR)	26%	42%	68%
Volume of substituted energy from the grid	2,977 kWh	4,809 kWh	7,786 kWh
Export to the network (Net Credit)	8,473 kWh	6,641 kWh	3,664 kWh

Source: compiled by the authors

The economic efficiency of the project was assessed by constructing a detailed cash flows model for the 25-year life cycle of the SPP. To ensure transparency of NPV calculations and payback period, annual revenue tables were developed, which considered the combination of savings from replacing own consumption and accrued loans for energy exports to the grid using the Net Billing model. To reflect the real cost of capital, changes in the value of money over time were considered through a discount rate of 10%, which was applied separately from the rate of tariff growth. This approach distinguished between financial risks and long-term market development scenarios (Sotnyk *et al.*, 2024). Substantiation of the baseline scenario of tariff growth at the level of 15% annually for the first five years was made based on analysis of the capacity deficit in the Ukrainian energy system and obligations to bring prices to market-based levels. For alternative scenarios, conservative (5% growth) and optimistic (20% growth) options were considered.

The formation of DAM price indicators, which are the basis for Net Billing, was implemented through the use of weighted average hourly prices for 2024. To consider market volatility, a stochastic coefficient of fluctuations within ±7% was introduced into the model, which allowed simulating market instability and its impact on the volume of funds on a special prosumer account. Operating expenses (OPEX) were set at 1% of CAPEX annually, which covered the costs of insurance, monitoring, and planned depreciation of components.

Equipment degradation (0.5% per year) was integrated into financial calculations as a reduction factor to the generation volumes of each subsequent year. This automatically resulted in a reduction in the monetary equivalent of savings in each period, which was crucial for accurately determining the discounted payback period (DPP). Analysis of the sensitivity of the results to changes in key parameters showed that the most significant impact on NPV was the change in initial capital investment and the volatility of DAM prices (Kurbatova *et al.*, 2024). In particular, a 10% change in the value of BESS resulted in a 0.6-year shift in the payback period in Scenario 3. Table 3 shows the generalised financial indicators obtained as a result of modelling.

Table 3. Financial performance indicators of the project according to scenarios

Indicator	Scenario 1 (Passive)	Scenario 2 (Active)	Scenario 3 (BESS Optimised)
Net present value (NPV), USD	8,450	14,200	20,850
Simple payback period (PBP), years	9.4	8.2	6.9
Discounted payback period (DPP), years	12.8	10.4	8.6
Profitability index (PI)	1.89	2.49	3.19

Source: compiled by the authors

Impact of physical wear and tear on the project life cycle. In the course of the study, the technical and economic stability of the project to physical wear and tear of the main components of the SPP was assessed over a 25-year period. The substantiation for the rate of degradation of photovoltaic panels was based on the technical specifications of Tier-1 modules, in particular, Longi Solar and Jinko Solar, which guarantee a reduction in power by no more than 1-2% in the first year (due to the LID effect) and by 0.4-0.55% annually in subsequent periods. Degradation was integrated into the financial model as a reduction factor (k_{deg}) which directly reduced the volume of annual generation ($E_{gen}(t)$), and hence the volume of cash flows from the replacement of energy consumption and exports. It was found that cumulative degradation of the panels amounting to 12.5% by the end of their life cycle resulted in a 6.8% reduction in the project's NPV compared with an idealised model that did not include depreciation, confirming the importance of considering technical factors when calculating the payback period.

Special attention was paid to BESS based on LiFePO4 batteries. The assumption of their wear was formed on the basis of the cyclic resource indicator (6,000 cycles at DoD of 80-90%). In the conditions of frequent power outages, which was typical for the Ukrainian energy system in the period 2022-2024, the non-linearity of the wear process was considered. An additional operating intensity factor was added to the model (Zgurovets & Kulyk, 2023), which simulated accelerated capacity loss due to daily deep cycling. It was found that with intensive operation of drives, their impact on network stability and payback requires the use of automatic load management systems. As noted by C. Scott *et al.* (2023), efficient operation of energy storage facilities in the residential sector requires accurate predictive data on insolation. The implementation of such intelligent algorithms in the control algorithms of the system developed by US allows preventing premature battery wear (BESS) and ensuring maximum financial benefits within the Net Billing model. This correlates with the finding of I.V. Blinov *et al.* (2022), according to which local accumulation and demand management on the consumer side are key tools for minimising the negative impact of solar generation on voltage stability in distribution nodes. The high self-consumption ratio (SCR = 68%) calculated in the third scenario demonstrates that the integration of a BESS helps to relieve excess technical pressure on the distribution network's transformer equipment during peak generation hours. The need to consider clear mathematical modes when charging and discharging BESS within the proposed control algorithm is consistent with the general principles of optimising energy flows. As demonstrated by V.G. Yagup & K.V. Yagup (2024), the use of analytical methods for calculating compensation parameters in local networks allows achieving maximum system stability with minimal active power losses. In the context of this research, accurate SCR scenario modelling provided a similar effect of minimising unbalances at the prosumer-external network interface. To assess the worst-case scenarios, conditions of accelerated equipment wear were modelled (panel degradation of 0.7% and BESS failure in the 8th year) (Kurbatova *et al.*, 2024). This resulted in DPP in Scenario 3 for 1.4 years. Analysis of the sensitivity of economic indicators showed that the project's NPV is more sensitive to the rate of BESS degradation than to the loss of photomodule power, since the cost of the accumulation system accounts for a significant share of CAPEX, and its functionality critically affects the SCR.

As of 2025, it has been proven that the use of intelligent monitoring systems and optimal charge/discharge modes has minimised the impact of nonlinear wear, ensuring the financial viability of the project even in scenarios with increased load on the power grid. Without the establishment of SPP, with the current tariff and its annual growth of 15%, the total household electricity costs for 25 years will amount to more than USD 45,000. The implementation of the Net Billing system in Scenario 3 allows not only to fully recoup the investment, but also to provide a total net profit (in the form of savings and loans) of USD 32,000 for the entire period of operation.

The study helped to comprehensively assess the transformation of the economic landscape for private solar energy producers in Ukraine in the context of the transition to the Net Billing model. The results confirmed the hypothesis that the financial stability of prosumer projects in the new regulatory environment has shifted from maximising total generation to maximising SCR. The central scientific contribution of this paper is to prove that the SCR coefficient is a dynamic result of simulation modelling, and not a static assumption. The above values (26%, 42%, and 68%) were obtained by hourly calculation of energy balances for various scenarios of household behaviour and technical equipment. The choice of a scenario approach for evaluating SCR indicators (26%, 42%, and 68%) is consistent with current methodological approaches in the field of construction and energy modelling. As noted by X. Liu & Z. Gou (2025), a multi-strategic scenario analysis is the most appropriate tool for accounting for consumption and generation uncertainty in the housing sector. The model of interaction of a hybrid SPP with a heat pump developed by the authors confirms their conclusions: the differentiation of scenarios allows clearly distinguishing between the technical and economic effects of implementing BESS accumulation systems under different operating conditions. The base value of 26% in the passive scenario reflects the natural level of combining generation and consumption graphs for a house of 160 m², which is an objective result of modelling, considering the absence of residents during the day and peak loads in the evening. The results of technical and economic modelling obtained confirmed the conclusions of A. Ordóñez *et al.* (2022) that the cost-effectiveness of prosumer under Net Billing conditions critically depends on the load profile and the ability of the system to store energy. Unlike Net-Metering, where energy volumes are physically balanced 1:1, the Net-Billing model at a low level of own consumption (as in our first scenario with SCR = 26%) significantly extends the return on investment due to the difference between the purchase rates and the sale price of the surplus. This proves the need to integrate solutions such as BESS to achieve acceptable financial performance. The SCR range of 42% in the second scenario was the result of the introduction of Demand Side Management (DSM), which indicates a significant potential for consumer behavioural adaptation, while the highest level (68%) was achieved only with the integration of BESS, which allowed the accumulation of surplus daily generation. The validity of these ranges was confirmed by their compliance with the real load profiles of modern energy-efficient homes, where a significant share of energy is spent on life support systems that work in the background regardless of the presence of a person.

It is important to detail the mechanism by which SCR is converted to financial performance in the Net Billing model. This model creates a two-tier energy valuation system: a unit of energy consumed locally is valued at the full retail rate due to the avoidance of purchase costs, while an exported unit is compensated only at the DAM price less transmission and distribution costs. Since the retail tariff for the population in Ukraine includes a significant infrastructure component, the cost of own consumption is 45-60% higher than the monetary equivalent of exports. The analysis showed that every percentage increase in SCR leads to a disproportionate increase in NPV. This is because a high SCR protects the investor from the price gap between buying and selling energy. Based on the simulation results, it was found that increasing the SCR from 26% to 68% reduces DPP by 4.2 years, which makes energy storage technologies a key financial instrument, and not just a technical addition. It is important to emphasise that achieving a high SCR level (68%) in the third scenario is not a purely financial result, but rather indicates a deep technical synergy between photovoltaic and the heat pump. In this architecture, the building begins to function as an energy damper: using the inertia capacity of enclosing structures, the system "shifts" the peaks of heat consumption by hours of maximum solar insolation. This allows turning excess generation into a cheap thermal resource, minimising exports to the grid during periods of low DAM prices. This approach makes the Net Billing model not just an accounting mechanism, but an incentive for creating intelligent local systems where each generated kWh is used as efficiently as possible within the consumption circuit.

The issue of transition from incentive tariffs to market mechanisms is covered in detail in the paper by M. Trela & A. Dubel (2022). Analysing the experience of Poland, the authors noted that the introduction of Net Billing reduced the financial attractiveness of SPP due to the extension of payback. The current results partially confirm this: for passive consumers, the payback period is close to ten years. However, in the Ukrainian reality, due to the high dynamics of tariff growth, payback remains acceptable for the middle class. This is conditioned by the energy vulnerability of Ukraine, where SPP is considered as a risk hedge, and not just an investment. The study of the mechanisms of energy storage allowed comparing the data with the results of A.S. Hassan *et al*. (2017). These researchers have proven that for the private sector, an SCR of more than 60% is crucial for the profitability of systems with BESS. The modelling for a 10-kilowatt SPP gave an identical result. The claim by A.S. Hassan *et al.* regarding the dominant role of price arbitrage is, however, open to debate in the context of Ukraine. In the face of network instability, the main driver of installing BESS is the premium for autonomy, and not margin profit, which was not fully considered by colleagues.

An important element of the discussion is the assessment of the technical and economic parameters of microgeneration operating in market conditions. The study by P. Olczak *et al*. (2022) confirmed that in the context of the transition to the Net Billing model, the financial stability of a household directly depends on the technological configuration of the system. In particular, the researchers noted the priority of implementing local drives to smooth out price peaks, which fully correlates with the results obtained by us regarding the effectiveness of integration of BESS systems for Ukrainian prosumers.

Special attention should be paid to the technical implementation of control algorithms within a three-phase hybrid inverter with a capacity of 10 kW. It was found that the dynamic response of the system to changes in the load in real time directly affects the purity of the present value by minimising "parasitic" energy flows to the network during periods of low DAM prices. The use of intelligent monitoring systems eliminates the impact of non-linear wear, ensuring stable operation in conditions of instability of the general energy system, which was typical for Ukraine in the period 2022-2024. This technical approach confirms the feasibility of switching from passive consumption to active DSM, since it allows the use of internal BESS resources not only to save money, but also to maintain a stable frequency and voltage within the household. This creates additional technical value of the system, which goes beyond a simple financial payback, turning a private SPP into an active element of a local micro-network.

The opinion of P. Benalcazar *et al*. (2025) regarding the social and networking role of Net Billing was supported in this paper. However, the conclusions of these researchers, given the results of the analysis, should be considered in a different plane. The researchers argued that the transition to self-production automatically encourages consumers to improve energy efficiency. Instead, sensitivity analysis showed that without intelligent automation, consumers are often unable to maintain high SCR levels on their own due to the inertia of everyday habits. This calls into question the automatism of the positive effects of Net Billing without additional technical support. Comparison with the findings of Ukrainian researchers also revealed certain discrepancies. S.P. Denysiuk & D.G. Derevianko (2021) argued that decentralisation should be based on intelligent micro-networks. The results of this simulation confirm this thesis, but indicate a significant barrier: the high level of capital investment as of 2025 makes such systems available only to a narrow segment. This problem of financial constraints in the development of decentralised systems based on renewable energy sources was also considered by T. Kurbatova *et al*. (2024), who focused on the specific economic risks of such projects. This is not consistent with the results of some previous forecasts, where the payback period for hybrid systems was estimated at five years. The reason for the discrepancies may be the underestimation of the real CAPEX indicator, which in early models was taken according to optimistic global trends without considering local logistics barriers and military risks, which is analysed in detail in the paper by T. Kurbatova *et al*.

L. Smiech *et al*. (2025) pointed out that for large residential properties, SCR naturally increases due to consistently high background loads. The analysis showed a different picture: it was found that the growth of the area is often accompanied by a disproportionate increase in evening consumption peaks, which, on the contrary, can reduce the annual SCR in passive operation mode. The reason for different interpretations may lie in the differences in the consumption structure: in the mentioned study, a significant share of the load was made up of full electric heating, while current model was based on combined systems. The conclusions made by foreign researchers about the feasibility of increasing the capacity of SPPs for private homes are appropriate from the standpoint of winter generation, however, given the Net Billing algorithms, this leads to excess exports in the summer at low prices, which significantly worsens the overall NPV indicator.

An important aspect of the discussion was the assessment of factors that influence the achievement of high levels of SCR. The sensitivity analysis showed that the scenario involving active consumption without storage is the most vulnerable to behavioural errors. A lack of discipline in using daytime devices can reduce the SCR from 42% to 32%, which automatically adds almost two years to the payback period. Instead, the scenario with BESS turned out to be the most resistant to the human factor, since the inverter automation independently maximised its own consumption. Factors affecting SCR can be classified as technical, behavioural, and climatic. Technical limitations include the inverter capacity and battery capacity, where a decreasing margin effect was set when the capacity increased by more than 10 kWh for the selected SPP capacity. Behavioural aspects, such as the ability to work remotely, make it much easier to achieve an SCR above 40%, even without accumulation systems. Climate volatility in Ukraine creates a significant seasonal unevenness, which makes an annual SCR above 75% almost unattainable without additional energy sources, since winter generation is insufficient even to meet basic needs.

Considering economic risks, it is necessary to detail the impact of the DAM price volatility coefficient, which was recorded at ±7% in the model. This allowed considering the volatility of pricing, which in the context of integration of the Ukrainian energy system with the ENTSO-E network can have both positive and negative consequences for the prosumer. Sensitivity analysis has shown that the premium for autonomy and security in today is often the dominant factor compared to net marginality. This is conditioned by the fact that for homes with an area of 120-200 m², the risks of energy loss from the grid are estimated by owners significantly higher than the potential maintenance costs of BESS (OPEX), which are 1% of CAPEX. Thus, the investment attractiveness of the project is supported by strategic hedging of energy costs, which in the long term provides total savings of more than USD 32,000. This proves that for the Ukrainian consumer, the Net Billing model becomes a mechanism not only for market interaction, but also for survival in conditions of power shortage.

A separate aspect that requires in-depth analysis in the context of implementing the Net Billing model in Ukraine is the problem of predictability of cash flows in conditions of high price volatility in the DAM. Unlike the fixed "green" tariff, where the revenue side has been stable for decades, the new model shifts market risks directly to the prosumer. The simulation with a stochastic oscillation coefficient of ±7% showed that even small price gaps between the generation time and consumption time can lead to a deviation of the actual payback period by 0.8-1.2 years. This correlates with the concerns expressed in by P. Benalcazar *et al.* (2025), however, in the Ukrainian scenario, this risk is offset by a rapid increase in retail tariffs, which makes each saved kWh more and more valuable in the structure of the family budget.

Additionally, it is worth considering the role of energy certification of buildings. Buildings with a higher energy efficiency class demonstrate better adaptability to the Net Billing model, since their thermal inertia allows for more efficient use of Load Shifting algorithms. As it was found in the course of calculations, the use of the house as a heat accumulator in combination with BESS creates a two-level system of protection against energy poverty. This confirms the thesis of L. Smiech *et al.* (2025) on the socio-economic significance of renewable energy sources, but with a significant clarification: in the Ukrainian reality of 2025, the social effect is achieved not through direct energy sales, but through reducing the vulnerability of households to system outages and power shortages in the general network.

Thus, the technical configuration of the system (10 kW PV + 10 kWh BESS) is optimal not only from the standpoint of SCR, but also due to equipment viability. Reducing the cyclic load on batteries by the intelligent priority of self-consumption allows maintaining the remaining capacity at the level of more than 80% even after 10 years of operation. This creates the basis for the future participation of such households in aggregated virtual power plants, where private drives will be able to provide network balancing services, generating additional income, which is not currently considered in conservative financial models, but is a logical step in the development of the market.

Despite the high detail, this study has certain limitations, since the model was based on weighted average prices in 2024, while future market conditions may change after the full integration of the Ukrainian energy system with the European ENTSO-E network. However, the conclusions of these researchers can be considered in a different plane, since the specifics of the Ukrainian market add new variables to the model. The synthesis of the obtained data indicates a high reliability of the model, since it includes both global trends and specific local challenges. In a broader context, Net Billing appears not only as a financial strategy for the individual owner, but also as a tool for improving national energy sustainability. This is confirmed by the fact that even in conservative scenarios of tariff growth, own generation provides a significant positive NPV. Summing up, it should be noted that the transition to Net Billing requires Ukrainian households to change the consumption paradigm. A comparative analysis with foreign and domestic studies confirmed that the success of prosumer model in 2025-2030 will depend on the availability of energy storage technologies and intelligent automation. The conclusions made by the researcher are quite appropriate, since they are based on real technical and economic challenges. The identified discrepancies with other researchers regarding payback periods are explained by the use of more detailed hourly profiles and the updating of capital expenditures for the Ukrainian market. This study lays the groundwork for further optimisation of state policy in the field of active consumer support, demonstrating that the future of decentralised energy lies in the plane of a high share of self-consumption and reasonable balancing of energy flows.

CONCLUSIONS

The subject of this study was the determination of the economic efficiency of solar power plants for private households with an area of 120-200 m² in the context of the transition of the Ukrainian energy market to the Net Billing model. The study fully achieved its objective of assessing the financial prospects of prosumerism and identifying the key factors influencing the payback period for investments under the new regulatory framework.

As part of the scientific research, a comprehensive analysis of the regulatory framework was carried out, which helped to establish the parameters of interaction between private producers and the common network. Based on hourly consumption and generation profiles, three SPP operation scenarios were modelled, which included passive behaviour, active demand management, and the use of BESSs. The results of the study showed that BESS integration provided the highest level of financial stability, despite significant initial investment. It was found that the efficiency of the project critically depends on the share of its own energy consumption, which in the best scenarios reached 68%. The data obtained suggest that the market compensation model makes solar generation an instrument of energy independence, and not just a way to generate passive income. Analysis of the dynamics of tariffs and DAM forecasts helped to establish that the discounted payback period for hybrid systems ranges from 8.6-10.4 years. The calculations also confirmed the significant impact of physical wear and tear of equipment on the final NPV indicators, which requires careful selection of technical components.

Summarising the results obtained, it can be noted that they are of great importance for understanding the processes of decentralisation of the energy system in the post-war period. The analysis means that the paradigm of private investment in the "green" energy sector of Ukraine has finally shifted from export maximisation to strategic self-sufficiency. This deepens the understanding of prosumer's economic behaviour, conceptualising them as an active market participant who can balance the load and reduce network pressure. All of the above suggests that the Net Billing model is viable and economically viable for the middle class, as it creates conditions for hedging the risks of rising retail energy prices. Conceptually, the results obtained indicate a transition to a qualitatively new stage in the development of small generation, where the technological perfection of the system is directly converted into the financial stability of the household.

Summing up the results of the study, it should be emphasised that the transition to the Net Billing model in Ukraine has become a catalyst for the qualitative transformation of the private sector of renewable energy. If the previous era of the "green" tariff stimulated quantitative capacity growth without reference to the actual consumption of the facility, the current stage requires prosumer to deeply integrate technical solutions and behavioural changes. It was proved that maximum economic efficiency is achieved only if there is synergy between generating capacities, energy storage systems, and intelligent demand management algorithms. The established payback rates in the range of 8.6-10.4 years, despite their growth compared to previous years, remain attractive for private investors, as they are accompanied by a critical factor of energy security.

SCR was defined as a key indicator of project success, which is directly converted into financial stability. The calculated SCR range (from 26% to 68%) serves as a practical guide for designers and property owners when choosing equipment configuration. An important conclusion is that the installation of hybrid systems with LiFePO4 batteries is not just a technical option, but an economic necessity to level the price difference between the purchase of energy from the grid and its sale at market prices of DAM. This suggests that the Net Billing model encourages the creation of sustainable distributed generation that is less dependent on government subsidies and more focused on the real needs of consumers.

The limitation of this study was the lack of long-term statistical information on the functioning of the Net Billing mechanism directly in the Ukrainian reality, which led to the need to use simulation methods based on current market price indicators. Promising areas for further research on this topic are the investigation of the impact of mass introduction of electric vehicles on the consumption profile of prosumers and the analysis of the possibilities of combining private SPPs into virtual power plants to provide auxiliary services to the power system.

ACKNOWLEDGEMENTS

None.

FUNDING

None.

CONFLICT OF INTEREST

None.

REFERENCES

[1] Benalcazar, P., Andrade, C., & Guamán, W. (2025). Prosumer policy options in developing countries: A comparative analysis of feed-in tariffs, net metering, and net billing for residential PV-battery systems. *Energy Policy Journal*, 28(1), 77-98. doi: 10.33223/epj/202801.

[2] Blinov, I.V., Trach, I.V., Parus, Y.V., Derevianko, D.G., & Khomenko, V.M. (2022). Voltage and reactive power regulation in distribution networks by the means of distributed renewable energy sources. *Technical Electrodynamics*, 2, 60-68. doi: 10.15407/techned2022.02.060.

[3] Buratynskyi, I., & Nechaieva, T. (2022). The least-cost optimization of PV-station's DC/AC equipment using battery energy storage system. *Latvian Journal of Physics and Technical Sciences*, 59(1), 53-62. doi: 10.2478/lpts-2022-0006.

[4] Denysiuk, S., & Derevianko, D. (2021). The cost-based DSM methods in microgrids with DG sources. In *2021 IEEE 2nd KhPI week on advanced technology (KhPIWeek)* (pp. 544-548). Kharkiv: IEEE. doi: 10.1109/KhPIWeek53812.2021.9570096.

[5] Fan, J., & Zhou, H. (2023). Optimization of a hybrid solar/wind/storage system with bio-generator for a household by emerging metaheuristic optimization algorithm. *Journal of Energy Storage*, 73, article number 108967. doi: 10.1016/j.est.2023.108967.

[6] Hassan, A.S., Cipcigan, L., & Jenkins, N. (2017). Optimal battery storage operation for PV systems with tariff incentives. *Applied Energy*, 203, 422-441. doi: 10.1016/j.apenergy.2017.06.043.

[7] Kabir, A., Sunny, M.R., & Siddique, N.I. (2021). *Assessment of grid-connected residential pv-battery systems in Sweden – a techno-economic perspective*. Kuala Lumpur: IEEE. doi: 10.1109/ICPEA51500.2021.9417835.

[8] Kurbatova, T., Sotnyk, I., Perederii, T., Prokopenko, O., Wit, B., Pysmenna, U., & Kubatko, O. (2024). On-grid hybrid wind-solar power plants in Ukraine's residential sector: Economic justification of installation under different support schemes. *Energies*, 17(20), article number 5214. doi: 10.3390/en17205214.

[9] Kyrylenko, O.V. (2022). Measures and means of transforming Ukraine's energy industry into an intelligent system. *Visnyk of the National Academy of Sciences of Ukraine*, 3, 18-31. doi: 10.15407/visn2022.03.018.

[10] Liu, X., & Gou, Z. (2025). Hybrid forecasting and optimization framework for residential photovoltaic-battery systems: Integrating data-driven prediction with multi-strategy scenario analysis. *Building Simulation*, 18, 1587-1609. doi: 10.1007/s12273-025-1319-6.

[11] Luthander, R., Widén, J., Nilsson, D., & Palm, J. (2015). Photovoltaic self-consumption in buildings: A review. *Applied Energy*, 142, 80-94. doi: 10.1016/j.apenergy.2014.12.028.

[12] Olczak, P., Matuszewska, D., Lishchenko, A., Zhydyk, I., Koval, V., & Iermakova, O. (2022). The economic efficiency of photovoltaic energy for energy prosumers. *Polityka Energetyczna – Energy Policy Journal*, 25(4), 95-114. doi: 10.33223/epj/155095.

[13] Ordóñez, A., Sánchez, E., Rozas, L., García, R., & Parra-Domínguez, J. (2022). Net-metering and net-billing in photovoltaic self-consumption: The cases of Ecuador and Spain. *Sustainable Energy Technologies and Assessments*, 53, article number 102434. doi: 10.1016/j.seta.2022.102434.

[14] Photovoltaic Geographical Information System (PVGIS). (n.d.). Retrieved from https://joint-research-centre.ec.europa.eu/photovoltaic-geographical-information-system-pvgis_en.

[15] Pysmenna, U.I., Trypolska, H.S., & Kubatko, O.V. (2023). Ukraine's energy market and small producers: Possibilities for integration. *Economy and Society*, 53. doi: 10.32782/2524-0072/2023-53-97.

[16] Scott, C., Ahsan, M., & Albarbar, A. (2023). Machine learning for forecasting a photovoltaic (PV) generation system. *Energy*, 278, article number 127807. doi: 10.1016/j.energy.2023.127807.

[17] Smiech, L., Kurbatova, T., & Kubatko, O. (2025). Assessing the impact of household energy efficiency and renewable energy developments on energy poverty reduction. *Environmental Economics*, 16(4), 83-94. doi: 10.21511/ee.16(4).2025.06.

[18] Sotnyk, I., Sasse, J.-P., & Trutnevyte, E. (2024). Decarbonizing Ukraine's electricity sector in 2035: Scenario analysis. *Energy and Climate Change*, 6(3), article number 100170. doi: 10.1016/j.egycc.2024.100170.

[19] Trela, M., & Dubel, A. (2022). Net-Metering vs. net-billing from the investors perspective-impacts of changes in RES financing in Poland. *Energies*, 15(1), article number 227. doi: 10.3390/en15010227.

[20] Yagup, V.G., & Yagup, K.V. (2024). Analytical method of determining conditions for full compensation of reactive power in the power supply system. *Electrical Engineering & Electromechanics*, 2, 75-80. doi: 10.20998/2074-272X.2024.2.11.

[21] Zgurovets, O., & Kulyk, M. (2023). Application of energy storage for automatic load and frequency control. In *Power systems research and operation. Studies in systems, decision and control* (Vol. 220; pp. 75-85). Cham: Springer. doi: 10.1007/978-3-031-17554-1_4.

Тарас Білас
Аспірант
Київський національний університет будівництва і архітектури
03037, просп. Повітряних Сил, 31, м. Київ, Україна
https://orcid.org/0009-0008-8477-3794

Володимир Ярас
Кандидат технічних наук, доцент
Київський національний університет будівництва і архітектури
03037, просп. Повітряних Сил, 31, м. Київ, Україна
https://orcid.org/0000-0003-2252-9418

Економічна ефективність моделі Net Billing для сонячних електростанцій у приватному секторі України (на прикладі будинків 120-200 м²)

Анотація. Стрімка трансформація українського енергетичного сектору та стійка тенденція до подорожчання електроенергії для побутових споживачів зумовлюють гостру необхідність пошуку шляхів енергонезалежності для власників приватного житла. Метою роботи була комплексна оцінка економічної ефективності сонячних систем під управлінням моделі Net Billing для домогосподарств середнього класу. Дослідження базувалося на імітаційному моделюванні погодинних балансів генерації та споживання з використанням методів математичного аналізу та розрахунку показників NPV. У ході наукової роботи було досліджено динаміку окупності капітальних витрат у межах трьох різних стратегій енергоспоживання, що дозволило визначити критичний вплив коефіцієнта власного споживання на фінансову життєздатність сонячного проєкту. Виявлено стійку залежність прибутковості від інтеграції літій-залізо-фосфатних акумуляторних батарей ємністю десять кіловат-годин, які забезпечують оптимальний баланс між початковими інвестиціями та можливістю повного перекриття вечірніх пікових навантажень домогосподарства. Встановлено, що за умови використання алгоритмів активного управління попитом реальний термін повернення інвестованих коштів скорочується до шести цілих та дев'яти десятих року, що відповідає критеріям високої інвестиційної привабливості. Проаналізовано такі техніко-економічні аспекти, як щорічна фізична деградація фотоелектричних панелей та операційні витрати, що дозволило довести збереження позитивної чистої приведеної вартості активу протягом усього двадцятип'ятирічного життєвого циклу. Зроблено висновок, що перехід на механізм самовиробництва за умови досягнення високого рівня SCR забезпечує власнику будинку сумарну економію та чисту фінансову вигоду в обсязі понад тридцять дві тисячі доларів. Сформовані рекомендації стануть основою для забудовників та проєктних компаній при технічному обґрунтуванні будівництва автономних систем в Україні

Ключові слова: просумерство; енергонезалежність; окупність інвестицій; децентралізована генерація; системи накопичення енергії; управління попитом; фотоелектричні системи

Machinery & Energetics
Vol. 17, No. 2. 2026

Journal homepage:
https://technicalscience.com.ua/en

UDC 537.212:667.634
DOI: 10.31548/machinery/2.2026.4

ISSN 2663-1334
e-ISSN 2663-1342

Vitalii Naumenko*
Postgraduate Student
National University of Life and Environmental Sciences of Ukraine
03041, 15 Heroiv Oborony Str., Kyiv, Ukraine
https://orcid.org/0009-0008-2393-1170

Leonid Chervinsky
Doctor of Technical Sciences, Professor
National University of Life and Environmental Sciences of Ukraine
03041, 15 Heroiv Oborony Str., Kyiv, Ukraine
https://orcid.org/0000-0001-7215-2474

Analysis of the influence of the geometry of the working zone on the distribution of the electric field in powder coating systems

Abstract. The aim of the study was to establish the features of the spatial formation of the electric field in electrostatic powder coating systems and its influence on the powder deposition indicators and coating uniformity. The methodology combined a bench-top comparative experiment, three-dimensional electrostatic modelling of the "corona electrode – charged torch – grounded product" system, non-destructive measurement of the dry film thickness, determination of the powder deposition efficiency and statistical analysis of electrostatic and technological indicators for four configurations of the working zone. It was established that the cylindrical configuration was characterised by the smallest spatial heterogeneity of the electric field: the coefficient of variation of the electric field strength was 0.178 versus 0.261 for the rectangular, 0.311 for the combined and 0.330 for the configuration with a variable interelectrode distance. For this configuration, the highest value of powder deposition efficiency was also recorded – 74.9%, the largest average coating thickness was 77.5 μm and the smallest value of the coefficient of variation of the coating thickness was 0.093. For the combined configuration and the configuration with a variable interelectrode distance, the powder deposition efficiency decreased to 63.1% and 60.7%, and the coefficient of variation of the coating thickness increased to 0.201 and 0.229, respectively, which reflected the transition of electrostatic heterogeneity into technological non-uniformity of the coating. Statistical analysis confirmed the significance of inter-configuration differences for the coefficient of variation of the electric field strength and the coefficient of variation of the coating thickness. Integral correlation analysis showed a close positive relationship between the coefficient of variation of the electric field strength and the coefficient of variation of the coating thickness ($r = 0.84$; $p = 0.001$), and local correlation analysis between the electric field strength and the coating thickness showed a statistically significant positive relationship ($r = 0.79$; $p < 0.001$). The practical significance of the results lies in the possibility of the use in the design, setup, and optimisation of working zones in electrostatic powder coating systems to improve the efficiency of powder deposition and coating uniformity

Keywords: electrostatic spraying; deposition efficiency; spatial heterogeneity; interelectrode distance; dry film thickness; coefficient of variation

INTRODUCTION

Electrostatic powder coating belongs to the technologies for forming protective and decorative coatings, in which the final result is determined not only by the process parameters, but also by the spatial conditions of powder deposition.

Article's History: Received: 08.01.2026; Revised: 06.04.2026; Accepted: 21.05.2026; Published: 29.05.2026.

Suggested Citation:
Naumenko, V., & Chervinsky, L. (2026). Analysis of the influence of the geometry of the working zone on the distribution of the electric field in powder coating systems. *Machinery & Energetics,* 17(2), 50-64. doi: 10.31548/machinery/2.2026.4.

*Corresponding author (vitaliinaumenko10@outlook.com)

The geometry of the working zone sets the configuration of the electric field, changes the trajectories of charged particles and affects the local intensity of the deposition on the surface of the part. As a result, the spatial features of the working volume can cause uneven layer thickness, the appearance of defective areas and a decrease in coating reproducibility even under the same technological conditions. Under such conditions, research attention shifts from general regime parameters to the spatial organisation of spraying and geometrically determined electrostatic factors. In the work of N. Ayrilmis (2022), electrostatic powder coating is considered as a technological system within which the result of the process is determined by the coordination of spraying parameters, substrate properties and powder deposition conditions. It is shown that the uniformity of the coating depends on the organisation of the application process no less than on the characteristics of the material, which deduces the spatial conditions of layer formation into a separate analytical plane. This approach is consistent with the work of J.M. Gimenez (2024), in which multiscale modelling of electrostatic powder spraying was used to describe the transport of particles and the formation of the deposited layer under the action of electrostatic forces. The results obtained showed that numerical modelling makes it possible to identify the influence of the configuration of the application zone and local conditions of particle motion on the nature of the distribution of the coating on the surface.

Consideration of the spatial variability of the layer thickness in automated spraying systems is presented in the work of C. Wang *et al*. (2025), where the uniformity of deposition was investigated based on a theoretical description, numerical modelling and experimental verification. The authors established that the spraying distance, movement speed and parameters of the processing zone directly affect the layer thickness and the degree of its spatial variability. In the article by Y. Tsapko *et al*. (2023), the authors examined the regularities of the formation of a polymer shell by powder paint under controlled technological process conditions. It was found that the characteristics of the formed layer changed depending on the application and heat treatment parameters. A similar relationship between the process conditions and the properties of the coating was also traced in the publication by O. Chyhyrynets *et al.* (2025), devoted to the optimisation of the system composition to increase the corrosion resistance of paint and varnish coatings. In this study, the functional properties of the layer are associated with the controlled parameters of the technological process, and not only with the characteristics of the initial components. In a similar aspect, V.I. Gots *et al*. (2023) considered powder coating as a technologically controlled system in which the final result depended on the conditions of layer formation and the consistency of the process parameters. The authors found that changing the technological parameters affected the operational properties of the coating, which indicated the dependence of its final characteristics on the formation mode. A similar approach is presented in the work of V. Korzhyk *et al*. (2025), where the structural features of multilayer epoxy composite coatings on a metal-ceramic basis were investigated. Within the framework of the analysis, a connection between the operational characteristics of the coating and the method of its formation was established, which indicated the dependence of the final result on the parameters of the technological environment.

Further development of this approach is presented in the study by V. Subbotina *et al*. (2020), where the influence of process conditions on the growth kinetics and phase-structural state of coatings on an aluminium alloy was analysed. It was found that changing the parameters of the working environment changed the mechanism of layer formation and its final characteristics. The applied value of the stability of powder coating parameters was highlighted in the work of A. Baxevani *et al*. (2025), where the influence of powder coating and preliminary anodising on the corrosion resistance of an aluminium alloy was considered. The authors showed that the quality of the formed layer determines not only the state of the surface, but also the nature of its functioning under operational conditions. A separate aspect of this issue was reflected in the work of A. Kasdi *et al*. (2023), where, based on experimental and numerical modelling of corona discharge in the "wire-cylinder-plane" system, it was established that changing the geometry of the electrode configuration changes the characteristics of the electrostatic field, spatial distribution of voltage, and charging efficiency. This provided grounds for considering the configuration of the working zone as a factor associated with the inhomogeneity of the electrostatic action and local features of particle deposition.

Thus, the available publications cover the issues of electrostatic spraying, numerical modelling of particle transport, layer formation conditions and functional properties of powder coatings. At the same time, the influence of the geometry of the working zone on the spatial distribution of the electric field with the subsequent transition to the indicators of powder deposition and uniformity of the formed coating is not fully covered. It also remains insufficiently determined to what extent a change in the shape of the working volume, the presence of local shielding elements and variations in the interelectrode distance change the inhomogeneity of the field and cause local deviations in the thickness of the coating.

In this regard, the purpose of the article was to analyse the influence of the geometry of the working zone on the distribution of the electric field in powder coating systems and to establish a relationship between the field parameters, the efficiency of powder deposition and the uniformity of the coating. To achieve this goal, the following tasks were defined: to establish the features of the electric field distribution for different geometric configurations of the working zone, to determine the impact of these changes on the efficiency of powder deposition and coating uniformity, and to compare the results of electrostatic modelling with experimental indicators of coating quality to justify the appropriate configuration of the working zone.

MATERIALS AND METHODS

The study was carried out during November 2025 – January 2026 on the basis of an experimental laboratory stand of electrostatic powder coating with thermal polymerisation. The study was conducted on the territory of a private enterprise in Kyiv, where painting work was performed. The study was conducted in the format of a bench comparative experiment, within which the physical application of powder coating was combined with three-dimensional electrostatic modelling. The geometry of the working zone within the work was defined as a set of spatial parameters of the working volume, the configuration of internal elements and the mutual location of the sprayer and the product. For comparative analysis, four basic configurations of the working zone were selected: a rectangular area measuring 600×600×900 mm, a cylindrical area with a diameter of 700 mm and a height of 900 mm, a combined configuration with local shielding elements, as well as a configuration with a variable geometry of the interelectrode space, within which the distance between the sprayer and the part varied from 180 to 260 mm. The configuration with a variable geometry was used as a model of a spatially inhomogeneous interelectrode space. This approach made it possible to compare the influence of the shape of the working volume, the presence of internal shielding elements and changes in the interelectrode interval on the nature of the electric field distribution and the conditions for the deposition of the powder material. To ensure a unified basis for the experiment, standard steel panels were used, the preparation of which was carried out in accordance with the requirements of ISO 1514:2024 (2024), which regulated the types of test panels and the procedures for the preparation before coating.

The materials of the study were thermosetting polyester powder paint Interpon 610 (AkzoNobel Powder Coatings, Netherlands), intended for protective and decorative coating of metal products for internal use, steel panels measuring 150×100×1 mm, interchangeable geometric inserts for forming different configurations of the working zone and grounded metal sample holders. The recommended polymerisation mode of 180°C for 15 min was adopted for the powder paint. The colour of the material was determined according to the RAL 7035 scale, which reduced the visual error when controlling the uniformity of the coating. The granulometric composition of the powder was controlled by laser diffraction according to ISO 8130-13:2019 (2019) on a Mastersizer 3000+ analyser (Malvern Panalytical, UK/Netherlands). The representative parameter of the particle size distribution was $d_{50} = 34.8$ μm. Only samples with the same substrate material, the same surface preparation scheme and stable electrical contact with ground were included in the sample. Surface preparation included abrasive matting, degreasing with isopropyl alcohol and drying. After completion of the preparatory operations, the average surface roughness was determined by a contact profilometer according to the Ra parameter. The obtained value was 1.3 ± 0.2 μm. Panels with deformations, traces of corrosion, residues of the previous coating, unstable fastening or deviation of geometric dimensions of more than 1% were excluded from the sample. The sample was formed as a target, non-random, consisting of 48 samples: 12 panels for each geometric configuration, with three independent repetitions and four samples in each series.

Experimental powder coating application was performed on a laboratory stand, which included a PEM-X1 electrostatic corona hand sprayer (WAGNER Group, Germany), a Sprint 2 Expert powder feed system (WAGNER Group, Germany), a coating chamber with interchangeable geometric modules, and a local ventilation exhaust unit. The sprayer provided the formation of a charged powder torch, the powder feed system provided the dosed transportation of powder paint to the sprayer, the coating chamber provided the reproduction of various configurations of the working zone, and the local ventilation exhaust unit removed excess powder phase from the spraying chamber. Polymerisation of the coatings was carried out in a BINDER FD 115 drying and polymerisation cabinet (BINDER GmbH, Germany). The main experimental indicator of the consequences of a geometrically determined change in the electrostatic field was the thickness of the dry film and its spatial distribution over the sample surface. The dry film thickness was determined using a digital thickness gauge Elcometer 456 Separate (Elcometer Limited, UK). Coating gloss and adhesion were considered as auxiliary characteristics of the formed layer, since these characteristics were used for accompanying quality control of the coating and were not the main indicators of geometrically determined redistribution of the powder material. Gloss was assessed using a Novo-Gloss 60° glossmeter (Rhopoint Instruments Ltd., UK), and adhesion was determined by the grid cut method using a 107 Cross Hatch Cutter adhesion meter (Elcometer Limited, UK). Three-dimensional modelling of the electrostatic field distribution in the working zone was performed in the Maxwell 2024 R2 software environment (ANSYS, USA).

The research procedure included four consecutive stages. At the first stage, the powder material was standardised and the stability of its particle size distribution was monitored. At the second stage, for each configuration of the working zone, powder coating was applied under the same operating parameters: the voltage on the electrode was 80 kV, the current strength was up to 80 μA, the powder flow rate was 110 g/min, the transport air pressure was 0.6 bar, the spraying distance within the basic series was 220 mm, the temperature in the laboratory was 22 ± 2°C, the relative humidity was 45 ± 5%, the polymerisation temperature was 180°C, and the holding time was 15 min after reaching the metal temperature. At the third stage, a three-dimensional model of the working zone was built in ANSYS Maxwell 2024 R2 and the electric potential distribution φ was calculated. The simulation was performed in a stationary setting for the system "corona electrode – charged torch – grounded product", in which the sprayer potential was set according to the experimental mode, and the surface of the test product was considered as a grounded conductive boundary. The boundary conditions were determined taking into account the geometry of the spraying chamber, the location of the internal elements and the interelectrode distance. The control volume for assessing the field inhomogeneity was formed within the space between the sprayer and the sample surface, i.e., in the zone that directly determined the conditions for the transfer and deposition of charged particles.

The electric field strength was determined as formula (1):

$$E = -\nabla\varphi, \tag{1}$$

where E – the electric field strength vector; φ – the electric potential; ∇ – gradient operator.

The spatial non-uniformity of the field was estimated by the coefficient of variation (formula (2)):

$$CV_e = \sigma_e/\bar{E}, \tag{2}$$

where σ_e – the standard deviation of the electric field strength in the control volume; $\bar{E}$ – the average value of the electric field strength.

The uniformity of the formed coating was determined by the ratio (formula (3)):

$$CV_h = \sigma_h/\bar{h} \tag{3}$$

where σ_h – the standard deviation of the coating thickness; $\bar{h}$ – the average layer thickness.

The powder deposition efficiency η was determined according to the provisions of ISO 8130-10:2021 (2021) as the ratio of the mass of powder material deposited on the surface of the test article to the mass of powder fed into the system during the controlled application interval (formula (4)):

$$\eta = (m_o/m_p) \times 100\%, \tag{4}$$

where m_o – the mass of powder deposited on the sample; m_p – the mass of powder fed to the sprayer during the spraying series.

In the fourth stage, the results of electrostatic modelling were compared primarily with the coating thickness and the coefficient of variation of its spatial distribution to determine whether a geometrically determined change in the electric field distribution caused differences in the conditions of powder deposition and the uniformity of the formed layer. Gloss and adhesion were additionally determined as accompanying coating characteristics, which made it possible to assess whether a change in the spatial uniformity of the layer was accompanied by differences in the external and functional characteristics of the coating. Non-destructive measurement of dry coating thickness was performed in accordance with ISO 2360:2017 (2017) and ISO 2808:2019 (2019), adhesion was determined according to ISO 2409:2020 (2020), and gloss was determined according to ISO 2813:2014 (2014). Within each sample, the coating thickness was measured at nine control points distributed between the central, edge and geometrically shaded areas. Statistical processing of the experimental data was carried out in Microsoft Excel 365 and IBM SPSS Statistics 26. The mean, standard deviation, coefficient of variation and 95% confidence interval were calculated for each series. The normality of the distribution was checked using the Shapiro-Wilk test. To compare two configurations, the Student's t-test for independent samples was used, and to compare three or more configurations, the one-way ANOVA analysis of variance at a statistical significance level of $p < 0.05$ was used. Pearson's correlation analysis was used to assess the relationship between the local electric field strength values at the model control points and the corresponding coating thickness values measured in spatially correlated areas of the sample surface. Error control was ensured by repeated measurements and preliminary calibration of the instruments before each series of experiments. Given the high-voltage nature of the electrostatic process, all operations were carried out under the conditions of mandatory grounding of the equipment, control of electrostatic hazards and compliance with the requirements of IEC TS 60079-32-1:2013 + AMD1:2017 CSV (2017). This approach ensured the reproducibility of experimental conditions and the correctness of comparison of results within the studied working zone configurations.

RESULTS

The influence of the geometry of the working zone on the spatial distribution of the electric field

A comparative analysis of the parameters of the spatial distribution of the electric field in the studied configurations of the working zone showed that the change in the geometry of the interelectrode space was accompanied by differences in the average value of the electric field strength, the degree of spatial dispersion of the field and the value of the coefficient of variation of the electric field strength (CV_e). The identified discrepancies concerned not only the integral level of the electrostatic action, but also the ratio between the areas of local field concentration and the zones of its weakening. With this approach, the coefficient of variation of the electric field strength (CV_e) characterised not the absolute level of intensity, but the measure of the spatial alignment of the field within the control volume. The generalised parameters of the electric field distribution in different configurations of the working zone are given in Table 1.

As shown in Table 1, the geometry of the working zone affected the spatial uniformity of the electric field, and the change in configuration was accompanied by a change in the coefficient of variation CV_e, the nature of local intensity maxima, and the severity of the shielded areas. The smallest value of CV_e was established for the cylindrical configuration, where it was 0.178. This corresponded to the smallest spatial variability of the field within the control volume among the studied variants. In the rectangular configuration, the spatial dispersion of the intensity was higher, and CV_e was equal to 0.261, which reflected a greater dependence of the field structure on the edge and corner segments of the working space. For the combined configuration and the configuration with a variable interelectrode distance, the values of CV_e were recorded as 0.311 and 0.330, respectively, which corresponded to a more pronounced spatial heterogeneity of the electrostatic action.

Table 1. Comparative parameters of electric field distribution for different configurations of the working zone

Work area configuration	$\bar{E}$, kV/m	σ_e, kV/m	CV_e	Local areas of the electric field strength concentration	Shielded/attenuated areas
Rectangular	21.8	5.7	0.261	Moderately pronounced near the central axis of the flare and near the edge transitions	Present in angular and peripheral segments
Cylindrical	23.1	4.1	0.178	Moderate, without sharply localised maxima	Minimally expressed, mainly on the periphery
Combined with local shielding elements	24.4	7.6	0.311	Expressed near shielding elements and in the periaxial zone	Clearly expressed by shielding elements
Variable-distance	20.6	6.8	0.330	Local maxima in areas of reduced interelectrode distance	Expressed in areas of increased interelectrode gap

Source: compiled by the authors

Quantitative differences showed that the average electric field strength did not coincide with the degree of its spatial uniformity. For the combined configuration, a higher average electric field strength was recorded with a simultaneously increased CV_e value. This indicated that the increase in the average strength was not accompanied by a corresponding spatial alignment of the field within the entire working volume. The increase in the local concentration of field lines near the internal elements was combined with the formation of adjacent areas of weakened field, as a result of which the spatial distribution of the strength became more contrasting. Thus, when comparing geometric configurations, not only the integral level of strength was important, but also the degree of its spatial alignment. The nature of the potential redistribution, areas of concentration of field lines and shielding areas is shown in Figure 1.

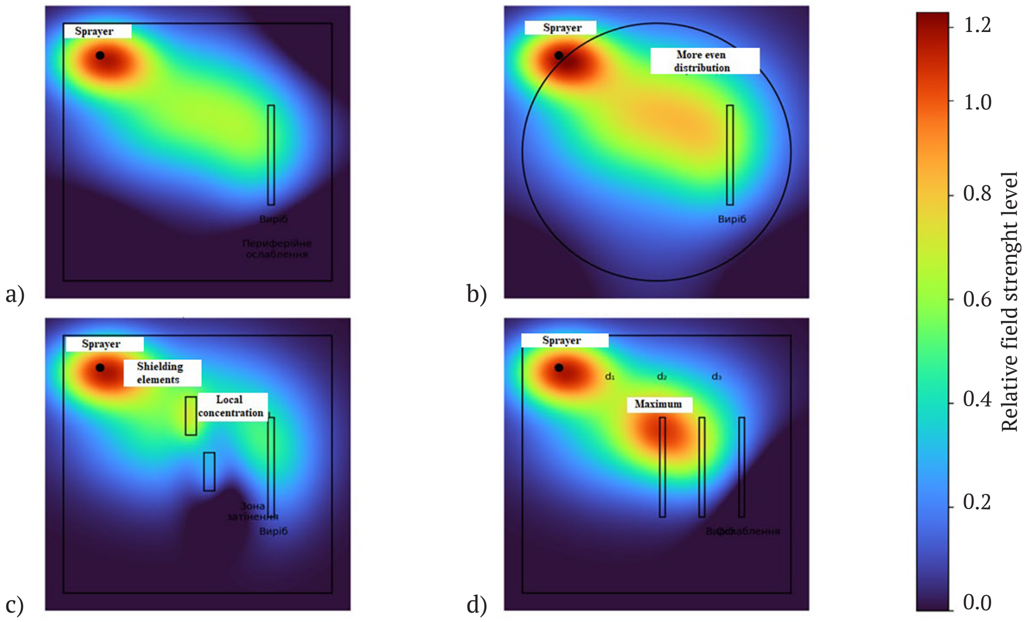

Figure 1. Spatial distribution of electric potential and electric field strength in the studied working zone configurations
Note: a – rectangular configuration; b – cylindrical configuration; c – combined configuration with local shielding elements; d – configuration with variable interelectrode distance. The colour scale reflects the relative level of electric field strength: warm tones correspond to higher values, cold tones to lower ones
Source: compiled by the authors

As shown in Figure 1, changing the geometry of the working zone changed not only the average level of electric field strength, but also its spatial structure, in particular the configuration of local maxima, shaded zones and peripheral areas of attenuation. In the rectangular configuration, the field distribution in the central part of the working volume remained relatively ordered, while in the edge segments and near the corner transitions a decrease in the density of field lines was recorded. Such a distribution reflected the axial organisation of the electrostatic action with peripheral attenuation, which increased with increasing distance from the central trajectory of the torch. This variant was characterised by a gradual change in the spatial uniformity of the field from the centre to the boundaries of the working space. In the cylindrical configuration, the redistribution of potential had a smoother character. The curvilinear boundary of the working space reduced the influence of sharp geometric transitions, as a result of which the lines of force were distributed more evenly, and the peripheral attenuation was less pronounced than in the rectangular variant. This field structure corresponded to the lowest value of CV_e given in Table 1. This configuration was not characterised by the formation of sharply localised maxima or extended shaded zones capable of changing the general structure of the field. This corresponded to the lowest spatial variability of the electrostatic action among the studied variants. The combined configuration with local shielding elements and the configuration with a variable interelectrode distance were characterised by increased spatial heterogeneity of the electric field, but the mechanisms of its formation were different. In the first case, the contrast distribution arose under the influence of internal obstacles: local densification of the lines of force was observed near the shielding elements, while in the shaded segments behind the shielding elements, the intensity decreased. This caused a combination of a high average value of $\bar{E}$ and an increased coefficient of variation CV_e, i.e., an increase in the spatial contrast of the field without a decrease in the general level of electrostatic action. In the second case, the heterogeneity was formed due to the variation of the interelectrode distance: in the zones of the atomiser approaching the surface of the product, local maxima of intensity appeared, while in the areas of the increased gap, the field weakened and dissipated. It was for this configuration that the highest CV_e value was recorded among all the studied options. A comparison of the configurations showed that a higher average level of intensity did not necessarily correspond to a greater spatial uniformity of the field, while CV_e reflected the degree of its spatial stability. The lowest CV_e value was recorded for the cylindrical configuration, while the combined and variable-distance configurations were characterised by a more contrasting distribution with a combination of zones of concentration and field weakening. Therefore, the geometry of the working zone determined not only the shape of the lines of force, but also the nature of the spatial redistribution of the electrostatic action, which formed the basis for analysing the efficiency of powder deposition and coating formation.

The influence of the working zone configuration on the efficiency of powder deposition and coating uniformity

The technological manifestation of the established electrostatic differences was traced in the indicators of the efficiency of powder deposition and the spatial distribution of the coating thickness. A comparison of η, $\bar{h}$, σ_h, CV_h and local thickness values in the control zones showed that changing the configuration of the working zone affected not only the integral level of powder material deposition, but also the nature of local layer growth in the central, edge and geometrically shaded segments of the surface. The differences were most noticeable between the configurations with a lower degree of spatial heterogeneity of the electric field and the variants in which the intensity distribution had a more contrasting nature. The distribution of the coating thickness at the control points is shown in Figure 2.

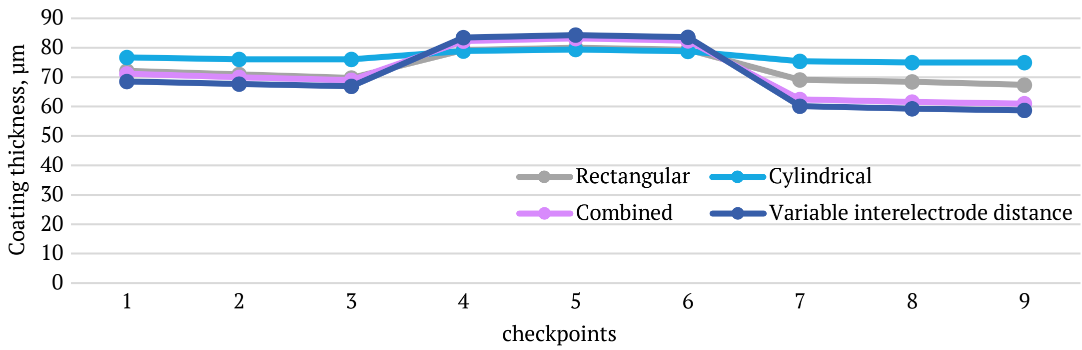

Figure 2. Distribution of coating thickness at control points for different working zone configurations

Source: compiled by the authors based on ISO 2360:2017 (2017), IEC TS 60079-32-1:2013+AMD1:2017 CSV (2017), ISO 2808:2019 (2019)

As shown in Figure 2, the nature of the spatial distribution of the coating thickness depended on the working zone configuration. The smallest zonal contrast was recorded for the cylindrical configuration: the difference between the central and geometrically shaded zones was 3.9 µm. This corresponded to the lower spatial variability of the deposition within the product surface. The rectangular configuration occupied an intermediate position: in the central part of the surface the thickness remained relatively stable, and in the direction of the edge and shaded segments it decreased gradually, without a sharp local decline. The combined configuration with local shielding elements was characterised by a pronounced zonal contrast: the coating thickness varied from 82.7 µm in the central zone to 61.8 µm in geometrically shaded areas, which reflected the influence of shielding effects on the spatial distribution of the deposited material. In the configuration with a variable interelectrode distance, the difference between the central and geometrically shaded zones reached 24.8 μm. In this variant, the central areas were characterised by increased layer growth, while the largest thickness decrease was recorded in the remote segments. Therefore, in the combined configuration and in the configuration with a variable interelectrode distance, the greatest contrast was observed between the zones of increased and decreased deposition, while the cylindrical configuration was characterised by a more uniform distribution of the coating. To summarise the technological consequences of changing the geometry of the working zone, the integral indicators of powder deposition efficiency and coating uniformity are given in Table 2.

Table 2. Powder deposition efficiency and coating uniformity indicators for different working zone configurations

Work area configuration	%	$\bar{h}$, μm	σ_h, μm	CV_h	Central zone, microns	Edge zone, μm	Geometrically shaded area, μm
Rectangular	68.4	74.8	10.9	0.146	79.6	71.2	68.7
Cylindrical	74.9	77.5	7.2	0.093	79.1	76.4	75.2
Combined with local shielding elements	63.1	73.6	14.8	0.201	82.7	70.4	61.8
Variable-distance	60.7	71.9	16.5	0.229	84.1	68.1	59.3

Source: compiled by the authors based on ISO 2360:2017 (2017), ISO 2808:2019 (2019), ISO 8130-10:2021 (2021)

In conformity with the data in Table 2, changing the configuration of the working zone affected both the efficiency of powder deposition and the spatial uniformity of the formed coating. For the cylindrical configuration, the highest value of η - 74.9% and the lowest value of CV_h -0.093 were recorded. This result corresponded to the lower degree of spatial heterogeneity of the electric field established in the previous subsection. Additional confirmation of this was the minimum difference between the central and geometrically shaded zones, which was 3.9 μm. For the configuration with a variable interelectrode distance, on the contrary, η decreased to 60.7%, and CV_h increased to 0.229, which reflected a simultaneous decrease in the efficiency of using the powder material and the spatial stability of the layer. In this case, the difference between the central and geometrically shaded zones reached 24.8 μm, that is, it was the largest among all configurations. The rectangular configuration occupied an intermediate position between these variants. For it, the deposition efficiency was 68.4%, and CV_h was 0.146, which reflected a moderate decrease in technological stability compared to the cylindrical variant. A characteristic feature of this case was not a sharp local deficiency of the coating, but a gradual decrease in thickness from the central areas to the periphery. The combined configuration with local shielding elements formed a different type of non-uniformity: with an average thickness close to the rectangular variant, the deposition efficiency decreased to 63.1%, and CV_h increased to 0.201. This reflected a local redistribution of the layer in a complicated working zone, as a result of which segments with a reduced thickness appeared next to the areas of increased deposition. The local increase in the coating thickness should not be considered separately from the spatial structure of its distribution. In the combined configuration and in the configuration with a variable interelectrode distance, individual central areas were characterised by higher local thickness values than in the cylindrical variant, however, this was accompanied by a weakening of the layer in the edge and shaded zones. As a result, the integral uniformity of the coating decreased, and the average thickness value could not be used as a single analytical reference point without taking into account its spatial structure. In this regard, the indicators η, CV_h and zonal thickness contrast were considered in relation to each other, and not in isolation and only as an indicator of the average layer thickness. The thickness distribution between the central, edge and geometrically shaded zones reproduced this pattern. The central zone in all configurations retained relatively higher thickness values, however, the degree of its superiority over other segments differed significantly. In the cylindrical variant, this difference remained limited, which corresponded to a more uniform nature of the deposition. In the rectangular configuration, the spatial contrast was moderate and was formed mainly due to peripheral attenuation. In the combined configuration and in the variant with a variable interelectrode distance, the central segments actually became zones of deposition concentration, while geometrically shaded or distant areas corresponded to zones of coverage deficiency. This reflected the transition of electrostatic heterogeneity into directly measured technological layer non-uniformity. The detected features corresponded to the nature of the spatial distribution of the electric field.

Configurations with lower CV_e values also showed less thickness variability, while local areas of field concentration, shielding or spatial attenuation were reproduced as areas of increased or decreased powder deposition. Therefore, spatial differences in the distribution of electrostatic action were technologically expressed in coating thickness values determined according to ISO 2808:2019 (2019) and ISO 2360:2017 (2017), as well as in powder deposition efficiency determined according to ISO 8130-10:2021 (2021). Auxiliary coating characteristics, in particular gloss and adhesion, determined according to ISO 2813:2014 (2014) and ISO 2409:2020 (2020), did not show comparable sensitivity to variations in the geometry of the working zone compared to the indicators of coating thickness and powder deposition efficiency. For different configurations of the working zone, gloss values remained close, and adhesion did not show noticeable differences, which indicated that the predominant effect of geometric variation was precisely on the spatial uniformity of the formed layer and the efficiency of powder material deposition.

Thus, changing the configuration of the working zone affected the efficiency of powder material use and the spatial stability of the formed coating. The highest value of η in combination with the lowest CV_h was found for the cylindrical configuration. The rectangular variant was characterised by moderate peripheral non-uniformity, while the combined configuration and the configuration with a variable interelectrode distance formed a more contrasting thickness distribution, but by different mechanisms: in the first case – through local shielding, in the second – through the contrast between the zones of convergence and divergence in the interelectrode space. This ratio of the indicators η, CV_h and the zonal thickness distribution determined the main technological manifestation of electrostatic differences caused by the geometry of the working zone.

Statistical confirmation of intergroup differences and the relationship between field parameters and coating thickness

Statistical analysis of the results for the spatial distribution of the electric field and the characteristics of the formed coating revealed interconfigurational differences that concerned both the field parameters and the powder deposition and uniformity of the formed coating. Checking the distribution of the main indicators using the Shapiro-Wilk test showed that the values of CV_e, η, $\bar{h}$ and CV_h did not have a statistically significant deviation from the normal distribution ($p > 0.05$), which provided grounds for further intergroup comparison. Within the comparison of the four configurations, the most pronounced statistical effects were recorded for the indicators of spatial heterogeneity of the field and spatial variability of the coating thickness, while the average layer thickness and deposition efficiency also changed between the groups, but with a lower degree of contrast. This reflected the primary influence of the geometry of the working zone on the nature of the spatial redistribution of the electrostatic action, and through it on the stability of the technological result. To verify the statistical significance of the established differences between the working zone configurations, the results of the intergroup comparison are presented in Table 3.

Table 3. Results of statistical comparison of indicators for different configurations of the working zone

Indicator	Shapiro-Wilk, p	ANOVA/t	p	The most pronounced differences between the configurations
CV_e	0.214	F = 18.72	< 0.001	cylindrical – combined; cylindrical – variable-distance
η, %	0.173	F = 9.46	0.002	cylindrical – variable-distance; rectangular – variable-distance
$\bar{h}$, μm	0.261	F = 6.18	0.008	cylindrical – combined; cylindrical – variable-distance
CV_h	0.148	F = 21.35	< 0.001	cylindrical – combined; cylindrical – variable-distance; rectangular – variable-distance
$CV_e \leftrightarrow CV_h$ (integral relation)	–	r = 0.84	0.001	positive relationship between field heterogeneity and thickness variability
$\bar{E} \leftrightarrow \eta$ (integral relation)	–	r = 0.58	0.041	moderate positive relationship

Source: compiled by the authors

As shown in Table 3, statistically significant intergroup differences were established for the key indicators of spatial field heterogeneity, powder deposition efficiency, and coating uniformity, which confirmed the influence of the geometry of the working zone on the course of the electrostatic spraying process. The most pronounced intergroup differences were recorded for the CV_e indicator. The value of $F = 18.72$ at $p < 0.001$ corresponded to a significant dependence of the spatial field distribution on the configuration of the working zone. The most clearly distinguished were the cylindrical configuration, for which the lowest CV_e value was previously established, and two configurations with increased spatial field contrast – combined and variable-distance. This result statistically reproduced the difference between a more aligned electrostatic state in a curvilinear geometry and increased spatial non-uniformity in the presence of internal obstacles or a non-constant interelectrode gap. Statistically significant differences were also established for the powder deposition efficiency indicator η. Although the magnitude of the between-group effect for this indicator was smaller than for CV_e and CV_h, the $p = 0.002$ value indicated that the change in the geometry of the working zone was associated not only with the field structure, but also with the transfer of powder material to the surface of the product. Differences were established between the cylindrical and variable-distance configurations, as well as between the rectangular and variable-distance, which was consistent with the differences in the organisation of the interelectrode space. Statistically significant differences were also established for the average coating thickness $\bar{h}$. At the same time, this indicator was less sensitive to the geometric factor than CV_h. This result corresponded to the integral nature of the average thickness, which reflected the total result within the entire sample surface, while the coating non-uniformity directly responded to local spatial deviations of the field. With this ratio, the geometric effect was manifested primarily not in the absolute change in the average thickness, but in the redistribution of the thickness between the central, edge and shaded zones.

One of the technological indicators, according to which statistically significant intergroup differences were established, was CV_h. The value of $F = 21.35$ at $p < 0.001$ indicated the dependence of the variability of the coating thickness on the geometry of the working zone. Statistically significant differences were established between the cylindrical and variable-distance configurations, between the cylindrical and combined, as well as between the rectangular and variable-distance configurations. This was consistent with the transition of spatial differences in electrostatic conditions into the non-uniformity of the formed layer. The smallest thickness variability corresponded to the configuration for which the lowest field heterogeneity was recorded, while geometries with local maxima and shaded zones were accompanied by a more uneven distribution of the coating. A generalised comparison of the indicators showed that a change in the configuration of the working zone was accompanied by a change in the spatial parameters of the electric field, and these differences were reflected in the powder deposition efficiency and the distribution of the coating thickness. The closest relationship was established for the pair of indicators CV_e and CV_h, between which a positive integral correlation was found ($r = 0.84$; $p = 0.001$). A positive relationship was also established for the average electric field strength level $\bar{E}$ and the deposition efficiency η, but of a lower strength ($r = 0.58$; $p = 0.041$). This indicated that the technological result was determined not only by the integral level of the field, but also by the nature of its spatial distribution.

The correlation between local values of electric field strength and coating thickness is shown in Figure 3.

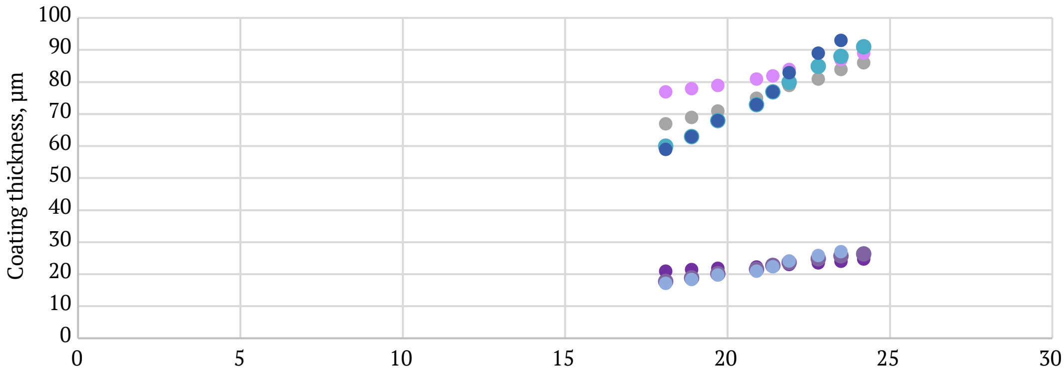

Figure 3. Correlation between local electric field strength values and coating thickness
Note: the points represent local values for different configurations of the working zone; the trend line shows the general trend of coating thickness change with increasing electric field strength strength: warm tones correspond to higher values, cold tones to lower ones
Source: compiled by the authors based on ISO 2360:2017 (2017), ISO 2808:2019 (2019)

As shown in Figure 3, a positive relationship was established between local electric field strength values and coating thickness in spatially correlated areas of the sample. The location of the experimental points for all studied configurations along the ascending trend line reflected the change in both indicators within the entire considered range. In the zone of lower local electric field strength values, smaller coating thickness values were recorded, while with increasing E, the h values also increased. The points corresponding to different configurations of the working zone formed a single trend, maintaining a certain spread relative to the trend line. Such a distribution reflected the relationship between local differences in the electrostatic state of the working zone and the thickness of the formed coating. Correlation analysis of local values of E and h confirmed a statistically significant positive relationship between these indicators: Pearson's coefficient was $r = 0.79$ at $p < 0.001$. The obtained result confirmed the presence of a relationship between the local electric field strength and the thickness of the deposited layer in spatially corresponding areas of the surface. Thus, statistical analysis showed that the differences between the studied configurations of the working zone were statistically significant for both electrostatic and technological indicators. The largest intergroup differences were established for the parameters CV_e and CV_h, which indicated a relationship between the spatial heterogeneity of the electric field and the non-uniformity of the coating. The local correlation between the electric field strength and the coating thickness showed that geometrically determined differences in the field distribution were accompanied by differences in powder deposition on the sample surface. This linked the results of electrostatic modelling with the actual spatial distribution of the formed coating.

The influence of the geometry of the working zone on the electrostatic and technological indicators of the powder coating system

The influence of the geometry of the working zone on the course of electrostatic powder coating was manifested both in the parameters of the spatial distribution of the electric field and in the technological indicators of powder deposition and coating formation. Comparison of the indicators CV_e, η, $\bar{h}$, CV_h and the thickness distribution at the control points showed that the configurations of the working zone differed not only in the intensity of the electrostatic action, but also in the nature of its spatial distribution. Electrostatic differences between the configurations were accompanied by differences in the efficiency of powder deposition, variability of the coating thickness and the presence of zones of local underspray. Within the framework of the comparison, technological indicators were associated not so much with the maximum local values of electric field strength, but with the nature of its distribution within the working volume. The generalised electrostatic and technological characteristics of the studied configurations are given in Table 4.

Table 4. Generalised comparative characteristics of working zone configurations by electrostatic and technological indicators

Work area configuration	CV_e	η, %	$\bar{h}$, μm	CV_h	Thickness distribution at control points	The expressiveness of geometrically shaded areas	Generalised characteristic
Rectangular	0.261	68.4	74.8	0.146	Moderately uneven; reduced thickness at the periphery	Moderate	Intermediate
Cylindrical	0.178	74.9	77.5	0.093	Most aligned; minimal local deviations	Minimum	Best overall balance of indicators
Combined with local shielding elements	0.311	63.1	73.6	0.201	Contrast; local reduction in thickness in shaded segments	Expressed	Increased heterogeneity
Variable-distance	0.330	60.7	71.9	0.229	Most uneven; significant difference between central and remote areas	High	Highest heterogeneity

Source: compiled by the authors based on ISO 2360:2017 (2017), ISO 2808:2019 (2019), ISO 8130-10:2021 (2021)

As shown in Table 4, the lowest CV_e and CV_h values were recorded for the cylindrical configuration, which were 0.178 and 0.093, respectively, while the powder deposition efficiency η was 74.9%. This was combined with a more uniform spatial distribution of the electric field and a smaller spread in the coating thickness. The highest CV_e and CV_h values were recorded for the variable-distance configuration, which were 0.330 and 0.229, respectively, and η was 60.7%. This configuration also recorded the largest thickness difference between the central and remote areas of the surface. For the rectangular configuration, the values $CV_e = 0.261$ and $CV_h = 0.146$ corresponded to moderate spatial heterogeneity, which was manifested mainly in the peripheral segments. For the combined configuration with local shielding elements, the values of $CV_e = 0.311$ and $CV_h = 0.201$ reflected increased heterogeneity associated with local redistribution of the field near internal obstacles. A combined comparison of the results showed that the technological indicators were associated not so much with local intensity maxima as with the nature of the spatial distribution of the field within the working volume. A decrease in CV_e was accompanied by a decrease in CV_h and higher values of η, while an increase in spatial heterogeneity of the field was combined with an increase in the variability of the coating thickness and a decrease in the efficiency of powder deposition.

Therefore, within the studied configurations of the working zone, a decrease in the spatial heterogeneity of the electric field was accompanied by an increase in the efficiency of powder deposition, a decrease in the variability of the coating thickness, and a weakening of the zonal contrast between the central, edge, and geometrically shaded areas. According to the set of indicators CV_e, η, CV_h, $\bar{h}$ and the nature of the thickness distribution for the cylindrical configuration, the lowest values of spatial field heterogeneity and coating thickness variability were recorded with the highest powder deposition efficiency at the same time. For the combined and variable-distance configurations, higher values of CV_e and CV_h were established, which was accompanied by a more uneven distribution of the coating. Thus, the spatial distribution of the electric field can be considered as an indicator related to the technological parameters of powder deposition and coating formation in electrostatic powder coating systems.

DISCUSSION

The study found that the influence of the geometry of the working zone on the technological result was realised primarily through the degree of spatial alignment of the electric field. The determining factor was not the fact of the local increase in the electric field strength itself, but the nature of its spatial distribution within the spraying zone. With less inhomogeneity of the electrostatic field, the efficiency of powder deposition increased, the variability of the coating thickness decreased, and the contrast between the central, edge, and geometrically shaded areas of the surface weakened. This result is consistent with the approach of B. Siyahhan *et al*. (2018), who linked the reliability of the numerical reproduction of the application process with the comparison of the calculated and experimental spatial distribution of the material. Within the framework of this work, this pattern is specified for powder coating systems through the interpretation of the spatial pattern of application as a consequence of the degree of electric field alignment. The revealed consistency is explained by the fact that in both cases the final state of the coating was determined not by the isolated action of a separate parameter, but by the spatially organised distribution of deposition conditions within the application zone. A similar pattern was observed when comparing the obtained results with the work of M.-R. Pendar & J.C. Páscoa (2019). In the study, it was found that the nature of the material transfer in the electrostatic field is directly related to the local distribution of the layer within the application zone. The results obtained in this work are consistent with this approach and specify it for powder coating systems, since a spatially more aligned field corresponded to higher deposition efficiency and lower variability of the coating thickness, while the contrasting electrostatic state was accompanied by local areas of insufficient powder deposition. Such consistency is explained by the common mechanism of the transition of spatial differences in electrostatic action into differences in the accumulation of powder material on the surface of the product. The study also found that the geometry of the working space changed the structure of the electric field and the nature of powder deposition even with unchanged operating parameters. A similar conclusion is given in the work of N. Guettler *et al*. (2020), where it is shown that the numerical description of electrostatic rotary atomisers significantly depended on the correct specification of the initial conditions of spraying and the parameters of the injection model. Within the framework of the work conducted, this pattern acquired a different interpretation, since it was not the input conditions of the formation of the torch that were decisive, but the configuration of the working zone in which the electrostatic interaction of the flow with the surface of the product was realised. The correspondence of the results is explained by the fact that in both cases the parameters of the spatial organisation of the process determined the final pattern of deposition, but at different levels: in one case, the conditions of the initial formation of the flow played a decisive role, in the other, the spatial conditions of its further transfer and deposition within the working zone.

Similar results are also observed when compared with the work of K. Sidawi *et al*. (2021). In it, the geometrically determined effect is associated with a change in the microgeometry of the spraying element, which restructured the atomisation conditions and the initial structure of the flow. In the study, a consequence close in physical logic was formed at a different level – due to a change in the macrogeometry of the working zone. The commonality of the conclusions is that the geometrically determined violation of the spatial symmetry of the process in both cases increased the inhomogeneity of the application. The difference is explained by the localisation of this factor: in one case, it was concentrated in the spraying unit itself, in the other – in the configuration of the working space, which determined the further conditions for the transfer and deposition of the powder material. It is advisable to consider the results on the zonal distribution of the coating thickness in a materials science context. M. Szala & E. Kot (2017), analysing the properties of polyester powder coatings after repainting, showed that the features of layer formation are important for the subsequent state of the coating as a material system. Although a direct analysis of the geometry of the working zone was not carried out in this work, such a comparison is appropriate, since in both cases the initial prerequisite for the following differences was the conditions for the formation of the coating layer. In view of this, the relationship established in the study between the geometry of the working zone, the variability of the thickness and the severity of local zones of reduced deposition can be considered as a factor that further affects the surface and operational characteristics of the coating. A comparison with works devoted to the optimisation of the application process also shows that the results obtained do not contradict the general logic of technological control, but clarify it at the level of spatial mechanisms. A.D. Karaoglan & E. Ozden (2021) linked the optimisation of electrostatic powder coating with the stabilisation of coating parameters through the rational selection of process factors. The data obtained in this work are consistent with this approach, but make it possible to specify that one of the sources of this stabilisation is the spatial alignment of the electric field. This correspondence is explained by the fact that in both cases the final technological effect was determined not by an isolated change in a separate parameter, but by the consistency of the conditions under which the coating layer was formed. The data of S. Kulothungan *et al*. (2022), who established the dependence of the material transfer efficiency on the conditions of electrostatic spraying, are interpreted in the same direction. The study shows that the increase in the spatial heterogeneity of the electric field was accompanied by a decrease in the efficiency of powder deposition. The consistency of these results is explained by a common mechanism: the spatially uneven nature of the material transfer increases powder losses and reduces the stability of its deposition on the target surface. That is why the spatial state of the electrostatic field should be considered not only as an accompanying characteristic of the process, but as one of the factors that directly determines the effectiveness of the application.

Comparison with the results of A.N. Khan *et al*. (2022) additionally showed that the target characteristics of the coating cannot be interpreted outside the spatial structure of the formation. The study found that a local increase in thickness in individual zones did not in itself provide higher uniformity of the coating as a whole. This conclusion is consistent with the approach of the aforementioned authors, who considered process optimisation through achieving the specified parameters of the coating layer. The consistency of the results is explained by the fact that local material growth does not eliminate inter-zone contrast if the spatial distribution of deposition generally remains uneven. A similar logic is also observed when comparing with works devoted to modelling the spatial structure of the torch and flow. R.I. Saye *et al.* (2023), in high-precision modelling of rotational spraying, showed the sensitivity of the process to the spatial organisation of the torch formation. Within the framework of the study, a similar result was obtained for the electrostatic field in the working zone. The consistency is explained by the fact that both the change in the spatial structure of the flow and the change in the spatial structure of the field are ultimately reflected in the local distribution of the material on the receiving surface. That is why the spatial parameters of the process should be considered as a direct prerequisite for the inhomogeneity or levelling of the coating layer.

The work of M. Scholl *et al.* (2023), in which electrostatic powder coating is considered as a technology for forming high-voltage insulation, also provides grounds for a meaningful correlation with the results obtained. Despite the different functional context, what is common is that in both cases the spatial control of the layer formation acquired a decisive importance. Such consistency is due to the fact that for coatings with specified functional properties, not only the presence of the layer itself is critical, but also the predictability of its spatial distribution over the surface.

The methodological dimension of the established results is additionally emphasised when compared with the approach of B. Christensen & M. Owkes (2023). These authors showed that a spatially detailed description of the process provides more explanation of the material distribution than integral averaged characteristics. The study revealed the same principle regarding the coating non-uniformity: it cannot be fully explained by integral indicators alone without taking into account the spatial structure of spraying and deposition. The consistency is explained by the fact that it is the spatial description that allows interpreting local differences in thickness that remain hidden when using only averaged parameters. Partial, but not complete, coincidence is observed when comparing with the results of J. Huang *et al.* (2023). In the authors' work, the improvement of the characteristics of the formed layer is associated with the use of ultrafine powder. In the study, a similar result was achieved due to another factor – the geometry of the working zone. What these approaches have in common is that a more controlled layer formation created the prerequisites for higher structural integrity of the coating. The difference is due to the nature of the control influence: in one case, the dispersion of the powder was of decisive importance, in the other, the configuration of the application space. A similar pattern is also revealed when correlated with the study by Y. Matsushita *et al.* (2024), where modelling of the painting process was used to reproduce the spatial structure of the application. Within the framework of this work, it was also established that the final distribution of the material was determined not only by the spraying mode, but also by the spatial organisation of the working zone. This consistency is explained by the fact that the spatial reproduction of the process in both cases was a necessary condition for explaining local differences in the thickness of the coating and the nature of its distribution over the surface.

The results also showed that local heterogeneity of material deposition can translate into differences in the structure and properties of the coating layer. A similar conclusion is given in the study by J. Xie *et al.* (2024), where the influence of particle size distribution on the flowability and film properties of organic powder coatings was established. Such a comparison is appropriate, since in both cases the coating properties depended on the conditions of layer formation, although the nature of the initial factor was different: in one case it was the granulometric composition, in the other – the geometry of the working zone. This confirms that the final state of the coating is determined not only by the material composition or the application mode, but also by the spatial conditions in which the powder deposition occurs. The study also showed that increasing the local electric field strength in itself did not provide the best technological result without spatial field alignment. This conclusion correlates with the results of A. Benmoussa *et al.* (2025), who showed the possibility of increasing the efficiency of electrostatic painting by modifying high-voltage conductors and using a pulsed electric field. The difference is that in the mentioned work the efficiency increased due to a change in the electrical conditions of the system, while in the results presented here, an independent role of the geometry of the working zone was traced. The mechanism itself remained common, since in both cases the control of the spatial distribution of the electrostatic action was of decisive importance, and not only the increase of individual local parameters. The results obtained also showed that the target coating thickness cannot be considered in isolation from the spatial uniformity of its distribution. This conclusion is consistent with the data of T. Šolić *et al.* (2025), who also considered the coating thickness as one of the central criteria for optimising the process parameters. In the conducted study, this indicator acquired a different analytical content, since it was evaluated not only by the average level, but also by the spatial variability and contrast between individual surface zones. The consistency is explained by the fact that in both cases the coating thickness was meaningful only in connection with the conditions of its formation, and not as an isolated self-sufficient indicator. The numerical aspect of the spatial organisation of electrostatic spraying is presented in the work of M. Herkins *et al.* (2026), devoted to the computational modelling of the electrostatic application system. Its results showed the possibility of increasing the efficiency of the process by optimising the spatial configuration and reducing losses in the flow. The obtained data are consistent with this approach, since the application efficiency was also determined by the spatial conditions of material transfer within the working zone. The coincidence of the conclusions is due to the fact that in both agro-engineering and coating applications, electrostatic spraying remains sensitive to the configuration of space, which determines the completeness of particle transfer to the target surface and the nature of the subsequent deposition.

The set of obtained results and the comparison with the data of related studies indicate that the geometry of the working zone is an independent engineering factor that determines the spatial organisation of the electric field, the conditions for the transfer of powder material and the nature of the formation of the coating layer. The established dependencies showed that the technological result in powder coating systems is determined not by the local increase of individual parameters, but by the degree of spatial alignment of the electrostatic action, on which the efficiency of powder deposition, the uniformity of the coating thickness and the severity of zones of reduced deposition depend. The revealed patterns are consistent with experimental, numerical and technological approaches, within which the spatial description of the process makes it possible to explain local differences in the application more accurately than the integral averaged characteristics. Therefore, the geometry of the working zone should be considered not as a secondary condition of the process, but as an independent factor controlling the spatial structure of the electrostatic action, through which the connection between the field parameters, the completeness of powder deposition, the uniformity of the coating and the potential quality of the formed layer is realised.

CONCLUSIONS

The study showed that the geometry of the working zone is an independent factor that determines the spatial distribution of the electric field in the electrostatic powder coating system, and through it affects the efficiency of powder deposition and the uniformity of the formed coating. A comparison of four configurations of the working zone established that a change in the shape of the working volume, the presence of local shielding elements and variations in the interelectrode distance were accompanied by a change in the spatial heterogeneity of the electric field, local zones of concentration of electric field strength and areas of its weakening. For the cylindrical configuration, the lowest value of the coefficient of variation of the electric field strength $CV_e = 0.178$ was recorded, while for the combined and variable-distance configurations this indicator was 0.311 and 0.330, respectively. For the rectangular configuration, the value $CV_e = 0.261$ corresponded to the intermediate nature of the spatial distribution of the field, with moderately pronounced peripheral weakening. This indicated that the reduction in spatial field heterogeneity was accompanied by more even electrostatic conditions within the control volume.

Technological indicators changed in accordance with the electrostatic characteristics. For the cylindrical configuration, the highest value of powder deposition efficiency $\eta = 74.9\%$, the largest average coating thickness $\bar{h} = 77.5$ μm and the smallest value of the coefficient of variation of the coating thickness $CV_h = 0.093$ were established. For the combined and variable-distance configurations, η decreased to 63.1% and 60.7%, and CV_h increased to 0.201 and 0.229, respectively. This distribution of indicators reflected the transition of electrostatic heterogeneity into technological layer non-uniformity and an increase in the contrast between the central, edge and geometrically shaded areas of the surface. Statistical analysis confirmed the significance of inter-configuration differences. The most pronounced between-group effects were established for CV_e ($F = 18.72$; $p < 0.001$) and CV_h ($F = 21.35$; $p < 0.001$). Integral correlation analysis showed a close positive relationship between CV_e and CV_h ($r = 0.84$; $p = 0.001$), and local correlation analysis between electric field strength and coating thickness confirmed a statistically significant positive relationship ($r = 0.79$; $p < 0.001$). According to the set of electrostatic and technological indicators, the most appropriate within the studied options was the cylindrical configuration of the working zone. The limitations of the study include the consideration of a limited number of geometric configurations and standard flat samples without taking into account complex-profile products and a wider range of spraying modes. Further research should be directed towards expanding the range of geometric models of the working zone, analysing spatial powder deposition on products with complex surface configurations, and combining electrostatic modelling with prediction of local coating thickness.

ACKNOWLEDGEMENTS

None.

FUNDING

None.

CONFLICT OF INTEREST

None.

REFERENCES

[1] Ayrilmis, N. (2022). A review on electrostatic powder coatings for the furniture industry. *International Journal of Adhesion and Adhesives,* 113, article number 103062. doi: 10.1016/j.ijadhadh.2021.103062.

[2] Baxevani, A., Lamprou, E., Mavropoulos, A., Stergioudi, F., Michailidis, N., & Tsoulfaidis, I. (2025). Investigation of corrosion resistance in powder-coated 6060 aluminum alloy: Effects of powder coating and pre-anodizing followed by powder coating. *Metals,* 15(10), article number 1062. doi: 10.3390/met15101062.

[3] Benmoussa, A., Pendar, M.-R., & Páscoa, J.C. (2025). Enhancing electrostatic spray-painting efficiency with modified high-voltage conductors: A numerical study on pulsed electric fields. *Journal of Aerosol Science,* 193, article number 106491. doi: 10.1016/j.jaerosci.2024.106491.

[4] Christensen, B., & Owkes, M. (2023). Efficient extraction of atomization processes from high-fidelity simulations. *Computers & Fluids,* 254, article number 105808. doi: 10.1016/j.compfluid.2023.105808.

[5] Chyhyrynets, O., Sanginova, O., Hu, J., Wu, Y., & He, X. (2025). Optimization of the composition of aluminum phosphate and walnut shell-based composition to increase the corrosion resistance of paint coatings. *Technology Audit and Production Reserves*, 4(3(84)), 12-17. doi: 10.15587/2706-5448.2025.334800.

[6] Gimenez, J.M. (2024). Multiscale simulation of electrostatic powder coating sprays. *Computational Particle Mechanics,* 11(3), 1441-1461. doi: 10.1007/s40571-023-00703-w.

[7] Gots, V.I., Kochetov, G.V., Lastivka, O.V., Samchenko, D.M., & Mehet, V.S. (2023). Corrosion resistance of powder coating with use of ferritization waste. *Modern Construction and Architecture*, 4, 49-55. doi: 10.31650/2786-6696-2023-4-49-55.

[8] Guettler, N., Knee, P., Ye, Q., & Tiedje, O. (2020). Initial droplet conditions in numerical spray painting by electrostatic rotary bell sprayers: A framework for optimization of injection model coefficients. *Journal of Coatings Technology and Research,* 17, 1091-1104. doi: 10.1007/s11998-020-00352-1.

[9] Herkins, M., Zhao, L., Zhu, H., & Jeon, H. (2026). CFD modelling of an electrostatic spraying system to optimise pesticide spray efficiency and reduce drift. *Biosystems Engineering,* 263, article number 104378. doi: 10.1016/j.biosystemseng.2025.104378.

[10] Huang, J., Yang, M., Wan, L., Tang, K., Zhang, H., Chen, J., Noël, J.J., Barker, I., Zhang, H., & Zhu, J. (2023). Ultrafine powder coating: Smooth surface, dense structure and enhanced corrosion resistance. *Chemical Engineering Journal,* 455, article number 140815. doi: 10.1016/j.cej.2022.140815.

[11] IEC TS 60079-32-1:2013+AMD1:2017 CSV. (2017). *Explosive atmospheres – part 32-1: Electrostatic hazards – guidance*. Retrieved from https://webstore.iec.ch/en/publication/60166.

[12] ISO 1514:2024. (2024). *Paints and varnishes – standard panels for testing*. Retrieved from https://www.iso.org/standard/85309.html.

[13] ISO 2360:2017. (2017). *Non-conductive coatings on non-magnetic electrically conductive base metals – measurement of coating thickness – amplitude-sensitive eddy-current method*. Retrieved from https://www.iso.org/standard/69943.html.

[14] ISO 2409:2020. (2020). *Paints and varnishes – cross-cut test*. Retrieved from https://www.iso.org/standard/76041.html.

[15] ISO 2808:2019. (2019). *Paints and varnishes – determination of film thickness*. Retrieved from https://www.iso.org/standard/71583.html.

[16] ISO 2813:2014. (2014). *Paints and varnishes – determination of gloss value at 20°, 60° and 85°*. Retrieved from https://www.iso.org/standard/56807.html.

[17] ISO 8130-10:2021. (2021). *Coating powders: Part 10: Determination of deposition efficiency*. Retrieved from https://www.iso.org/standard/80812.html.

[18] ISO 8130-13:2019. (2019). *Coating powders: Part 13: Particle size analysis by laser diffraction*. Retrieved from https://www.iso.org/standard/68405.html.

[19] Karaoglan, A.D., & Ozden, E. (2021). Electrostatic powder coating process optimisation by implementing design of experiments. *Transactions of the IMF,* 99(1), 46-52. doi: 10.1080/00202967.2020.1846349.

[20] Kasdi, A., Chouali, S., Bekakria, A., & Dascalescu, L. (2023). Experimental and numerical modeling of DC corona discharge in Wire-Cylinder-Plane configuration. *Journal of Electrostatics,* 123, article number 103814. doi: 10.1016/j.elstat.2023.103814.

[21] Khan, A.N., Goud, V., Alagirusamy, R., Mahajan, P., & Das, A. (2022). Optimization study on wet electrostatic powder coating process to manufacture UHMWPE/LDPE towpregs. *Journal of Industrial Textiles,* 51(4), 6686-6704. doi: 10.1177/15280837211070995.

[22] Korzhyk, V., Kopei, V., Stukhliak, P., Berdnikova, O., Kushnarova, O., Kolisnichenko, O., Totosko, O., Stukhliak, D., & Ropyak, L. (2025). Features of the structure of layered epoxy composite coatings formed on a metal-ceramic-coated aluminum base. *Materials,* 18(15), article number 3620. doi: 10.3390/ma18153620.

[23] Kulothungan, S., Lakshmanan, P., Krishnan, P., Palani, S., & Arumugam, A. (2022). Assessment of factors influencing the transfer efficiency in electrostatic spray coating process. *Materials Today: Proceedings,* 62(2), 1039-1044. doi: 10.1016/j.matpr.2022.04.283.

[24] Matsushita, Y., Katayama, T., Saito, Y., Matsukawa, Y., Okabe, T., Shirota, M., Inamura, T., Daikoku, M., Fukuno, J., & Aoki, H. (2024). A spray painting simulation using high-speed rotary atomizer – model development and comparison of LES and RANS. *Results in Engineering,* 21, article number 101697. doi: 10.1016/j.rineng.2023.101697.

[25] Pendar, M.-R., & Páscoa, J.C. (2019). Numerical modeling of electrostatic spray painting transfer processes in rotary bell cup for automotive painting. *International Journal of Heat and Fluid Flow,* 80, article number 108499. doi: 10.1016/j.ijheatfluidflow.2019.108499.

[26] Saye, R.I., Sethian, J.A., Petrouskie, B., Zatorsky, A., Lu, X., & Rock, R. (2023). Insights from high-fidelity modeling of industrial rotary bell atomization. *Proceedings of the National Academy of Sciences of the United States of America,* 120(4), article number e2216709120. doi: 10.1073/pnas.2216709120.

[27] Scholl, M., Vogel, N., & Lang, S. (2023). Electrostatic powder coating as a novel process for high-voltage insulation applications. *Advanced Engineering Materials,* 25(19), article number 2300465. doi: 10.1002/adem.202300465.

[28] Sidawi, K., Moroz, P., & Chandra, S. (2021). Bell-cup serrations and their effect on atomization in electrostatic rotating bell atomizers. *Experiments in Fluids,* 62, article number 180. doi: 10.1007/s00348-021-03266-9.

[29] Siyahhan, B., Boldrini, M., Hauri, S., Reinke, N., & Boiger, G. (2018). Procedure for experimental data assessment for numerical solver validation in the context of model based prediction of powder coating patterns. *The International Journal of Multiphysics,* 12(4), 373-392.

[30] Šolić, T., Marić, D., Peko, I., & Samardžić, I. (2025). Optimization of coating process parameters by analysis of target powder thickness and regression modeling. *Applied Sciences,* 15(2), article number 673. doi: 10.3390/app15020673.
[31] Subbotina, V., Sobol, O., Belozerov, V., Subbotin, A., & Smyrnova, Y. (2020). A study of the phase-structural engineering possibilities of coatings on D16 alloy during micro-arc oxidation in electrolytes of different types. *Eastern-European Journal of Enterprise Technologies,* 4(12(106)), 14-23. doi: 10.15587/1729-4061.2020.209722.
[32] Szala, M., & Kot, E. (2017). Influence of repainting on the mechanical properties, surface topography and microstructure of polyester powder coatings. *Advances in Science and Technology Research Journal,* 11(2), 159-165. doi: 10.12913/22998624/69680.
[33] Tsapko, Y., Likhnyovskyi, R., Buiskykh, N., Horbachova, O., Mazurchuk, S., Lastivka, O., Tsapko A., Sokolenko, K., & Matviichuk, A. (2023). Determining patterns in the formation of a polymer shell by powder paint on wood surface. *Eastern-European Journal of Enterprise Technologies*, 1(10(121)), 37-45. doi: 10.15587/1729-4061.2023.273364.
[34] Wang, C., Jian, X., Yang, Q., Sun, K., & Zhang, S. (2025). Theoretical and experimental study on coating uniformity in automatic spray-coating of pipeline weld repairs. *Coatings,* 15(10), article number 1193. doi: 10.3390/coatings15101193.
[35] Xie, J., Zhu, X., Shao, Y., Zhang, H., Zhang, H., & Zhu, J. (2024). An experimental and theoretical study on effects of particle size distribution on flowability and film properties of organic powder coatings. *Progress in Organic Coatings,* 195, article number 108668. doi: 10.1016/j.porgcoat.2024.108668.

Віталій Науменко
Аспірант
Національний університет біоресурсів і природокористування України
03041, вул. Героїв Оборони, 15, м. Київ, Україна
https://orcid.org/0009-0008-2393-1170

Леонід Червінський
Доктор технічних наук, професор
Національний університет біоресурсів і природокористування України
03041, вул. Героїв Оборони, 15, м. Київ, Україна
https://orcid.org/0000-0001-7215-2474

Аналіз впливу геометрії робочої зони на розподіл електричного поля в системах порошкового фарбування

Анотація. Метою дослідження було встановлення особливостей просторового формування електричного поля в системах електростатичного порошкового фарбування та його впливу на показники осадження порошку і рівномірність покриття. Методологія поєднувала стендовий порівняльний експеримент, тривимірне електростатичне моделювання системи “коронний електрод – заряджений факел – заземлений виріб”, неруйнівне вимірювання товщини сухої плівки, визначення ефективності осадження порошку та статистичний аналіз електростатичних і технологічних показників для чотирьох конфігурацій робочої зони. Установлено, що циліндрична конфігурація характеризувалася найменшою просторовою неоднорідністю електричного поля: коефіцієнт варіації напруженості електричного поля становив 0,178 проти 0,261 для прямокутної, 0,311 для комбінованої та 0,330 для конфігурації зі змінною міжелектродною відстанню. Для цієї конфігурації також було зафіксовано найвище значення ефективності осадження порошку – 74,9 %, найбільшу середню товщину покриття 77,5 мкм і найменше значення коефіцієнта варіації товщини покриття – 0,093. Для комбінованої конфігурації та конфігурації зі змінною міжелектродною відстанню ефективність осадження порошку знижувалася до 63,1 % і 60,7 %, а коефіцієнт варіації товщини покриття зростав до 0,201 і 0,229 відповідно, що відображало перехід електростатичної неоднорідності у технологічну нерівномірність покриття. Статистичний аналіз підтвердив значущість міжконфігураційних відмінностей для коефіцієнта варіації напруженості електричного поля і коефіцієнта варіації товщини покриття. Інтегральний кореляційний аналіз показав тісний позитивний зв’язок між коефіцієнтом варіації напруженості електричного поля та коефіцієнтом варіації товщини покриття ($r = 0,84$; $p = 0,001$), а локальний кореляційний аналіз між напруженістю поля та товщиною покриття - статистично значущий позитивний зв’язок ($r = 0,79$; $p < 0,001$). Практичне значення результатів полягає в можливості їх використання під час проєктування, налаштування та оптимізації робочих зон у системах електростатичного порошкового фарбування для підвищення ефективності осадження порошку та рівномірності покриття

Ключові слова: електростатичне напилення; ефективність осадження; просторова неоднорідність; міжелектродна відстань; товщина сухої плівки; коефіцієнт варіації

Machinery & Energetics
Vol. 17, No. 2. 2026

Journal homepage:
https://technicalscience.com.ua/en

UDC 681.587.3
DOI: 10.31548/machinery/2.2026.5

Oksana Hanpantsurova
PhD in Technical Sciences
Bosch Rexroth AG
97816, 1 Zum Eisengießer, Lohr am Main, Germany
https://orcid.org/0000-0002-4709-0336

Oleksandr Hubarev
Doctor of Technical Sciences, Professor
National Technical University of Ukraine "Igor Sikorsky Kyiv Polytechnic Institute"
03056, 37 Beresteyskyi Ave., Kyiv, Ukraine
https://orcid.org/0000-0002-0924-4103

Kostyantyn Bielikov
PhD in Technical Sciences, Associated Professor
National Technical University of Ukraine "Igor Sikorsky Kyiv Polytechnic Institute"
03056, 37 Beresteyskyi Ave., Kyiv, Ukraine
https://orcid.org/0000-0002-7393-1848

Alyona Murashchenko*
PhD in Technical Sciences, Associated Professor
National Technical University of Ukraine "Igor Sikorsky Kyiv Polytechnic Institute"
03056, 37 Beresteyskyi Ave., Kyiv, Ukraine
https://orcid.org/0000-0003-1059-5768

Oleh Levchenko
PhD in Technical Sciences, Associated Professor
National Technical University of Ukraine "Igor Sikorsky Kyiv Polytechnic Institute"
03056, 37 Beresteyskyi Ave., Kyiv, Ukraine
https://orcid.org/0000-0002-7620-9009

Synthesis and decomposition of a mechatronic system with hydro-pneumatic automation devices

Abstract. The relevance of this study is driven by the increasing complexity of mechatronic systems with hydropneumatic automation devices and the need to improve the efficiency of their design in the context of Industry 4.0 development. The aim of the study was to substantiate the suitability of the cyclic-modular approach for decomposing a mechatronic system into macromodules, synthesising these modules, and subsequently integrating them without compromising the system's properties. The research methodology was based on the application of systems analysis, decomposition, and logical synthesis principles for the design and investigation of mechatronic systems with hydropneumatic automation devices. Within the synthesis object, the electronic component was represented by the control algorithm of the system's actuating devices. The authors consider efficient and competitive technical solutions aimed at introducing new functions and increasing the level of automation in accordance with Industry 4.0 trends. An abstract model of a mechatronic system element, referred to as a macromodule, is proposed. The advantages of autonomous configuration and testing of macromodules were demonstrated, showing a significant reduction in development time and simplification of system design. The consequences of deep

Article's History: Received: 13.01.2026; Revised: 17.04.2026; Accepted: 21.05.2026; Published: 29.05.2026.

Suggested Citation:
Hanpantsurova, O., Hubarev, O., Bielikov, K., Murashchenko, A., & Levchenko, O. (2026). Synthesis and decomposition of a mechatronic system with hydro-pneumatic automation devices. *Machinery & Energetics,* 17(2), 65-77. doi: 10.31548/machinery/2.2026.5.

*Corresponding author (a0976478579@gmail.com)

fragmentation of a mechatronic system were analysed, and the relationship between module complexity and control architecture is established. The results of the control model analysis demonstrated that excessive decomposition leads to the emergence of a separate hierarchical level responsible for coordinating interactions among simplified elements. It was substantiated that the division of a system into macromodules cannot be arbitrary; rather, it was strictly constrained by the physical properties of the equipment and the functions of the design object. The paper proposed evaluating the quality of decomposition not by the number of elements but by the practical reduction in system development time before and after scaling. The optimal size of macromodules is unique to each specific project because it was determined by the functional and physical content of the components. Effective decomposition achieves a balance between macromodule autonomy and the complexity of coordination links, thereby enabling the rapid implementation of sophisticated automation systems

Keywords: control architecture; macro-module; hydraulic devices; functional decomposition; logical control; modular synthesis; control architecture; Industry 4.0

INTRODUCTION

Efficient and competitive technical solutions for any industry are impossible without adding new functions and increasing the degree of automation, which is in line with the trends of Industry 4.0. Authors such as E.H. Aboul *et al*. (2022) presented AI applications in industry, including Internet of Things (IoT) and Industrial Internet of Things (IIoT) technologies. H. Sikandar *et al*. (2021) found that Industry 4.0 is primarily focused on the fields of engineering and computer science. These changes lead to the scaling up of mechatronic and automation systems, as noted by M. Becker *et al*. (2025). A consequence of the increased number of controlled devices in a technical system, from 2-5 to 30-100, is system segmentation. The segments are combined into a larger system that forms a common operating space for all segments. System composition and decomposition are recognised as key approaches in the development, testing, and modernisation of automated technical systems with a significant number of managed and controlled components and multiple operating modes (Mesarovic & Takahara, 1975; Li *et al*., 2025). Similar tasks have also arisen in computing and information technology. As programmable controllers (Programmable Logic Controllers, Smart Relays and Industrial PCs) have spread to other technology fields, developers of traditional hydropneumatic and mechatronic systems have faced similar challenges (Barbanera, 2021; Webert *et al*., 2022; Belgacem *et al*., 2026). If different areas of technology are considered from the point of view of dividing a larger technical system into smaller subsystems, followed by the development of these subsystems and their subsequent integration into a unified system, many common principles and approaches can be identified.

The peculiarities of certain automatic and mechatronic technical systems can be imparted into several aspects that do not allow the direct application of informatics and computer science approaches and methods for the development of automated systems, including the variety of devices and functions both within a single system and among the available technical means used for design (Lambert & Herder, 2016; Cherkashenko, 2023), the natural asynchronicity of pneumatic and hydraulic devices, the non-deterministic timing of repetitive actions in pneumatic and hydraulic processes, the dependence of the duration of hydraulic and pneumatic processes on environmental conditions and the system state, and differences in the representation of safety-related pneumatic, hydraulic, and mechanical elements compared with components used in computer science (Vieira *et al*., 2021).

The aim of the research was to substantiate the suitability of the cyclic-modular approach for dividing a mechatronic system into parts and combining the parts into a mechatronic system without violating the system properties. To achieve this aim, the following tasks were addressed: the formation of a generalised structure of a macromodule for hydraulic and pneumatic automation and mechatronic systems; the determination of the relationships between the macromodule and the system; the determination of the connections between the system and the macromodule; and the verification of the proposed approach through a practical example involving the development of a hydraulic and pneumatic automation system.

MATERIALS AND METHODS

The number of different means, for example, control and monitoring in pneumatic automation, is measured in thousands, and in hydraulic automation and mechatronics even more. The diversity of the element base of such models as finite state machines or EF networks, or Petri nets, which are the basis of the language for compiling control algorithms, is measured in tens and differs thousands of times from the diversity of mechatronics technical means (Findeisen & Helduser, 2015; Albrecht & Taylor, 2020; Lu *et al*., 2022).

Secondly, it is the natural asynchrony of processes in pneumatic and hydraulic devices (the time of their state transformation). For these devices, the time difference between the operation periods differs from tens to hundreds of thousands of times. The third is the unregulated time of the same hydraulic, mechanical or pneumatic transformations when they are repeated (Subramanya, 2010; Khond *et al*., 2019; Zhang *et al*., 2024). That is, a single transformation of the state of a hydraulic or pneumatic device, depending on the state of the environment and system parameters, may have a repeated operating time with a difference of several dozen times (Peterson, 1981). The fourth difference relates to the prevention of physical destruction of system elements and is focused on the features of mechanical, pneumatic or hydraulic devices that differ significantly from the representation of elements in information technology (Parr, 2011; Adedigba *et al*., 2016). In the case of simultaneous issuance of two commands to transform the state of a mechanical device in opposite directions, its physical destruction or uncontrollable actions occur (Polishchuk *et al*., 2018; Kozlov *et al*., 2023). Also, peculiarities can be extended by differences in Power from a tenth of watts to tens of kW and oscillations of variables in transition processes.

The listed features are sufficient to define the basic requirements for the components attribute and its representation in tasks of decomposition and composition of hydraulic automation and mechatronic systems (Tiboni, 2023; Nazarova *et al*., 2024; López *et al*., 2026). The universal form of a system element should be suitable for the variety of technical means used in the system. This does not mean that each means is an element or component; conversely, each element has a certain technical device as its prototype (Mesarovic & Takahara, 1975; Subramanya, 2010; Cherkashenko, 2023). In a formal representation, a system element must have the properties of controllability and self-control of transformations of its state, regardless of the physical nature of the structure and complexity of the technical devices used (Fig. 1).

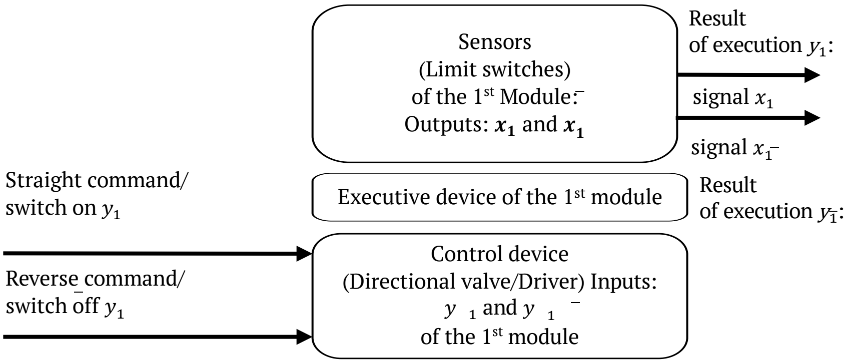

Figure 1. Example of the 1st module structure

Source: compiled by authors

In other words, an element of the system, in terms of information, includes a command to change its state and a signal that confirms the expected change:

$$X_i = \phi\,(Y_i, t_i), \tag{1}$$

where X_i – signal of changed state, $\phi\,(Y_i)$ – transition function of changing state by command, t_i – time of transition. This option takes into account the first feature and largely covers the second and third features of the class of systems under consideration. As for the fourth feature, all components have a long-term unregulated transient state, which requires the use of three-digit logic (0 – ready to operate, * – transient state or uncertainty, 1 – testing is completed): $X_i \in \{1, 0, *\}$. Thus, the form of a system element will have meaningful content (based on a physical prototype) beyond its formal description. The physical content of the system element (involved devices) will not affect the system properties of the element. Only the function of changing the state and the function of self-monitoring the state of the element are taken into account, not time of transition.

Prevention of mechanical destruction, as a result of applying opposite commands to an element, module or system, can be ensured by taking into account a cycling feature (Lishchenko *et al*., 2024; Fu *et al*., 2026). Every element has two opposite actions ("switch on + action" and "switch off + action") – execution and control of result:

$$\begin{cases} X_i = \phi(Y_i, t_i) \\ X_{\bar i} = \phi(Y_i, t_i) \end{cases}, \tag{2}$$

where $X_{\bar i}$ – signal of returning to initial state, result of reverse command $Y_{\bar i}$, $t_{\bar i}$ – time of transition. Two opposite functions (main and reverse) of one element form a sequential cycle (Fig. 2).

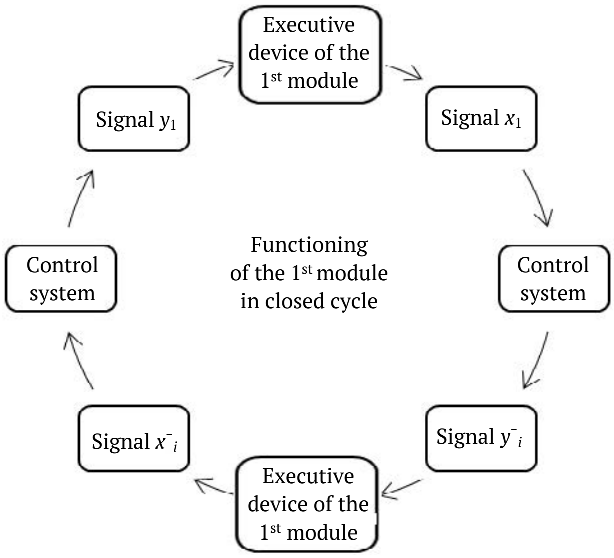

Figure 2. Example of function diagram of the 1st module

Source: compiled by authors

In this form, any separate part of the system, if it meets the listed requirements, can obtain the status of a system element with standard functions for the developer such as connection to the system using the main and reverse control commands and interaction with other elements via state control signals.

A separate system that has "switch-on" functions with control of the result obtained after switching on, and "switch-off" functions also with control of the result obtained after switching off, can be used as a system element and, therefore, is suitable for the synthesis of an automated system of a technical object (Fig. 3). The main and reverse functions performed by such a system element or macro module form their technological cycle, divided into smaller functions and modules. But for the main system, such a macro module is an ordinary element with a three-digit cyclic logic of state changes (1, 0, *) based on the issuance of "switch on" and "switch off" commands:

$$MM_{Mi} = \{Y_{Mi}, X_{Mi}, t_{Mi}, Y_{M\bar{i}}, X_{M\bar{i}}, t_{M\bar{i}},\} = \\ = \{\{Y_j, X_j, t_j\}_{YMi}, \{Y_j, X_j, t_j\}_{YM\bar{i}}\}\Big|_{j=1}^{j=k}, \tag{3}$$

where i – serial number of macro module, j – serial number of unit/module of macro module, k – quantity of units/modules of macro model.

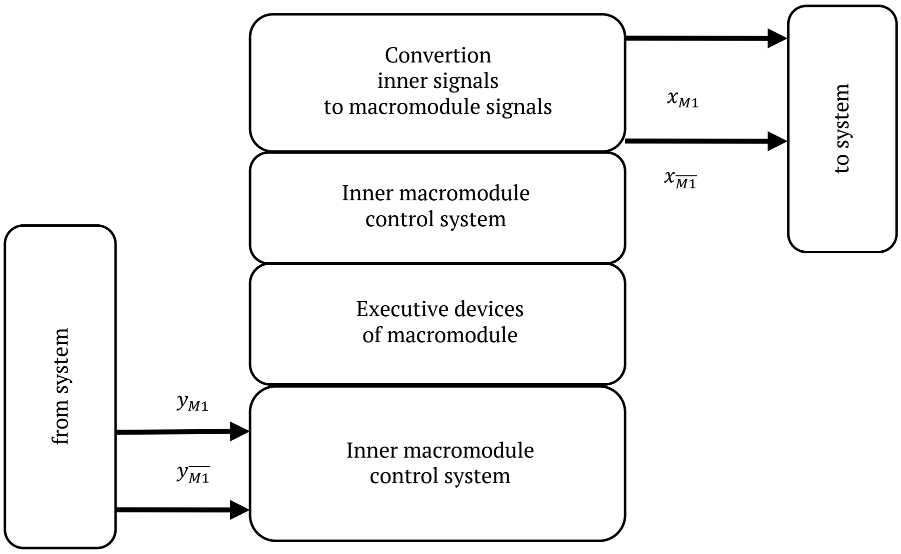

Figure 3. Structure diagram of macro module $M1$

Source: compiled by authors

The issue is rules for adding macro module in to the system and for separating part of the system as macro module. The function of the macro module for the main command Y_{Mi} includes several actions of system units $k(Mi)$. This means the macro module is a system of units/modules, which include actuators with control signals and commands. There are no differences in using of inputs $\{Y_{Mi}, Y_{M\bar{i}}\}$ and outputs $\{X_{Mi}, X_{M\bar{i}}\}$ of a macro module and unit. But they can be different, in the physical meaning, of the main and reverse action of the macro module. It means inputs are not connected with one specific unit and outputs – give information about state of the macro module. Output signal is a combination of control signals of units in the macromodule. An additional advantage of using macro modules is the removal of complex functions from the main system and their transfer to macro modules. The functions may be more complex than the main system, but their provisioning, testing, and debugging can be performed simultaneously with the development of the entire facility. This significantly speeds up the development of a new system.

Application of the method on the example of a system with pneumatic actuators Example. The technical solution is considered using pneumatic automation. Pneumatic grippers are widely used in assembly plant manipulators to perform several actions. The gripper combines several actuators with monitoring and control devices. A pneumatic workpiece holding mechanism, horizontal and vertical movement drives (Fig. 4). Before starting work, the workpiece holding mechanism is in the open position. At the command to perform the main function of the macro module: the vertical feed drive lowers the holding mechanism to the workpiece (position control), then – if the workpiece is present – the mechanism grabs the workpiece (pressure control X^{*}_{2M1}, signal from detector of workpiece $X^{'}_{2M1}$), Next, the vertical feed drive lifts the workpiece (position control). If necessary, the horizontal feed drive moves the workpiece to the shipping position. On a command to perform the reverse function of the macro module: the vertical feed drive lowers the mechanism with the held part (position control), then the mechanism releases the part (inverse pressure control $X_{\overline{2M1}}$, no signal from detector of workpiece $\overline{X}'_{2M1}$). The vertical feed drive then lifts the mechanism without the part (position control). The macro module returns to its original state.

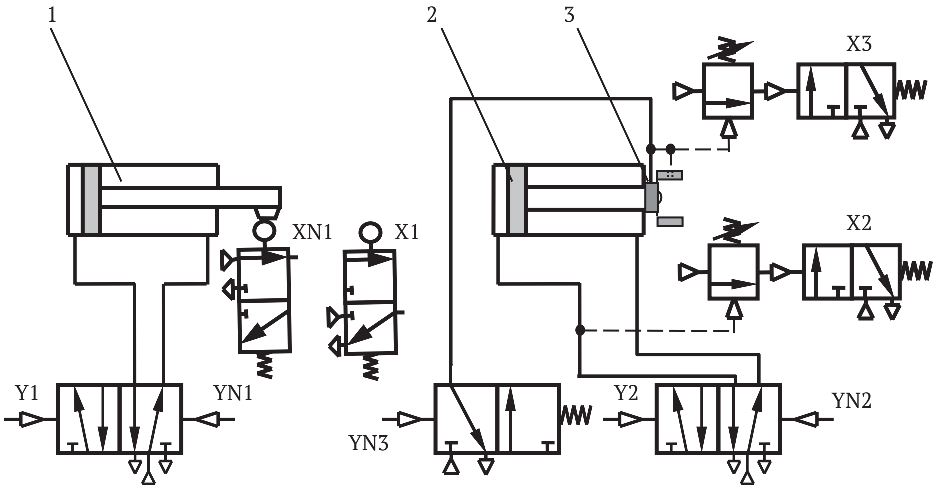

Figure 4. Macro module "Manipulator" (pneumatics)
Note: actuators: 1 – pneumatic cylinder (horizontal axis), 2 – pneumatic cylinder (vertical axis), 3 – gripper; signals: Y1, YN1– commands for horizontal displacement, X1, XN1 – end position switches for the horizontal axis, Y2, YN2 – commands for vertical displacement, X2 – end position of the vertical axis (pressure sequence valve), YN3 – gripper (command "release"), X3 – signal from gripper
Source: compiled by authors

The first step is to identify the macro module and the modules that make up the macro module, and to name the macro module, as well as the modules and signals that make up the macro module. Consider the name of the macro module. Suppose that the grab macro module has the name "M1" in the system, then the commands to turn it on and off will receive the designation: Y_{M1}, $Y_{\overline{Mi}}$. Macromodule components: 1M1 vertical feed drive (1st module of Macromodule 1), 2M1 holding mechanism module (2nd module of Macromodule 1). Command marked as Y with index, control signals marked as X with the same index. The second step is to build detailed descriptions of the main and return functions of the macro module. The execution of the main function "part capture" will have the following detailed form:

$$Y_{M1} = Y_{1M1} \rightarrow Y_{2M1} \rightarrow Y_{\overline{1M1}}. \quad (4)$$

The opposite function of "part capture" will look like this:

$$Y_{\overline{M1}} = Y_{1M1} \rightarrow Y_{\overline{2M1}} \rightarrow Y_{\overline{1M1}}. \quad (5)$$

The third step is the formation of the content of the logical conditions for controlling the performance of macro module functions. For the example under consideration, t he logical condition that states the fulfilment of the main function of the macro module "approval" is as follows:

$$X_{M1} = X_{\overline{1M1}} * X_{2M1}, \quad (6)$$

(top position, workpiece is held). The logical condition that states the execution of the reverse function of the macro module is as follows:

$$X_{\overline{M1}} = X_{\overline{1M1}} * X_{\overline{2M1}}, \quad (7)$$

(top position, no workpiece in gripper). In general, logical conditions are drawn up by means of logical synthesis, which will be discussed in the example.

The fourth step is to formalise the description of the macro module. By its actions and their ordering, the macro module is a cyclic system. The difference lies in the division of the cycle into two segments. The first segment contains the part of the cycle that corresponds to the main function. To execute it, you need an enable signal from the main command of the macro module. Similarly, the second segment contains the rest of the cycle, which is responsible for executing the return function of the macro module. To execute it, you need the enable signal of the return command of the macro module. That is, for a macro module, there is a functional graph built according to the rules of cyclic systems and the methods of the cyclic-modular approach (Peterson, 1981; Wu *et al.*, 2014; Vanegas-Ayala *et al.*, 2022) can be applied to it. The macromodule graph has two externally controlled gaps such as the "RUN" signal. They separate the segments of the main and return functions (Fig. 5). If necessary, the system of the macro module can be supplemented with memory elements, and logical expressions of control commands for individual modules that make up its structure can be compiled (Wu *et al.*, 2014; Zhao *et al.*, 2021).

Fifth step is establishing a logical connection between the macro module and the external system. According to the diagram (Fig. 3), the macro module should supply the system with signals to control the performance of its main and reverse functions, the logical expressions of which were built in the third step. X_{M1} and $X_{\overline{M1}}$ will be used in control commands for the logical synthesis of the external system to which the macro module belongs. Two commands that will be formed during the logical synthesis for the macro module Y_{M1}, $Y_{\overline{M1}}$, will be used as external signals when performing the main and return functions of the macro module. Logical commands for controlling the macro module Y_{M1}, $Y_{\overline{M1}}$, will be multipliers in the expressions of commands that start the execution of the main function segment and in the expressions of commands that start the execution of the inverse function segment.

RESULTS AND DISCUSSION

The system acquires a homogeneous structure. This is because the macromodule takes the form of a regular module. That is, a complex subsystem is represented as a memory element with turn-on and turn-off time delays. This allows for synthesising the interaction logic of all system modules using a single set of rules. Consequently, this enables the investigation of such system properties as reachability, safeness, liveness, and boundedness, which are commonly applied in Petri nets. Formally, the macro module does not exist in the system. As an example, the gripper macromodule (Fig. 5) is involved in an automated system that provides the following actions:

1. Loading the part into the system – the main action of module 1;
2. Picking up the part by the macromodule – the main action of the macromodule *M*2;
3. Transferring the gripper with the part to the working position – the main action of module 3;
4. Returning the loader to its initial state – the reverse action of module 1;
5. Release of the part by the macro module – the reverse action of the macro module *M*2;
6. Clamping the part – the main action of module 4;
7. Performing technological processing of the part – the main action of module 5;
8. Returning the technological equipment to its original state – the reverse action of module 5;
9. Releasing the part – the reverse action of module 4;
10. Picking up the processed part by the macromodule – the main action of the macromodule *M*2;
11. Returning the gripper with the workpiece to its original position – the reverse action of module 3;
12. Release of the workpiece by the macromodule – the reverse action of the M2 macromodule;
13. Removal of the part by the extractor – the main action of module 6;
14. Returning the extractor to its original position – reverse action of module 6. Then the cycle is repeated.

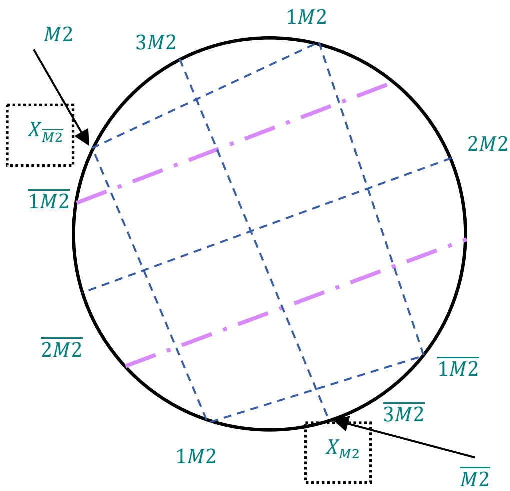

Figure 5. Functional diagram of macro module *M*2: dotted – connection lines, dash-dotted – uncertainty lines, 3*M*2 – memory element

Source: compiled by authors

The first step is to identify the macro module and its components. The grip macro module is named "*M*2" in the system, and the commands will be designated: main Y_{M2}, reverse . Components of the macro module: vertical feed drive 1*M*2 (1st module of Macromodule 2), module of the holding mechanism 2*M*2 (2nd module of Macromodule 2). Second step is detailed descriptions of the main and reverse functions of the macro module. Performing the main function of capturing a part: $Y_{M2} = Y_{1M2} \rightarrow Y_{2M2} \rightarrow Y_{\overline{1M2}}$. Performs a reverse "part release" function: $Y_{\overline{M2}} = Y_{1M2} \rightarrow Y_{\overline{2M2}} \rightarrow Y_{\overline{1M2}}$. Third step is the formation of logical conditions for controlling the execution of macro module functions. The logical condition for capturing a part: $X_{M2} = X_{\overline{1M2}} * X_{2M2}$ (top position, workpiece is held). A logical condition for releasing a workpiece: $X_{\overline{M2}} = X_{\overline{1M2}} * X_{\overline{2M2}}$ (upper position, no workpiece). The fourth step is formalisation and logical synthesis of the macro module. By the actions of the macro module components and their ordering

$$Y_{M2} = Y_{1M2} \rightarrow Y_{2M2} \rightarrow Y_{\overline{1M2}} \text{ and } Y_{\overline{M2}} = Y_{1M2} \rightarrow Y_{\overline{2M2}} \rightarrow Y_{\overline{1M2}}$$

a functional graph of the macromodule was constructed (Fig. 5). According to the results of the memory test, two uncertainty lines (dashed and dotted lines) were obtained.

To get rid of the memory deficit, a module (memory element, $3M2$ and $\overline{3M2}$). Specify external commands to the main function ($M2$) and reverse function ($\overline{M2}$) of the macro module (marked with arrows on Fig. 5). Based on the created graph, the module control commands and logical expressions of the macro module status signals were compiled. Control commands:

$$Y_{1M2} = X_{3M2} * X_{\overline{2M2}} + X_{\overline{3M2}} * X_{2M2} * Y_{\overline{M2}};$$
$$Y_{2M2} = X_{1M2} * X_{3M2}; Y_{3M2} = X_{\overline{1M2}} * X_{\overline{2M2}} * Y_{M2};$$
$$Y_{\overline{1M2}} = X_{2M2} * X_{3M2} + X_{\overline{2M2}} * X_{\overline{3M2}}; Y_{\overline{2M2}} = X_{1M2} * X_{\overline{3M2}};$$
$$Y_{\overline{3M2}} = X_{\overline{1M2}} * X_{2M2}.$$

The main command of the third module contains an external signal to turn on the macro module, and the second addition of the 1st module command contains an external command signal to turn off the macro module. The expressions of these commands (Y_{M2} and $Y_{\overline{M2}}$) should be built by logical synthesis of the main system. Composing logical expressions of the macro module state (X_{M2} and $X_{\overline{M2}}$, shown with the frames, Fig. 5) corresponds to the conditions of termination of the main function and the inverse function of the macro module. On the graph, the vertex of the end of the last action of the main function has the logical expression $X_{M2} = X_{\overline{3M2}} * X_{\overline{1M2}} * X_{2M2}$. As soon as the reverse function starts, the signal will disappear (state $X_{\overline{1M2}}$) and the macro module will lose its state X_{M2}. Similarly, for the vertex of the end of the last action of the inverse function: $Y_{M2} = X_1 + X_{\overline{4}} * X_{\overline{7}} * X_3$. Compared to the meaningful conditions of the macro module state, multipliers have been added to take into account the addition of a memory element.

Fifth step is ensuring the interaction between the macro module and the external system. The logical connection between the macromodule and the external system is provided by the expressions of the commands to turn the macromodule on and off (Y_{M2} and $Y_{\overline{M2}}$). These expressions are built through the state signals of the external system. The logical connection between the external system and the macro module is provided by the expressions of the macro module status signals (X_{M2} and $X_{\overline{M2}}$), built through the state signals of the macro module components. Based on the results of the logical synthesis of the external system, the logical expressions of all commands, including those of the macro module (Fig. 6), are obtained.

$$Y_1 = X_{\overline{6}} * X_7 * X_{\overline{3}} * X_{\overline{M2}}; Y_{\overline{1}} = X_{M2};$$
$$Y_{M2} = X_1 + X_{\overline{4}} * X_{\overline{7}} * X_3; Y_{\overline{M2}} = X_3 * X_{\overline{1}} * X_7 + X_{\overline{3}} * X_{\overline{7}};$$
$$Y_3 = X_{M2} * X_7; Y_{\overline{3}} = X_{M2} * X_{\overline{7}}; Y_4 = X_{\overline{M2}} * X_7 * X_3;$$
$$Y_{\overline{4}} = X_{\overline{5}} * X_{\overline{7}}; Y_5 = X_4 * X_7; Y_{\overline{5}} = X_{\overline{7}};$$
$$Y_6 = X_{\overline{M2}} * X_{\overline{7}} * X_{\overline{3}}; Y_{\overline{6}} = X_7; Y_7 = X_6; Y_{\overline{7}} = X_5 \quad .$$

Macro module state signals X_{M2} and $X_{\overline{M2}}$ should be replaced with their expressions obtained in step 3 or during the logical synthesis of the macro module: $X_{M2} = X_{\overline{3M2}} * X_{\overline{1M2}} * X_{2M2}$ and $Y_{M2} = X_1 + X_{\overline{4}} * X_{\overline{7}} * X_3$;.

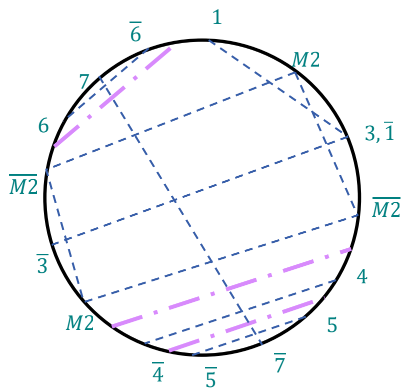

Figure 6. Functional diagram of system with the 2nd Macro Module: dashed – connection lines; dotdash – uncertainty; 7 and $\overline{7}$ – memory

Source: compiled by authors

The command expressions of the external system after replacement are as follows:

$$Y_1 = X_{\overline{6}} * X_7 * X_{\overline{3}} * X_{\overline{1M2}} * X_{\overline{2M2}} * X_{\overline{3M2}},$$
$$Y_{\overline{1}} = X_{\overline{3M2}} * X_{\overline{1M2}} * X_{2M2},$$
$$Y_3 = X_{\overline{3M2}} * X_{\overline{1M2}} * X_{2M2} * X_7,$$
$$Y_{\overline{3}} = X_{\overline{3M2}} * X_{\overline{1M2}} * X_{2M2} * X_{\overline{7}},$$
$$Y_4 = X_{\overline{1M2}} * X_{\overline{2M2}} * X_{\overline{3M2}} * X_7 * X_3,$$
$$Y_6 = X_{\overline{1M2}} * X_{\overline{2M2}} * X_{\overline{3M2}} * X_{\overline{7}} * X_{\overline{3}}.$$

This ensures that the external system is connected to the state of the macro module components.

The logical connection of the macro module with the external system is made through the macro module control commands from the external system. The signals of these commands are present as multipliers in the expressions of the control commands of the macro module components. Instead Y_{M2} and $Y_{\overline{M2}}$ in the expressions of the commands of the macro module components must be:

$$Y_{M2} = X_1 + X_{\overline{4}} * X_{\overline{7}} * X_3 ;$$
$$Y_{\overline{M2}} = X_3 * X_{\overline{1}} * X_7 + X_{\overline{3}} * X_{\overline{7}}.$$

This replacement ensures that the macro module switches from its own event counting to the event counting of the external system. The command expressions for the components of the macro module are determined as follows:

$$Y_{1M2} = X_{3M2} * X_{\overline{2M2}} +$$
$$+X_{\overline{3M2}} * X_{2M2} * (X_3 * X_{\overline{1}} * X_7 + X_{\overline{3}} * X_{\overline{7}});$$
$$Y_{2M2} = X_{1M2} * X_{3M2};$$
$$Y_{3M2} = X_{\overline{1M2}} * X_{\overline{2M2}} * (X_1 + X_{\overline{4}} * X_{\overline{7}} * X_3);$$
$$Y_{\overline{1M2}} = X_{2M2} * X_{3M2} + X_{\overline{2M2}} * X_{\overline{3M2}};$$
$$Y_{\overline{2M2}} = X_{1M2} * X_{\overline{3M2}};\ Y_{\overline{3M2}} = X_{\overline{1M2}} * X_{2M2}.$$

The construction of the “gripper” macromodule for the system and the system with the macromodule is complete. The resulting expressions allow us to develop a control system: to design electrical relay circuits, to design pneumatic automation circuits, to design a control algorithm (Zhao *et al.*, 2021; Vanegas-Ayala *et al.*, 2022).

The use of a macromodule as a tool by a developer when creating systems provides another opportunity – to use the principle of reversibility of the system and its parts. According to formal features, an external system that includes a macro module that operates once per cycle meets all the requirements for building a separate “macro module”. Main and reverse functions Y_{M1} and $Y_{\overline{M1}}$ of the macro module that has already been built and is named “$M1$”, divides the system’s action cycle into two segments (Busi, 2002; Gomes & Barros, 2005; Reisig, 2013). In comparison, a common feature is the logical structure of the control systems. In other models, the system architecture is fixed. In the proposed model, within its foundational premises, the system architecture is open. That is, cyclic modules have specific logical interaction conditions among themselves. The operational process is a consequence of fulfilling (executing) these conditions.

The first segment between switching on the macromodule $M1$ and switching off the macromodule $M1$. The second segment from the switching off of macromodule $M1$ to the next switching on of macromodule $M1$ (Fig. 7). Since the system’s development of the first process segment leads to the state of the beginning of the second segment, and the development of the second segment leads to the state of the beginning of the first segment, it can be said that the segments are mutually reversible. That is, by analogy with the cyclic modules of the system, these segments can be designated as follows: the main action of the external system Y_{Syst}, reverse action of the external system $Y_{\overline{Syst}}$. According to the graph (Fig. 7), to start the main action Y_{Syst} the reverse function of the macro module must be completed $Y_{\overline{M1}}$. To start performing the reverse action $Y_{\overline{Syst}}$ the main function of the macro module must be completed Y_{M1}. That is, logical commands are enough for the macro module and the external system to interact:

$$Y_{M1} = X_{\overline{Syst}};\ Y_{\overline{M1}} = X_{Syst};$$
$$Y_{Syst} = X_{M1};\ Y_{\overline{Syst}} = X_{\overline{M1}}.$$

At the same time, the system state signals X_{Syst} and $X_{\overline{Syst}}$ will have a structure similar to the status signals of the of the macro module, i.e., they are logical expressions for a single vertex of the expanded graph of the system. will have a structure similar to the status signals of the of the macro module, i.e., they are logical expressions for a single vertex of the expanded graph of the system.

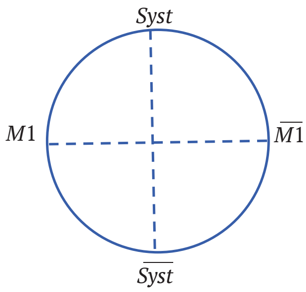

Figure 7. Functional graph with the inverse image of the system and macromodule $M1$

Note: dotted lines are communication lines, *Syst* – main action of the system, $\overline{Syst}$ – reverse action of the system

Source: compiled by authors

The number of actuating and controlling devices and monitoring devices is the same for the homogeneous system and the system with macromodules. This number is due to the same set of functions and control devices for both system variants. Quantitative indicators for the homogeneous system (Fig 9) and the system after decomposition have approximately the same values (Table 1).

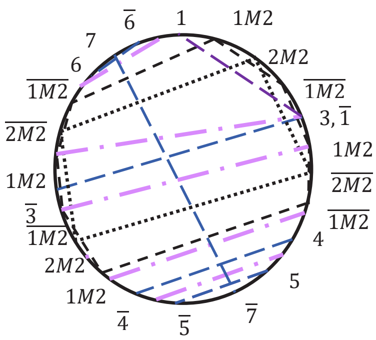

$$\quad_{1M2} \qquad _{3M2} \qquad _{\overline{2M2}} \qquad _{\overline{3M2}} \qquad _{2M2}$$
$$* (X_3 * X_{\overline{1}} * X_7 + X_{\overline{3}} * X_{\overline{7}});$$
$$Y^*{}_{1M2} = X_1 * X_{2M2} + X_3 * X_{\overline{1}} * X_{2M2} * X_7 +$$
$$+X_{\overline{4}} * X_{\overline{7}} * X_{\overline{2M2}} * X_3 + X_{\overline{3}} * X_{\overline{7}} * X_{2M2}$$
$$Y_{2M2} = X_{1M2} * X_{3M2};$$
$$Y^*{}_{2M2} = X_{1M2} * X_1 + X_{1M2} * X_{\overline{7}} * X_3$$
$$Y_1 = X_{\overline{6}} * X_7 * X_{\overline{3}} * X_{\overline{1M2}} * X_{\overline{2M2}} * X_{\overline{3M2}},$$
$$Y^*{}_1 = X_{\overline{6}} * X_7 * X_{\overline{2M2}} * X_{\overline{3}}$$
$$Y_{\overline{1}} = X_{\overline{3M2}} * X_{\overline{1M2}} * X_{2M2},$$
$$Y^*{}_{\overline{1}} =* X_{\overline{1M2}} * X_{2M2} * X_7.$$

Figure 9. Functional graph of the homogeneous system of the first example, comparison of logical expressions of commands

Note: * commands are marked in the case of a homogeneous system, without marking – command expressions for a system with a macromodule $M2$

Source: compiled by authors

Table 1. Comparative indicators of the example

Indicator	Homogeneous	2 macro modules
Quantity of transitions	23	15 + 9 = 24
Logical uncertainty	6	3 + 2 = 5
Elements of memory	1	1 + 1 = 2
Quantity of modules	8	7 + 3 = 10
Quantity of logical connections (modules 1*M*1, 2*M*2 and 1)	10 + 4 + 5 = 19	8 + 1 + 7 = 16
Relative dimensionality	23 * 8 = 184	15 * 7 + 9 * 3 = 132

Source: compiled by authors

The main difference in the approach is related to the relative dimensionality of the system $\tilde{N}$, which is calculated as the product of the number of transitions in the process z and number of modules in the system m: $N = z * m$. In terms of content, this is the maximum number of logical conditions that determine a certain action of a certain module in a certain state of the system, applied for each action.

These conditions are the formal basis for the content of the system's algorithm. For the above example of a homogeneous system, this figure is 184. For a distributed system, the developer must synthesise the main system and the macro module subsystem. For the main system, the relative dimensionality is 105, and for the macromodule 27. For the developer, this means that the required number of synthesised and minimised logical conditions that he must check is reduced by 1.4 times.

$$\tilde{t}_{sin\,t}\frac{t_{cont}^{sin\,t}}{t_{mod\,ul}^{sin\,t}} = \tilde{t}_{test}\frac{t_{cont}^{test}}{t_{mod\,ul}^{test}} = 1.4.$$

This will result in a proportional reduction in development time, a reduction in testing time, a proportional reduction in the number of technical errors in the development, testing, and design of the control algorithm, and the time required to correct them. The total reduction in development time using the macromodular approach will be:

$$\tilde{t} = {}^{t_{cont}}/_{t_{mod\,ul}} = \tilde{t}_{sin\,t}\frac{t_{cont}^{sin\,t}}{t_{mod\,ul}^{sin\,t}} + \tilde{t}_{test}\frac{t_{cont}^{test}}{t_{mod\,ul}^{test}} + \tilde{t}_{mistake}\frac{t_{cont}^{mistake}}{t_{mod\,ul}^{mistake}},$$

where $\tilde{t}_{sin}\ t$, $\tilde{t}_{test}$, $\tilde{t}_{mistake}$ – percentage of development time spent on synthesis $\tilde{t}_{sin\,t}$ (5 – 15%), testing $\tilde{t}_{test}$ (60-90%) and fixing errors $\tilde{t}_{mistake} = 100\% - (\tilde{t}_{sin}\,t + \tilde{t}_{test})$ (up to 30%). The time to correct errors is further reduced by reducing the dimensionality of the objects (system or macro module) in which the correction is performed. For the example under consideration, the parameter falls within the range from 1.4 to 2.1. The second value corresponds to the absence of errors (qualified developer), and the first value corresponds to the presence of typical technical errors in the construction of the circuit and the design of the control algorithm.

The effectiveness of the approach depends on the relative dimensionality of both the system and the macromodules: the number of modules in the system m, number of transitions in the process z, quantity of macro modules K_{mod}, uniformity of distribution of functional modules across macromodules. Clarification: the total number of transitions when adding each macro module can increase by 1, due to the addition of memory elements that compensate for the absence of a macro module in the system: $z_{mod\,u\,l} = z_{sist} + K_{mod}$. For a system consisting of three macromodules, each of which has the conditional dimension of the entire system of the previous example, the following indicators are obtained (Table 2).

Table 2. Comparative indicators of the 2nd example

Quantity of transitions	Homogeneous	3 macro modules
Logical uncertainty	69	23 + 23 + 23 + 3 = 72
Elements of memory	18	$nD_1 + nD_2 + nD_3 \leqslant 18$
Quantity of modules	nM	nM + 3
Quantity of logical connections	24	24 + 3 = 27
Relative dimensionality	69 * 24 = 1656	3 * (24 * 8) = 576

Source: compiled by authors

For the developer, this means that the number of synthesised and minimised logical conditions is reduced by 2.8 times. Accordingly, the reduction in the development time, depending on the ratio of the stages' terms, will range from 2.15 (in the absence of errors) to 7.5. The division of the same system into 2 macromodules of larger dimension (12 functional modules each) leads to the following indicators (Table 3).

Table 3. Comparative indicators of the 3rd example

Quantity of transitions	Homogeneous	3 macro modules
Quantity of transitions	69	35 + 35 + 2 = 72
Logical uncertainty	18	$nD_1 + nD_2 \leqslant 18$

Continued Table 3.

Quantity of transitions	Homogeneous	3 macro modules
Elements of memory	nM	nM + 2
Quantity of modules	24	24 + 2 = 26
Quantity of logical connections (modules 1*M*1, 2*M*2 and 1)	69*24=1656	2*(35*12)=840

Source: compiled by authors

Separating one macromodule in the system (decomposition into 2 components: 2 to 5) reduced the relative dimensionality by 1.4 times. Dividing the system into 2 macromodules of the same dimension reduced the relative dimension by 2 times. Dividing the system into 3 macromodules of the same dimensionality reduced the relative dimensionality by 2.8 times. Further fragmentation of the system will lead to simplification of macromodules and complication of connections between them. In fact, a second layer of the control system is created – a coordinator of macromodules. In the ultimate variant, an initial system will be obtained that will serve as a coordinator of the initial functional modules identified with macromodules. These data provide a quantitative characterisation of the simplification of an abstract system when it is decomposed into macromodules. Since mechatronic systems are subject to the properties of equipment and technological process, an arbitrary division of the system into a given number of macromodules and the desired dimension of macromodules is not realistic. The separation of macromodules, as a rule, has a substantive basis, which determines the number of macromodules and their dimensions, as was the case in the example with the manipulator, and the qualifications of the developer. In other words, the decomposition efficiency indicator will be the reduction of development time and the ability to automate larger-scale processes. This indicator will be formed for each practical system based on its output data and the equipment involved.

CONCLUSIONS

The cyclic-modular methodology for decomposing systems into macromodules provides a structured and efficient framework for the development of hydropneumatic automation and mechatronic systems. By introducing macromodules, the influence of scale factors on development time is reduced, and conditional dimensionality is minimised through the elimination of unnecessary logical connections between system components. This simplification accelerates design processes and enhances the transparency and manageability of complex architectures.

A prerequisite for effective application is the ability to isolate distinct subsystems. Such isolation is feasible when sequences of actions involve equipment not shared with other functions, or when complex functions exist independently of the subsequent technological cycle. Under these conditions, macromodules can be treated as autonomous units, facilitating both circuit design and algorithmic control. Quantitative analysis confirms the efficiency of this approach: the use of N macromodules in a system of n modules can reduce development time by approximately N times, provided that the system contains more than 3N modules and each macromodule incorporates at least three modules. This ensures meaningful decomposition and maximises the benefits of modularisation.

Future development should focus on the integration of simulation tools to validate system behaviour, reliability, and fault tolerance prior to physical implementation. Embedding macromodule decomposition into simulation environments will allow predictive testing and optimisation of performance. Additionally, the methodology can be aligned with Industry 4.0 principles, enabling flexible, reconfigurable production systems that leverage modular control units within smart manufacturing frameworks. In conclusion, the cyclic-modular methodology for macromodule decomposition offers significant advantages in reducing complexity, shortening development cycles, and promoting scalability. Its extension through simulation-based validation and integration with Industry 4.0 paradigms positions it as a universal design strategy capable of transforming system development into a more efficient, modular, and future-ready process.

ACKNOWLEDGEMENTS

None.

FUNDING

None.

CONFLICT OF INTEREST

None.

REFERENCES

[1] Aboul, E.H., Jyotir, M.C., & Vishal, J. (2022). *Artificial intelligence and industry 4.0.* Amsterdam: Elsevier Science.

[2] Adedigba, S.A., Khan, F., & Yang, M. (2016). Dynamic safety analysis of process systems using nonlinear and non-sequential accident model. *Chemical Engineering Research and Design*, 111, 169-183. doi: 10.1016/j.cherd.2016.04.013.

[3] Albrecht, O., & Taylor, C.J. (2020). Unknown and time-varying time delays in the modelling and control of hydraulic actuators. In *2020 Australian and New Zealand control conference (ANZCC)* (pp. 232-237). Gold Coast: Institute of Electrical and Electronics Engineers (IEEE). doi: 10.1109/ANZCC50923.2020.9318375.

[4] Barbanera, F., Dezani-Ciancaglini, M., Lanese, I., & Tuosto, E. (2021). Composition and decomposition of multiparty sessions. *Journal of Logical and Algebraic Methods in Programming*, 119, article number 100620. doi: 10.1016/j.jlamp.2020.100620.

[5] Becker, M., Karaoglu, S., Makansi, F., Radtke, J., & Schmitz, K. (2025). Industry 4.0: Review of the state of the art in fluid power research and industry. *International Journal of Fluid Power*, 26(4), 573-624. doi: 10.13052/ijfp1439-9776.2643.

[6] Belgacem, H., Abuabiah, M., Boulescu, A., & Chihi, I. (2026). A three-level hierarchical fault diagnosis framework for APS mechatronic systems with adaptive Bayesian root-cause analysis. *Results in Engineering*, 30, article number 111163. doi: 10.1016/j.rineng.2026.111163.

[7] Busi, N. (2002). Analysis issues in Petri nets with inhibitor arcs. *Theoretical Computer Science*, 275(1-2), 127-177. doi: 10.1016/S0304-3975(01)00127-X.

[8] Cherkashenko, M. (2023). Synthesis of discrete drives control systems. *Bulletin of the National Technical University "KhPI". Series: "Hydraulic machines and hydraulic units"*, 1, 12-17. doi: 10.20998/2411-3441.2023.1.02.

[9] Findeisen, D., & Helduser, S. (2015). *Oil hydraulics. Handbook of hydraulic drives and controls*. Berlin: Springer Vieweg. doi: 10.1007/978-3-642-54909-0.

[10] Fu, Z., Zhang, H., Zhu, S., Jiang, Z., & Zhang, L. (2026). A diagnosis and classification method for energy efficiency anomalies in mechatronic equipment based on multi-condition inherent energy efficiency benchmark. *Energy*, 342, article number 139671. doi: 10.1016/j.energy.2025.139671.

[11] Gomes, L., & Barros, J.P. (2005). Structuring and composability issues in Petri net modeling. *IEEE Transactions on Industrial Informatics*, 1(2), 112-123.

[12] Khond, V.V., Kavale, P.K., & Dixit, N.S. (2019). An approach to mechatronics system design. *International Journal of Engineering Development and Research*, 7(2), 360-366.

[13] Kozlov, L., Poliakov, A., Yakobinchuk, O., Gubarev, O., & Makarova, T. (2023). Mechatronic hydraulic system with adaptive regulator for a manipulator of the mobile working machine. In V. Ivanov, I. Pavlenko, O. Liaposhchenko, J. Machado & M. Edl (Eds.) *Advances in design, simulation and manufacturing VI. DSMIE 2023. Lecture notes in mechanical engineering* (pp. 64-73). High Tatras: Sumy State University. doi: 10.1007/978-3-031-32774-2_7.

[14] Lambert, P., & Herder, J.L. (2016). Parallel robots with configurable platforms: Fundamental aspects of a new class of robotic architectures. *Proceedings of the Institution of Mechanical Engineers, Part C: Journal of Mechanical Engineering Science*, 230(3), 463-472. doi: 10.1177/09544062156025.

[15] Li, J., Lu, Y., He, Y., Zhou, G., & Miao, L. (2022). Analysis and compensation control of engine valve response delay based on the electro-hydraulic variable valve actuator. *Machines*, 10(8), article number 701. doi: 10.3390/machines10080701.

[16] Li, J., Sun, Y., Wang, Y., & Su, Q. (2025). Identifying critical nodes in cyber-physical power systems based on an improved mixed degree decomposition method. *Advanced Engineering Informatics*, 68(Part B), article number 103630. doi: 10.1016/j.aei.2025.103630.

[17] Lishchenko, N., & Gushchin, A., & Larshin, V. (2024). Hierarchical control in mechatronic technological systems. *Machines*, 12(10), article number 697. doi: 10.3390/machines12100697.

[18] López, E.J., Ruiz, J.E.P., Chávez, O.L., Muñoz, F., Velásquez, L.A.G., & Lugo, J.G.C. (2026). The evolution of mechatronics engineering and its relationship with industry 3.0, 4.0, and 5.0. *Technologies*, 14(2), article number 81. doi: 10.3390/technologies14020081.

[19] Mesarovic, M.D., & Takahara, Y. (1975). *General systems theory: Mathematical foundations*. London: Academic Press.

[20] Nazarova, O., Osadchyy, V., Hutsol, T., Glowacki, S., Nurek, T., Hulevskyi, V., & Horetska I. (2024). Mechatronic automatic control system of electropneumatic manipulator. *Scientific Reports*, 14, article number 6970. doi: 10.1038/s41598-024-56672-4.

[21] Parr, A. (2011). *Hydraulics and pneumatics: A technician's and enginee's guide*. Oxford: Butterworth-Heinemann.

[22] Peterson, J.L. (1981). *Petri net theory and the modeling of systems*. Englewood Cliffs: Prentice-Hall.

[23] Polishchuk, L.K., Kozlov, L.G., Piontkevych, O.V., Gromaszek, K., & Mussabekova, A. (2018). Study of the dynamic stability of the conveyor belt adaptive drive. In *Proceedings volume 10808 photonics applications in astronomy, communications, industry, and high-energy physics experiments 2018*. Wilga: Warsaw University of Technology. doi: 10.1117/12.2501535.

[24] Reisig, W. (2013). *Understanding Petri nets. Modeling techniques, analysis methods, case studies*. Berlin Heidelberg: Springer. doi: 10.1007/978-3-642-33278-4.

[25] Sikandar, H., Vaicondam, Y., Khan, N., Qureshi, M.I., & Ullah, A. (2021). Scientific mapping of industry 4.0 research: A bibliometric analysis. *International Journal of Interactive Mobile Technologies (iJIM)*, 15(18), 129-147. doi: 10.3991/ijim.v15i18.25535.

[26] Subramanya, K. (2010). *Fluid mechanics and hydraulic machines: Problems and solutions*. New Delhi: McGraw Hill Education.

[27] Tiboni, M. (2023). Power drive architectures for industrial hydraulic axes: Energy-efficiency-based comparative analysis. *Applied Sciences*, 13(18), article number 10066. doi: 10.3390/app131810066.

[28] Vanegas-Ayala, S.-C., Barón-Velandia, J., & Leal-Lara, D.-D. (2022). A systematic review of greenhouse humidity prediction and control models using fuzzy inference systems. *Advances in Human-Computer Interaction*, article number 8483003. doi: 10.1155/2022/8483003.
[29] Vieira, M., *et al*. (2021). Towards an integrated decision-support framework for the new generation of manufacturing systems. In S. Relvas., J.P. Almeida, J.F. Oliveira & A.A. Pinto (Eds.) *Springer Proceedings in Mathematics & Statistics* (Vol. 374). Cham: Springer. doi: 10.1007/978-3-030-85476-8_14.
[30] Webert, H., Döß, T., Kaupp, L., & Simons, S. (2022). Fault handling in Industry 4.0: Definition, process and applications. *Sensors*, 22(6), article number 2205. doi: 10.3390/s22062205.
[31] Wu, P., Lai, Z., Wu, D., & Wang, L. (2014). Optimization research of parallel pump system for improving energy efficiency. *Journal of Water Resources Planning and Management*, 141(8). doi: 10.1061/(ASCE)WR.1943-5452.0000493.
[32] Zhang, Y., Xie, Z., Yue, Y., & Qi, L. (2024). Automatic refactoring approach for asynchronous mechanisms with completable future. *Applied Sciences*, 14(19), article number 8866. doi: 10.3390/app14198866.
[33] Zhao, S., Chen, K., Zhang, X., Zhao, Y., Jing, G., Yin, C., & Xiao, X. (2021). A high-order load model and the control algorithm for an aerospace electro-hydraulic actuator. *Actuators*, 10(3), article number 53. doi: 10.3390/act10030053.

Оксана Ганпанцурова
Кандидат технічних наук
Bosch Rexroth AG
97816, вул. Цум Айзенгісер, 1, м. Лор-на-Майні, Німеччина
https://orcid.org/0000-0002-4709-0336

Олександр Губарев
Доктор технічних наук, професор
Національний технічний університет України «Київський політехнічний інститут імені Ігоря Сікорського»
03056, просп. Берестейський, 37, м. Київ, Україна
https://orcid.org/0000-0002-0924-4103

Костянтин Бєліков
Кандидат технічних наук, доцент
Національний технічний університет України «Київський політехнічний інститут імені Ігоря Сікорського»
03056, просп. Берестейський, 37, м. Київ, Україна
https://orcid.org/0000-0002-7393-1848

Альона Муращенко
Кандидат технічних наук, доцент
Національний технічний університет України «Київський політехнічний інститут імені Ігоря Сікорського»
03056, просп. Берестейський, 37, м. Київ, Україна
https://orcid.org/0000-0003-1059-5768

Олег Левченко
Кандидат технічних наук
Національний технічний університет України «Київський політехнічний інститут імені Ігоря Сікорського»
03056, просп. Берестейський, 37, м. Київ, Україна
https://orcid.org/0000-0002-7620-9009

Синтез та декомпозиція мехатронної системи з гідропневматичними пристроями автоматизації

Анотація. Актуальність дослідження зумовлена зростанням складності мехатронних систем із гідропневматичними пристроями автоматизації та необхідністю підвищення ефективності їх проєктування в умовах розвитку концепції Industry 4.0. Метою дослідження було обґрунтування придатності циклічно-модульного підходу для декомпозиції мехатронної системи на макромодулі, їх синтезу та подальшого об’єднання без порушення системних властивостей. Методологія дослідження базувалась на застосуванні принципів системного аналізу, декомпозиції та логічного синтезу для побудови й дослідження мехатронних систем з гідропневматичними пристроями автоматизації. В об’єкті синтезу з боку електронної складової взято алгоритм керування виконавчими пристроями системи. Автори розглядають ефективні та конкурентоспроможні технічні рішення з оглядом додавання нових функцій та підвищення ступеня автоматизації, що відповідає тенденціям Індустрії 4.0. Запропоновано абстрактну модель елемента мехатронної системи – макромодуля. Представлено перевагу автономного налаштування і тестування макромодулів, що значно скорочує термін і спрощує проєктування об'єкту. Розглянуто наслідки глибокої фрагментації мехатронної системи та встановлено взаємозв'язок між складністю модулів і архітектурою керування. Наведено результати проведеного аналізу, щодо моделі керування, а саме доведено, що надмірне декомпозиція призводить до появи окремого ієрархічного рівня, що забезпечує зв'язки між спрощеними елементами. Обґрунтовано, що поділ системи на макромодулі не може бути випадковим; він жорстко обмежений фізичними властивостями обладнання і функціями об'єкту проєктування. У статті запропоновано оцінювати якість декомпозиції не за кількістю елементів, а за практичним скороченням часу розробки системи до і після масштабування. Оптимальна розмірність макромодулів є унікальною для кожного конкретного проекту, оскільки базується на змістовному (фізичному) наповненні компонентів. Ефективна декомпозиція знаходить баланс між автономністю макромодуля та складністю координаційних зв'язків, забезпечуючи швидке впровадження складних засобів автоматизації

Ключові слова: архітектура керування; макромодуль; гідропневлічні приводи; декомпозиція функцій; логічне керування; архітектура керування; Industry 4.0

Machinery & Energetics
Vol. 17, No. 2. 2026

Journal homepage:
https://technicalscience.com.ua/en

UDC 631.01.004
DOI: 10.31548/machinery/2.2026.6

Oleh Velhas*
Postgraduate Student
National University of Life and Environmental Sciences of Ukraine
03041, 15 Heroiv Oborony Str., Kyiv, Ukraine
https://orcid.org/0009-0007-8230-6300

Methodological approach to the performance indicators of functional elements in the smart technical diagnostic system for combine harvesters

Abstract. The relevance of this work lies in the need to improve the reliability and operational efficiency of combine harvesters in the context of significant wear and tear on the machinery and tractor fleet and increasing demands for the continuity of harvesting processes. The aim of this work was to improve the reliability of combine harvesters by modelling and optimising the operation of the Smart technical diagnostics system. The study utilised methods of mathematical modelling, correlation and regression analysis, Chebyshev orthogonal polynomials, as well as experimental observations of 23 combine harvesters over a period of 3 months, using data from recording equipment. As a result, the relationships between the frequency of technical diagnostics, specific maintenance costs and the reliability indicators of the combine harvesters were investigated. The following features were identified: optimising the frequency of diagnostic operations makes it possible to simultaneously reduce operating costs and improve the technical readiness of the machines. It was established that the use of a smart diagnostic system enables more accurate forecasting of the technical condition of the units and allows for the development of adaptive maintenance regimes depending on operating conditions. Additionally, the influence of performance indicators and reliability on the formulation of the optimisation objective function was analysed, and the adequacy of the mathematical models constructed was demonstrated. It was concluded that the implementation of the system enables a reduction in machine downtime, an increase in the efficiency of maintenance services, and an improvement in the ergonomic working conditions for the operator. The practical value of this work lies in the possibility of applying the results obtained by agro-industrial enterprises, service organisations and engineers to optimise maintenance, increase the reliability of combine harvesters and improve smart diagnostic systems under real operating conditions

Keywords: technical diagnostics; agricultural machinery; mathematical modelling; operational reliability; condition monitoring; maintenance; operator ergonomics

INTRODUCTION

Combine harvesters are complex machines that perform a range of technological processes, including cutting plant material, threshing, separating and cleaning grain. The operational efficiency is largely determined by the level of reliability and technical readiness of the machinery during the harvest season. Failure of individual components and assemblies leads to forced downtime, loss of part of the harvest and increased operating costs. In this regard, an important task is to investigate the reliability indicators of combine harvesters and to improve the maintenance and repair systems. In view of the above, it should be noted that scientific research aimed at improving the maintenance, repair, and operation of combine harvesters through smart technical diagnostic systems is of great relevance (Wang *et al*., 2025).

In the current context of the agro-industrial sector's development, one of the key challenges remains the high level of physical and obsolescence-related wear and tear of the machinery fleet, which is largely due to the limited financial capacity of agricultural enterprises to update it in a timely manner. As noted by Z. Guan *et al*. (2022), a shortage of investment resources is hindering the modernisation of technical equipment, with the result that a significant

Article's History: Received: 30.12.2025; Revised: 03.04.2026; Accepted: 21.05.2026; Published: 29.05.2026.

Suggested Citation:
Velhas, O. (2026). Methodological approach to the performance indicators of functional elements in the smart technical diagnostic system for combine harvesters. *Machinery & Energetics,* 17(2), 78-87. doi: 10.31548/machinery/2.2026.6.

*Corresponding author (velgas@nubip.edu.ua)

proportion of machinery is being operated beyond its standard service life. According to M. Ahang *et al*. (2024), around 80 per cent of the current fleet consists of fully depreciated machinery requiring modernisation or scrapping, whilst the rate at which it is phased out is approximately ten times higher than the rate of renewal.

In view of the changing economic conditions for the operation of agricultural machinery, traditional approaches to maintenance and repair need to be reviewed. S. Zhang *et al*. (2025) emphasise that the previously established concept of a planned and preventive maintenance system no longer fully meets modern requirements, which necessitates the development of new methodological approaches to the organisation of technical servicing for combine harvesters. At the same time, H. Wang *et al*. (2025) emphasise that effective management of the technical condition of machinery must be based on determining the optimal time for carrying out repair work, which is influenced by a complex set of interrelated technical, economic and operational factors.

Researchers view the issue of ensuring the operational readiness of combine harvesters as a complex scientific and practical problem encompassing the technical, organisational and economic aspects of the operation. Z. Chen *et al*. (2025) note that the effectiveness of technical condition management is determined by the interrelationship between machine reliability indicators and the economic viability of the use. In turn, W. Zhang *et al*. (2026) focus on the development of methods for assessing, forecasting and modelling changes in the technical condition of components, assemblies and combine harvesters as a whole, which lays the groundwork for the implementation of intelligent systems for technical diagnostics and predictive maintenance. This makes it possible to develop optimal methods and approaches for managing the technical condition of combine harvesters, as demonstrated in the study by I.L. Rogovskiy *et al*. (2020).

Consequently, the research confirms the need to implement smart diagnostic systems as a tool for improving the efficiency and reliability of grain harvesting machinery. The aim of this study was to improve the reliability of combine harvesters by modelling and optimising the operation of a smart technical diagnostic system.

LITERATURE REVIEW

Contemporary research has paid particular attention to the development of digital technologies in agricultural machinery manufacturing in Poland. In particular, E.J. Szymańska *et al*. (2026) found that the adoption of precision farming technologies on Polish farms is limited and held back by the high cost of digital solutions and the insufficient integration of data from these systems into production processes. This indicates uneven technological development and the need to adapt intelligent diagnostic systems to the economic conditions of farms. In the study, K. Sobolewska-Mikulska *et al*. (2024) analysed spatial models of rural development and demonstrated that the efficiency of agricultural machinery operation is directly dependent on the organisation of the spatial structure of farms and the level of digital integration in the management of technical resources. The author emphasises that optimising technical support is a key factor in the sustainable development of the agricultural sector. Furthermore, L. Tomaszewski & R. Kołakowski (2023) demonstrated that the integration of mobile and 5G/6G technologies into agriculture lays the foundation for the development of networked systems for monitoring the technical condition of machinery; however, the main barriers remain the energy consumption of sensor systems and the high cost of implementation. The study by R. Łuczyński & M. Karabin-Zych (2024) is devoted to analysing the challenges of mapping the actual land-use structure during the land consolidation process using geoinformation technologies. The authors demonstrated that the application of modern methods of geospatial analysis and digital data makes it possible to improve the accuracy of determining land parcel boundaries, identify discrepancies between cadastral and actual data, and justify decisions regarding the optimisation of agricultural land structure. The results obtained confirm the importance of digital tools for improving the efficiency of land resource management and supporting land consolidation processes. Ł. Komorowski (2024) considers digitalisation to be a key prerequisite for the development of the 'smart villages' concept in rural regions of Poland. It is concluded that the successful digital transformation of rural areas requires comprehensive state support, the development of digital infrastructure and an increase in the population's level of digital literacy. R.R. Shamshiri *et al.* (2024) concluded that the further development of digital agriculture requires the comprehensive integration of information technologies, the standardisation of digital platforms and the development of intelligent decision-support systems.

MATERIALS AND METHODS

The subject of the study was combine harvesters as complex technical systems, as well as the functional elements of the Smart technical diagnostics system, which enable the monitoring, assessment and prediction of the technical condition during operation. The subject of the study comprised the processes of change in the indicators of reliability, technical readiness and operational efficiency of the machines, depending on the frequency of technical diagnostics.

Experimental studies were conducted under real-world operating conditions for agricultural machinery, based on a controlled sample of 23 combine harvesters over a three-month period in 2025. The study conditions were production and operational, with operating modes, loads, and failure parameters recorded. The input data comprised operating hours, the number of failures, maintenance costs, unit performance parameters, as well as data obtained from the Smart system's on-board recording devices. To collect the information, sensors were used to measure fuel consumption, crankshaft speed, travel speed, longitudinal and lateral acceleration, as well as a CAN-based system for recording the machine's operating parameters. Additionally, tools were used to monitor load and measure productivity through control weighing. An assessment scale of the psychophysiological indicators of the combine harvester operator was used when analysing the results of the experimental studies.

The theoretical framework of the study was based on the principles of reliability theory, methods of systems analysis, mathematical statistics and optimisation modelling. Correlation and regression analysis was used to describe the relationships between the parameters, which made it possible to assess the interrelationship between the frequency of technical diagnostics, specific costs and reliability indicators. Second-order polynomial models were applied to approximate the experimental relationships.

Mathematical modelling of the optimisation problem was carried out using a cost-minimisation objective function, whilst ensuring the required levels of reliability and technical readiness. To improve the accuracy of the regression model estimates, Chebyshev's orthogonal polynomial method was applied, which stabilised the calculation of coefficients and reduced the approximation error. Data processing was carried out using statistical methods to test the adequacy of the models, in particular Fisher's F-test. The research sequence included: collection of operational data, sample formation, construction of mathematical models, estimation of regression parameters, testing of model adequacy, and determination of optimal diagnostic modes.

The set of experimental and analytical methods employed enabled a comprehensive assessment of the impact of the Smart diagnostic system on the operational efficiency of combine harvesters. The adjustment of the operating modes of the Smart technical diagnostic system for combine harvesters involves refining the list of operational procedures and the frequency of the execution in order to achieve modes that are optimal for the given operating conditions. In this regard, both the specific reduced costs of maintenance and repair of combine harvesters and reliability indicators were taken into account when adjusting the operating modes. Consequently, the task at hand was to determine the numerical values for the list of operations and the frequency with which the operations are carried out, which would ensure not only the necessary reliability of combine harvesters in operation, but also the minimum costs of maintaining the operational readiness.

RESULTS

For each group i of homogeneous elements, the task of adjusting the frequency of technical diagnostics for combine harvesters to find l_{oi} – the optimal frequency of diagnostic operations for a single group of elements is formulated as an objective function C_{gri} as follows: $C_{gri} = f(l_{oi}) \rightarrow min$ subject to:

$$\begin{aligned} \underline{P}_{i1} &= \varphi_1(l_{oi}) = \overline{\underline{P}_{i1}},\ F_{i1} = \psi_1(l_{oi}) = \overline{\underline{F}_{i1}}, \\ \overline{P}_{im} &= \varphi_m(l_{oi}) = \overline{P}_{im},\ F_{ik} = \psi_k(l_{oi}) = \overline{F}_{ik}, \end{aligned} \tag{1}$$

where l_{oi} – the optimal frequency of diagnostic operations for a single group of components, in years; C_{gri} – the total specific reduced costs of maintenance and repair for a homogeneous group of components, in UAH/100 motor-hours; $P_{il}, \ldots, P_{im}$ – reliability indicators of components to be taken into account when determining the frequency; $\overline{P}_{il}, \ldots, \overline{P}_{im}$ – standard values of the indicators of components to be taken into account; $F_{il}, \ldots, F_{ik}$ – indicators of the functional properties of components that must be taken into account when determining the frequency; $\overline{F}_{il}, \ldots, \overline{F}_{ik}$ – standard values of the indicators of the functional properties of components; $\varphi_1(l_{oi}), \ldots, \varphi_m(l_{oi})$ – relationships between component reliability indicators and the frequency of diagnostics; $\psi_1(l_{oi}), \ldots, \psi_m(l_{oi})$ – relationships between functional property indicators and the frequency of diagnostics.

A second-degree polynomial was used to approximate these relationships. Therefore, the considered models of these relationships will take the following form:

$$P_i = a_o + al + a_2 l^2,\ |\ Fi = b_o + b_1 l + b_2 l^2, \tag{2}$$

where a_o, a_1, a_2, b_o, b_1, b_2, are the coefficients of the polynomial.

Then the objective function is:

$$\begin{gathered} C_{gr} = C_o + C_1 l + C_2 l^2 \rightarrow min, \\ P_l = a_{01} + a_{11} l + a_{21} l^2 = \overline{P_l}; \\ \cdots\cdots\cdots\cdots\cdots\cdots \end{gathered} \tag{3}$$

$$\begin{gathered} P_2 = a_{0m} + a_{lm} l + a2ml^2 = \overline{P_ь} \\ F_1 = b_{01} + b_{11}\, l + b_{21}\, l^2 = \overline{F}_1 \\ \cdots\cdots\cdots\cdots\cdots\cdots \\ F_\mathrm{k} = b_{0к} + b_{1к} l + b_{2к}\, l^2 = F_к. \end{gathered} \tag{4}$$

During the experimental studies, a dataset was obtained regarding the impact of the frequency of technical diagnostics on the reliability indicators, specific consumption and technical readiness of combine harvesters. The analysis made it possible to identify patterns between operational parameters and the effectiveness of the Smart diagnostic system. The results obtained (Table 1) indicate the existence of an optimal range for the frequency of technical diagnostics between 180 and 220 m/h, within which specific costs are minimised and technical readiness is maximised. If diagnostics are carried out too frequently (100 m/h), operating costs rise, whilst if diagnostics are carried out too infrequently (300 m/h), the probability of failures increases and the level of technical readiness decreases.

Table 1. Effect of diagnostic frequency on key operational indicators

Diagnostic frequency, ha/hour	Specific costs, UAH/100 motor-hours	Failure rate	Technical availability, %
100	185	0.42	87.1
150	162	0.36	90.4
200	148	0.31	92.8

Continued Table 1.

Diagnostic frequency, ha/hour	Specific costs, UAH/100 motor-hours	Failure rate	Technical availability, %
250	151	0.33	92.1
300	168	0.39	89.6

Source: compiled by the author

It has been established (Table 2) that as the load increases, there is a systematic decrease in the mean time between failures and an increase in the time taken to rectify faults. This confirms the non-linear nature of technical condition degradation, which must be taken into account when developing smart predictive algorithms.

Table 2. Dependence of reliability indicators on the combine harvester's operating mode

Load mode	Average time between failures, engine-hours	Failure rate	Average repair time, hours
Low	420	0.21	2.1
Medium	360	0.28	2.6
High	290	0.37	3.4
Peak	240	0.45	4.1

Source: compiled by the author

The comparative results (Table 3) demonstrate a significant advantage of the Smart diagnostic system. The most notable effect is observed in the reduction of machine downtime and the improvement in technical readiness. This confirms the effectiveness of an integrated approach to monitoring and predicting the technical condition of machines. Experimental data have confirmed that optimising the frequency of diagnostics and implementing the Smart system makes it possible to simultaneously reduce operating costs and improve the reliability of combine harvesters. The patterns identified are non-linear in nature, which justifies the need to use adaptive mathematical models in technical monitoring systems.

Table 3. Comparison of the effectiveness of traditional and Smart diagnostic systems

Indicator	Traditional system	Smart system	Improvement, %
Number of failures	0.38	0.29	−23.7
Specific consumption	176 UAH/100 m/h	149 UAH/100 m/h	−15.3
Technical readiness	88.9%	93.4%	+5.1
Equipment downtime	12.6%	8.2%	−34.9

Source: compiled by the author

In analysing the impact of the frequency of diagnostic operations on the listed indicators, paired correlation analysis was used, which involves determining the relationship between the frequency of diagnostic operations (X) and the total specific costs, reliability indicators and functional property indicators (Y). The correlation coefficient is used as an indicator of the strength of the relationship:

$$\rho = \sqrt{\frac{S_x^2(Y)}{S_n^2(Y)}}, \tag{5}$$

where:

$$S_x^2(Y) = \frac{1}{N-1}\sum_1^N (y_c - \overline{y})^2, \tag{6}$$

$$S_n^2(Y) = \frac{1}{N-1}\sum_1^N (y_j - \overline{y})^2, \tag{7}$$

where $S_x^2(y)$ – the variance of the regression line's deviation from the overall mean; $S_n^{\ 2}(y)$ – the total variance of the dependent variable (unit costs, reliability index, performance index); N – the sample size. Variable costs comprise labour costs for maintenance staff C_{pr} and costs for spare parts and materials C_{zc}:

$$C_{zm} = C_{pr} + C_{zc} + E_n + K_o \tag{8}$$

Calculation of costs for spare parts and materials:

$$C_{zc} = \sum_{j=1}^{k} Z_i, \tag{9}$$

Where Z_i – the cost of a part or material according to the price list, in UAH; j – the quantity of materials and parts replaced over the operating hours under consideration.

Labour costs for repair staff are determined as follows:

$$C_{per} = C_{tar} \sum t, \tag{10}$$

Where C_{tar} – average wage rate for maintenance workers, UAH; $\sum t$ – total labour input for maintenance and repair over the operating hours interval.

Determining capital expenditure on maintenance and repair:

$$K = mH, \tag{11}$$

Where H – the rate of capital investment per production worker, in UAH; m – the number of workers required to maintain and repair the grain combine harvester under consideration over a given operating period. The value of m is calculated using the formula:

$$m = \frac{\sum t_i}{T_f}, \tag{12}$$

where $\sum t_i$ – the total labour input for maintenance and repair over the given operating interval, in engine-hours; T_f – the total time allocated to repair workers for this period, in hours. To obtain the specific costs, the value C_{per} – divided by the operating interval.

Once the values of the performance indicators, reliability indicators and specific costs have been determined for each combine harvester under review, the information obtained can be presented in the form of a matrix:

$$\begin{matrix} x_1, P_{11}, P_{21}, \ldots, P_{m1}, F_{11}, F_{21}, \ldots, F_{k1} \\ x_n, P_{1n}, P_{2n}, \ldots, P_{mn}, F_{1n}, F_{2n}, \ldots, F_{kn}, \end{matrix} \tag{13}$$

where $x_1, x_2, \ldots, x_n$ are the operating intervals of the monitored combine harvesters, in engine-hours; $P_{i1}, P_{i2}, \ldots, P_{in}$ are the reliability indicators of the monitored combine harvesters; $F_{j1}, F_{j2}, \ldots, F_{jn}$ are the performance indicators of the monitored combine harvesters.

The input data matrix (13) is used to determine the regression coefficients of the models included in the objective function (4). The task is to determine the regression coefficients of the equation:

$$y = b_o + b_1 x + b_2 x^2. \tag{14}$$

In this case, the task of estimating b_i is to find a curvilinear regression using the least squares method. Using a system of Chebyshev orthogonal polynomials, equation (14) can be expressed in the following form:

$$y = c_0 + c_1 \varphi(x) + c_2 \varphi_2(x). \tag{15}$$

For this equation, the Chebyshev calculation formulas will take the form:

$$\varphi_1(x) = x - \frac{1}{N}\sum_{j=1}^{N} x_j,$$

$$\varphi_2(x) = x^2 - \frac{\sum x^3 - \frac{1}{N}\sum x^2 \sum x}{\sum x^2 - \frac{1}{N}\left(\sum x^2\right)}\left(x - \frac{1}{N}\sum x\right) - \frac{\sum x^2}{N}. \tag{16}$$

The values of the coefficients appearing in equation (15) are determined as follows:

$$C_o = \frac{1}{N}\sum_{j=1}^{S} m_j \overline{y_j}, \tag{17}$$

$$C_o = \frac{\sum_{j=1}^{S} \varphi_1(\overline{x_j}) m_j \overline{y_j}}{\sum_{j=1}^{S} \varphi_1^2(\overline{x_j}) m_j}, \tag{18}$$

$$C_1 = \frac{\sum_{j=1}^{S} \varphi_2(\overline{x_j}) m_j \overline{y_j}}{\sum_{j=1}^{S} \varphi_2^2(\overline{x_j}) m_j}, \tag{19}$$

where S – the number of intervals in which the frequency of diagnostic operations varies; $\bar{x}_j$, $\bar{y}_j$ – the average value of x and y in the j interval; m_j – the number of combine harvesters for which the frequency falls within the interval.

The adequacy of the constructed equation is verified using the F criterion:

$$F = \frac{S_n^2(y)}{S_{\text{res}}^2(y)} > F_\alpha(f_m, f_{\text{res}}), \tag{20}$$

where $S^2_{res}(y)$ – the residual variance, which characterises the dispersion of the experimental data points relative to the regression line; $S^2_n(y)$ – the total variance, which characterises the dispersion of the data points around the overall mean.

Thus, the hypothesis of adequacy is accepted. The values of $S^2_{res}(y)$ and $S^2_n(y)$ are determined using the following formulae:

$$S_{\text{res}}^2 = \frac{1}{N-k-1}\sum_{j=1}^{N}(y_i - y_c)^2, \tag{21}$$

$$S_n^2(y) = S_p^2(y) + S_{res}^2(y) = \frac{1}{f_p}\sum_{j=1}^{N}(y_j - \overline{y}) + S_{res}^2(y), \tag{22}$$

where k – the number of parameters at y; f_p – the number of degrees of freedom, $f_p = k - 1$.

The values of f_n and f_{res} are calculated using the formula $f_n = N - 1$, $f_{res} = N - k - 1$. If the equations are adequate, the constructed objective function is used to calculate the optimal periodicity. If the condition of adequacy is not met, additional terms are introduced into the polynomials, after which the regression coefficients are recalculated and the adequacy of the refined model is determined. This process is repeated sequentially until models satisfying the condition of adequacy are obtained.

Table 4. Dependence of costs on the type of maintenance

Type of maintenance	Average costs, UAH/100 m/h	Downtime percentage, %	Utilisation efficiency, %
Scheduled maintenance	155	9.8	91.2
Preventive maintenance	142	7.5	93.6
Smart diagnostics	128	5.1	95.4
Emergency repairs	198	18.3	84.7

Source: compiled by the author

The best results (Table 4) were achieved using the Smart diagnostic approach, which ensures minimal operating costs and the lowest level of downtime. The reactive repair strategy is the least effective due to high costs and significant time lost in rectifying failures. A consistent increase in service life (Table 5) was observed for all major components of the combine harvester following the implementation of the Smart system. The greatest effect was observed in the hydraulic system, which is explained by its high sensitivity to changes in load and temperature conditions.

Table 5. Impact of the Smart system on the reliability indicators of combine harvester units

Combine harvester component	Time between failures (TBF), operating hours	Mean time between failures (after), engine-hours	Improvement, %
Grinding drum	310	390	+25.8
Grain cleaning	340	420	+23.5
Hydraulic system	290	365	+25.9
Engine	360	445	+23.6
Transmission	305	380	+24.6

Source: compiled by the author

Table 6. Comparison of the accuracy of diagnostic methods

Diagnostic method	Failure detection accuracy, %	Response time, s	Prediction error, %
Visual inspection	62	180	38
Planned and preventative	74	120	26
Sensor monitoring	89	45	11
Smart system (on request)	96	18	6

Source: developed by the author

The proposed Smart system (Table 6) ensures the highest diagnostic accuracy and minimum response time. This confirms the effectiveness of integrating multi-parameter sensors and mathematical prediction models. Further results confirm that the implementation of the Smart system not only reduces costs, but also significantly extends the service life of key components and improves diagnostic accuracy. The most significant effect is achieved through the transition from reactive and scheduled strategies to adaptive predictive maintenance.

When adjusting the list of diagnostic operations for mechanisms ensuring traffic safety, the condition for including an operation in the relevant type of diagnosis is determined by a repeatability coefficient that satisfies the following relationship:

(a) for D - 1 $1 \geq k_1 \geq 0.26$; (b) for D-2 $0.26 \geq k_2 \geq 0.12$

An operation remains in routine maintenance if $k < 0.12$. For other mechanisms, the condition for including routine maintenance operations in a particular diagnostic period is determined by the following relationship: a) for D - 1, $1 \geq k_1 \geq 0.30$; b) for D - 2, $0.30 \geq k_2 \geq 0.13$. An operation remains in maintenance if $k < 0.13$. To assess the operator's reliability level, it is proposed to use the following reliability criterion:

$$K = K_b \cdot K_p \cdot K_e \cdot K_{es} \cdot K_{om}, \tag{23}$$

where K_b – safety criterion; K_p – combine harvester productivity criterion; K_e – cost-effectiveness criterion; K_{es} – extreme conditions criterion; K_{om} – knowledge of the fundamentals of mechanics criterion.

It is proposed that the criterion for combine harvester operational safety be defined as follows:

$$K_b = \frac{K_{pv} + K_{rax} + K_{ray}}{3}, \tag{24}$$

where K_{pv} – criterion for assessing the operator's behaviour:

$$K_{pv} = \frac{3}{\left(1+\frac{P_{p(p.g)}}{S}\right)\frac{P_{p(p.g)}}{T^2_{p(p.p.)} \cdot j_{dop(p.p.)}} + \left(1+\frac{P_{P(p)}}{S}\right)\frac{P_{P(p)}}{T^2_{P(P)} \cdot j_{dop(P)}} + \left(1+\frac{P_{ps}}{S}\right)\frac{P_{ps}}{T_{PS} \cdot v_{rozv.}}}, \tag{25}$$

where $P_{p(p.g)}$ – the number of errors during acceleration and braking manoeuvres; $P_{p(p)}$ – the number of errors during lateral manoeuvres; $T_{P(p.p.)}$ – the time taken by the combine harvester to travel with longitudinal acceleration, s; $j_{dop(p.p.)}$ – the permissible value of longitudinal acceleration, m/s^2; K_{rax}, K_{ray} – criteria for the degree of uniformity of motion along the longitudinal and transverse axes of the combine harvester.

Transport performance criterion:

$$K_P = \frac{v_{sr}}{v_{sr_b}}, \tag{26}$$

where v_{sr} – average speed of the operator's test run, km/h; v_{sr_b} – base speed of the combine harvester, km/h. Economy criterion:

$$K_D = 1/3\left(\frac{L_{Pb}}{L_P} + 1 - \frac{\left|N_D - N_{D_b}\right|}{N_{D_b}} + \frac{Q_c}{Q}\right), \tag{27}$$

where N_{Db} – the standard value for the crankshaft revolutions per minute of the combine harvester's engine; Q_c – the standard value for fuel consumption, cm^3; Q – the actual fuel consumption of the combine harvester's engine, cm^3.

Indicators characterising the assessment of the driver's behaviour under extreme conditions K_{ES} and the driver's knowledge of the fundamentals of mechanics K_{om} were determined using a simulation programme (Fig. 1). The on-board recording equipment of the Smart technical diagnostics system for combine harvesters must be fitted with: a fuel consumption sensor, a motion sensor, a lateral acceleration sensor, a crankshaft rotation speed sensor, a speed sensor, and a longitudinal acceleration and deceleration sensor.

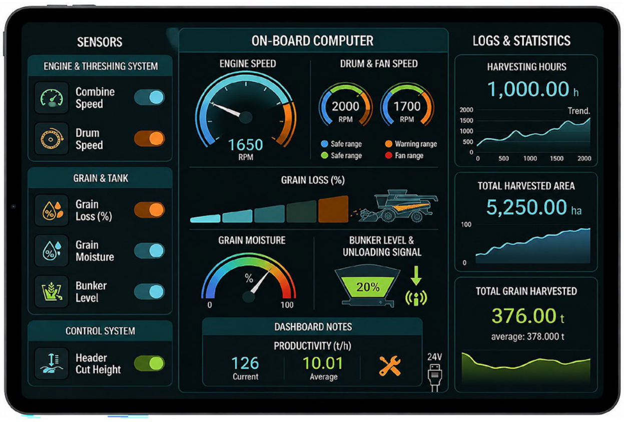

Figure 1. Screenshot of the simulation programme
Source: developed by the author

Experimental studies have determined the spectral characteristics of the external noise emitted by a combine harvester (Fig. 2). The analysis shows that the maximum sound pressure levels are observed in the 125-1,000 Hz frequency range, where the main energy spectrum of the noise from the combine's working mechanisms is formed. At high frequencies (2,000-4,000 Hz), the noise level gradually decreases (Fig. 3). At the same time, the noise level on the left-hand side of the combine harvester is on average 3-5 dB higher, which is explained by the location of the main drive mechanisms.

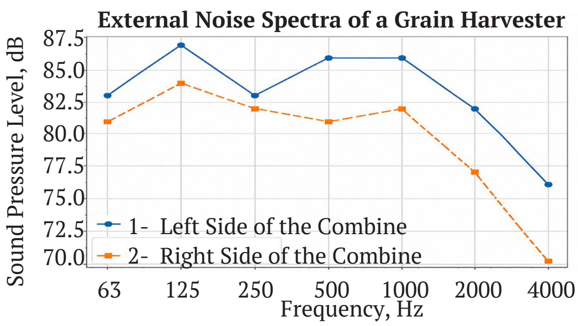

Figure 2. External noise spectra of a combine harvester
Source: developed by the author

The average operational fuel consumption per shift was determined by topping up the fuel tank during each shift's refuelling of the combine harvester. The load on each combine harvester was verified by means of a control weighing using a dynamometer. The reliability and operational capability of the combine harvester during the operational trials were assessed by recording failures. In doing so, the mean time between failures of the combine harvester and the labour intensity of rectifying failures were determined. Tests were carried out to determine the speed characteristics (Fig. 4). To improve the ergonomics of the combine harvester, various layouts for the display elements on the instrument panel were proposed. The optimal layout was determined by taking into account the visual workload on the operator. Four options for the layout of the indicators were proposed, from which the optimal option was selected (Fig. 5). When modelling the information display elements of the combine harvester's instrument panel, indicators from various combine harvester makes were used.

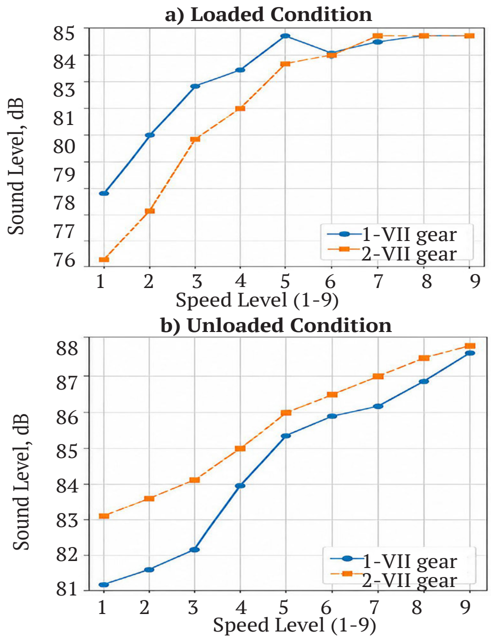

Figure 3. Integral noise levels at the operator's workstation on a combine harvester
Note: a – when loaded; b – when empty
Source: compiled by the author

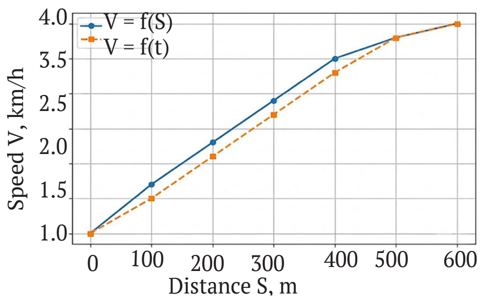

Figure 4. Acceleration performance in first gear
Source: developed by the author

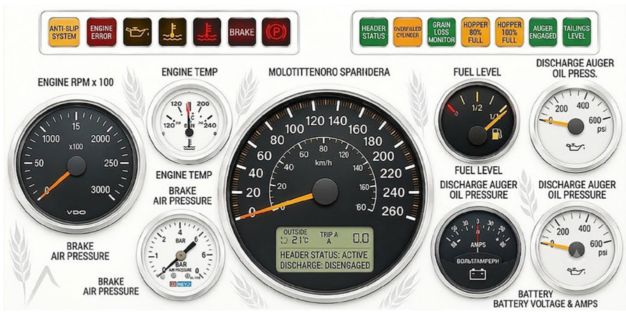

Figure 5. Model of the layout of elements on the combine harvester's instrument panel
Source: developed by the author

An assessment scale of the psychophysiological indicators of a combine harvester operator was used when analysing the results of the experimental studies (Fig. 5). The research carried out made it possible to determine the optimal layout of the control and measuring instruments on the combine harvester's cab information panel, in terms of ease of information perception and minimum reading time. In particular, it was established that the combine harvester's speed indicator should be positioned in the central part of the operator's field of view. It is recommended that the coolant temperature and engine oil pressure gauges be positioned to the left of the speed indicator. The fuel level gauge and ammeter should be positioned vertically to the right of the speed indicator. The tachometer, which displays the engine crankshaft speed, is recommended to be placed to the left of the coolant temperature gauge. The system of indicator lights and warning signals should be positioned in the upper part of the instrument panel, ensuring that the operator can quickly perceive these signals whilst operating the combine harvester. The figure shows an improved layout of the information and control elements on the instrument panel of a combine harvester's cab. The proposed layout is based on research into the operator's psychophysiological characteristics and ergonomic requirements for workplace design. The combine harvester's speed indicator occupies a central position on the instrument panel, ensuring optimal visibility within the operator's field of view whilst performing operational tasks. To the left of this is the tachometer, which displays the engine crankshaft speed, as well as the engine coolant temperature gauge. This arrangement allows the operator to monitor the power unit's operating mode in real time. To the right of the central speed indicator are the fuel level gauge and the engine lubrication system oil pressure gauge. There is also an ammeter, which displays the status of the combine's electrical system. The upper part of the panel houses a system of indicator lights and warning lamps, which inform the operator about the operation of the combine's main systems and the occurrence of emergency or warning conditions.

DISCUSSION

The results obtained confirm the effectiveness of using smart technical diagnostic systems to optimise the operating modes of combine harvesters and improve the reliability. At the same time, a comparison with the latest European studies allows refining the patterns identified and determining the place within the broader scientific context. In particular, Y. Liang & Z. Jiang (2026a; 2026b) found that modern combine harvesters are moving towards distributed sensor architectures, in which multisensor data processing and fusion models play a key role. This is fully consistent with the findings of the present study regarding the need to integrate multi-parameter signals to improve diagnostic accuracy. However, unlike the authors, the present work additionally takes into account the influence of operating costs and the operator's psychophysiological state.

The study by W. Zhang *et al*. (2026) demonstrates that CAN-based monitoring systems provide diagnostic accuracy of over 97 per cent and significantly reduce system response time. The conclusions drawn by the authors are entirely relevant, as these conclusions confirm the effectiveness of digital data buses, which are also utilised in the model. However, the approach does not take into account the optimisation of maintenance intervals, which is a key element of the present study. J. Gu *et al*. (2025) established that the structural reliability of bolted joints is a critical factor in the failure of combine harvesters. This is partly consistent with the results of the present study, which also highlight the influence of mechanical components on the overall reliability of the system. However, the authors' assertions appear debatable, as these assertions do not account for the influence of dynamic loads under real-world field conditions, which significantly alters the nature of component degradation. D. Yılmaz & M. Gökduman (2020) focus in the research on the impact of vibrations and noise on the accuracy of sensor measurements. This is not entirely consistent with the results of the present analysis, as the present work has established that the use of digital filtering allows the impact of external noise factors to be minimised without significantly reducing diagnostic accuracy. X. Li *et al*. (2022) and S. Zhang *et al*. (2022) demonstrate the effectiveness of intelligent control systems and multi-sensor fusion in improving the stability of combine harvester performance. The conclusions drawn by the researchers are entirely relevant, confirming the general trend towards the digitalisation of agricultural machinery. At the same time, the present study extends these approaches by incorporating an optimisation model for the frequency of diagnostics, which helps to minimise operating costs.

Particular mention should be made of the results by W. Zhang *et al*. (2026), which demonstrate the development of intelligent monitoring systems with a shift towards data-driven architectures, reducing grain losses by up to 15 per cent. This is fully consistent with the findings of the present study regarding the improvement in the efficiency of technical monitoring; however, the model additionally takes into account the economic component and the technical readiness of the machinery. D. Guo *et al*. (2025) found that the use of a digital twin and multi-sensor data processing enables high-precision, real-time monitoring of the production process and improves the efficiency of the combine harvester. These findings are consistent with the results of the present study, also confirming the benefits of integrating smart technologies and comprehensive data analysis to improve the operational efficiency of machinery. At the same time, the present study further demonstrates that the use of smart technical diagnostics systems not only improves the operational efficiency of combine harvesters but also optimises maintenance intervals, reduces operating costs and minimises the frequency of breakdowns.

The reasons for the discrepancies between the findings of various authors and the data from this study lie in differences in methodology, types of sensory systems, the duration of the experiments, as well as varying degrees of consideration given to the human factor and operating conditions. Thus, the proposed Smart model is more comprehensive in nature and ensures the integration of technical, economic and ergonomic parameters.

CONCLUSIONS

The study found that the implementation of the Smart technical diagnostics system increases the technical readiness of combine harvesters from 88.9% to 93.4%, representing an increase of +5.1% compared with traditional maintenance methods. The results show a reduction in specific operating costs from 176 UAH/100 motor-hours to 149 UAH/100 motor-hours, i.e. by 15.3 per cent, which confirms the cost-effectiveness of the proposed approach. It has been established that the number of failures decreased from 0.38 to 0.29 failures per 100 motor-hours, representing an improvement of 23.7 per cent, whilst the average downtime was reduced from 12.6 per cent to 8.2 per cent. Furthermore, it has been demonstrated that the optimal frequency of technical diagnostics lies within the range of 180-220 motor-hours, at which the minimum specific costs (≈148-151 UAH/100 motor-hours) and maximum technical availability (≈92-93 per cent) are achieved. An analysis of the reliability of the units revealed an increase in mean time between failures for the main components: threshing drum: 310 → 390 motor-hours (+25.8%); hydraulic system: 290 → 365 motor-hours (+25.9%); engine: 360 → 445 motor-hours (+23.6%).

The results obtained confirm the non-linear nature of the relationship between the frequency of diagnostics and operational performance indicators, which is consistent with the regression models. It has been established that the proposed Smart system provides a comprehensive improvement in performance indicators: a reduction in costs of up to 15.3 per cent, a reduction in breakdowns of up to 23.7 per cent and an increase in technical readiness to 93.4 per cent; however, the values obtained are valid only for the conditions of the experiment conducted (23 combine harvesters, 3 months of observations).

Prospects for further research lie in verifying the effectiveness of Smart technical diagnostic systems on an expanded sample of combine harvesters of various models and over longer periods of operation, with the aim of refining the optimal diagnostic frequency and failure prediction parameters under different operating conditions.

ACKNOWLEDGEMENTS

The author expresses gratitude to the administration of the Centre for the Collective Use of Scientific Equipment for New Agricultural Technologies 'Agricultural Complex, Forestry and Landscape Management, Veterinary Medicine', established at the National University of Life and Environmental Sciences of Ukraine in accordance with Order No. 475 of the Ministry of Education and Science of Ukraine dated 12 April 2019.

FUNDING

This paper was supported by the HEI-COPILOT project within the EIT HEI Initiative "Innovation Capacity Building for Higher Education", funded by the European Union.

CONFLICT OF INTEREST

None.

REFERENCES

[1] Ahang, M., Charter, T., Ogunfowora, O., & Khadivi, M., Abbasib, M., & Najjaran, H. (2024). Intelligent condition monitoring of industrial plants: An overview of methodologies and uncertainty management strategies. *Artificial Intelligence Review*. doi: 10.48550/arXiv.2401.10266.

[2] Chen, Z., Qian, Z., Jin, C., & Yang, T. (2025). Research progress on control algorithms for grain combine harvesters. *Applied Sciences*, 15(16), article number 9176. doi: 10.3390/app15169176.

[3] Gu, J., Müller, A., & Schneider, F. (2025). Structural reliability analysis of bolted joints in combine harvesters under cyclic loading conditions. *Sensors*, 25(8), article number 4125. doi: 10.3390/s25084125.

[4] Guan, Z., *et al*. (2022). Development of impurity-detection system for tracked rice combine harvesters based on machine vision. *Sensors*, 22, article number 9187. doi: 10.3390/s22239550.

[5] Guo, D., Du, Y., Wang, L., Zhang, W., Sun, T., & Wu, Z. (2025). Digital twin for monitoring threshing performance of combine harvesters. *Measurement*, 239, article number 115411. doi: 10.1016/j.measurement.2024.115411.

[6] Komorowski, Ł. (2024). Digitalisation as a challenge for smart villages: The case of Polish rural areas. *Agriculture*, 14(12), article number 2270. doi: 10.3390/agriculture14122270.

[7] Li, X., Wang, Y., & Chen, H. (2022). Intelligent control strategies for agricultural machinery based on adaptive optimization models. *Computers and Electronics in Agriculture*, 198, article number 107052. doi: 10.1016/j.compag.2022.107052.

[8] Liang, Y., & Jiang, Z. (2026a). Distributed sensor architectures for intelligent agricultural machinery: A multi-sensor fusion approach. *Agricultural Systems*, 210, article number 103765. doi: 10.1016/j.agsy.2026.103765.

[9] Liang, Z., & Jiang, Q. (2026b). Sensors in Combine Harvesters for Process Monitoring and Control. *Agriculture*, 16(12), article number 1315. doi: 10.3390/agriculture16121315.

[10] Łuczyński, R., & Karabin-Zych, M. (2024). The issue of inventorying the actual state of the area structure of farms in the process of land consolidation. *GIS Odyssey Journal*, 4(1), 93-106. doi: 10.57599/gisoj.2024.4.1.93.

[11] Rogovskiy, I.L., *et al*. (2020). Research of diagnostic of combine harvesters at levels of hierarchical structure of systems and units of hydraulic system. *Journal of Physics: Conference Series*, 1679, article number 042038. doi: 10.1088/1742-6596/1679/4/042038.

[12] Shamshiri, R.R., Sturm, B., Weltzien, C., Fulton, J., Khosla, R., Schirrmann, M., Raut, S., Basavegowda, D.H., Yamin, M., & Hameed, I.A. (2024). Digitalization of agriculture for sustainable crop production: A use-case review. *Frontiers in Environmental Science*, 12, article number 1375193. doi: 10.3389/fenvs.2024.1375193.

[13] Sobolewska-Mikulska, K., Gołębiewska, B., Bielska, A., Sajnóg, N., Grontkowska, A., & Gębska, M. (2024). Models of farms in spatial terms in sustainable and multifunctional development of rural areas in Poland. *Sustainable Development*, 32(3), 2325-2341. doi: 10.1002/sd.2785.

[14] Szymańska, E.J., Krasnodębski, A., & Bilik, A. (2026). Regional differentiation of precision agriculture in Poland – economic aspects and limitations of its development. *Sustainability*, 18(7), article number 3342. doi: 10.3390/su18073342.

[15] Tomaszewski, L., & Kołakowski, R. (2023). Mobile services for smart agriculture and forestry, biodiversity monitoring, and water management: Challenges for 5G/6G networks. *Telecom*, 4(1), 67-99. doi: 10.3390/telecom4010006.

[16] Wang, H., Lao, L., Zhang, H., Tang, Z., Qian, P., & He, Q. (2025). Structural fault detection and diagnosis for combine harvesters: A review of data-driven methods. *Sensors*, 25(13), article number 3851. doi: 10.3390/s25133851.

[17] Yılmaz, D., & Gökduman, M. (2020). Vibration and noise analysis in agricultural machinery: Effects on sensor accuracy and operational reliability. *Biosystems Engineering*, 197, 45-58. doi: 10.1016/j.biosystemseng.2020.06.012.

[18] Zhang, S., Yang, Z., & Liu, P. (2022). Multi-sensor fusion and intelligent monitoring system for combine harvesters. *Computers and Electronics in Agriculture*, 193, article number 106669. doi: 10.1016/j.compag.2022.106669.

[19] Zhang, S., Zang, C., Yang, Z., Tang, L., Wang, K., Wang, A., Chen, W., Song, Q., & Wei, X. (2025). Research on fault prediction and speed control system for unmanned combine harvesters based on IPSO-SVM and fuzzy logic. *Frontiers in Plant Science*, 16, article number 1577175. doi: 10.3389/fpls.2025.1577175.

[20] Zhang, W., Guo, H., Bo, Z., Liu, S., Zhou, L., Wang, F., Li, Z., & Liu, Y. (2026). Integrated operational monitoring and fault early warning system for wheat combine harvesters based on CAN bus. *International Journal of Agricultural and Biological Engineering*, 19(1), 170-178. doi: 10.25165/j.ijabe.20261901.8941.

Олег Вельгас

Аспірант

Національний університет біоресурсів і природокористування України

03041, вул. Героїв Оборони, 15, м. Київ, Україна

https://orcid.org/0009-0007-8230-6300

Методологічність показників функціональних елементів Smart системи технічного діагностування зернозбиральних комбайнів

Анотація. Актуальність роботи полягає у необхідності підвищення надійності та ефективності експлуатації зернозбиральних комбайнів в умовах значного зношення машинно-тракторного парку та зростання вимог до безперервності збиральних процесів. Метою роботи є підвищення надійності зернозбиральних комбайнів шляхом моделювання та удосконалення функціонування Smart системи технічного діагностування. У дослідженні використано методи математичного моделювання, кореляційно-регресійного аналізу, ортогональних поліномів Чебишева, а також експериментальні спостереження за 23 зернозбиральними комбайнами протягом 3 місяців із застосуванням даних реєструвальної апаратури. У результаті було досліджено залежності між періодичністю технічного діагностування, питомими витратами на обслуговування та показниками надійності комбайнів. Виявлено такі особливості: оптимізація періодичності діагностичних операцій дозволяє одночасно зменшити експлуатаційні витрати та підвищити технічну готовність машин. Було встановлено, що застосування Smart системи діагностування забезпечує більш точне прогнозування технічного стану агрегатів і дозволяє формувати адаптивні режими технічного обслуговування залежно від умов експлуатації. Додатково було проаналізовано вплив функціональних показників і надійності на формування цільової функції оптимізації, а також доведено адекватність побудованих математичних моделей. Було узагальнено, що впровадження системи дозволяє знизити простої техніки, підвищити ефективність сервісного обслуговування та покращити ергономічні умови роботи оператора. Практична цінність роботи полягає у можливості застосування отриманих результатів агропромисловими підприємствами, сервісними організаціями та інженерами для оптимізації технічного обслуговування, підвищення надійності комбайнів і вдосконалення систем Smart діагностування в реальних умовах експлуатації

Ключові слова: технічна діагностика; сільськогосподарська техніка; математичне моделювання; експлуатаційна надійність; прогнозування стану; сервісне обслуговування; ергономіка оператора

Machinery & Energetics
Vol. 17, No. 2. 2026

Journal homepage:
https://technicalscience.com.ua/en

UDC 631.004.01
DOI: 10.31548/machinery/2.2026.7

Oleksandr Shvydun[*]
Postgraduate Student
National University of Life and Environmental Sciences of Ukraine
03041, 15 Heroiv Oborony Str., Kyiv, Ukraine
https://orcid.org/0000-0002-0270-1762

Intelligent system of operating parameters for monitoring the technical condition of combine harvesters

Abstract. The relevance of this study stems from the need to improve real-time monitoring of the technical condition of combine harvesters, given the large number of rapidly changing telemetry parameters and the complexity of processing them promptly. The study aimed to develop and validate, through computational modelling, a method for selecting the minimum sufficient set of rapidly changing diagnostic characteristics of a combine harvester. The method was designed to maximise the entropy-based monitoring completeness index under specified constraints on frequency resolution and the computational speed of telemetry signal-processing algorithms. The research employed methods of systems analysis, information theory, including an entropy-based monitoring completeness index, optimisation, signal spectral analysis, fast Fourier transform, wavelet analysis, and window-function modelling for telemetry data processing. The structure of rapidly changing diagnostic parameters of a combine harvester was examined, and it was established that increasing the number of such parameters did not produce a linear increase in the informativeness of the monitoring system. The greatest improvement in diagnostic completeness was provided by the most informative parameters, particularly vibration characteristics, component temperatures, rotational speed, and hydraulic pressure. The relationship between residual uncertainty and the number of monitored parameters was analysed, revealing a saturation effect whereby each additional feature produced a progressively smaller increase in accuracy. The proposed method made it possible to optimise the selection of diagnostic characteristics while accounting for the requirements of accuracy and real-time data-processing speed. Combining the entropy-based approach with computational complexity criteria was found to reduce the solution space effectively when developing diagnostic algorithms. The practical value of the study lies in the potential application of its findings to the development of intelligent systems for monitoring and diagnosing combine harvesters at service centres and during field operation

Keywords: on-board systems; telemetry parameters; monitoring completeness index; optimisation methods; rapidly changing parameters; real time; diagnostics

INTRODUCTION

The development of modern agro-industrial production is accompanied by the increasing structural complexity of combine harvesters, higher levels of automation, and the integration of electronic on-board systems for monitoring and controlling technological processes. These developments impose increasingly stringent requirements on the quality of technical condition monitoring and diagnostics at different stages of combine harvester operation. Meeting these requirements poses considerable challenges when monitoring the technical condition of on-board combine harvester systems, particularly in real time during harvesting operations. Current developments in systems for monitoring the technical condition of agricultural machinery are characterised by a shift towards intelligent, multi-parameter, and telemetry-based approaches that enable the continuous real-time monitoring of machine operation. H. Wang *et al.* (2025) noted that improving the reliability of combine harvesters requires

Article's History: Received: 23.12.2025; Revised: 30.03.2026; Accepted: 21.05.2026; Published: 29.05.2026.

Suggested Citation:
Shvydun, O. (2026). Intelligent system of operating parameters for monitoring the technical condition of combine harvesters. *Machinery & Energetics,* 17(2), 88-97. doi: 10.31548/machinery/2.2026.7.

*Corresponding author (shvidun22@gmail.com)

the development of structural diagnostic methods and the early detection of failures using sensor-system data. The authors emphasised the difficulty of processing noisy signals and the need to improve the robustness of diagnostic models. W. Zhang *et al.* (2022) examined integrated monitoring systems and demonstrated that consolidating telemetry data within a single platform substantially improves the efficiency of combine harvester maintenance.

S. Li *et al.* (2023) proposed a hybrid PARAFAC-APSO-SVM model for the intelligent diagnosis of faults in complex mechanical systems using multichannel gearbox vibration data. The results showed that the model effectively eliminated redundant information while retaining significant features and enabled the rapid and accurate identification of different fault types. Z.Y. Xu *et al.* (2026) noted that the application of artificial intelligence throughout the combine harvester life cycle can improve data-processing efficiency and enable the prediction of technical condition on the basis of large telemetry datasets. R. Li *et al.* (2022) developed an online monitoring system for the hydraulic actuators of a combine harvester. Using multi-sensor data acquisition, the system monitored operating parameters and issued real-time fault alerts. Field tests showed that the fault-alert accuracy was 96.5%, while automatic diagnosis took no longer than 1 min 18 s. A.E. Chaleshtori & A. Aghaie (2022) emphasised the effectiveness of data-fusion methods in diagnosing complex technical systems, as these methods increase the informativeness of diagnostic parameters and reduce the influence of noise. L. Nadai *et al.* (2020) investigated hybrid ANN–PSO models and demonstrated that combining neural networks with optimisation algorithms can substantially improve the accuracy of technical condition prediction. S. Gawde *et al.* (2022) proposed an intelligent bearing diagnosis method based on CNN-MLP models and established that deep learning was highly effective in detecting complex defects in mechanical systems. J. Shen *et al.* (2023a) examined federated learning for equipment diagnosis and showed that distributed models can protect data while maintaining high diagnostic accuracy.

Z. Qiu *et al.* (2022) developed a remote monitoring system for combine harvesters based on the integration of data from multiple sources. The system enabled technical condition monitoring, fault diagnosis, and remote supervisory control. Tests demonstrated that it identified the operating condition of the combine harvester with an accuracy of 97.46%, confirming the reliability and effectiveness of the proposed system. J. Paredes *et al.* (2025) investigated real-time monitoring of the technical condition of combine harvester on-board systems through the prompt processing of telemetry and diagnostic information received from sensors installed in the engine, hydraulic system, threshing and separating mechanism, cleaning systems, and other functional units of the machine. At the real-time information-processing stage, the following tasks were addressed: ensuring the continuous and safe operation of the combine harvester during harvesting; monitoring the operating parameters of the engine, transmission, hydraulic system, and working mechanisms; and improving harvesting productivity by enabling prompt decisions concerning the technical condition of the machine. The existing approaches to monitoring the technical condition of combine harvester onboard systems examined by J. Shen *et al.* (2023b) did not always provide sufficiently effective fault detection during the operational stage. This limitation arose from the large number of rapidly changing parameters, the restricted time available for processing them, and the difficulty of making prompt diagnostic decisions under field conditions. Research aimed at improving monitoring completeness and the efficiency of real-time telemetry data processing in combine harvesters was therefore relevant and of considerable practical importance for ensuring the reliable and efficient operation of modern agricultural machinery. The study aimed to substantiate and test, through computational modelling, an approach to forming a minimum sufficient set of rapidly changing diagnostic characteristics of a combine harvester. This approach was intended to maximise the entropy-based monitoring completeness index while meeting specified requirements for frequency resolution and the processing speed of telemetry signal-processing algorithms.

MATERIALS AND METHODS

Computational modelling involved fast Fourier transform (FFT), wavelet analysis, informationtheory methods, and methods for optimising the selection of diagnostic features. FFT and wavelet analysis were used to process rapidly changing telemetry signals from the combine harvester, including vibration signals from the engine, threshing drum, cleaning system, straw walker bearings, hydraulic pump, header cutterbar, and transmission. Each signal was processed sequentially in moving time windows. At a sampling frequency of 8 kHz and a window duration of 1 s, each window contained 8,000 samples. To reduce spectral leakage, a rectangular, triangular, Hanning, or Blackman window function was applied to the signal before transformation. The window was selected with regard to its coherent gain and the required frequency resolution. Signal processing was performed in a moving time window, taking account of the sampling frequency and the algorithmic complexity of the calculations. Monitoring completeness was a quantitative indicator describing the extent to which monitoring the technical condition of a combine harvester using a selected set of diagnostic parameters represented the full set of parameters characterising machine operation. The monitoring completeness index was calculated as follows:

$$V = \frac{H^{(n)}}{H}, \tag{1}$$

where H is the initial uncertainty regarding the technical condition of the combine harvester or its onboard systems, expressed as system entropy; $H^{(n)}$ is the uncertainty eliminated on the basis of monitoring and processing diagnostic parameters; n is the number of monitored diagnostic parameters of the combine harvester.

To improve the completeness of technical condition monitoring of combine harvesters during the real-time processing of telemetry and diagnostic information, three approaches were considered: hardware, hardware-software, and software-based. The hardware approach involved expanding the monitoring system by installing additional sensors on the engine, hydraulic system, threshing and separating mechanism, cleaning system, transmission, and other functional units of the combine harvester. In this study, this approach was regarded as a means of increasing the number of monitored parameters. However, the methodology also took account of the fact that adding technical equipment increases the structural complexity of the machine, raises the cost of the monitoring system, and expands the volume of data to be transmitted, stored, and processed. Subsequent assessment therefore focused not only on increasing the number of parameters but also on determining their diagnostic informativeness.

The hardware-software approach involved integrating on-board electronic monitoring systems, telemetry, data transmission, and distributed processing of diagnostic data. Its application made it possible to establish a unified information environment for monitoring the parameters of the engine, threshing and separating system, hydraulic system, transmission, automatic control systems, and sensors. Methodologically, this approach was implemented by defining groups of monitored parameters, diagnostic methods, monitoring intervals, data accumulation periods, and automated workstations for operators and service personnel. By combining these components, a set of possible algorithms for assessing the technical condition of the combine harvester was generated for each diagnostic characteristic. The software-based approach focused on improving the methods used to select, process, and analyse telemetry data without a proportional increase in hardware resources. This approach provided for the combined analysis of slowly varying parameters and rapidly changing parameters, the latter reflecting deviations in the operation of components and assemblies more promptly. Particular attention was paid to rapidly changing characteristics of vibration signals, rotational speed, pressure pulsations, and temperature fluctuations, which were processed in real time. The proposed methodology comprised the development of an information model, entropy-based assessment of uncertainty, spectral signal analysis, optimisation of the set of diagnostic parameters, and evaluation of algorithm accuracy and computational complexity. The study was based on computational modelling and included the mathematical formalisation of the procedure for selecting diagnostic characteristics and algorithms for processing rapidly changing telemetry signals. To test the proposed methodology, a model set of ten characteristics was formed. These characteristics represented the principal functional systems of a combine harvester and were suitable for continuous measurement and spectral analysis. The set of possible algorithms was generated by combining three diagnostic methods, five groups of monitored parameters, five monitoring intervals, and five data accumulation periods. The algorithms were selected sequentially according to their compliance with the specified frequency resolution and their minimum computational complexity. Changes in residual uncertainty and monitoring completeness were then assessed for sets containing 0, 2, 4, 6, 8, and 10 characteristics. A model probability value of 0.97 was used to verify the form of the mathematical relationship rather than as an empirically established measure of diagnostic accuracy.

RESULTS AND DISCUSSION

The selection of informative diagnostic features is a common task in systems designed to detect, classify, and identify the technical condition of machines, processes, and phenomena. Such tasks are difficult to formalise because their solution depends heavily on heuristic methods, operational experience, and accumulated statistical data. This applies to slowly varying parameters, while the real-time processing and analysis of rapidly changing parameters also require consideration of computational capacity, time constraints, and the operating conditions of machinery in the field. The selection of parameters for real-time monitoring therefore depended on the nature and scope of the diagnostic tasks. The same information feature could be highly effective in detecting certain faults but of limited value in identifying others. To process the rapidly changing parameters of a combine harvester in real time, a set of diagnostic parameter characteristics was defined. An analysis of the technical documentation for modern combine harvesters showed that, with approximately 35 rapidly changing parameters, the number of monitored characteristics could exceed 400. Accordingly, the set of characteristics of rapidly changing parameters may be expressed as follows:

$$I = \{i_j \mid j = \overline{1{,}400}\}. \tag{2}$$

However, examining all these characteristics within the scope of the article was impractical. For illustrative purposes, only 10 were selected, forming the following set:

$$I = \{i_{1\ldots10} \mid j = \overline{1{,}10}\}, \tag{3}$$

where i_1 is the maximum value of the amplitude–frequency spectrum of combine harvester engine vibration within the frequency range of 10-250 Hz; i_2 is the maximum vibration spectral density of the threshing drum within the frequency range of 15-180 Hz; i_3 is the maximum value of the amplitude–frequency spectrum of cleaning-system oscillations within the frequency range of 5120 Hz; i_4 is the maximum vibration spectral density of the straw walker bearings within the frequency range of 20-300 Hz; i_5 is the maximum vibration spectral density of the hydraulic pump within the frequency range of 25-400 Hz; i_6 is the maximum fluctuation in threshing-drum rotational speed within the range of 450-1,200 rpm; i_7 is the maximum amplitude of pressure pulsations in the combine harvester hydraulic system within the range of 12-28 MPa; i_8 is the maximum temperature fluctuation in bearing assemblies within the range of 40°C-110°C; i_9 is the maximum vibration spectral density of the header cutterbar within the frequency range of 30-250 Hz; i_{10} is the maximum value of the amplitude–frequency spectrum of combine harvester transmission vibrations within the frequency range of 50-500 Hz.

In addition to these characteristics, it was necessary to account for the heterogeneity of diagnostic information received from the different on-board systems of the combine harvester, as well as the possibility of distributed processing of rapidly changing parameters at different automated workstations used by operators and service personnel. The set of automated workstations was denoted as follows:

$$J=\{j_1, ..., j_7\}. \tag{4}$$

The principal methods for monitoring and diagnosing the technical condition of combine harvesters formed the following set:

$$M=\{m_w \mid w=\overline{1,3}\}, \tag{5}$$

where (m_1) is the visual diagnostic inspection; (m_2) is the instrumental diagnosis using sensor systems; (m_3) is the computer-based diagnosis and analysis of combine harvester operating parameters.

To overcome the limitations associated with the simultaneous monitoring of all combine harvester systems, a local parameter analysis system was incorporated into the technical condition assessment algorithm. The principal groups of monitored parameters were represented by the following set:

$$G=\{g_e \mid e=\overline{1,5}\}, \tag{6}$$

where (g_1) is the engine parameters; (g_2) is the threshing and separating system parameters; (g_3) is the hydraulic system parameters; (g_4) is the transmission parameters; (g_5) is the automatic control system and sensor parameters.

To account for the possibility of periodic monitoring of combine harvester operating parameters, a set of possible monitoring intervals was defined:

$$S=\{a_d \mid d=\overline{1,5}\}, \tag{7}$$

where s_1 is 1 h; s_2 is 2 h; s_3 is 4 h; s_4 is 8 h; s_4 is 12 h.

The possible time intervals for accumulating diagnostic information were represented by the following set:

$$K=\{k_l \mid l=\overline{1,5}\}, \tag{8}$$

where k_1 is the 10 operating hours; k_2 is the 20 operating hours; k_3 is the 30 operating hours; k_4 is the 40 operating hours; k_5 is the 50 operating hours.

The set (A_j) was then considered, each element of which represented an algorithm for processing the technical condition parameter (i_j) of the combine harvester. Each algorithm employed one diagnostic method ($m_w \in M$), one group of monitored parameters ($g_e \in G$), one monitoring interval ($s_d \in S$), and one data accumulation period ($k_l \in K$). This produced the set $A_j=\{a^j_{mgeskz} \mid z=1,375\}$, which comprised the algorithms for assessing the technical condition of the combine harvester on the basis of characteristic (i_j). The set (A_j) was represented by the vector $A^T_{j(375)}$, consisting of 374 zero-valued elements and one unit-valued element. All possible combinations of these vectors formed the identity square matrix $A_{j[375]}$. An algorithm meeting the specified accuracy and processing-speed requirements had to be selected from this matrix $A_{j[375]}$. Initially, those elements a^j_{zz} (z = 1,375) that met the accuracy requirements were selected. The accuracy index for each element was calculated as follows:

$$P=\frac{1}{\frac{\beta f_s}{N \Delta f_{\text{res}}}+1}, \tag{9}$$

where f_s is the signal sampling frequency; N is the number of samples included in the window function; and β is the coherent gain coefficient of the window function, which accounts for the bandwidth characteristics of the selected window. For a rectangular window, $\beta=1$; for a Hanning window, $\beta={}^{0,5}$; for a triangular window, 0.5; and for a Blackman window, $\beta=0.36$. Δf_{res} is the required frequency resolution of the algorithm, corresponding to 10% of the monitored frequency interval. $\Delta f_{res}=0.1(f_1 - f_2)$, (Fig. 1), where f_1 and f_2 are the boundaries of the frequency range within which the characteristic was evaluated.

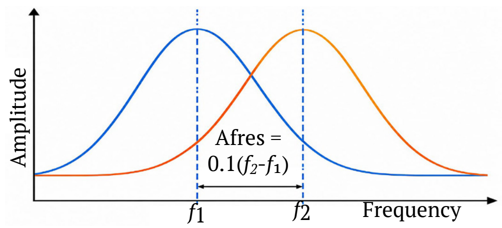

Figure 1. Graphical representation of the minimum required frequency resolution
Source: developed by the author

The accuracy index had the same value for elements a^j_{zz} ($z=\overline{1,375}$) that employed the same method $m_w \in M$ and the same window-function step $s_d \in S$. Accordingly, the rows of the matrix $A_{j[375]}$ formed 15 blocks of 25 values, corresponding to the number of combinations of the elements $m_w \in M$ and $s_d \in S$ used to determine the accuracy index. A specified accuracy threshold therefore made it possible to select several blocks of elements a^j_{zz} ($z=\overline{1,375}$), whose accuracy index exceeded the required value, thereby substantially reducing the matrix $A_{j[375]}$. The next step was to select, from the remaining elements a^j_{zz} ($z=\overline{1,375}$), the one that employed the fastest algorithm for processing the characteristic. The processing-speed index was expressed as follows:

$$B = O(n) = O\left(\frac{Nk}{S}\right), \quad (10)$$

where $O(n)$ is the algorithmic complexity of the selected method for processing rapidly changing parameters.

Algorithmic complexity depends on the number of diagnostic parameter samples N included in the observation window, the width or duration of the window function k, and its step size S. For example, when vibration signals from bearing assemblies, the engine, the threshing drum, or other combine harvester units are analysed, the fast Fourier transform is used for rapid spectral analysis:

$$O(n) = \frac{Nk}{S}\log\left(\frac{Nk}{S}\right), \quad (11)$$

whereas wavelet analysis and other multiscale processing methods have the following complexity:

$$O(n) = \left(\frac{Nk}{S}\right)^2. \quad (12)$$

The number of samples depended on the duration of the observation window and the polling frequency of the sensors in the combine harvester technical condition monitoring system. For example, at a sensor polling frequency of 8~kHz and a time-window width of 1~s, N = 8,000. The processing speed of the diagnostic system therefore directly affected the rate at which faults could be detected and the effectiveness of predicting the technical condition of combine harvester components and assemblies. This procedure was used to select an algorithm for processing one characteristic. The same procedure was then applied to the remaining characteristics of the rapidly changing parameters. As a result, a set of 10 characteristics was formed, each processed using the algorithm with the best processing-speed index among those that satisfied the accuracy requirements. At the second stage, the objective function had to be maximised. In other words, the characteristics that produced the highest monitoring completeness index had to be selected from the 10 rapidly changing parameter characteristics. The objective function was expressed as follows:

$$V = \frac{H_{(n)}}{H} \rightarrow 1. \quad (13)$$

In this formulation, the objective function represents an increase in monitoring completeness through a reduction in the overall uncertainty concerning the technical condition of the combine harvester. The higher the monitoring completeness index, the greater the number of potential faults in components and assemblies that can be detected. This, in turn, reduces the time required to obtain diagnostic results and make decisions concerning machine maintenance or repair. Greater monitoring completeness enables the timely detection of deviations in the operation of the engine, threshing mechanism, cleaning systems, running gear, and other functional systems of the combine harvester. It therefore helps reduce the number of unexpected failures and periods of downtime during the harvesting season, while improving the operational efficiency of the machinery. The uncertainty eliminated through the selected set of monitored parameters of the combine harvester technical condition was expressed as follows:

$$H_{(n)} = H - H_o, \quad (14)$$

where H_o is the uncertainty remaining after the selected set of indicators has been monitored.

The initial uncertainty H was calculated as follows:

$$H = -P\log(P) - (1-P)\log(1-P), \quad (15)$$

where P is the probability that the values of the characteristics $i_j (j = \overline{1,10})$, fall within the informative interval. It was calculated using the following formula:

$$P = 1 - \prod_{j=1}^{10}(1 - \mathrm{p}_j), \quad (16)$$

where p_j is the probability that the measured value of parameter $i_j (j = \overline{1,10})$, falls within the informative interval, which was calculated using the formula:

$$p_j = \frac{\Delta Z_{norm} + \Delta Z_{abn}}{D}, \quad (17)$$

where ΔZ_{norm} is the interval of characteristic values corresponding to the normal operation of the monitored unit. The length of the interval ΔZ_{norm} is represented by the segment |CD|. ΔZ_{abn} is the interval of characteristic values corresponding to abnormal operation. Its length is calculated as the sum of the segments $\Delta Z^-_{abn} = |BC|$ and $\Delta Z^+_{abn} = |DE|$. D is the entire measurement range of the characteristic, represented by the segment $|AF|$ in Figure 2.

The residual uncertainty remaining after monitoring a set of characteristics was calculated as follows:

$$H_o = \prod_{j\in I_n} p_j \left(-\prod_{j\in I_H} p_j \log\left(\prod_{j\in I_H} p_j\right) - \right.$$
$$\left. - \left(1 - \prod_{j\in I_H} p_j\right)\log\left(1 - \prod_{j\in I_H} p_j\right)\right), \quad (18)$$

where I_H is the set of unmonitored characteristics and I_n is the set of monitored characteristics. The union of I_H and I_n forms the set of all characteristics. Taking the above relationships into account, the expression becomes:

$$H_n = H - \prod_{j\in I_n} p_j \left(-\prod_{j\in I_H} p_j \log \prod_{j\in I_H} p_j\right) -$$
$$- \left(1 - \prod_{j\in I_H} p_j\right)\log\left(1 - \prod_{j\in I_H} p_j\right)). \quad (19)$$

The relationship between residual uncertainty and the number of characteristics is shown in Figure 3. The graph was obtained using the following calculations. Ten rapidly changing parameter characteristics $i_j (j = \overline{1,10})$, were considered, and p_j was set at 0.97. Residual uncertainty H_o was then calculated for the following sets of characteristics: when no characteristics were monitored, $H_o = H$, meaning that residual uncertainty was equal to the initial uncertainty; when two characteristics were monitored, $H_o = 0.066$; when four were monitored, $H_o = 0.024$; when six were monitored, $H_o = 0.014$; when eight were monitored, $H_o = 0.010$; and when all ten characteristics were monitored, $H_o = 0.007$.

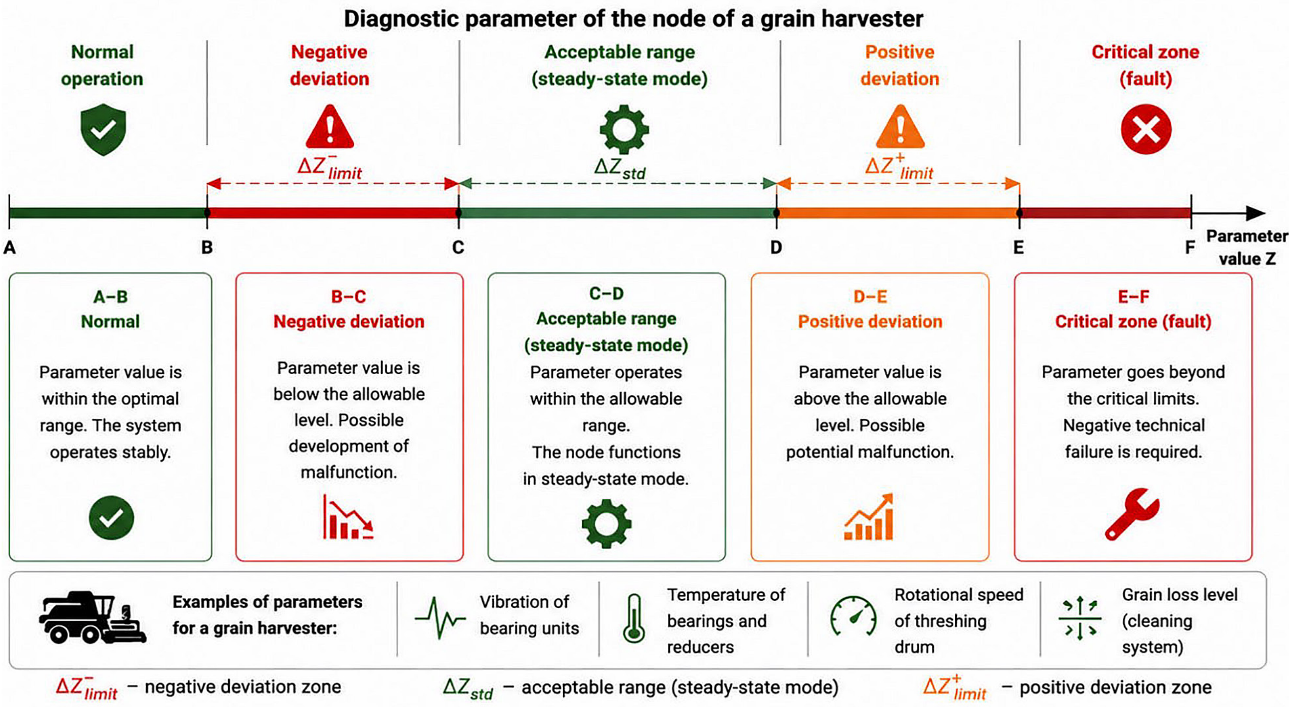

Figure 2. Graphical representation of the informative interval

Note: A-B is the normal operating zone of the unit; B–C is the zone of negative parameter deviations; C-D is the permissible operating range of the parameter; D-E is the zone of positive parameter deviations; and E-F is the critical zone requiring technical intervention

Source: developed by the author

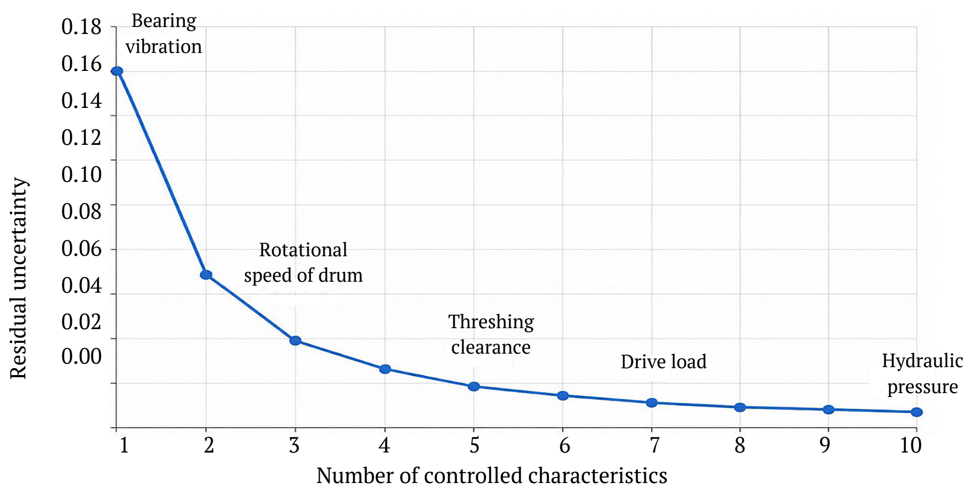

Figure 3. Relationship between residual uncertainty and the number of monitored combine harvester characteristics

Source: developed by the author

Substitution of the corresponding relationships gives the following expression:

$$V = 1 - \frac{\prod_{j \in I_n} p_j \left(-\prod_{j \in I_H} p_j \log\left(\prod_{j \in I_H} p_j\right) - \left(1 - \prod_{j \in I_H} p_j\right) \log\left(1 - \prod_{j \in I_H} p_j\right)\right)}{H}. \quad (20)$$

The completeness index represented the extent to which monitoring the selected set of characteristics reduced the initial uncertainty. When all possible characteristics were monitored, the completeness index was equal to 1 because the residual uncertainty was then 0. When none of the characteristics was monitored, the residual uncertainty was equal to the initial uncertainty and the completeness index, V, was 0. The relationship between monitoring completeness and the number of monitored characteristics is shown in Figure 4.

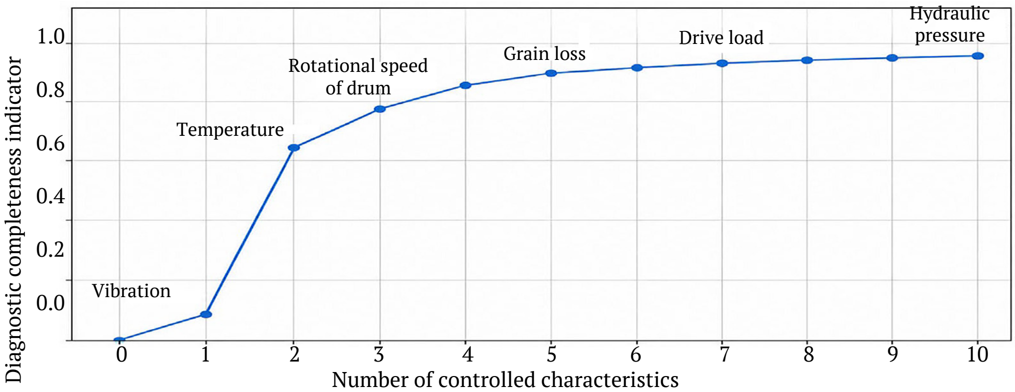

Figure 4. Relationship between the diagnostic completeness index and the number of monitored combine harvester characteristics

Source: developed by the author

In Figure 4, the ordinate represents the completeness index, while the abscissa represents the number of monitored characteristics in the set. The graph was obtained using the following calculations. Ten rapidly changing parameter characteristics $i_j(j=\overline{1,10})$, were considered, and was set at 0.97. The completeness index V was then calculated for the following sets: without monitoring, $V=0$; with two parameters monitored, $V=0.63$; with four parameters monitored, $V=0.86$; with six characteristics monitored, $V=0.92$; with eight characteristics monitored, $V=0.94$; and with all characteristics monitored, $V=1$. The value of the diagnostic completeness index increases along with the number of monitored combine harvester characteristics. The most significant jump was observed upon introduction of the first diagnostic parameters characterising the technical condition of the main components and assemblies of the machine. With an increasing number of parameters, the graph reaches saturation, since the contribution of each additional characteristic to the informational capacity of the monitoring system is lower.

This confirms the possibility of obtaining high diagnostic efficiency if only the most informative parameters are monitored, such as bearing vibration, temperature of the working units, rotational speed of the threshing drum, drive loads, and harvesting process parameters. A non-linear increase in diagnostic completeness and the saturation of the information model, established in this study, is also consistent with the modern trends of intelligent diagnosis of agricultural machines and combines. K. Ofosu-Ampong (2024) states that when applying artificial intelligence methods to the analysis of agricultural machinery operation, there is an almost linear increase in the accuracy of predictions as the amount of initial data increases. This conclusion is relevant to large information systems. The present study, however, showed that real combine harvester on-board systems exhibited a saturation effect: increasing the number of parameters beyond the optimum set did not produce a substantial improvement in the diagnostic completeness index. This finding differed from the results reported by I. Shevchenko *et al.* (2026), which may be explained by limited computational resources and the noisy nature of field data.

H. Wang *et al.* (2025) noted that multi-sensor diagnostic systems substantially improved the accuracy of fault detection in harvesting machinery, particularly when deep-learning methods were applied. The present study likewise found that the addition of key parameters, including vibration, temperature, and rotational speed, increased the informativeness of the system. However, further expansion of the feature set produced progressively smaller gains in efficiency, indicating that the number of sensors should be optimised rather than maximised. In relation to the study of S. Zhang *et al.* (2025), hybrid IPSO-SVM models for fault prediction were considered, confirming that the combination of intelligent algorithms can maintain consistently high accuracy. W. Jiang *et al.* (2023) proposed a method for diagnosing combine harvester bearings that combined self-optimised variational mode decomposition, multiscale dispersion entropy, and a Softmax classifier. Experimental evaluation using vibration signals showed that this approach reliably extracted informative diagnostic features and improved fault-recognition accuracy under complex non-stationary conditions. S. Zang *et al.* (2025), in turn, demonstrated the advantages of multiparameter approaches over single-sensor solutions. W. Zhang *et al.* (2026) showed that CAN bus systems were effective for transmitting diagnostic data in real time. Although their conclusions were valid, they did not account for the optimisation of the information load. G. Yang *et al.* (2022) proposed the SDAE-RCmvMSE method, which combined the denoising of multichannel vibration signals using stacked autoencoders, diagnostic feature extraction based on refined composite multivariate multiscale entropy, and bearing-condition classification using a support vector machine. The technical solutions presented by I. Rogovskii *et al.* (2026) were considered from a different perspective: not as a means of increasing model complexity, but as a problem of optimising the information sufficiency of diagnostic parameters. D. She *et al.* (2024) proposed a few-shot fault-diagnosis method for combine harvester gearboxes based on transfer meta-learning, designed for variable operating conditions and limited training data. Experimental validation showed that combining domain-adaptive feature extraction with loss-function optimisation improved both the accuracy and robustness of gearbox condition recognition. The findings therefore showed that, as the number of monitored characteristics increased, residual uncertainty regarding the technical condition of the combine harvester steadily decreased, while diagnostic completeness increased. The greatest gain in informativeness occurred when the number of characteristics rose from two to four: the completeness index increased from 0.63 to 0.86, while residual uncertainty fell from 0.066 to 0.024. Further expansion of the parameter set produced less pronounced improvements, indicating the gradual saturation of the monitoring system. For practical applications, it is therefore advisable to identify a minimum set of the most informative characteristics that can provide sufficient diagnostic completeness at an acceptable computational cost.

CONCLUSIONS

This study addressed the problem of improving the efficiency of combine harvester technical condition monitoring by optimising the set of rapidly changing telemetry parameters and assessing diagnostic completeness using an entropy-based approach. The proposed methodology formalised the selection of informative features while accounting for computational complexity constraints and the need for rapid real-time data processing. The results showed that, as the number of monitored characteristics increased from 0 to 10, the diagnostic completeness index V rose non-linearly. When two parameters were monitored, $V = 0.63$; with four parameters, $V = 0.86$; with six parameters, $V = 0.92$; with eight parameters, $V = 0.94$; and with the full set of characteristics, it reached its maximum value of $V = 1.0$. This confirmed the presence of an information saturation effect, whereby further expansion of the diagnostic parameter set did not produce a proportional increase in accuracy. Residual uncertainty regarding the technical condition was also found to decrease from approximately $H \approx 0.16$ with the smallest parameter set to $H < 0.01$ when an optimised set of 8-10 characteristics was used. This demonstrated the high efficiency of the selected strategy for optimising diagnostic features. The analysis of algorithmic complexity showed that the use of FFT and wavelet analysis reduced diagnostic signal-processing time compared with multiscale methods that did not include window-function optimisation. The proposed approach therefore achieved a modelled monitoring completeness index of 0.94-1.00 using 8-10 characteristics. Further research should examine the feasibility of developing intelligent real-time monitoring systems for combine harvesters that reduce the risk of critical failures and machinery downtime during harvesting operations.

ACKNOWLEDGEMENTS

The author gratefully acknowledges the administration of the Center for Collective Use of Scientific Equipment from the newest agrotechnologies “Agroindustrial complex, Forestry and Landscape-Park Management, Veterinary Medicine”, for providing the opportunity to conduct this research. The Centre was established at the National University of Life and Environmental Sciences of Ukraine pursuant to Order No. 475 of the Ministry of Education and Science of Ukraine, dated 12 April 2019.

FUNDING

This article was prepared with the support of the HEI-CO-PILOT project under the EIT HEI Initiative “Innovation Capacity Building for Higher Education”, funded by the European Union.

CONFLICT OF INTEREST

None.

REFERENCES

[1] Chaleshtori, A.E., & Aghaie, A. (2022). Data fusion techniques for fault diagnosis of industrial machines: A survey. In *2nd international conference on organizational of production and service systems*. Rasht: University of Guilan. doi: 10.48550/arXiv.2211.09551.

[2] Gawde, S., Patil, S., Kumar, S., Kamat, P., Kotecha, K., & Abraham, A. (2022). Multi-fault diagnosis of industrial rotating machines using data-driven approach: A review of two decades of research. *arXiv*. doi: 10.48550/arXiv.2206.14153.

[3] Jiang, W., Shan, Y., Xue, X., Ma, J., Chen, Z., & Zhang, N. (2023). Fault diagnosis for rolling bearing of combine harvester based on composite-scale-variable dispersion entropy and self-optimization variational mode decomposition algorithm. *Entropy*, 25(8), 1111. doi: 10.3390/e25081111.

[4] Li, R., Cheng, Y., Xu, J., Li, Y., Ding, X., & Zhao, S. (2022). Research on on-line monitoring system of hydraulic actuator of combine harvester. *Processes*, 10(1), 35. doi: 10.3390/pr10010035.

[5] Li, S., Chen, H., Chen, Y., Xiong, Y., & Song, Z. (2023). Hybrid method with parallel-factor theory, a support vector machine, and particle filter optimization for intelligent machinery failure identification. *Machines*, 11(8), article number 837. doi: 10.3390/machines11080837.

[6] Nadai, L., Imre, F., Ardabili, S., Gundoshmian, T.M., Gergo, P., & Mosavi, A. (2020). Performance analysis of combine harvester using hybrid model of artificial neural networks particle swarm optimization. *arXiv*. doi: 10.48550/arXiv.2002.11041.

[7] Ofosu-Ampong, K. (2024). Artificial intelligence research: A review on dominant themes, methods, frameworks and future research directions. *Telematics and Informatics Reports*, 14, article number 100127. doi: 10.1016/j.teler.2024.100127.

[8] Paredes, J., Chávez, D., Isa-Jara, R., & Vargas, D. (2025). A hybrid machine learning algorithm approach to predictive maintenance tasks: A comparison with machine learning algorithms. *Results in Engineering*, 26, article 105137. doi: 10.1016/j.rineng.2025.105137.
[9] Qiu, Z., Shi, G., Zhao, B., Jin, X., & Zhou, L. (2022). Combine harvester remote monitoring system based on multi-source information fusion. *Computers and Electronics in Agriculture*, 194, article number 106771. doi: 10.1016/j.compag.2022.106771.
[10] Rogovskii, I., Krushelnytskyi, V., & Dombrovskyi, M. (2025). Oscillations of heating platform for 3D printing of agricultural drone parts. In *25th International scientific conference engineering for rural development* (pp. 1050-1055). Jelgava: Latvia University of Life Sciences and Technologies. doi: 10.22616/ERDev.2026.25.TF192.
[11] She, D., Yang, Z., Duan, Y., & Pecht, M.G. (2024). A meta transfer learning-driven few-shot fault diagnosis method for combine harvester gearboxes. *Computers and Electronics in Agriculture*, 227, article number 109605. doi: 10.1016/j.compag.2024.109605.
[12] Shen, J., Yang, S., Zhao, C., Ren, X., Zhao, P., Yang, Y., Han, Q., & Wu, S. (2023a). FedLED: Label-free equipment fault diagnosis with vertical federated transfer learning. *arXiv*. doi: 10.48550/arXiv.2312.17451.
[13] Shen, J., Yang, S., Zhao, C., Ren, X., Zhao, P., Yang, Y., Han, Q., & Wu, S. (2023b). FedLED: Label-free equipment fault diagnosis with vertical federated transfer learning. *arXiv*. doi: 10.48550/arXiv.2312.17451.
[14] Shevchenko, I., Golub, G., Tsyvenkova, N., Martynyuk, A., Rogovskii, I., Medvedskyi, O., Kulykivskyi, V., Zayets, M., & Biletskii, V. (2026). Determining design parameters of disk working bodies for overcompacted soils. *Eastern-European Journal of Enterprise Technologies*, 1(1), 105-115. doi: 10.15587/1729-4061.2026.352033.
[15] Wang, H., Lao, L., Zhang, H., Tang, Z., Qian, P., & He, Q. (2025). Structural fault detection and diagnosis for combine harvesters: A critical review. *Sensors*, 25(13), article number 3851. doi: 10.3390/s25133851.
[16] Xu, Z.-Y., Ren, R.-X., Mao, J.-Y., Yu, Y., Chen, J., Lei, Y.-J., Han, L.-L., Fan, W., Chen, C., & Wang, Y. (2026). The application of AI technology across the entire technical chain of combine harvesters: A systematic review. *Agriculture*, 16(9), article number 935. doi: 10.3390/agriculture16090935.
[17] Yang, G., Cheng, Y., Xi, C., Liu, L., & Gan, X. (2022). Combine harvester bearing fault-diagnosis method based on SDAE-RCmvMSE. *Entropy*, 24(8), article number 1139. doi: 10.3390/e24081139.
[18] Zang, S., Zang, C., Yang, Z., Tang, L., Wang, K., Wang, A., Chen, W., Song, Q., & Wei, X. (2025). Research on fault prediction and speed control system for unmanned combine harvesters based on IPSO-SVM and fuzzy logic. *Frontiers in Plant Science*, 16, article number 1577175. doi: 10.3389/fpls.2025.1577175.
[19] Zhang, W., Guo, H., Bo, Z., Liu, S., Zhou, L., Wang, F., Li, Z., & Liu, Y. (2026). Integrated operational monitoring and fault early warning for wheat combine harvesters based on CAN bus. *International Journal of Agricultural and Biological Engineering*, 19(1), 170-178. doi: 10.25165/j.ijabe.20261901.8941.
[20] Zhang, W., Zhao, B., Zhou, L., Wang, J., Niu, K., Wang, F., & Wang, R. (2022). Research on comprehensive operation and maintenance based on the fault diagnosis system of combine harvester. *Agriculture*, 12(6), article number 893. doi: 10.3390/agriculture12060893.

Олександр Швидун
Аспірант
Національний університет біоресурсів і природокористування України
03041, вул. Героїв Оборони, 15, м. Київ, Україна
https://orcid.org/0000-0002-0270-1762

Інтелектуальна система експлуатаційних параметрів контролю технічного стану зернозбиральних комбайнів

Анотація. Актуальність дослідження полягала у необхідності підвищення ефективності моніторингу технічного стану зернозбиральних комбайнів у реальному часі через значну кількість швидкозмінних телеметричних параметрів та складність їх оперативної обробки. Метою роботи було розробити та перевірити шляхом розрахункового моделювання методику вибору мінімально достатнього набору швидкозмінних діагностичних характеристик зернозбирального комбайна, яка забезпечує максимізацію ентропійного показника повноти контролю за заданих обмежень частотної роздільної здатності та обчислювальної оперативності алгоритмів обробки телеметричних сигналів. У дослідженні було використано методи системного аналізу, теорії інформації (ентропійний показник повноти контролю), оптимізації, спектрального аналізу сигналів, швидкого перетворення Фур'є, вейвлет-аналізу та моделювання віконних функцій для обробки телеметричних даних. Було досліджено структуру швидкозмінних діагностичних параметрів зернозбирального комбайна та встановлено, що збільшення їх кількості не лінійно підвищує інформативність системи контролю. Виявлено, що найбільший внесок у підвищення повноти діагностування забезпечували найбільш інформативні параметри, зокрема вібраційні характеристики, температуру вузлів, частоту обертання та гідравлічний тиск. Було проаналізовано залежність залишкової невизначеності від кількості контрольованих параметрів і встановлено ефект насичення, за якого додаткові ознаки давали поступово менший приріст точності. Запропонована методика дозволила оптимізувати вибір діагностичних характеристик з урахуванням вимог точності та оперативності обробки даних у реальному масштабі часу. Було визначено, що комбінування ентропійного підходу та критеріїв обчислювальної складності забезпечувало ефективне скорочення простору рішень при формуванні алгоритмів діагностування. Практична цінність полягала у можливості використання результатів для створення систем інтелектуального моніторингу та діагностики зернозбиральних комбайнів у сервісних центрах та під час польової експлуатації техніки

Ключові слова: бортові системи; телеметричні параметри; показник повноти контролю; методи оптимізації; швидкозмінні параметри; реальний масштаб часу; діагностування

Machinery & Energetics
Vol. 17, No. 2. 2026

Journal homepage:
https://technicalscience.com.ua/en

UDC 631.004.01
DOI: 10.31548/machinery/2.2026.8

Ruslan Shatrov*
Postgraduate Student
National University of Life and Environmental Sciences of Ukraine
03041, 15 Heroiv Oborony Str., Kyiv, Ukraine
https://orcid.org/0000-0001-7469-8657

Analytical structural and energy model of agrotronics for combine harvesting of grain crops

Abstract. The relevance of the study is conditioned by the need to improve the accuracy of reliability assessment and service-life prediction for grain combine harvester components under intensive energy loading and the effects of internal material defects. The purpose of the study was to substantiate and develop an analytical approach to the development of a structural and energy model of agrotronics for combine harvesting of grain crops. The research used methods of structural and energy modelling, probability theory, in particular the Poisson distribution, mathematical modelling of damage accumulation processes, and approaches to non-destructive testing and experimental testing of machine elements. It was established that the process of element failure is determined by energy accumulation and the development of microstructural damage, which allows describing the transition of the system to the limit state through probabilistic dependencies. It was proved that the model parameters (n and α) depend on the size and nature of material defect structures and can change monotonically with their increase. It was shown that the probability of failure-free operation is a function of the energy impact and operating time, which allows predicting the remaining service life of elements. The significant influence of internal material defects on the durability of parts, even under the same external load conditions, has been experimentally confirmed. It was shown that the use of the results of non-destructive testing, in particular tomographic methods, allowed identifying critical parameters of structure defects. It was generalised that the use of the structural and energy approach increases the accuracy of assessing the technical condition and allows considering the microstructural features of materials. The proposed approach can be used to create intelligent systems for predicting failures and maintenance. The practical significance of the study lies in the possibility of applying the results for non-destructive diagnostics, resource forecasting, and improving systems for monitoring the technical condition of combine harvesters

Keywords: reliability of technical systems; combine harvester; microstructural damage to materials; remaining service life forecasting; non-destructive diagnostics; probabilistic failure modelling; energy-based fracture processes

INTRODUCTION

Grain combine harvesters operate as complex agrotronic systems, the effectiveness of which is determined not only by the design features of individual components, but also by the nature of their energy interaction during technological operations. The increase in machine productivity, the intensification of operating modes, and the need to minimise downtime require the use of more advanced approaches to modelling the processes of damage accumulation, estimating the remaining life and predicting when components reach their limit state. Of particular relevance is the use of analytical structural and energy models of agrotronics for combine grain harvesting, which allow comprehensively considering the transformation and distribution of energy flows, the features of loading functional elements, and the influence of structural heterogeneity of materials on the processes of origin and occurrence of fracture.

Recent studies indicate an increase in attention to the use of a structural and energy approach for assessing the reliability of complex technical systems, in particular agrotronic complexes. N. Reznik *et al*. (2025) substantiated

Article's History: Received: 18.12.2025; Revised:12.03.2026; Accepted: 21.05.2026; Published: 29.05.2026.

Suggested Citation:
Shatrov, S. (2026). Analytical structural and energy model of agrotronics for combine harvesting of grain crops. *Machinery & Energetics,* 17(2), 98-107. doi: 10.31548/machinery/2.2026.8.

*Corresponding author (umansky60@gmail.com)

the feasibility of using structural and energy models to describe the processes of degradation of elements of agricultural machinery, showing that failure mechanisms can be represented as the result of energy accumulation in the material under the influence of operational loads. This approach allows moving from a statistical description of failures to an analysis of their physical nature, which is especially important for highly loaded components of grain harvesting equipment.

The physical prerequisites for structural and energy modelling are based on the fundamental provisions of deformable solid mechanics and the law of energy conservation. W. Ahang *et al*. (2024) considered a solid as a system capable of storing external energy, whereas H. Wang *et al*. (2025) showed that the input energy is distributed among different forms of internal energy of the material according to their conversion coefficients. However, W. Zhang *et al*. (2022) noted that the process of energy storage is limited, and exceeding the critical energy level is accompanied by the transition of the material to transition to an unstable state and undergo fracture. Similar conclusions were reached by B. Wang *et al*. (2020), who linked the occurrence of failures to the achievement of a critical internal energy reserve.

The mathematical description of such a process is mainly based on probabilistic models. I.L. Rogovskii (2021) substantiated the existence of a critical number of active quasiparticles required to initiate fracture, whereas J. Shen *et al*. (2023) propose to define the concentration of quasiparticles as a function of the energy load. To describe the random nature of the accumulation of elementary damage, V. Sinitsin *et al*. (2021) applied the Poisson distribution, which helped to obtain analytical dependences of the probability of failure-free operation on the intensity of the energy impact. A similar approach was used by Y. Zhou *et al*. (2023) and X. Zhou *et al*. (2023) for modelling material degradation processes under cyclic loading conditions.

Despite the significant development of structural and energy models, contemporary research has a number of limitations. Most models do not directly use the magnitude of the energy impact, but derived characteristics, in particular, the number of quasiparticles formed, which complicates the practical application of such models when estimating the resource of real technical systems. In addition, conventional statistical methods for evaluating reliability, generalised by Y. Qiao (2021), were based mainly on operational failure statistics and do not consider the physical mechanisms of damage accumulation in the material. This reduces the accuracy of predicting the durability of elements under variable load modes and limits the ability to predict early failures. In this regard, the actual line of further research is the improvement of structural and energy models that directly link the energy parameters of the load with the failure probability of agrotronic systems of combine harvesters.

The purpose of the study was to formulate and substantiate an analytical approach to the development of a structural and energy model of agrotronics for combine harvesting of grain crops.

MATERIALS AND METHODS

The subject of the study was a structural and energy model of agrotronics for combine harvesting of grain crops. The object of research was combine harvesters. The failure process can be considered as the transition of a component from one state to another under the influence of energy loading E. As a result of this effect, active quasiparticles are formed, some of which are absorbed by the sensitive micro-volumes of the element. A schematic representation of this process is shown in Fig. 1. Notation (S_i) determines the i-th state of the element, characterised by the absorption of its sensitive micro-volumes of active quasiparticles, where (i = 0, 1, ..., n). Parameter is used as the transition coefficient of an element from one state to another. The probability of transition between states is determined by the intensity of the energy impact and the number of active quasiparticles absorbed. The accumulation of quasiparticles in sensitive microobjects was accompanied by a gradual change in the physical properties of the element. Reaching the limit state (S_n) corresponded to the occurrence of failure and loss of functionality of the element.

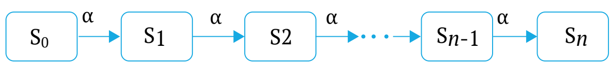

Figure 1. Diagram of failure occurrence (α = const)
Source: developed by the author

Experimental objects were engine turbocharger blades used as samples of highly loaded elements of the power unit. To eliminate ambiguity, the revised text clarifies the connection of these details with the technical systems of combine harvesters. The experimental sample consisted of five types of blades, 15 examples of each type. The tests were carried out under laboratory conditions at room temperature of approximately 20°C on electrodynamic vibration stands according to the first form of bending vibrations. Variable stresses of 16.0, 18.5, 22.0 and 61.5 kgf/mm² were used for individual types of blades. The level of alternating stresses was controlled using strain gauges, and tuning and calibration of strain gauge equipment was performed using a tuning fork-calibration device.

The theoretical basis of the study included the law of conservation of energy, the structural and energy concept of failures, probability theory, Poisson distribution, and mathematical modelling of discrete damage accumulation. Switching an element between states S_0, S_1, ..., S_n was represented by a system of differential equations. Using this system, the probabilities of the element being in working states were determined and dependencies were formed for calculating the probability of failure-free operation and failure. Parameter n characterised the critical amount of elementary damage required for a failure to occur, and the parameter α reflected the efficiency of interaction of the energy effect with defective micro-volumes of the material. The mean value and dispersion of the fracture energy were used to identify the model parameters. The relationships between parameters n and α and the characteristic size of defective structures was analysed using exponential and hyperbolic functions.

RESULTS AND DISCUSSION

The possibility of constructing structural and energy models of failures follows from the physical nature of failures of agrotronics of technical systems. Based on the results of the analytical study by W. Ahang *et al*. (2024), solids exposed to external or internal energy sources (capable of accumulating it, according to H. Wang *et al*. (2025). According to the law of conservation of energy, when an element is affected, the following equality must be fulfilled:

$$E_i = \sum_{j=1}^{n} k_i^j e_j, \tag{1}$$

where E_i – i-th shape of the energy supplied to the element; e_j – j-th form of stored energy element; k_i^j – conversion factor showing the relationship between the energy of the input of i-th form and the stored energy of the j-th form.

As can be seen from equation (1), the relationship between the supplied and stored energy is linear, however, a solid of certain sizes cannot absorb energy indefinitely, i.e., at a certain point there are conditions under which the law of energy accumulation by an element ceases to be observed, which was investigated by S.-C. Tien *et al*. (2022). The moment when such a violation occurs is the element's failure. In other words, with an increase in the stored energy in an element above a certain critical value, its failure occurs, according to the publication of B. Wang *et al*. (2020). This fact allows comparing the probability of element failure as an indicator of reliability from the results of analytical research by Y. Qiao (2021), with the amount of energy supplied, and get the functional dependence $q=f(E)$.

The structural units of an element are atoms, molecules, and ions, so physical and chemical transformations in it, such as breaking, repairing, or forming new bonds, occur at the atomic and molecular level, which was studied by Sinitsin *et al*. (2021). Thus, at the microscopic level, the processes that lead to failures are discrete in nature, according to B. Wang *et al*. (2021). Given that the degrees of freedom of atomic particles in a solid are ordered, according to the findings of H. Wang *et al*. (2025), various processes that occur in a solid can be described in statistical physics using the concept of quasiparticles (Nadai *et al*., 2020), characterised by certain energy states. Thus, the process of failure can be considered as the passage of active quasiparticles through a potential energy barrier, according to J. Shen *et al*. (2023), as a result of which quasiparticles are excluded from the process, expending energy to overcome the forces of structural interaction and causing the failure of the element studied by Y. Zhou *et al*. (2023). Therefore, for the occurrence of failure, it is necessary to absorb quasiparticles by certain micro-volumes of the element, according to the results of studies by X. Qiu *et al*. (2020).

Consequently, sensitive microobjects have a catalytic effect on the processes of failure occurrence, that is, for the failure of an element, it is necessary for them to absorb the critical value of n quasiparticles, according to the results of the analytical study by I.L. Rogovskii (2021). To formulate the problem of mathematically describing the energy effects on components, the following conditions were used based on the findings of L. Nadai *et al.* (2020). Let a set consisting of N elements, each of which contains $m \geqslant 1$ sensitive microvolumes that are identical in shape, size and arrangement, be subjected to an energy input E. As a result of this effect, quasiparticles appear in the element, the number of which per unit of the characteristic size of the element is equal to: $\varepsilon = kE$, where k – conversion factor, according to publication by J. Shen *et al*. (2023). Quasiparticles can be randomly absorbed by sensitive microobjects, causing a certain probability of failure of the element q, which is the inverse of the probability of failure-free operation P. It is necessary to determine the pattern of element failures if the magnitude of the energy impact E, the number t, and the size ϑ of sensitive micro-volumes, according to the results of research by Y. Zhou *et al*. (2023):

$$q = f(E, m, \vartheta) = 1 - P. \tag{2}$$

Assuming that the absorption of one quasiparticle is equivalent to the occurrence of one damage in an element, then the equation of the processes of occurrence of failures of elements, as the process of energy accumulation by sensitive micro-volumes to a certain value, and the process of accumulation of elementary damage that occurs in sensitive micro-volumes of elements as a result of energy influence on them, according to the analytical research by X. Zhou *et al*. (2023).

Considering the fact that the absorption process of active quasiparticles is discrete in nature, the solution to this problem can be reduced to the following, according to W. Ahang *et al*. (2024). Let the absorption events of active quasiparticles or the occurrence of elementary damage in sensitive micro-volumes of elements as a result of energy on them occur randomly and independently of each other. The probability that exactly (i) active quasiparticles are absorbed in the sensitive microvolume or that exactly (i) elementary defects are generated can then be described by a Poisson distribution with mean value $P=\Theta G=\vartheta ke$:

$$P[i] = \frac{(\vartheta\varepsilon)^i \exp(-\vartheta\varepsilon)}{i!}, \tag{2}$$

where $P[i]$ – probability of the sensitive microvolume of the element absorbing exactly (i) active quasi-particles (the probability of exactly (i) elementary defects occurring).

Since failure occurs as a result of the absorption of active quasi-particles (the formation of elementary defects), the equation for determining the failure-free operating time of the component assumes $i=n-1$. Thus, the equation of failure-free operation depending on the energy impact, without considering the time factor, will have the form:

$$P(\varepsilon) = \exp(-\vartheta\varepsilon) \sum_{i=0}^{n-1} \frac{(\vartheta\varepsilon)^i}{i!}, \tag{3}$$

However, it cannot be argued that any absorption of an active quasiparticle will be effective, i.e., be sure to cause damage. Therefore, instead of the geometric size 3 of the sensitive micro-volume, it is necessary to consider the effective size of IFEF = IFR, where I – probability that the absorption event of the active quasiparticle will be effective. Then equation (2.3) should be written as:

$$P(\varepsilon) = \exp\left(-\vartheta_{ef}\varepsilon\right) \sum_{i=0}^{n-1} \frac{\left(\vartheta_{ef}\varepsilon\right)^i}{i!}, \tag{4}$$

The disadvantage of the presented model is that the magnitude of the energy impact on the elements is not given explicitly, but by the number of quasiparticles that arise in the element as a result of the energy impact on it, which makes it difficult to use it in practice. Using statistical methods, it is impossible to explain the nature of development and the onset of destruction in elements, which casts doubt on the objectivity of such an assessment. Furthermore, the failure rate figures used in the calculation presented here are obtained by testing a small batch of samples, and only subsequently, under operating conditions, by collecting data on failure modes, which may lead not only to the failure of individual components but also to damage to the entire engine structure. Therefore, increasing the accuracy in the process of calculating the reliability of aircraft engines requires the use of promising evaluation methods using innovative technologies.

A system of differential equations for the probabilities of states P_i, which corresponds to Figure 1, has the form:

$$\frac{dP_0(E)}{dE} = -\alpha P_0(E), \tag{5}$$

$$\frac{dP_1(E)}{dE} = \alpha P_0(E) - \alpha P_1(E), \tag{6}$$

$$\frac{dP_i(E)}{dE} = \alpha P_{n-1}(E) - \alpha P_i(E). \tag{7}$$

Solving this system of equations under initial conditions $R_0(0) = 1$ and $P_i(0) = 0$ when $i = 0$, the following obtained:

$$P_0(E) = exp(-\alpha E),$$

$$P_1(E) = \alpha E exp(-\alpha E), \tag{8}$$

$$P_i(E) = \frac{(\alpha E)^i}{i!} \exp(-\alpha E). \tag{9}$$

Since the failure of an element requires the absorption of active quasiparticles or the occurrence of elementary damage n, the probabilities $P_0(E), P_1(E), \ldots, P_{n-1}(E)$ will characterise the operating states of the element.

Therefore, the possibility of trouble-free operation of the element will be determined by the following equation:

$$P(E) = \sum_{i=0}^{n-1} P_i(E) = \exp(-\alpha E) \sum_{i=0}^{n-1} \frac{(\alpha E)^i}{i!}. \tag{10}$$

Given (10), the expression for the probability of failure will have the form:

$$q(E) = 1 - \exp(-\alpha E) \sum_{i=0}^{n-1} \frac{(\alpha E)^i}{i!}. \tag{11}$$

The failure model given by equation (11) does not explicitly contain the structural parameters of the element (the number and size of sensitive micro-cavities). These parameters are considered by the transition coefficient A, which, based on equations (4) and (10), characterise the size of the sensitive micro-cavity of the element and the efficiency of the absorption event of the active quasiparticle $\alpha = \vartheta_{ef} = \vartheta P$. The proposed structural and energy model of agrotronics (11) is based on the fundamental assumption that the failure of an element is a consequence of the accumulation of energy in its material structure and the achievement of a critical level of internal damage. In this context, external energy influence E is interpreted as a control parameter that determines the intensity of generation of microscopic disturbances in the element material. According to the energy concept, the supplied energy is not evenly distributed, but is localised in the form of discrete energy portions — quasiparticles that interact with structural inhomogeneities of the material. It is these interactions that lead to the occurrence of elementary damage. Thus, the transition from an energy description to a structural one is carried out through the interpretation of quasiparticles as carriers of micro-damage.

Analytical dependence $\varepsilon = kE$ formalises the relationship between the macroscopic energy load and the microscopic intensity of quasiparticle occurrence. Coefficient k in this case reflects the physical and structural properties of the material, which determine the efficiency of energy conversion into defects. In addition, the failure process is considered as a stochastic process of damage accumulation in sensitive microobjects, each of which has a discrete probability of quasiparticle absorption. This allows proceeding to a statistical description of the system, where the state of the element is determined by the number of absorbed quasiparticles and the corresponding level of structural degradation.

Probability of failure-free operation P in this approach is interpreted as the probability that none of the sensitive microobjects reached the critical value of accumulated damage n. Accordingly, the probability of failure $q = 1 - P$ describes the achievement of a critical energy and structural state at which the system loses its functionality. Parameter n in the structural and energy model has the physical meaning of the critical amount of elementary damage required to initiate failure, whereas the parameter α is interpreted as an integral characteristic of the efficiency of interaction of quasiparticles with the defective structure of the material, which is determined by the size and concentration of sensitive microobjects. Therefore, the transition from the energy model to the analytical description is carried out through a sequence of physically justified steps: energy → quasiparticles → micro-damage → stochastic states → probability of failure, which ensures consistency between the physical nature of the degradation process and the mathematical apparatus of the model.

As a characteristic of the fracture energy distribution function, the concept of relative steepness S was introduced, by which the equation is interpreted:

$$S = \frac{\bar{E}^2}{\sigma_{\bar{E}}^2}. \tag{12}$$

where $\bar{E}$ – average value of the energy of destruction of elements, J·h/mm³; σ_E – dispersion of the fracture energy, J·h/mm³.

The relative steepness S determines the nature of the dependence of the probability of failure on the magnitude of the energy impact. Namely, the steeper the curve, the greater the value of S. According to equation (2), the value of N, the number of elementary damage events that cause failure, is at least not less than S. From this condition, and considering the fact that $N = \alpha$E, the equation for determining another parameter of the model was determined:

$$n = \frac{\bar{E}^2}{\sigma_{\bar{E}}^2}; \quad \alpha = \frac{n}{\bar{E}} = \frac{\bar{E}}{\sigma_{\bar{E}}^2}. \tag{13}$$

Thus, using equation (13) to determine the parameters P and α, it becomes possible to calculate the reliability of elements based on data obtained during experimental tests with a given energy effect. However, for the practical value of the structural and energy theory of failures, it is necessary to determine the regularities of changes in the parameters P and α depending on the size of defective (sensitive) structures of element materials, because in this case it becomes possible to evaluate the reliability and predict the durability of elements using the results of non-destructive testing. The average value and dispersion of the fracture energy are monotonically decreasing functions of the size of defective structures of materials. From the class of monotonically decreasing functions, exponential and hyperbolic functions are most widely used in practice, so to establish possible patterns of changes in the parameters n and α of the structural and energy failure model depending on the size of defective structures, it is enough to focus on these two types of functions.

The following section examines some possible cases of dependence of the average value and the average square deviation of the fracture energy on the value of the characteristic size l, mm³, and defective structures of element materials.

1. Dependencies of the average value $\bar{E}$ and the mean square deviation of the fracture energy are defined by the following expressions:

$$\bar{E} = K_1 \exp\left(-\left[\frac{l}{L}\right]^b\right); \tag{14}$$

$$\sigma_E = K_2 \exp\left(-\left[\frac{l}{L}\right]^c\right). \tag{15}$$

where K_1 – material tensile strength, J/mm³; K_2 – material yield strength, J/mm³; L – characteristic size of the element material, mm³.

Substituting (14) and (15) into equations (13), the following expressions for the parameters of the structural-energy failure model are obtained:

$$n = \frac{\bar{E}^2}{\sigma_{\bar{E}}^2} = \frac{\left\{K_1 \exp\left(-\left[\frac{l}{L}\right]^b\right)\right\}^2}{\left\{K_2 \exp\left(-\left[\frac{l}{L}\right]^c\right)\right\}^2} = \left(\frac{K_1}{K_2}\right)^2 \exp 2\left[-\left(\frac{l}{L}\right)^b + \left(\frac{l}{L}\right)^c\right]; \tag{16}$$

$$\alpha = \frac{\bar{E}}{\sigma_{\varepsilon}^2} = \frac{\left\{K_1 \exp\left(-\left[\frac{l}{L}\right]^b\right)\right\}}{\left\{K_2 \exp\left(-\left[\frac{l}{L}\right]^c\right)\right\}^2} = \left(\frac{K_1}{K_2^2}\right)^2 \exp\left[-\left(\frac{l}{L}\right)^b + 2\left(\frac{l}{L}\right)^c\right]. \tag{17}$$

2. Dependences of the average value and the average square deviation of the fracture energy from the value of the characteristic size of defective structures of element materials are given by the equation:

$$\bar{E} = \frac{K_3}{\left(\frac{l}{L}\right)^b}; \tag{18}$$

$$\sigma_E = \frac{K_4}{\left(\frac{l}{L}\right)^c}, \tag{19}$$

where K_3 – material ultimate strength, J/mm³; K_4 – yield strength in the case of static load and endurance limit in the case of cyclic load, J/mm³.

Then the parameters n and α of the structural and energy failure model will be determined by the equations:

$$n = \frac{\bar{E}^2}{\sigma_{\bar{E}}^2} = \frac{K_3^2\left(\frac{l}{L}\right)^{2b}}{K_4^2/\left(\frac{l}{L}\right)^{2c}} = \left(\frac{K_3^2}{K_4^2}\right)\left(\frac{l}{L}\right)^{2c-2b}; \tag{20}$$

$$\alpha = \frac{\bar{E}}{\sigma_{\varepsilon}^2} = \frac{K_3 \;/\left(\frac{l}{L}\right)^b}{K_4^2/\left(\frac{l}{L}\right)^{2c}} = \frac{K_3}{K_4^2}\left(\frac{l}{L}\right)^{2c-b}. \tag{21}$$

3. Dependence of the average value of the fracture energy on the value of the characteristic size of defective structures of element materials was given by equation (14), and the root-mean-square deviation is given by equation (19). In this case, the parameters of the structural and energy failure model will be determined by the equations:

$$n = \frac{\bar{E}^2}{\sigma_{\bar{E}}^2} = \frac{\left\{K_1 \exp\left(-\left[\frac{l}{L}\right]^b\right)\right\}^2}{\left[K_4/\left(\frac{l}{L}\right)^c\right]^2} = \left(\frac{K_1}{K_4}\right)^2 \left(\frac{l}{L}\right)^{2c} \exp\left[-2\left(\frac{l}{L}\right)^b\right]; \tag{22}$$

$$\alpha = \frac{\bar{E}}{\sigma_{\bar{E}}^2} = \frac{K_1 \exp\left[-\left(\frac{l}{L}\right)^b\right]}{\left[K_4/\left(\frac{l}{L}\right)^c\right]^2} = \frac{K_1}{K_4^2}\left(\frac{l}{L}\right)^{2c} \exp\left[-\left(\frac{l}{L}\right)^b\right]. \tag{23}$$

4. Dependence of the average value of the fracture energy on the value of the characteristic size of defective structures of element materials is given by equation (18), and the root-mean-square deviation is given by equation (13).

In this case, the expressions for defining the parameters p_0 and α will have the form:

$$n = \frac{\bar{E}^2}{\sigma_{\bar{E}}^2} = \frac{\left[K_3/\left(\frac{l}{L}\right)^b\right]^2}{\left\{K_2 \exp\left[-\left[\frac{l}{L}\right]^c\right]\right\}^2} = \left(\frac{K_3}{K_2}\right)^2 \left(\frac{l}{L}\right)^{-2b} \exp 2\left(\frac{l}{L}\right)^c; \tag{24}$$

$$\alpha = \frac{\bar{E}}{\sigma_{\bar{E}}^2} = \frac{K_3/\left(\frac{l}{L}\right)^b}{\left\{K_2 \exp\left[-\left(\frac{l}{L}\right)^c\right]\right\}^2} = \frac{K_3}{K_2^2}\left(\frac{l}{L}\right)^{-b} \exp 2\left(\frac{l}{L}\right)^c. \tag{25}$$

Analysis of equations (16), (17), and (20)-(25) shows that, depending on the values of indicators b and c, the following regularities of changes in the parameters of the structural and energy failure model are possible:

1. n and α – monotonically increasing functions of the dimensions of defective (sensitive) structures of element m;

2. n and α – monotonically decreasing functions of the dimensions of defective (sensitive) structures of materials;

3. n = const; α – monotonically increasing function of the size of defective (sensitive) structures. These patterns are obtained if equations (16), (17) and (20), (21) have b = c = d.

Then:

$$n = \left(\frac{K_1}{K_2}\right)^2 = const; \quad \alpha = \frac{K_1}{K_2^2}\exp\left(\frac{l}{L}\right)^d, \tag{26}$$

– for the exponential law of change of the mean value and the mean square deviation of the fracture energy and:

$$n = \left(\frac{K_3}{K_4}\right)^2 = const; \quad \alpha = \frac{K_3}{K_4^2}\exp\left(\frac{l}{L}\right)^d, \tag{27}$$

– for hyperbolic dependence.

4. n_0 = const; α = const. This case will be for b = c = 0 in equations (16), (17), and (20) - (25). However, the simultaneous constancy of the parameters n and α is almost unlikely. This follows at least from the fact that for b = c = 0, as can be seen from equations (14), (15) and (18), (19), the mean value and the mean square deviation of the fracture energy must be constant values, but this is possible only if there are no defects in the materials of the elements, i.e., if $m = 0$, or if the number of microscopic defects tends to infinity.

Thus, first of all, the first three possible patterns of changes in the parameters of the structural energy failure model are subject to understanding and explanation. When considering a batch of elements of the same type, the materials of which contain defective structures of the same size, the first and third types of patterns of changes in model parameters within the framework of the structural and energy concept of reliability can be explained as follows.

The constancy of parameter n means that the absorption of one quasiparticle corresponds to the appearance of one damage in the element material, and since the critical number of damage causing element failure is a constant value for the given material, the number of absorbed quasiparticles, i.e., the parameter n must also be a constant value. An increase in the parameter n indicates that the efficiency of absorbed quasiparticles decreases with increasing size of defective structures of materials, that is, one damage in the element material is caused not by one quasiparticle, but by several. But since the critical number of damages, as in the first case, remains the same, the number of absorbed quasiparticles must increase. As for the parameter α, in both cases it must be an increasing function of the size of the defective structures, since it is a measure of the value of the characteristic size of the defective structure of the material.

The second type of pattern, that is, a decrease in the parameters n and with an increase in the size of defective structures of materials can be observed only in cases where the batch of elements is inhomogeneous, i.e., it consists of elements whose materials have different sizes of defective structures. It follows from this that in practice three types of regularities of changes in the parameters of the structural and energy failure model can be observed, and by the type of pattern observed, it is possible to judge the mechanism of energy influence and the degree of uniformity of the batch of elements. It is equally important that the presence of certain patterns of changes in model parameters allows developing a methodology for evaluating, and most importantly predicting reliability and determining the critical dimensions of defective structures of materials that provide a given level of reliability of elements in specific operating conditions. After determining the parameters n and α of the structural and energy failure theory based on internal defects contained in the material, it becomes possible to determine the dependence of the probability of trouble-free operation on the operating time under a given energy influence.

From the condition $E = I{\cdot}t$, where I – intensity of the energy impact, J/mm^3, t – operating time of the element, h, using equation (5):

$$P(t) = \exp(-\alpha I t)\sum_{i=0}^{n-1}\frac{(\alpha I t)^i}{i!}, \tag{28}$$

or, considering the sensitivity threshold by the equation:

$$P(t) = \exp[-\alpha I(t - t_0)]\sum_{i=0}^{n-1}\frac{[\alpha I(t-t_0)^i]}{i!}. \tag{29}$$

for $t > t_0$ plot the graphs showing how the probability of failure-free operation, $P(t)$, varies with time when $I = const$ for different values of α_i, Figure 2.

Given the required reliability levels of the components $P(t)$ during operation, using the graph shown in Figure 2, determine the corresponding maximum mean time between failures for a fixed value of the parameter α. Or calculate the reliability indicator by setting the required operating time of the element. Thus, the structural and energy theory of failures allows both determining the reliability and predicting the number of hours of operating time of the element at a given level of trouble-free operation, based on the determination of internal defects in the element material by means of non-destructive testing. To obtain accurate data on internal deviations in the product, tomography should be used as the most advanced method of non-destructive testing.

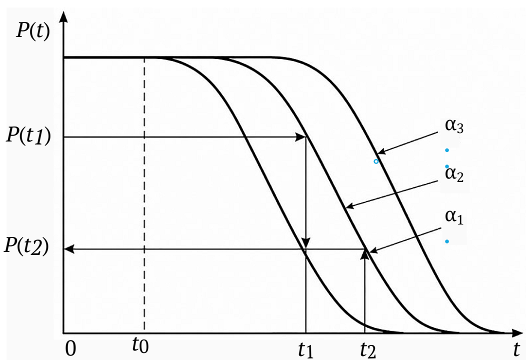

Figure 2. Function $P(t)$ for different parameter values α at T = const

Source: developed by the authorr

To implement the structural and energy theory in practice, it is necessary to determine the operating time to the destruction of the blades under a given load in order to determine the indicators of the material n and a, which characterise the dimensions V and the number m of sensitive micro-volumes of the element material and the number of elementary damages necessary for the onset of failure. Destructive tests of the engine's turbocharger blades were carried out on electrodynamic vibration stands of the first form of bending vibrations, at room temperature (~20°C). Before testing, the blades were prepared with strain gauges, which were used to set and control the AC voltage level. Adjustment and calibration of strain gauges was carried out using a tuning fork-calibration device. The blades were tested for 108 cycles, the remaining for 2,107 cycles, which is approximately 2,800 and 560 hours. The loads during the tests are shown in Table 1. The results of operating time before the destruction of the tested blades are presented in Table 2.

Table 1. Values of blade loads during testing

Blade type	Load kgf/mm^2
1	18.5
2	22
3	16
4	61.5
5	61.5

Source: developed by the author

Table 2. Operating time of the blades to destruction at specified loads

No. of blade	Operating time of the blades before destruction, h				
	1	2	3	4	5
1	5,254	4,838	2,641	2,053	1,617
2	1,108	2,777	3,963	8,139	8,781
3	963	5,444	3,983	9,652	4,361
4	763	2,183	1,628	1,111	8,227
5	1,111	2,105	3,986	1,513	6,060
6	1,750	1,965	3,697	1,724	8,714
7	1,666	2,100	3,619	1,596	9,025
8	5,555	2,073	3,158	1,389	1,072
9	4,222	2,349	3,061	2,151	7,951
10	3,194	5,039	2,988	1,100	3,469
11	3,916	2,537	2,497	2,079	1,954
12	5,176	2,752	1,138	1,957	9,538
13	5,475	3,978	3,852	1,110	8,367
14	5,447	1,503	3,933	3,444	7,448
15	5,333	5,138	3,369	6,713	8,715

Source: developed by the author

The durability of the elements under the same load conditions differed hundreds of times, which indicates the decisive influence of internal defects in the material. For example, for restored 5-th type blades, the time to destruction varied from 60.6 hours to 10,727.8 hours, that is, almost 177 times. Undoubtedly, the restored blades are subjected to lower loads during operation than the new ones, but for the clarity of experiments and calculations, the same test and operation modes were adopted for them. The tests were conducted on resources up to 10^8 and 2×10^7 cycles, which corresponds to approximately 28,000 hours and 5,600 hours of operation, respectively. The results obtained confirmed that consideration of the internal structure of the material allows not only to assess the reliability of elements, but also to predict their durability based on the structural and energy model.

As can be seen from the conducted tests (Table 2), the operating time of different blades may differ significantly, despite the same loads, materials, geometry, and manufacturing method. Moreover, blades that have not yet been in operation can withstand loads for a longer time than the same load of the same type, but restored. Since all experiments were conducted under the same external conditions, the results obtained can only be explained by the difference in the internal structure of materials, namely the different content of internal defects and the presence of internal deviations.

In conclusion, it should be emphasised once again that insufficient attention is paid to controlling the internal structure of element materials. Moreover, based on the conducted experimental tests, it follows that the state of the material of the studied elements of combine harvesters is a parameter that must be considered first of all when assessing reliability. The results obtained showed a significant change in the durability of elements even under identical load conditions, geometry, and materials. In particular, resource differences of hundreds of times were recorded, which indicates the determining influence of the internal structure of the material on the processes of damage accumulation and failure.

Within the proposed structural and energy model, this variation is explained by the inhomogeneity of the energy capacity of the material due to different densities, sizes, and spatial distribution of defective zones. It is these structural features that determine the local conditions of energy storage and the intensity of micro-damage occurrence under cyclic loading. Accordingly, the model parameters n, α, and ϑ acquire individual values for each element, reflecting its actual structural and energy state.

Special attention should be paid to the difference between new and restored blades. Within the model, the reduced elements are characterised by an increased probability of hidden defects, microcracks, and zones of local degradation of the material, which leads to a change in the efficiency of energy absorption by quasiparticles. This, in turn, increases the speed of reaching a critical state and increases the probability of system failure. Thus, the decrease in the resource of recovered elements is determined not only by the operational history, but primarily by changes in the structural and energy parameters of the material.

Experimental load modes (10^8 and 2×10^7 cycles corresponding to different equivalent operating time intervals) are interpreted in the model as a discrete cumulative energy effect. Each load cycle is considered as an elementary act of energy supply, which leads to a gradual accumulation of micro-damage in accordance with the stochastic mechanism laid down in the structural and energy theory of failures.

The obtained experimental data are not isolated observations, but directly confirm the position of the structural and energy model. The observed change in durability is a consequence of the implementation of a stochastic process of energy accumulation and damage occurrence in the material, which ensures the physical validity of the proposed approach and confirms its suitability for predicting the resource of elements of combine harvesters.

DISCUSSION

The results of structural and energy modelling of failures obtained in this study show that the reliability of elements of combine harvesters is determined primarily by the internal structural state of the material and the processes of energy accumulation in microdefect zones. A similar emphasis on the role of structural defects in failure formation can also be traced in the study by H. Wang *et al*. (2025), where the mechanisms of structural degradation and diagnostics of combine harvester systems were considered. However, the above analysis showed a different picture: in contrast to the purely diagnostic approach of H. Wang *et al*. (2025), in the proposed model, the physical failure process is described as a stochastic mechanism for energy transition to micro-damage, which allows not only to fix the defect according to A. Eshaghi & A. Aghaie (2022), but also to predict its evolution over time. Thus, the coincidence is observed in the interpretation of the role of defects, while the difference lies in the level of formalisation of the failure process.

W. Zhang *et al*. (2022) and S. Zhang *et al*. (2025) and the main focus is on building failure prediction systems based on multiparametric data and machine learning algorithms for technical condition monitoring. The conclusions made by the researchers are quite appropriate, since they confirm the possibility of effective detection of degradation processes in real time. Nevertheless, the approaches proposed by Z.Y. Xu *et al.* (2024) are predominantly empirical and do not consider the physical nature of damage accumulation. The technical solutions proposed by X. Zhou *et al.* (2023), and in light of the findings of this study, can be viewed from a different perspective – as an example of an external interpretation of the system's state, which could be supplemented by the proposed structural and energy model to enhance the physical validity of the predictions.

V. Sinitsin *et al*. (2021) proposed combined diagnostic models based on neural networks that can improve the accuracy of fault classification. However, the statement of X. Zhou *et al*. (2023) seem controversial because such approaches do not provide a direct link between the structural characteristics of the material and the probability of failure according to Y. Liu & H. Zhang (2022), because they are limited to processing state signals. This is not consistent with the results of the above analysis, because in the proposed model, failure is a consequence of a physically interpreted process of energy accumulation and the occurrence of micro-damage, which allows moving from a correlation to a causal description of degradation according to S. Zhang *et al*. (2023).

Thus, it can be concluded that existing approaches to the diagnosis and prediction of failures are mainly based on statistical or data-driven models, while the proposed structural and energy concept provides a physically sound mechanism for the occurrence of failures. This allows the results obtained to be regarded as a development of existing methods, aimed at their physical interpretation and at improving their predictive power.

CONCLUSIONS

The paper developed a structural and energy approach to modelling failures of combine elements, which was based on the formalisation of energy storage processes and its transformation into microstructural damage to the material. The key parameters of the model were the critical amount of damage n, energy impact efficiency coefficient α, and the characteristic size of sensitive micro-volumes ϑ, defining the conditions under which an element transitions from an operational state to failure.

It was established that the probability of trouble-free operation of elements is determined by the functional dependence on the energy impact and operating time through the parameters n, and α. In this case, the nature of changes in the model parameters relative to the size of defective material structures can be classified as monotonically increasing, monotonically decreasing, or combined, which is determined by the type of fracture energy distribution and the assumption of uniformity of the internal structure of the material.

It was shown that the proposed model allows interpreting failure as a stochastic process of accumulation of micro-damage, where each load cycle is considered as an elementary act of energy impact, which leads to a discrete increase in the level of material degradation. This provided a transition from an empirical description of reliability to a physically valid causal model of degradation. The practical implementation of the approach consists in using non-destructive testing data to estimate the parameters of the internal structure of the material, in particular, the size and distribution of defective zones. The obtained characteristics were directly used to identify parameters n, α, and ϑ, which allowed quantifying the probability of failure-free operation and predicting the remaining resource of elements. It was established that a significant change in the durability of elements under the same external load conditions is explained by the statistical heterogeneity of the internal structure of the material and the different ability of defective zones to store energy. This confirmed that the main factor in the resource spread is not the operating conditions, but the microstructural features of the material.

The prospects for further research are experimental verification of the proposed structural and energy model on elements of combine harvesters, integration of non-destructive testing methods to identify its parameters, and development of algorithms for predicting the remaining resource in real operating conditions.

ACKNOWLEDGEMENTS

The author expresses gratitude to the administration of the Centre for Collective Use of Scientific Equipment for Advanced Agricultural Technologies, "Agro-Industrial Complex, Forestry and Landscape Gardening, Veterinary Medicine," established at the National University of Life and Environmental Sciences of Ukraine pursuant to Order No. 475 of the Ministry of Education and Science of Ukraine dated 12 April 2019, for the opportunity to conduct the research.

FUNDING

This paper was supported by the HEI-COPILOT project within the EIT HEI Initiative "Innovation Capacity Building for Higher Education", funded by the European Union.

CONFLICT OF INTEREST

None.

REFERENCES

[1] Ahang, W., Guo, H., Zhao, B., Liu, S., Zhou, L., Wang, F., Li, Z., & Liu, Y. (2026). Integrated operational monitoring and fault early warning system for wheat combine harvesters based on CAN bus. *International Journal of Agricultural and Biological Engineering*, 19(1), 170-178. doi: 10.25165/j.ijabe.20261901.8941.

[2] Eshaghi, C.A., & Aghaie, A. (2022). Data fusion techniques for fault diagnosis of industrial machines: A survey. *Computational Sciences and Engineering, 2*(2), 239-250. doi: 10.22124/cse.2023.23757.1040.

[3] Liu, Y., & Zhang, H. (2022). Stochastic damage accumulation in materials under fatigue loading. *International Journal of Fatigue*, 29(6). doi: 10.1016/j.ijfatigue.2006.09.009.

[4] Nadai, L., Felde, I., Ardabili, S., Mesri Gundoshmian, T., Pinter, G., & Mosavi, A. (2020). Performance analysis of combine harvester using hybrid model of artificial neural networks particle swarm optimization. *arXiv*.

[5] Qiao, Y., Wang, S., Shi, J., Liu, D., & Tao, M. (2024). Reliability model based on fault energy dissipation for mechatronic system. *Reliability Engineering & System Safety*, 250, article number 110295. doi: 10.1016/j.ress.2024.110295.

[6] Qiu, Z., Shi, G., Zhao, B., Jin, X., & Zhou, L. (2022). Combine harvester remote monitoring system based on multi-source information fusion. *Computers and Electronics in Agriculture*, 194, article number 106771. doi: 10.1016/j.compag.2022.106771.

[7] Rahman, M. S., & Guo, H. (2023). Sensitivity analysis of the DehumReq model to evaluate the impact of predominant factors on dehumidification requirement of greenhouses in cold regions. *Information Processing in Agriculture,* 10(2), 216-228. doi: 10.1016/j.inpa.2022.06.006.

[8] Reznik, N., Rogovskii, I., Havrylyuk, V., Riepina, I., Khodakyvskyy, V., Demchenko, T., & Kotliarov, V. (2025). Engineering and security management of technological transformation trends of agrotronics. In B. Alareeni (Ed.), *Big data in finance: Transforming the financial landscape* (pp. 289-298). New York: Springer. doi: 10.1007/978-3-031-75095-3_23.

[9] Rogovskii, I.L. (2021). *Development of complex technical and technological measures for improving the operability of agricultural machines*. (Doctoral dissertation, National University of Life and Environmental Sciences of Ukraine, Kyiv, Ukraine).

[10] Shen, J., Yang, S., Zhao, C., Ren, X., Zhao, P., Yang, Y., Han, Q., & Wu, S. (2023). Federated learning for equipment fault diagnosis. *IEEE Access*, 11, 99821-99835. doi: 10.1109/ACCESS.2023.3270001.

[11] Sinitsin, V., Ibryaeva, O., Sakovskaya, V., & Eremeeva, V. (2021). Bearing fault diagnosis using hybrid CNN-MLP models. *Engineering Applications of Artificial Intelligence, 103*, article number 104295. doi: 10.1016/j.engappai.2021.104295.

[12] Tien, S.-C., Wei, H., Chen, J., & Liu, Y. (2022). Energy-based time derivative damage accumulation model under uniaxial and multiaxial random loadings. *Fatigue & Fracture of Engineering Materials & Structures*, 45(1), 159-173. doi: 10.1111/ffe.13591.

[13] Wang, B., Zhong, S., Lee, T.-L., Fancey, K. S., & Mi, J. (2020). Non-destructive testing of composite materials: A review. *Advanced in Medical Engeneering*, 12(4), 1-8.

[14] Wang, B., Zhong, S., Lee, T.-L., Fancey, K. S., & Mi, J. (2020). Non-destructive testing and evaluation of composite materials/structures: A state-of-the-art review. *Advances in Mechanical Engineering*, 12(4). doi: 10.1177/1687814020913760.

[15] Wang, H., Lao, L., Zhang, H., Tang, Z., Qian, P., & He, Q. (2025). Structural fault detection and diagnosis for combine harvesters: A critical review. *Sensors*, 25(13), article number 3851. doi: 10.3390/s25133851.

[16] Xu, R., Xu, D., Zhang, J., Zhang, H., Li, B., He, K., Li, W., Zhang, J., & Feng, Z. (2024). A framework for constructing agricultural cognitive intelligence services and its application practice. *Journal of Nanjing University(Natural Sciences)*, 60(4), 613-624. doi: 10.13232/j.cnki.jnju.2024.04.008.

[17] Zhang, S., Zang, C., Yang, Z., Tang, L., Wang, K., Chen, W., Song, Q., & Wei, X. (2025). Fault prediction and control systems for unmanned harvesters based on IPSO-SVM. *Frontiers in Plant Science*, 16, article number 1577175. doi: 10.3389/fpls.2025.1577175.

[18] Zhang, S., Zhai, Q., & Li, Y. (2023). Degradation modeling and remaining useful life prediction with Wiener process considering measurable and unobservable external impacts. *Reliability Engineering & System Safety*, 231, article number 108921.

[19] Zhang, W., Zhao, B., Zhou, L., Wang, J., Niu, K., Wang, F., & Wang, R. (2022). Comprehensive operation and maintenance of combine harvesters based on fault diagnosis systems. *Agriculture*, 12(6), article number 893. doi: 10.3390/agriculture12060893.

[20] Zhou, X., Xu, X., Zhang, J., Wang, L., Wang, D., & Zhang, P. (2023). Fault diagnosis of silage harvester based on a modified random forest. *Information Processing in Agriculture,* 10(3), 301-311. doi: 10.1016/j.inpa.2022.01.004.

Руслан Шатров

Аспірант

Національний університет біоресурсів і природокористування України

03041, вул. Героїв Оборони, 15, м. Київ, Україна

https://orcid.org/0000-0001-7469-8657

Аналітична структурно-енергетична модель агротроніки комбайнового збирання зернового збіжжя

Анотація. Актуальність роботи зумовлена необхідністю підвищення точності оцінювання надійності та прогнозування ресурсу елементів зернозбиральних комбайнів в умовах інтенсивного енергетичного навантаження та впливу внутрішніх дефектів матеріалів. Метою роботи було обґрунтування та розвиток аналітичного підходу до формування структурно-енергетичної моделі агротроніки комбайнового збирання зернового збіжжя. У дослідженні використано методи структурно-енергетичного моделювання, теорії ймовірностей, зокрема розподілу Пуассона, математичного моделювання процесів накопичення пошкоджень, а також підходи неруйнівного контролю та експериментальні випробування елементів машин. Встановлено, що процес відмови елементів визначається накопиченням енергії та формуванням мікроструктурних пошкоджень, що дозволяє описати перехід системи у граничний стан через ймовірнісні залежності. Доведено, що параметри моделі (n та α) залежать від розмірів і характеру дефектних структур матеріалу та можуть змінюватися монотонно з їх збільшенням. Показано, що ймовірність безвідмовної роботи є функцією енергетичного впливу та часу експлуатації, що дає змогу прогнозувати залишковий ресурс елементів. Експериментально підтверджено суттєвий вплив внутрішніх дефектів матеріалу на довговічність деталей, навіть за однакових зовнішніх умов навантаження. Показано, що використання результатів неруйнівного контролю, зокрема томографічних методів, дозволяє ідентифікувати критичні параметри дефектних структур. Узагальнено, що використання структурно-енергетичного підходу підвищує точність оцінювання технічного стану та дозволяє враховувати мікроструктурні особливості матеріалів. Запропонований підхід може бути використаний для формування інтелектуальних систем прогнозування відмов та технічного обслуговування. Практична цінність роботи полягає у можливості застосування результатів для неруйнівної діагностики, прогнозування ресурсу та вдосконалення систем моніторингу технічного стану зернозбиральних комбайнів

Ключові слова: надійність технічних систем; зернозбиральний комбайн; мікроструктурні пошкодження матеріалів; прогнозування залишкового ресурсу; неруйнівна діагностика; ймовірнісне моделювання відмов; енергетичні процеси руйнування

Machinery & Energetics
Vol. 17, No. 2. 2026

Journal homepage:
https://technicalscience.com.ua/en

UDC 631.004.01
DOI: 10.31548/machinery/2.2026.9

Mikhailo Umanskyi*
Postgraduate Student
National University of Life and Environmental Sciences of Ukraine
03041, 15 Heroiv Oborony Str., Kyiv, Ukraine
https://orcid.org/0009-0006-5746-9717

Agricultural drone routing based on the artificial bee colony algorithm

Abstract. The relevance of the study is conditioned by the need to improve the reliability, energy efficiency, and quality of data transmission in self-organised agricultural drone networks that operate in conditions of high mobility, variable topology, and limited node resources. The purpose of the study was to improve the efficiency of traffic routing in self-organised agricultural drone networks by developing an adaptive algorithm based on artificial bee colony swarm intelligence. The study used methods of discrete and computational mathematics, heuristic optimisation, mathematical statistics, and simulation modelling using C++, Python, MATLAB, and the NS-2 environment. The principles of operation of a multi-agent routing model, including packers, scouts, foragers, and swarms, which provide decentralised search and support for multiple data transmission routes, were investigated. Such criteria for choosing routes as bandwidth, end-to-end delay, battery level of nodes, and network life were analysed, which allowed adapting the algorithm to various scenarios of agricultural drones. It was revealed that for the agricultural drone swarm scenario, it is advisable to use the network lifetime metric, for the transit network – the lifetime and delay metrics, and for the monitoring scenario – the charge level metric of power supplies. It was found that the proposed algorithm, compared to the AODV and OLSR protocols, provides a higher packet delivery rate, increased average throughput, reduced normalised load, and reduced routing overhead. It was concluded that the use of artificial bee colony swarm intelligence enables more efficient allocation of network resources, supports QoS requirements, and reduces the risk of network congestion. The practical significance of the study lies in the possibility of using the results obtained by software developers for agricultural drones, specialists in wireless self-organised networks, agricultural technology engineers, and researchers in the design of energy-efficient routing systems for agricultural monitoring and management of unmanned complexes

Keywords: self-organising wireless networks; multi-criteria optimisation; node energy efficiency; end-to-end delay; channel bandwidth; quality of service; simulation modelling

INTRODUCTION

The rapid introduction of unmanned technologies in agriculture and the development of wireless communications contributed to the establishment of self-organised networks that can function without centralised management. Such networks are a promising tool for performing a wide range of agricultural tasks, in particular, survey of agricultural territories, video surveillance, control of agricultural infrastructure facilities, and providing wireless broadband access. Their widespread adoption is associated, in particular, with the development of agricultural quadcopters as a type of agricultural multicopter system with an electric propulsion system. Due to their distributed, peer-to-peer, and multi-link topologies, such networks are characterised by increased fault tolerance.

One of the key problems of ensuring the functional stability of such systems is the risk of loss of connectivity between nodes. U. Kaur *et al.* (2026) noted that the ability of a network to support data transmission largely depends on the effectiveness of adaptive protocols, which should ensure the construction of routes in conditions of high node mobility and constant topology changes. There is no universal solution that would fully consider all the features

Article's History: Received: 09.01.2026; Revised: 22.04.2026; Accepted: 21.05.2026; Published: 29.05.2026.

Suggested Citation:
Umanskyi, M. (2026). Agricultural drone routing based on the artificial bee colony algorithm. *Machinery & Energetics,* 17(2), 108-120. doi: 10.31548/machinery/2.2026.9.

*Corresponding author (umansky60@gmail.com)

of the operation of self-organised agricultural drone networks (Fatemidokht *et al.*, 2026). That is why the search for new approaches to engineering management of information flows in such systems remains relevant.

A significant amount of research is devoted to the application of algorithms based on the principles of swarm intelligence, to optimise the network operation. Further development of this area is associated with the use of models of collective behaviour of social insects. B. Zhao & Q. Ding (2019), and N.N. Hamadneh *et al.* (2022) considered the possibilities of applying behavioural models of termites, ants, and bees to solve tasks of finding optimal routes and optimising network processes. An important element of such approaches is the use of multi-agent systems. As noted by H. Tan (2016), software agents provide decentralised decision-making by individual nodes of the network, which increases its resistance to topology changes and external influences.

A separate area of research is devoted to the application of bee colony algorithms in telecommunications networks of unmanned aerial vehicles. A.N. Khan *et al.* (2019) showed the prospects of using this approach to optimise the operation of UAV networks. Developing this idea, S.O. Oubbati *et al.* (2020) characterised the bee colony algorithm as a modern multi-agent optimisation method, and C. Wang *et al.* (2025), described it as effective for solving routing problems in self-organised networks. Similar conclusions were reached by F. Pasandideh *et al.* (2022), who confirmed the effectiveness of this algorithm in various scenarios of network functioning by the solution of S.S. Banihashemian & F. Adibnia (2019). The closest approach to the subject of this study is the approach proposed by B. Sharma *et al.* (2020), who used the ant colony algorithm to plot routes in a network of unmanned aerial vehicles. Their proposed solution demonstrated the possibility of effective adaptation of routes to changes in the network topology and confirmed the feasibility of using swarm intelligence algorithms in agricultural drone networks.

Therefore, the development and research of a bee colony algorithm for optimising routing in self-organised agricultural drone networks is an urgent scientific and technical task. Its solution is important for improving the efficiency of agricultural unmanned systems, developing agricultural engineering, and creating adaptive methods for managing network information flows.

The purpose of the study was to improve the efficiency of traffic routing in self-organised agricultural drone networks using the developed adaptive routing algorithm based on artificial bee colony swarm intelligence. Research objectives:

- to formulate a methodology for evaluating the effectiveness of routing methods in self-organised agricultural drone networks;
- to develop a software implementation of the proposed routing algorithm for the simulation environment;
- to evaluate the effectiveness of the proposed algorithm by comparative analysis of the results of simulation modelling with existing routing protocols in typical scenarios for using self-organised agricultural drone networks.

MATERIALS AND METHODS

The object of the study was a self-organised network of agricultural drones that operated in conditions of dynamic topology, high node mobility, and limited energy resources. The subject was an adaptive traffic routing algorithm based on swarm intelligence of a bee colony, designed to improve the efficiency of data transmission in such networks. The study was conducted under simulation conditions using typical scenarios for the use of self-organised agricultural drone networks: the swarm of agricultural drones, a transit network, and monitoring.

The methodological basis of research was the principles of swarm intelligence, multi-agent control, multi-criteria optimisation, and adaptive routing in wireless self-organised networks. To build the algorithm, a bee colony behaviour model was used, in which four types of agents performed functional roles: packers, scouts, foragers, and swarms. Packers provided data transmission from the transport layer, scouts searched for new routes, foragers delivered packages to the destination node, and the swarm was used for official return of route information. To limit the distribution of broadcast queries, the "expanding ring" search principle was applied. The study used general scientific methods of analysis, analogy, and abstraction, methods of discrete and computational mathematics, heuristic optimisation, mathematical statistics, and simulation modelling. Using mathematical methods, criteria for evaluating routes were formed that considered end-to-end delay (EED), bandwidth, the level of residual battery charge of nodes, and network life. Heuristic optimisation methods were used to select an effective route based on the current state of the network and a given metric.

The software implementation of the algorithm was performed using the C++, Python, and MATLAB programming languages, and simulation modelling was performed in the NS-2 environment (USA). At the first stage, the algorithm structure was developed and the interaction of agents was described. At the second stage, simulation models of typical scenarios for the functioning of the agricultural drone network were constructed and simulation parameters were configured. At the third stage, a series of simulations were performed for different routing metrics and the most effective options for each scenario were determined. At the final stage, a comparative analysis of the proposed algorithm was performed with the AODV and OLSR protocols.

The efficiency of the algorithm was evaluated by the following indicators: packet delivery rate (PDR), average EED, average throughput, normalised routing load (NRL), number of transitions, and routing overhead. The results obtained were used to determine the feasibility of applying the proposed approach in self-organised agricultural drone networks.

Description of performing simulation modelling. Simulation modelling of the proposed routing algorithm was carried out to check its operability and efficiency in typical conditions of functioning of self-organised agricultural drone networks. For this purpose, three simulation scenarios were created that reflected different modes of application of agricultural drones in the agricultural environment: the agricultural drone swarm scenario, the transit network scenario, and the monitoring scenario. All scenarios were modelled in the NS-2 environment using a software implementation of the proposed algorithm developed using C++, Python, and MATLAB.

The first scenario, "Drone Swarm", simulated the operation of a group of mobile nodes that jointly performed tasks within a certain agricultural area. In this case, the network was characterised by high dynamics of topology changes" since agricultural drones could change positions relative to each other, forming temporary multi-track data transmission routes. The purpose of modelling this scenario was to evaluate the algorithm's ability to maintain network connectivity, ensure packet delivery, and distribute traffic between multiple routes without overloading individual nodes.

The second scenario, "Transit Network", reflected the conditions under which individual agricultural drones served as intermediate repeater nodes between the data source and the destination node. This scenario was typical for situations where information was transmitted through several intermediate nodes, and the effectiveness of the route depended on the stability of connections, the number of transitions, and the level of service load. In this scenario, special attention was paid to estimating EED, the number of transitions, and the NRL.

The third scenario, "Monitoring" simulated the use of agricultural drones to monitor agricultural objects or territories with data transmission to the information collection node. For this mode, the stability of packet delivery, energy efficiency of the route, and maintaining the functionality of nodes for a long time were important. That is why this scenario separately considered the impact of metrics related to the level of remaining battery power and network life.

In each scenario, the algorithm worked with different route metrics: bandwidth, EED, power supply charge level, and network lifetime. The following performance indicators were used to compare algorithm variants: PDR, average EED, NRL, and average hop count (HC). The PDR indicator characterised the reliability of data delivery, EED determined the time spent transmitting a packet from source to recipient, NRL reflected the volume of service traffic relative to the number of packets delivered, and HC characterised the topological length of the route.

The modelling technique involved sequential execution of the following stages: forming a network scenario, setting parameters for the movement and interaction of nodes, running a routing algorithm with different metrics, registering the values of PDR, EED, NRL, and HC, and comparing the results obtained between scenarios. The obtained values were used to determine which route metric was most appropriate for each type of agricultural drone application. The simulation results were presented in the next section as comparison tables for the three scenarios.

RESULTS AND DISCUSSION

The proposed adaptive routing algorithm based on artificial bee colony swarm intelligence for self-organising agricultural drone networks belongs to the class of reactive source-initiated multipath routing methods. An agent model was created based on the principles of decentralisation and locality. By analogy with the natural world, it comprises four types: packer, scout, forager, and swarm. The theoretical and methodological basis for the development of the algorithm was the provisions of bionics, biomimetics and swarm intelligence, according to which the mechanisms of self-organisation of natural systems can be used to create adaptive technical solutions. E. Bonabeau *et al.* (1999) and Z. Zhang *et al.* (2014) showed that the collective behaviour of social insects is an effective model for creating decentralised, scalable, and fault-tolerant artificial systems. Algorithms inspired by the behaviour of the bee colony are of particular importance for this study, since they combine mechanisms of local search, exchange of information about the quality of solutions found, and collective choice of the optimal direction of further movement.

The agent model of the proposed algorithm is formed considering the principles of bee feeding and communication. In particular, in BeeAdHoc, the use of scout and forager agents helped to implement energy-efficient reactive routing in mobile ad hoc networks (Wedde *et al.*, 2005), and the BeeIP protocol confirmed the feasibility of applying bee principles for adaptive route selection under dynamic network conditions (Giagkos & Wilson, 2013; 2014). In this study, these ideas were adapted to self-organised networks of agricultural drones through the introduction of agents such as packer, scout, forager, and swarm, which perform the functions of data preparation, route search, packet transmission, and service update of route information. Packers copy the functions of harvesting bees in the hive. Their main task is to get data D_s from the transport level and transfer them to foragers F_r. Scout S_s is used to find new routes from the source node d to the destination node d. The scout is transmitted via broadcast to all neighbours of the node with a lifetime timer that controls the number of relays S_s.

To limit the uncontrolled distribution of broadcast queries, a search algorithm based on the "expanding ring" principle is used. Each scout is identified using a unique key based on the identification number and source node. Upon reaching d, the scout returns back the same way. The receiving node sends all scouts back to guarantee multiple routes. Returning to s, scouts S_s recruit foragers F_r using the dance metaphor.

Foragers F_r get data packets from packers P_s and deliver them to the destination node d. Forager can have four types: minimum latency, maximum bandwidth, network lifetime, and node battery level. The first type delivers packages on routes with minimal delay. The second is through routes with maximum throughput. The third one sends packets in such a way as to maximise the life of the network. The fourth one builds routes through the nodes with the highest battery level. The forager gets the full route as a sequence of intermediate nodes i to the node d from scout S_s or another forager F_r. To do this, it uses point-to-point transfer mode to the node , while collecting information about the network according to its type. After reaching the node d forager F_r stays there until it is delivered back to the source node s. This mechanism allows reducing the amount of service traffic. If the TCP transport protocol is used, delivery is carried out using a special forager F_{TCP}. Back at the source node, foragers also use the dance metaphor.

Forager delay F_r in the destination node d by the time it returns to the source node, s is an important element of the proposed routing mechanism, since it allows reducing the amount of service traffic and avoiding excessive duplication of route information. After delivery of the package to node d, the forager is not immediately sent back as a separate service message, but waits for the possibility of returning together with confirmation of delivery or as part of a special service mechanism. This reduces the number of individual control packets in the network, reduces the number of retransmissions, and reduces the load on intermediate nodes, which is especially important for self-organised agricultural drone networks with limited energy resources and variable topology.

This approach is consistent with the principles of swarm intelligence, according to which the effective global behaviour of a system is formed not through centralised management, but through local interactions of individual agents. In natural bee colonies, individuals do not duplicate each other's actions unnecessarily, but coordinate the search and use of resources through the exchange of information about the quality of the source found. Similarly, in the proposed algorithm, foragers do not create redundant service traffic, but accumulate and transmit route information only when it is necessary to update the state of the route, confirm delivery, or recruit new agents. This allows minimising energy costs, increasing the efficiency of group work of agents, and ensuring the stability of routing in conditions of dynamic changes in the position of nodes.

For the TCP transport protocol, the forager return mechanism is formally consistent with the availability of delivery confirmations, since TCP provides feedback between the destination node d and the source node s. In this case, the forager can be returned to the source along with confirmation, which allows not only to confirm the fact of data delivery, but also to transmit up-to-date information about the quality of the route travelled. Thus, the node (s) gets updated route data without having to create additional queries or run a repeated path search.

For the UDP protocol, which does not guarantee delivery confirmation and does not have a built-in mechanism for returning service information, a similar function is implemented using service packets or swarms R_s. In this case, one forager is randomly selected, which acts as a carrier of service information and returns to the source node (s), while other foragers are placed in the useful data field D_u. This mechanism provides a balance between the need to control the route and maintaining network bandwidth: on the one hand, the source receives information to confirm delivery and update routes, and on the other – the network is not overloaded with a large number of individual service messages.

Thus, the stay of the forager F_r in the node d by the time of return to the node s is justified from the standpoint of reducing the service load, energy efficiency, and improving the reliability of data transmission. This mechanism allows combining delivery control, route information updates, and optimal use of network resources without excessively increasing the number of control packets. As a result, the proposed model provided decentralised, adaptive and fault-tolerant routing that meets the principles of bionic design and swarm coordination of agents.

The UDP protocol does not send confirmation of successful receipt data and does not have a built-in forager return mechanism F_r to the source node s. This problem is solved using special service packs or swarms R_s. Foragers are sent back to the node after a certain time has elapsed or when a threshold value is reached in the node d. As a swarm, one source node forager is randomly selected, and other foragers are placed in the useful data field D_u. When the swarm arrives at the node , foragers are extracted in the same way as in the case of TCP. A general block diagram of the functioning of the proposed routing algorithm and the interaction of its main agents is shown in Figure 1.

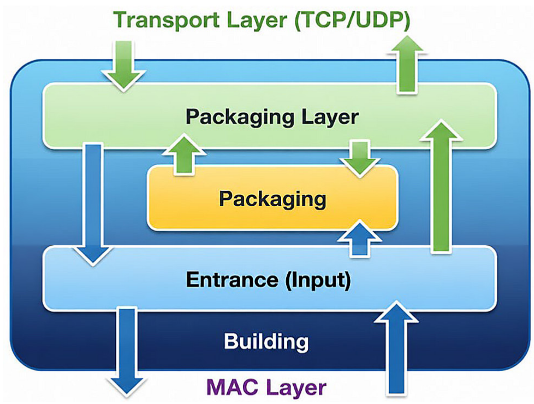

Figure 1. Block diagram of the algorithm
Source: developed by the author

Data D_s from the transport level are placed in packers P_s and are passed on to foragers F_r located on the dance floor T_p, after which the packers die. If the packer does not find a suitable forager, it waits for a while and then sends the scout S_s to search for a new route to the destination node d. The scout who appeared at the entrance I_{MAC}, passed on if its TTL timer (Time To Live – counter or limiter that determines how many times a service packet, such as scoutS_c, can be transmitted from one network node to another) is not exhausted or if it has not reached the node *d*. Data about the scout ID and its source node are stored in a special table. If a copy of the previously received scout appears at the entrance, it is destroyed. If there is already a forager F_r on a dancefloor T_p with the same destination node as the scout, the route to the destination is reported to the scout by adding the known forager route to its current route. If the current node is the final recipient of the forager, it is sent to the packaging level P_s; if not, then in the MAC interface of the next node in the direction of *d*.

The dance floor is the heart of the hive, because T_p stores information about routes. When forager F_r returns to the source node *s*, it "recruits" new foragers, using the dance metaphor. In the proposed algorithm, the use of the dance metaphor should be considered as a formalised mechanism for exchanging information between agents about the quality of the found route. In natural bee colonies, the forager dance serves as a communication protocol through which other individuals receive information about the direction, distance, and attractiveness of the resource source. In particular, the direction of movement during the dance is related to the direction to the source, the duration of individual phases of movement reflects the distance, and the intensity and repeatability of the dance can be interpreted as indicators of the quality or feasibility of using the found resource. Therefore, in bionic and swarm models, this mechanism is considered as a natural way to encode, transmit, and collectively evaluate information.

By analogy with a bee colony, in the developed algorithm "dance" of the forager F_r in the source node *s* is a procedure for updating route information and recruiting new agents for data transmission. After completing the route, the forager returns to the node (*s*) with information about the path status, including EED, bandwidth, remaining battery level of intermediate nodes, or network lifetime. These parameters serve as a formalised "resource quality", that is, the quality of the route, and the number of dances, or the probability of choosing a suitable forager can be related to the effectiveness of the path travelled. In this way, better routes are more likely to be reused, while less efficient ones are gradually being pushed out of the routing process.

This approach corresponds to the principles of swarm intelligence, according to which complex global behaviour of a system is formed through local interactions of simple agents without centralised control. In the context of a self-organised agricultural drone network, this means that the source node does not need complete global information about the state of the entire network. There is enough information that foragers return after passing specific routes. Based on these local messages, the system dynamically redistributes traffic between available paths, keeps routes updated, and reduces the risk of overloading individual nodes.

Thus, the dance metaphor in the proposed algorithm is a biomimetic model of agent communication, in which the natural mechanism of transmitting information about a resource is transformed into a technical procedure for evaluating and selecting routes. It provides decentralised decision-making, adaptation to changes in topology, rational use of energy resources, and increasing the fault tolerance of data transmission in self-organised agricultural drone networks.

Number of dances D_d is calculated according to the quality of the route travelled. Quality indicator for each forager F_r differs depending on its type. Equation for determining the number of dances D_d (*v*) is proposed by the researchers as a generalised normalising relationship between the quality of the route travelled and the intensity of forager recruitment. It is not literally borrowed from a separate source, but is based on the principles of bionic routing BeeAdHoc, in which "dance" is considered as a formalised mechanism for recruiting agents, and the number of recruited foragers depends on the quality of the route found (Wedde *et al.*, 2005). This interpretation is also consistent with the BeeIP protocol, where the intensity of the artificial forager's dance is related to the quality of the path and is used to make a decision on further recruitment or start a new route search process (Giagkos & Wilson, 2010).

From the dance floor, T_p a suitable forager is sent to the packaging level P_s in response to a request from P_s. If there are several suitable foragers, one of them is selected stochastically. A copy of the selected forager is sent to the packaging level P_s, and the original forager remains on the dance floor only because of the decrease in the number of dances D_d. If $D_d = 0$, the original forager is sent to P_s, and its recording is removed from the dance floor. Foragers whose life span T_r ends are excluded from the selection process. The use of this principle ensures the process of updating foragers F_r, that is, replacing "old" with "young" ones with current routes. The approach also allows distributing foragers along several routes, which prevents overloading and optimises the use of resources, for example, a uniform discharge of the agricultural drone battery.

Scientific originality of the proposed mechanism for updating foragers F_r consists in combining the lifetime limit of agents T_r with a multi-criteria assessment of the route status. Unlike classical swarm optimisation algorithms, where ageing of agents or reducing the influence of previous solutions is most often implemented through pheromone evaporation, reducing the weight of the solution, or replacing the population of agents, in the proposed approach, the exclusion of "old" foragers is associated not only with the time parameter, but also with the need to update routes in conditions of changing topology, residual charge of nodes, and network load.

Thus, the mechanism T_r can be defined as the author's version of adaptive age-based pruning, supplemented by energetically and topologically determined updating of route information. Its difference from classical age-based pruning is that the forager is excluded from the selection process not only because its life cycle has ended, but because over time, information about the route it has travelled loses its reliability for a dynamic self-organised network of agricultural drones. In such conditions, the "old" forager may contain a route that no longer corresponds to the current state of the network: intermediate nodes may change position, partially lose battery power, get into a high-load zone, or become unavailable for data transmission.

In classical ACO approaches, the relevance of solutions is mainly determined by the pheromone trace mechanism, where the intensity of route use decreases due to pheromone evaporation (Dorigo & Gambardella, 1997). In ant-based routing and AntHocNet, route support is provided through reactive path setting, proactive sensing, updating pheromone tables, and the use of agents that periodically check route quality (Di Caro *et al.*, 2005). In BeeAdHoc, routing is based on scout agents and foragers, which reduces the number of service packets and increases the energy efficiency of data transmission in mobile ad hoc networks (Wedde *et al.*, 2005). The mechanism proposed in this paper differs in that the life cycle of the forager T_r is used as an internal regulator of route relevance, which simultaneously restricts the use of outdated routes, encourages the appearance of new foragers with updated information, and maintains a balance between the research of new routes and the use of already known ones.

The causal link between updating foragers and improving system performance is that excluding agents with outdated route information reduces the likelihood of data being transmitted through overloaded or energy-depleted nodes. If the forager F_r has a limited lifetime, then the route it represents cannot remain active indefinitely without rechecking. This helps to periodically update routes, distribute traffic more evenly between several paths, and reduce the risk of local congestion of individual nodes. In addition, replacing "old" foragers with "young" ones allows considering the current battery level of intermediate nodes, which supports more uniform power consumption in the network.

Therefore, the proposed foraging renewal scheme is not a simple procedural removal of agents after the lifetime has elapsed. It performs the function of adaptive updating of routes, monitoring the relevance of route information, and load balancing in a self-organised network of agricultural drones. The improvement of system characteristics in this case has the status of an experimentally confirmed result of simulation modelling, since in comparison with AODV and OLSR, the proposed algorithm demonstrated an increase in the PDR and throughput, and a reduction in normalised load and routing overhead. Theoretically, this effect is explained by the fact that the restriction T_r reduces the use of outdated routes and supports constant updating of agents, but the full formal proof of this mechanism requires a separate mathematical analysis in further research. If the last forager for the node is the destination *d* leaves the hive, the source node temporarily loses the route to the recipient. It is assumed that if the route to *d* exists, forager will soon return to *s*; if no forager returns within a certain time, the source node probably lost the route to the node *d*.

Indicator D_N is used as an integral characteristic of the efficiency of the proposed algorithm, since it reflects the intensity of recruiting foragers depending on the quality of the route travelled. The higher the value D_N, the more appropriate the route is considered for further data transmission, which allows the algorithm to adaptively select efficient paths and reduce the use of overloaded or outdated routes. The use of this mechanism eliminates the need for explicit monitoring of the reliability or relevance of routes using special "welcome" packages and route error messages, which reduces the volume of service traffic and reduces energy costs. To ensure optimal routing of data streams, a multi-criteria approach is used, which provides support for several routing metrics: bandwidth, draft latency, node battery level, and network lifetime. Earlier it was noted that D_N is the main indicator that characterises the efficiency of the proposed algorithm.

One of the simplest and most widely used optimisation metrics is an EED for routes *T*. One of the basic indicators for evaluating the quality of a route is the EED, which characterises the time when a data packet passes from the source node *s* to the destination node *d*. For the forager F_r, the route that passes between these nodes, the EED value is determined by the equation:

$$T = t_r - t_s, \tag{1}$$

where t_r – time to receive the forager's package F_r by recipient node *d*, t_s – time of sending the package F_r by source node *s*. Therefore, equation (1) shows the actual time it takes for a package to complete the entire route. The lower the value t_r, the faster and better the route is considered.

A normalised estimate is used to convert the delay value to a route quality indicator D_d which allows comparing different routes with each other:

$$D_d = \alpha \times \left(\frac{1}{2}\right)^{\left(\frac{R}{2} \times \frac{T}{\beta \times \gamma}\right)}, \tag{2}$$

where α – weight coefficient that determines the maximum value of the number of dances for F_r, β – nominal value of the draft delay, γ – weighting factor, R – number of transitions (hops) performed by F_r between *s* and *d*, $R \in [1;9]$, $R \in N$. Equation (2) is needed to ensure that routes with lower delays receive a higher quality rating. If the route delay is close to the minimum, the value D_d approaches 1, and if the route has a long delay when the indicator approaches 0.

Based on the normalised quality of the route, the number of dances D_d performed by the forager after returning to the source node is determined. Another widely used routing metric is network bandwidth *F*. Determination of the value *F* on the route from *s* to *d* is performed using the equation:

– data packet size, T_i – time of receiving the package F_r by current transit hub *i*.

Then the indicator D_N is calculated using the equation:

$$DN = \frac{BW}{\delta} \times \frac{\alpha}{\eta}, \tag{4}$$

where $BW_{min} = \min BW_i$ – minimum bandwidth value for the packet F_r,

$$\delta - BW_i = \frac{F_r}{T_i - T_{i-1}}, \tag{3}$$

where F_r – maximum possible channel speed value, η – number of packages F_r on the dance floor F for the node d, because they consist of nodes with the highest battery level. At each intermediate node , the residual battery charge E_i is determined. A battery level metric is often used in self-organised networks, which is based on an estimate of the residual energy of each transit node on the way from s to d. At each intermediate node , the residual battery charge E_i is determined. Then D_d is defined by expression (2).

Weighting factor (α) in the expression (2) is used to scale the impact of the energy component on the overall assessment of route quality. Within the proposed model (α), it is not a physical constant, but is considered as an empirical parameter for configuring an algorithm that determines the sensitivity of routing to changes in the remaining battery charge of intermediate nodes. The larger the value (α), the stronger the algorithm prefers routes passing through nodes with a higher level of energy resource; accordingly, at a lower value (α), the energy criterion has a weaker effect compared to other metrics, such as latency, throughput, or number of transitions.

Engineering content of the coefficient (α) consists in the fact that it reflects the degree of energy priority of the route in the operating conditions of a self-organised network of agricultural drones. In networks where the battery life of nodes is a critical parameter, the value of (α) is advisable to be increased, since data transmission through energy-depleted nodes can lead to loss of connectivity, route disruption, and reduced reliability of packet delivery. If the main task is to minimise latency or maximise throughput, the value (α) can be reduced so that the energy component does not dominate other route selection criteria.

In the proposed model, (α) can be set experimentally during simulation modelling and adjusted depending on the application scenario of the agricultural drone network. In particular, for scenarios of long-term monitoring of agricultural territories, it is advisable to use higher values of , since the uniform use of energy resources of nodes directly affects the lifetime of the network. For short-term data transfer or transit routing scenarios, the value of (α) may be lower, because latency or channel bandwidth may be more critical.

Normalised value ($E_i \in [0;1]$) characterises the relative level of residual battery charge (i)-th route node. Normalisation is carried out with respect to the boundary energy states of the node: ($E_i = 0$) corresponds to a fully charged or maximum available level of energy resource, and ($E_i = 0$) at a critically low or unavailable charge level for routing. In general, rationing can be presented as follows:

$$E_i = \frac{E_i^{cur} - E_i^{min}}{E_i^{max} - E_i^{min}}, \tag{5}$$

where (E_i^{cur}) – current battery level of the (i)-th node; (E_i^{max}) – maximum or rated charge level; – minimum allowable charge level at which the node can still participate in data transmission.

Minimum value of the energy indicator on the route:

$$E_{\min}^{route} = \min(E_i) \tag{6}$$

displays the weakest node in the route in terms of energy state. This interpretation is important because even a single node with a low charge level can cause route loss, an increase in the number of retransmissions, or a break in network connectivity. Thus, the use of ($E_{\min}^{route}$) allows the algorithm to avoid routes that pass through energy-unstable nodes, and contributes to a more even distribution of the load between agricultural drones.

Thus, the coefficient (α) acts as a regulator of the energy sensitivity of the algorithm, and the normalised indicator (E_i) ensures comparability of the energy state of different network nodes. Together, these parameters allow considering not only the current suitability of the route for data transmission, but also its impact on the overall lifetime of a self-organised network of agricultural drones.

Then the indicator D_N is defined as:

$$D_N = \alpha \times \frac{E}{R} \tag{7}$$

where $E = min\ E_i$ – minimum value of the remaining battery charge at intermediate nodes of the route from s to d, – weighting factor that scales the impact of the energy component on the route assessment . Another approach to optimising information flows based on energy efficiency is to use the “network lifetime” metric. Due to the distribution of packets over several routes, the node’s batteries will be discharged evenly, which increases total network lifetime.

The paper uses an interval transformation of a continuous normalised indicator C_i, not an independent categorical variable. Discrete levels 0-7 are used to simplify route selection and increase the algorithm’s sensitivity to critical battery levels. For every i-th transit node that is a link in the chain between s and d, the level of residual value of power supply capacities C_i is determined by the equation:

$$C_i = \begin{cases} 0, C_i \in [0; 0.09] \\ 1, C_i \in [0.09; 0.14] \\ 2, C_i \in [0.14; 0.20] \\ 3, C_i \in [0.20; 0.27] \\ 4, C_i \in [0.27; 0.35] \\ 5, C_i \in [0.35; 0.45] \\ 6, C_i \in [0.45; 0.65] \\ 7, C_i \in [0.65; 1] \end{cases}, \tag{8}$$

where $C_i \in (0,65;1]$ – residual power supply capacity of the current transit node i. The obtained data is aggregated in foragers F_r, and then used by the source node s to calculate D_d. Equation for calculating the indicator D_d has a form:

$$D_N = \alpha \times \frac{((\psi-(R-1))*C_{min}*C_{avg})}{\omega}, \quad (9)$$

where ω – scaling factor, C_{avg} – average value of the level of residual capacity of the power supply on the route between s and d, $C_{min} = min\ C_i$, C_i – minimum value of the residual capacity level of the power supply. Scaling factor ω is calculated using the equation:

$$\omega = C_{\max} \times C_{\min} \times \psi + 1, \quad (10)$$

where $C_{max} = max\ C_i$, C_{max} – maximum value of the level of residual capacity of the power supply on the route between s and d, ψ – maximum number of transitions (hops) between s and d; in the current implementation of the algorithm $\psi = 9$.

The following is a description of the packet formats of the developed algorithm, the process of setting the route, transmitting data, and managing the distribution of broadcast service messages. A brief description of the software implementation of the proposed algorithm for the NS-2 simulation environment is also provided. The influence of setting parameters on the algorithm's behaviour was investigated, and the range of possible values and default values were determined.

Since the proposed routing algorithm was developed for FANET, when studying the dependence of its behaviour on the selected routing metric, a comprehensive simulation modelling was carried out using the developed realistic models of typical scenarios for the use of self-organised agricultural drone networks.

At this stage, the following indicators are used to evaluate performance:

- average value of the package delivery coefficient (P_{DR}),
- average EED value (EE_{delay}),
- average value of the NRL (NL),
- average number of hops (H).

To evaluate the effectiveness of the proposed routing algorithm, a set of network metrics is used that characterise various aspects of the FANET network functioning: delivery reliability, transmission time costs, service load, and topological complexity of the route. The main indicators include the package delivery rate (P_{DR}), average EED (EE_{delay}), NRL (NL), and the average number of hops (H). These metrics are not considered fully equivalent or independent criteria, since there are functional and operational relationships between them. For example, reducing the number of traffic may reduce latency, but simultaneously lead to traffic concentration on individual nodes; increasing the PDR may be accompanied by an increase in the service load; and reduction (NL) indicates more efficient use of network resources, but does not always guarantee minimal latency.

In this study, these indicators were used not as components of a single integral index, but as separate criteria for multi-criteria analysis. Their aggregation into one generalised indicator was not carried out, since the purpose of the experiment was not to obtain a single rating of route metrics, but to identify which of them is more appropriate for a specific scenario of agricultural drone network operation. This approach allows separately assessing the trade-off between delivery reliability, time efficiency, service load, and route structure.

Indicator (P_{DR}) determines the proportion of successfully delivered packets relative to the total number of sent packets and is used as a basic criterion for routing reliability. The results of evaluating the effectiveness of various route metrics for PDR, EED, NRL, and HC indicators for the "Drone Swarm" scenario are shown in Table 1.

Table 1. Simulation results for the "Drone Swarm" scenario

Metric	Performance indicators			
	P_{DR}, %	EED, ms	NRL	HC
BeeAdHoc TH	98.24	101.65	24.26	3.60
BeeAdHoc DL	98.20	102.29	24.22	3.61
BeeAdHoc EH	98.32	112.26	24.28	3.57
BeeAdHoc LT	98.44	104.34	24.19	3.56

Source: developed by the author

Indicator (EE_{delay}) characterises the average packet travel time from the source node to the destination node. Deviation of values (EE_{delay}) in the range from 8.7 to 68.1, different routing metrics respond differently to changing scenarios and topological conditions. These differences may be due to the choice of route based on the minimum latency, bandwidth, remaining battery power, or network life. In other words, they are not random numerical discrepancies, but a consequence of different logic for making a route decision within each metric. Comparative results of applying route metrics in the "Transit Network" scenario are shown in Table 2.

Table 2. Simulation results for the "Transit Network" scenario

Metric	Performance indicators			
	P_{DR}, %	EED, ms	NRL	HC
BeeAdHoc TH	99.98	1.71	30.58	4.73
BeeAdHoc DL	99.98	1.05	28.05	4.95
BeeAdHoc EH	99.98	1.14	23.42	4.68
BeeAdHoc LT	99.98	1.75	31.47	4.46

Source: developed by the author

NRL (*NL*) displays the ratio between the number of service route messages and the number of successfully delivered data packets. Significant deviation (*NL*), which in some cases reaches 63.2, indicates a different intensity of service exchange during the search, maintenance, and updating of routes. Lower value (*NL*) means that the algorithm spends less service resources on delivering a unit of useful information, which is important for FANET networks with limited bandwidth and energy resources of nodes. Indicator (*H*) characterises the average HC between the source node and the destination node. It is used to estimate the topological length of a route and indirectly affects latency, power consumption, and the probability of packet loss. Simultaneously, the minimum value (*H*) does not always mean the best route, as a shorter path can pass through overloaded or energy-depleted nodes. Therefore, this indicator should be interpreted together with (P_{DR}), (EE_{delay}) and (*NL*). The values of the performance indicators of the proposed algorithm for various route metrics in the "Monitoring" scenario are shown in Table 3.

Table 3. Simulation results for the "Monitoring" scenario

Metric	Performance indicators			
	P_{DR}, %	EED, ms	NRL	HC
BeeAdHoc TH	98.68	42.67	33.01	4.68
BeeAdHoc DL	98.54	37.09	32.68	4.74
BeeAdHoc EH	96.82	26.10	20.32	5.77
BeeAdHoc LT	96.57	27.61	20.54	4.32

Source: developed by the author

In Tables 1-3, the values (P_{DR}) for most variants of the algorithm, are close to the maximum: in the "Drone Swarm" scenario they are approximately 98.20-98.44, in the "Transit Network" scenario – 99.98, and in the "Monitoring" scenario – from 96.57 to 98.68. It is these absolute values that allow interpreting the results as almost identical in terms of packet delivery within the corresponding script. Simultaneously, the difference between the options should not be interpreted in isolation from the simulation conditions, since its statistical significance depends on the number of simulation runs, node mobility parameters, traffic intensity, and network load level.

Thus, the selected metrics reflect the key requirements for the routing algorithm in FANET networks: delivery reliability, transfer speed, saving service traffic, and rational route construction. In this study, they were not normalised to a common scale and were not aggregated into an integral metric, since the analysis is aimed at comparing the behaviour of the algorithm in different scenarios, and not at constructing a universal numerical estimate. To increase the reproducibility of further studies, it is advisable to additionally indicate the number of repetitions of simulation simulations, traffic parameters, node speed ranges, network density, and statistical criteria for checking the significance of the differences obtained.

Based on the results obtained (shown in Tables 1, 2, and 3), it can be seen that the studied metrics showed almost identical, close to the maximum, values for the indicator (P_{DR}) (the discrepancy between the results does not exceed 2.2%). However, considering the delay indicators (EE_{delay}) (the difference between the results varies between 8.7% -68.1%) and the NRL of *NL* (the difference in results reaches 63.2%). Therefore, it was found that for the "Drone Swarm" scenario, it is recommended to use the lifetime of the BeeAdHoc LT network as the default metric. For the "Transit Network" scenario, the best choice is the network lifetime and latency metrics BeeAdHoc LT and BeeAdHoc DL. In the monitoring scenario, the BeeAdHoc EN power supply charge level indicator showed the best results.

In the second series of experimental studies, a comparative analysis of the proposed routing algorithm with the AODV and OLSR protocols was performed. The results obtained confirmed the effectiveness of applying the algorithm in a self-organised UAV network. The proposed algorithm provided high network performance in each of the scenarios, surpassing the AODV and OLSR protocols in many respects. The best results were demonstrated in terms of indicators:

- package delivery rate (P_{DR}),
- average throughput (T_{avg}),
- NRL (*NL*),
- routing overhead ($O_{routing}$).

Figure 2 shows the results of simulation modelling for the average throughput indicator T_{avg} for the "Drone Swarm" scenario.

Results on the NRL indicator *NL* for the "Drone Swarm"

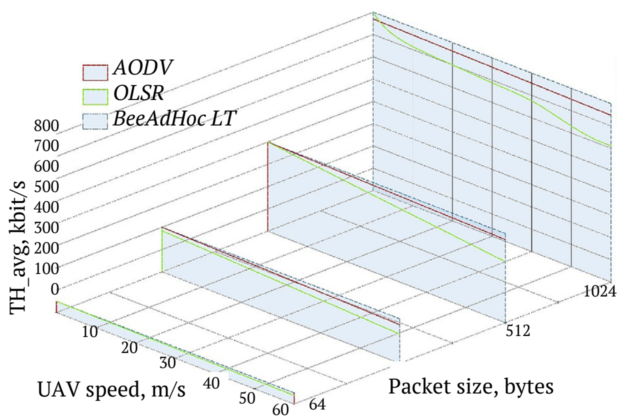

Figure 2. Average bandwidth value T_{avg} for BeeAdHoc LT, AODV, and OLSR in the "Drone Swarm" scenario

Source: developed by the author

scenario is shown in Figure 3. Figure 4 shows the results of experimental studies for the indicator of the average value of routing overhead $O_{routing}$ in the "Drone Swarm" scenario.

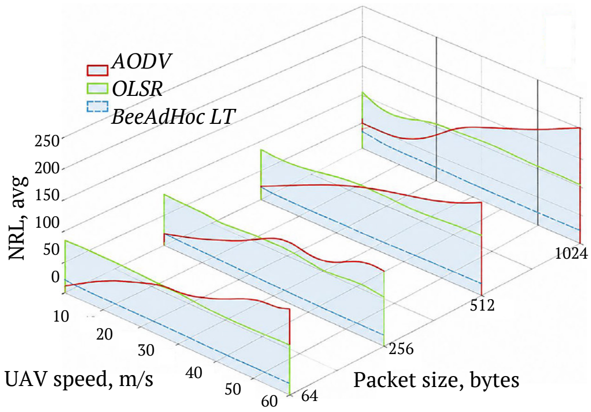

Figure 3. Average value of NRL NL for BeeAdHoc LT, AODV, and OLSR in the "Drone Swarm" scenario
Source: developed by the author

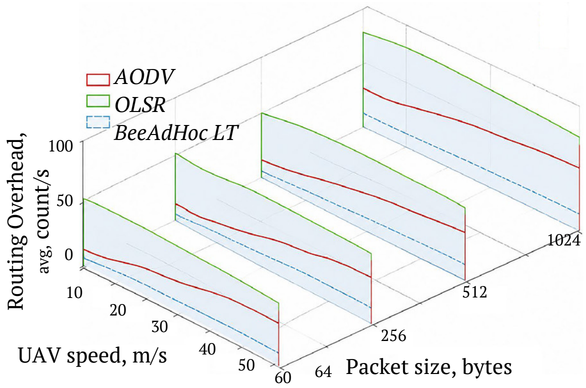

Figure 4. Average routing overhead $O_{routing}$ for BeeAdHoc LT, AODV and OLSR in the "Drone Swarm" scenario
Source: developed by the author

On EED indicators (EE_{delay}) and jitter (J), the proposed algorithm is somewhat inferior to the OLSR protocol, but exceeds AODV. It can be concluded that the proposed algorithm is an effective adaptive solution for routing problems in self-organised agricultural drone networks. It allows selecting the appropriate metric and configuring parameters to optimise the use of network resources, meet QoS requirements, and reduce the risk of network congestion within the FANET usage scenarios under study. It was concluded that the proposed algorithm can be considered as a universal solution to the routing problem in self-organised agricultural drone networks. It allows selecting the appropriate metric and optimise configuration parameters to efficiently use network resources, meet QoS requirements, and prevent network congestion in the selected usage scenario.

The results of the study confirm that the proposed routing algorithm provides an improved balance between latency, jitter, and network load in FANET settings compared to the classic AODV and OLSR protocols. However, the advantages vary depending on the QoS metrics: the algorithm performs better than AODV in terms of EED (EE_{delay}) and jitter (J), but in a number of scenarios it is outperformed by OLSR.

According to RFC 3561, AODV as a reactive protocol provides efficient use of resources in networks with variable topology, but its performance decreases with increased mobility and node density due to frequent route rearrangements. The results obtained are consistent with these provisions, since AODV demonstrates the highest latency and jitter values in heavy FANET traffic (Perkins *et al.*, 2003). According to RFC 3626 described by T. Clausen & P. Jacques (2003), OLSR provides low latency due to proactive route support. However, the above analysis shows a different picture in FANET conditions: an increase in the control load leads to a decrease in the efficiency of using the communication channel at high network dynamics. This explains why OLSR shows better latency but worse performance when scaling the network. The findings of I. Bekmezci *et al.* (2013) and L. Gupta *et al.* (2016) emphasised that FANET is characterised by three-dimensional mobility, a high rate of topology change, and instability of communication channels, which significantly limits the effectiveness of classical MANET protocols. This is fully consistent with the results obtained, where none of the underlying protocols (AODV or OLSR) shows a stable advantage across all metrics simultaneously.

Review studies by A. Fotouhi *et al.* (2017), Y. Zeng *et al.* (2018) showed that adaptive and hybrid routing approaches in UAV networks provide a better balance between QoS parameters by dynamically selecting optimisation metrics. The results obtained partially confirm these conclusions, since the proposed algorithm allows adapting routing parameters in accordance with the usage scenario. However, the above analysis shows a different picture regarding the concept of "universal" routing protocols. Statements about universality should be considered critically, since the effectiveness of algorithms significantly depends on the density of nodes, the level of mobility, and the traffic intensity. This is not consistent with the results of the analysis performed, since no protocol demonstrates a stable advantage in all FANET scenarios.

Thus, the proposed algorithm should be considered as an adaptive routing solution in self-organised FANET, which provides an improvement in individual QoS indicators compared to AODV and competitive performance relative to OLSR in the scenarios under study. Further research should be aimed at expanding the set of modelling scenarios, increasing the number of protocols for comparison, and evaluating the statistical significance of the results obtained.

CONCLUSIONS

It was established that routing algorithms based on the principles of swarm intelligence have key properties for self-organised networks and are superior to most deterministic classical routing algorithms of agricultural drones. Existing swarm intelligence algorithms based on a bee colony were analysed, their features and modifications were studied to effectively solve the routing problem in various types of self-organised networks. A new adaptive routing algorithm based on swarm intelligence of a bee colony has been developed using an "expanding ring" search algorithm for a self-organising network of agricultural drones. A software implementation of the proposed algorithm for the simulation environment has been developed. The influence of setting parameters on the algorithm's behaviour was investigated, and the range of possible values and default values were determined.

Realistic simulation models of typical application scenarios for self-organised agricultural drone networks have been developed. Numerical characteristics and parameters were defined for each scenario, and their substantiation was carried out. The assumptions and limitations used in creating simulation models were formulated. A comparative analysis was carried out, the results of which confirmed the effectiveness of the proposed algorithm and its superiority over the popular routing protocols AODV and OLSR by many indicators, depending on the scenario of using a self-organised network of agricultural drones: the PDR increased by 2-11%; the average throughput increased by 3-12%; the NRL decreased by 22-82%; the overhead cost of routing decreased by 33-79%.

Scientific research should be continued in the line of substantiation of rational engineering management of agricultural drones, since further improvement of the efficiency of their application requires comprehensive consideration of technical, energy, information, and organisational aspects of the operation of self-organised networks. Scientific interest involves the development of adaptive mechanisms for managing agricultural drones' resources, optimising their interaction, and integrating the proposed routing algorithms with intelligent agricultural process management systems. A promising area may be the creation of more efficient and reliable systems for operating groups of agricultural drones in real conditions of agricultural production.

ACKNOWLEDGEMENTS

The author expresses sincere gratitude to the administration of the Shared Research Facility for Advanced Agricultural Technologies, Agricultural Production, Forestry and Landscape Gardening, and Veterinary Medicine, established at the National University of Life and Environmental Sciences of Ukraine in accordance with Order No. 475 of the Ministry of Education and Science of Ukraine dated 12 April 2019, for providing the opportunity to conduct this research.

FUNDING

This paper was supported by the HEI-COPILOT project within the EIT HEI Initiative "Innovation Capacity Building for Higher Education", funded by the European Union.

CONFLICT OF INTEREST

None.

REFERENCES

[1] Banihashemian, S.S., & Adibnia, F. (2019). A new range-free PCA-based localization algorithm in wireless sensor networks. *International Journal of Communication Systems,* 33(6), article number e4291. https://doi.org/10.1002/dac.4291.

[2] Bekmezci, I., Sahingoz, O.K., & Temel, Ş. (2013). Flying ad-hoc networks (FANETs): A survey. *Ad Hoc Networks*, 11(3), 1254-1270. doi: 10.1016/j.adhoc.2012.12.004.

[3] Bonabeau, E., Dorigo, M., & Theraulaz, G. (1999). *Swarm intelligence: From natural to artificial systems*. Oxford: Oxford University Press.

[4] Clausen, T., & Jacquet, P. (2003). Optimized link state routing protocol (OLSR) (RFC 3626). *Internet Engineering Task Force*. doi: 10.17487/RFC3626.

[5] Di Caro, G., Ducatelle, F., & Gambardella, L.M. (2005). AntHocNet routing protocol. *European Transactions on Telecommunications,* 16(5), 443-455. doi: 10.1002/ett.1062.

[6] Dorigo, M., & Gambardella, L. (1997). Ant colony system: a cooperative learning approach to the traveling salesman problem. *IEEE Transactions on Evolutionary Computation*, 1(1), 53-66. doi: 10.1109/4235.585892.

[7] Fatemidokht, H., Rafsanjani, M., Arya, V., & Gupta, B. (2026). Routing protocols in FANETs: A comprehensive survey and taxonomy. *Journal of Systems Architecture,* 175, article number 103774. doi: 10.1016/j.sysarc.2026.103774.

[8] Fotouhi, A., Ding, M., & Hassan, M. (2017). Understanding autonomous drone maneuverability for Internet of Things applications. *IEEE Communications Surveys & Tutorials*, 21(4), 3454-3490. doi: 10.1109/WoWMoM.2017.7974336.

[9] Giagkos, A., & Wilson, M. (2013). Swarm intelligence to wireless ad hoc networks: Adaptive honeybee foraging during communication sessions. *International Journal of Intelligent Systems*, 21(6), 651-663. doi: 10.1177/1059712313500797.

[10] Giagkos, A., & Wilson, M.S. (2014). BeeIP: A swarm intelligence based routing for wireless ad hoc networks. *Information Sciences,* 265, 23-35. doi: 10.1016/j.ins.2013.12.038.

[11] Gupta, L., Jain, R., & Vaszkun, G. (2016). UAV communication networks survey. *IEEE Communications Surveys & Tutorials*, 18(2), 1123-1152. doi: 10.1109/COMST.2015.2495297.

[12] Hamadneh, N.N., Atawneh, S., Khan, W.A., Almejalli, K.A., & Alhomoud, A. (2022) Using artificial intelligence to predict students' academic performance in blended learning. *Sustainability*, 14, article number 11642. doi: 10.3390/su141811642.

[13] Kaur, U., Kapila, D., Bharany, S., Rehman, A.U., Adol, D.M.D., & Hamam, H. (2026). Next generation FANET routing: A systematic review of mobility models, routing protocol families, and future research roadmap. *International Journal of Networked and Distributed Computing*. doi: 10.1007/s44227-026-00104-4.

[14] Khan, A.N., Aftab, F., & Zhang, Z. (2019). Bio-inspired clustering scheme for FANETs (BICSF). *IEEE Access*, 7, 31446-31456. doi: 10.1109/ACCESS.2019.2902940.

[15] Oubbati, O.S., Atiquzzaman, M., Lorenz, P., Tareque, M.H., & Hossain, M.S. (2020). Routing in flying ad hoc networks: Survey, constraints, and future challenge perspectives. *IEEE Access,* 7, 81057-81105. doi: 10.1109/ACCESS.2019.2923840

[16] Pasandideh, F., da Costa, J.P.J., Kunst, R., Islam, N., Hardjawana, W., & Pignaton de Freitas, E. (2022). A review of flying ad hoc networks: Key characteristics, applications, and wireless technologies. *Remote Sensing,* 14(18), article number 4459. doi: 10.3390/rs14184459.

[17] Perkins, C.E., Belding-Royer, E.M., & Das, S.R. (2003). Ad hoc on-demand distance vector (AODV) routing (RFC 3561). *Internet Engineering Task Force*. doi: 10.17487/RFC3561.

[18] Sharma, B., Obaidat, M.S., Sharma, V., & Hsiao, K.-F. (2020). Routing and collision avoidance techniques for unmanned aerial vehicles: Analysis, optimal solutions, and future directions. *International Journal of Communication Systems*, 33(18), article number e4628. doi: 10.1002/dac.4628.

[19] Tan, H.C., Ma, M., Labiod, H., Chong, P.H.J., & Zhang, J. (2016). A non-biased trust model for wireless mesh networks. *International Journal of Communication Systems,* 30(9), article number e3200. doi: 10.1002/dac.3200.

[20] Wang, C., Zhang, S., Ma, T., Xiao, Y., Chen, M. Z., & Wang, L. (2025). Swarm intelligence: A survey of model classification and applications. *Chinese Journal of Aeronautics*, 38(3), article number 102982. doi: 10.1016/j.cja.2024.03.019.

[21] Wedde, H.F., Farooq, M., Pannenbaecker, T., Vogel, B., Mueller, C., Meth, J., & Jeruschkat, R. (2005). BeeAdHoc: An energy efficient routing algorithm for mobile ad hoc networks inspired by bee behavior. In *Proceedings of the 7th annual conference on genetic and evolutionary computation (GECCO '05)* (pp. 153-160). New York: Association for Computing Machinery. doi: 10.1145/1068009.1068034

[22] Zeng, Y., Lyu, J., & Zhang, R. (2018). Cellular-connected UAV: Potential, challenges, and promising technologies. *IEEE Wireless Communications,* 26(1), 120-127. doi: 10.1109/MWC.2018.1800023.

[23] Zhang, Z., Long, K., Wang, J., & Dressler, F. (2014). On swarm intelligence inspired self-organized networking: its bionic mechanisms, designing principles and optimization approaches. *IEEE Communications Surveys & Tutorials,* 16(1), 513-537. doi: 10.1109/SURV.2013.062613.00014.

[24] Zhao, B., & Ding, Q. (2019). Route discovery in FANET based on bee colony algorithm. In *IEEE international conference on artificial intelligence and computer* (pp. 364-368). Dalian: IEEE. doi: 10.1109/ICAICA.2019.8873436.

Михайло Уманський
Аспірант
Національний університет біоресурсів і природокористування України
03041, вул. Героїв Оборони, 15, м. Київ, Україна
https://orcid.org/0009-0006-5746-9717

Маршрутизація агродронів на основі ройового інтелекту бджолиної колонії

Анотація. Актуальність роботи зумовлена необхідністю підвищення надійності, енергоефективності та якості передавання даних у самоорганізованих мережах агродронів, які функціонують в умовах високої мобільності, змінної топології та обмежених ресурсів вузлів. Метою роботи було підвищення ефективності маршрутизації трафіку в самоорганізованих мережах агродронів шляхом розроблення адаптивного алгоритму на основі ройового інтелекту бджолиної колонії. У дослідженні використано методи дискретної й обчислювальної математики, евристичної оптимізації, математичної статистики, а також імітаційне моделювання із застосуванням C++, Python, MATLAB та середовища NS-2. Було досліджено принципи функціонування мультиагентної моделі маршрутизації, що включає упаковщиків, розвідників, фуражирів і рій, які забезпечують децентралізований пошук та підтримку кількох маршрутів передавання даних. Було проаналізовано такі критерії вибору маршрутів, як пропускна здатність, наскрізна затримка, рівень заряду батареї вузлів і час життя мережі, що дозволило адаптувати алгоритм до різних сценаріїв роботи агродронів. Виявлено, що для сценарію рою агродронів доцільно застосовувати метрику часу життя мережі, для транзитної мережі – метрики часу життя та затримки, а для сценарію моніторингу – метрику рівня заряду джерел живлення. Було встановлено, що запропонований алгоритм у порівнянні з протоколами AODV та OLSR забезпечує вищий коефіцієнт доставки пакетів, збільшення середньої пропускної здатності, зменшення нормалізованого навантаження та скорочення накладних витрат на маршрутизацію. Зроблено висновок, що використання ройового інтелекту бджолиної колонії дає змогу ефективніше розподіляти мережеві ресурси, підтримувати вимоги QoS і знижувати ризик перевантаження мережі. Практична цінність роботи полягає в можливості використання отриманих результатів розробниками програмного забезпечення для агродронів, фахівцями з бездротових самоорганізованих мереж, інженерами аграрних технологій та дослідниками під час проєктування енергоефективних систем маршрутизації для сільськогосподарського моніторингу й управління безпілотними комплексамиї

Ключові слова: самоорганізовані бездротові мережі; багатокритеріальна оптимізація; енергоефективність вузлів; наскрізна затримка; пропускна здатність каналу; якість обслуговування; імітаційне моделювання

Machinery & Energetics
Vol. 17, No. 2. 2026

Journal homepage:
https://technicalscience.com.ua/en

UDC 631.004.01
DOI: 10.31548/machinery/2.2026.10

Vadym Hrytsiuk*
Postgraduate Student
National University of Life and Environmental Sciences of Ukraine
03041, 15 Heroiv Oborony Str., Kyiv, Ukraine
https://orcid.org/0009-0001-8943-6307

Analytical assessment of the use of plant material shredder

Abstract. The problem of efficient cutting of plant materials is relevant for agricultural engineering, as it determines the energy efficiency and quality of feed preparation. The purpose of the study was to substantiate the need to improve the mathematical description of the machine utilisation process for a plant material shredder. The study used an analytical review of scientific sources, methods of theoretical cutting mechanics, comparative analysis of normal and sliding cutting models, and elements of mathematical modelling of force interactions in the cutting zone. It was established that the existing theoretical models of cutting plant stems do not provide sufficient accuracy in predicting resistance forces and do not fully consider the heterogeneity of the material structure and the dynamics of the destruction process. It was found that a change in the interaction angle τ and the ratio of the normal and tangent components of the force significantly affects the transition between the normal and sliding cutting modes, which determines the nature of deformations in the stems. It was shown that the sliding cutting mode is more energy efficient than normal cutting, since it provides rational load distribution and reduces the specific energy intensity of the process. It was concluded that improving cutting efficiency can be achieved by taking into consideration the design and operating parameters of the working element, particularly the knife sharpening angle, the clearance between the cutting elements, and operating speed. It was established that the cutting efficiency is significantly affected by the angle of sharpening of the knife, the gap between the elements of the cutting pair, the speed of movement of the knife, and the physical and mechanical properties of raw materials. The expediency of complex accounting of these parameters in a mathematical model was substantiated. The practical significance of the research lies in the possibility of using the results obtained in the design and improvement of drum shredders of plant materials in agricultural and processing engineering

Keywords: cutting process; vegetable raw materials; energy costs; mathematical modelling; cutting mechanisms; stem structure; technological parameters

INTRODUCTION

One of the key areas of livestock production involves the rearing of bovine cattle. Ensuring high efficiency of this area is impossible without the use of innovative technologies and technical means of agricultural engineering, in particular, in the field of feed production and preparation (Yiğit *et al.*, 2024). The basis of cattle diets consists of plant-based feed components, the nutritional value and digestibility of which are largely determined by the quality of their preliminary preparation for feeding, which was highlighted by T. Lasch *et al*. (2025). Among the technological operations of feed preparation, shredding is of particular importance, since this process is characterised by significant energy costs and is one of the most energy-intensive stages of feed preparation, since it was studied by L. Lin *et al*. (2026).

For the implementation of shredding of feed raw materials in the industry, A. Curtis & R. Sarc (2021) offered a wide range of machines and technological complexes. According to L. Kandlbauer *et al*. (2021), a significant part of the existing equipment does not provide the necessary degree of shredding in accordance with zootechnical requirements and is characterised by increased energy intensity,

Article's History: Received: 02.01.2026; Revised: 01.04.2026; Accepted: 21.05.2026; Published: 29.05.2026.

Suggested Citation:
Hrytsiuk, V. (2026). Analytical assessment of the use of plant material shredder. *Machinery & Energetics,* 17(2), 121-130. doi: 10.31548/machinery/2.2026.10.

*Corresponding author (vadym.hrytsiuk@ukr.net)

significant material consumption, and large dimensions. In addition, V. Sheichenko *et al*. (2021) argued that individual shredder designs have complexity of operation and insufficient level of reliability. The limited versatility of most shredders makes them difficult to use for processing a wide range of roughages, particularly crops with robust stem structures, such as maize, sweet sorghum, sorghum-Sudangrass hybrids, etc. An additional problem, according to R. Pérez del Rio *et al*. (2022), remains the high cost of equipment, which limits the possibility of its use in small farms and private subsidiary farms. In this regard, the development of a universal shredder that would provide the necessary productivity, low energy intensity of the process (Zastempowski *et al*., 2023), and the corresponding quality of shredding for farms with different livestock, is an urgent scientific and technical task that requires a comprehensive study and substantiation of constructive solutions.

The study by K. Kishore *et al*. (2022) considered the physical regularities of the process of shredding coarse and stem feeds, identified the main theoretical aspects of this process, and proposed mathematical models for its description. However, due to the adoption of a number of assumptions and simplifications, according to M. Rahman & J. Till (2024), certain aspects of the process remain insufficiently investigated, which makes it necessary to conduct further research in this area. A separate line of research is related to multiphysical modelling. The CFD–DEM approach presented in the XDEM framework (Hadian *et al*., 2024) allows describing in detail the interaction of particles with working bodies. Additionally, S. Rodino *et al*. (2024) emphasised that the key factors for shredding efficiency are humidity, density, and mechanical strength of raw materials. This is consistent with the conclusions obtained in this paper regarding the influence of the physical and mechanical properties of stems on the transition between cutting modes. However, these researchers did not consider the dynamics of contact interaction of the knife with the material, which limited the accuracy of their models.

Thus, the technical solutions proposed by contemporary researchers can be divided into three main areas: systems and ecological approaches, digital and intelligent technologies, and multiphysics approaches. The comparison showed that despite the high accuracy of numerical and AI models, analytical approaches focused on the physics of the cutting process remain the most suitable for engineering design of plant material shredders. The purpose of the study was to improve the process of machine use of the plant material shredder

LITERATURE REVIEW

Current research in the field of plant biomass shredding demonstrates the transition from empirical approaches to multi-factor modelling using numerical methods and intelligent algorithms. In particular, C.A. Ligarda-Samanez *et al*. (2025) emphasised the importance of systematic optimisation of agricultural residues in circular bioeconomics, where shredding was considered as the basic operation of preparing raw materials for further processing. This approach is consistent with the results of M. Ayamga *et al*. (2025), who found that the efficiency of agricultural waste use largely depends on technologies for pre-mechanical destruction of the material structure. S. Rodino *et al*. (2024) emphasised the role of shredding parameters in shaping the quality of biofuels, in particular pellets, which confirms the critical role of particle geometry. Furthermore, G.W. Sileshi *et al*. (2025) summarised global data on agricultural residues and showed that the heterogeneity of raw materials is a key factor that complicates universal modelling of shredding processes. A. Babii & I. Vovk (2025) developed a mathematical model of the contact interaction between a rotary shredder knife and plant stems based on the Euler-Bernoulli beam theory, considering pulsed load and modal damping, to describe the processes of deformation and destruction of stems. The proposed model helped to determine the minimum circular speed of the knife required for the destruction of plant material, and established rational speed modes depending on the translational speed of the aggregate and a given length of shredded particles. The obtained results provide a theoretical basis for justifying the kinematic parameters of rotary shredders and improving the efficiency of processing plant residues.

Special attention in contemporary research was paid to digital modelling of processes. Y. Shi *et al*. (2025) proved the effectiveness of hybrid models that combine physical equations and machine learning methods. Similarly, S. Kordoghli *et al*. (2025) showed that the integration of AI algorithms in modelling thermochemical processes of biomass can improve the accuracy of predicting energy indicators. However, the above analysis indicated a different picture: such models are computationally complex and not always suitable for engineering design of cutting mechanisms in real time. The study by Q. Hernandez-Escobedo *et al*. (2025) summarised the development of renewable technologies in the agricultural sector and confirmed the growing role of biomass as an energy resource. Simultaneously, this was not consistent with the results of the above analysis, since the researchers considered the macro level of energy systems without detailing the mechanics of material destruction at the level of individual stems.

Thus, the analysis of contemporary research showed that the main attention in the field of plant biomass shredding is focused on improving the efficiency of using agricultural residues, optimising the properties of the obtained raw materials, and developing digital models for predicting technological processes. The mechanical patterns of destruction of heterogeneous plant materials at the level of individual structural elements, and the relationship between the design parameters of shredding mechanisms, equipment operation modes, and energy characteristics of the process, remain insufficiently investigated. Existing approaches based on complex numerical or intelligent models cannot always be directly applied to practical engineering design and operational control of machine operation. This determines the need for further improvement of the processes of machine cutting of plant materials by establishing rational parameters of equipment operation, evaluating the power characteristics of the process, and developing practically oriented technical solutions.

MATERIALS AND METHODS

The theoretical foundations of the process of cutting roughage from stem crops were based on an analysis of the conditions governing the interaction between the cutting element and the material. When the layer of stem material was securely fixed during cutting and cannot deform by deflection, the nature of the cutting process depended on the angle τ between the normal to the cutting edge and the direction of the applied cutting force Pp. There was a natural transition between individual types of cutting, determined by a change in the angle τ. As it increased, the nature of the interaction of the cutting body with the material gradually changed. Under the condition $\tau = 0$, normal cutting occured. At values of $0 < \tau \leqslant \varphi$, normal-tangent cutting without sliding is realised, and at $\tau > \varphi$, the process turns into normal-tangent cutting with sliding (Fig. 1).

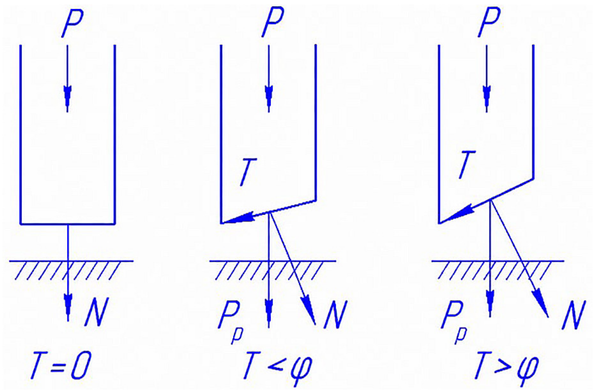

Figure 1. Approaches to cutting plant materials
Source: developed by the author

Notably, the value of the angle τ affected not only the determination of the nature of the cutting process, but also the features of the development and distribution of deformations in the cross-section of the stem material. An increase in the concentration of deformations in the cutting area can be achieved in two main ways: by increasing the speed of the cutting process or by changing the direction of action of deformations, that is, their redistribution from the normal plane to the tangent. This effect was provided by an increase in the angle τ, which contributed to the transition of the process to cutting with a more pronounced tangent component (Fig. 2). The study of the efficiency of the cutting machine was carried out using a theoretical and analytical approach aimed at establishing conditions for reliable pinching of plant material between a movable knife and a fixed anti-cutting plate and determining factors affecting the quality and energy efficiency of the cutting process. The available design and regulatory-technical documentation, together with the results of previous theoretical and experimental studies of the plant material cutting process, was used to determine the initial design and operating parameters of the cutting mechanism.

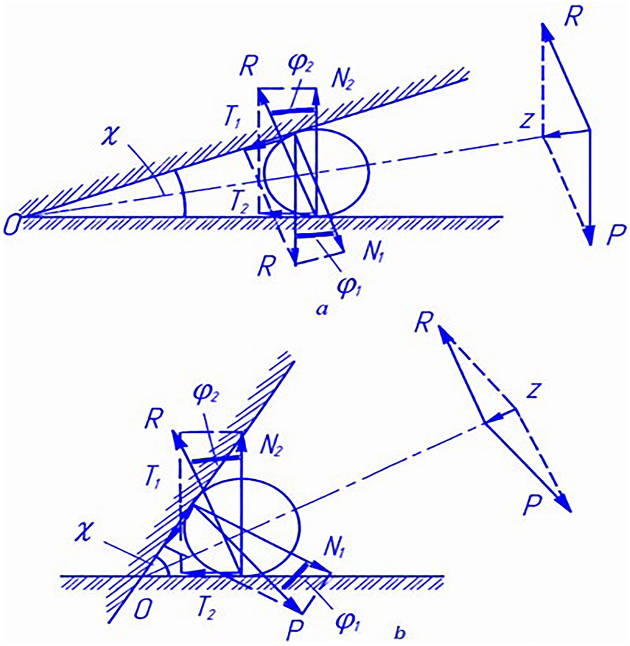

Figure 2. Pinching the material in the opening of the blades and ejection of the material out of the opening of the blades
Note: *a* – pinching of the material; *b* – ejection
Source: developed by the author

The study was performed in several consecutive stages. At the first stage, the existing theoretical approaches to describing the cutting process of stem materials were analysed and the main factors affecting the operation of the cutting machine were identified. These included the nature of the knife sliding relative to the material, the conditions of pinching the stems, the specific work of cutting, the physical and mechanical characteristics of plant raw materials, the speed of movement of the knife, the structural and geometric parameters of the cutting element, and the size of the gap between the elements of the cutting pair.

At the second stage, a calculated scheme for the interaction of plant material with a cutting pair was chosen for further theoretical analysis. The material was modelled as a circular cross-sectional element located in the area between a movable knife and a fixed anti-cutting plate. This scheme allowed formalising the process of pinching the material and determining the force and geometric conditions under which its displacement from the cutting zone was limited. When formulating the theoretical model, the anisotropy of plant materials was taken into consideration. The nature of destruction was considered depending on the spatial position of the stem, the orientation of its fibres relative to the cutting plane, and the direction of movement of the knife. The longitudinal, transverse, and lateral cross-section types were considered as basic. To approximate the calculated model to the actual operating conditions of the cutting machine, the possibility of intermediate cut types, in particular, oblique, inclined, and longitudinal and lateral, was also considered.

At the third stage, the mathematical framework of the study was formed. The process analysis was carried out on the basis of static equilibrium conditions of the material in the zone of interaction with the knife and the anti-cutting plate. For the calculation scheme, the forces acting on the material from the elements of the cutting pair, their normal and tangent components, and the friction forces were determined. Based on the ratio of these forces, the conditions under which the material was held in the cutting zone and not squeezed out of the gap between the knife and the anti-cutting plate were established. Special attention was paid to the influence of the geometric parameters of the cutting pair on the pinching conditions. For this purpose, the relative positions of the knife, counter-cutting plate, and stem, the angular parameters of the cutting element, the clearance between the elements of the cutting pair, and the direction of application of the resultant forces were analysed. Based on the calculation scheme, analytical dependences were obtained that characterised the conditions of stable material retention during cutting. During the interaction of the knife with the material layer (Fig. 3), a system of forces acts on the element under study, which includes the vertical load P, the normal reactions of the support surfaces N_2 and N_2, the friction forces F_1 and F_2 that occur on the side faces, and the cutting resistance force P_p, which is formed due to the destruction of the material by the cutting edge of the knife.

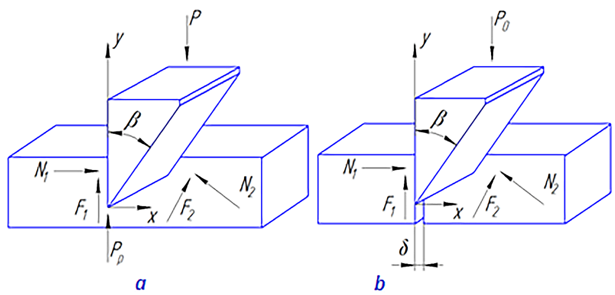

Figure 3. Diagram of the forces acting on the knife during normal cutting

Note: *a* – interaction of the knife with the material layer; *b* – diagram for simplified research

Source: developed by the author

At the fourth stage, the obtained calculated dependencies were analysed. The nature of changes in pinching conditions depending on the design and kinematic parameters of the cutting machine was determined and their impact on the stability of the cutting process was evaluated. Stem deflection and deformation during interaction with the knife were also considered as potential causes of additional axial force components. Such components were considered as a factor that can increase energy consumption, degrade the quality of the cut surface, and increase the load on the cutting elements. At the final stage, the theoretical results obtained were interpreted from the standpoint of ensuring a stable technological process. The criterion for rational operation of the cutting machine was to ensure such a ratio of power and geometric parameters, in which the material is reliably pinched between the elements of the cutting pair, does not shift from the cutting zone, and is destroyed with minimal additional deformations. Thus, the applied method provided for a consistent transition from the analysis of scientific and technical sources and the choice of a calculation model to the development of a mathematical description of the force interaction of elements of the system "knife, plant material, anti-cutting plate", obtaining analytical dependencies, their further analysis, and determination of the conditions for effective pinching of the material during cutting.

RESULTS AND DISCUSSION

Assuming that the movement of the cutting blade occurs at a constant speed, the equilibrium conditions of forces acting on the material during the cutting process can be represented as a system of equations written in projections on the coordinate axes Ox and Oy:

$$\begin{cases} N_1 - N_2\cos\beta + F_2\sin\beta = 0; \\ -P + P_p + F_1 + F_2\cos\beta + N_2\sin\beta = 0. \end{cases} \quad (1)$$

Equation (1) contains five unknown variables (n_2, N_2, F_1, F_2, Pp). The following solution to this equation is proposed: during the movement of the knife, considering the process of sliding between the material and the side faces, the following relations were obtained:

$$F_1 = fN_1; \quad F_2 = fN_2. \quad (2)$$

where f – sliding friction coefficient. Next, it is assumed that the material layer has already been previously separated by a thin cutting element, and the knife only pushes the two parts of the layer apart by δ during further movement (Fig. 3), which corresponds to the thickness of the cutting edge. Under such conditions, there is no resistance force to cutting with the blade, i.e., $P_p = 0$, and the external force acting on the knife is defined as $P = P_0$. Thus, considering the above, obtain:

$$N_1 = \frac{P_0(\cos\beta - f\sin\beta)}{2f\cos\beta + (1-f^2)\sin\beta}; \quad N_2 = \frac{P_0}{2f\cos\beta + (1-f^2)\sin\beta}. \quad (3)$$

By experimentally determining the values of the forces P and P_0, the cutting resistance force can be calculated: $P_p = P - P_0$. The normal type of cutting is characterised by the fact that the direction of action of the forces P and P_0 is perpendicular to the longitudinal axis of the material layer. If the cutting speed is small compared to the propagation speed of deformation processes in the stem material, the deformations are distributed almost evenly over the entire cross-sectional area of the stem. This indicates that during normal cutting at low rates, the destruction of the main structural components of the stem, namely, the outer shell, the reinforcing part, and the inner filler, occurs almost simultaneously. However, this method has certain limitations, the main one of which is the need to conduct a significant number of preliminary experimental studies to determine the value of the P_0 force. In addition, the proposed approach does not consider the influence of such important process parameters as cutting speed and humidity of plant material. When the cutting pattern changes, the ratio between the normal and tangent components of the cutting force changes (Fig. 4).

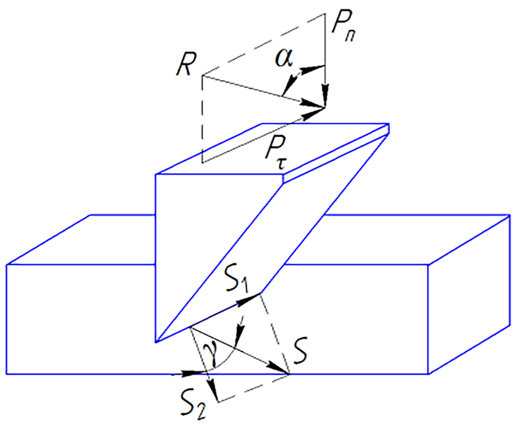

Figure 4. Diagram of active forces
Source: developed by the author

It was established that with a decrease in the normal component of the force P_n, there is a corresponding increase in the tangent component $P\tau$, which is necessary to ensure the cutting process. In this case, the resulting force R, which is the geometric sum of these components, remains unchanged:

$$R = \sqrt{(P_n^2 + P_\tau^2)}. \tag{4}$$

Simultaneously, a change in the angle of inclination of the resultant force R relative to the normal to the blade (α) from 0 to 39° corresponds to a change in the direction-of-motion angle of the cutting element γ. That is, in the range of values 0-39°, the angles α and γ are the same. The correspondence of the areas of the equidistant force R and the movement of the blade indicates that there is no relative sliding of the cutting edge on the surface of the material in the specified angle range α. This mode corresponds to normal and tangent cutting without sliding. However, with a further decrease in the normal component of the force and a simultaneous increase in the tangent component of the cutting force $P\tau$, the dependence $\alpha = \gamma$ is broken, and the difference between these angles begins to increase rapidly. Under the condition $\gamma > \alpha$, the sliding mode of the cutting element occurs relative to the material to be cut.

Redistribution of deformations in the cross-section of the stem is ensured by micro-roughness and micro-teeth of the cutting edge. This mechanism contributes to the gradual destruction of plant material fibres and is explained by facilitating the penetration of the blade into the stem structure during normal-tangent cutting without sliding, and especially during cutting with sliding.

At low cutting speeds, the necessary contact stresses for fibre destruction are formed due to significant deformations of the material, which are characterised by a relatively low concentration. As the cutting speed increases, the value of total deformations decreases, while their local concentration increases. As a result, the interaction zone between the fibre contact points and the cutting edge is reduced. Under such conditions, the influence of the knife sharpening angle on the process of blade penetration into the material becomes insignificant. However, the advantages of using small sharpening angles remain obvious, since they provide an increase in the concentration of deformations in the plant material and facilitate the process of its destruction.

The method of forming the theory of normal and tangent cutting with sliding is based on the analysis of the force interaction of the cutting element with the material. During the interaction of the knife with the material layer (Fig. 5a) it is affected by a complex of forces, which include the vertical force P_n, the normal reactions N_1 and N_2, the friction forces F_1 and F_2 on the side surfaces of the knife, the friction force F_3 in the contact zone with the cutting edge, and the cutting resistance force Q.

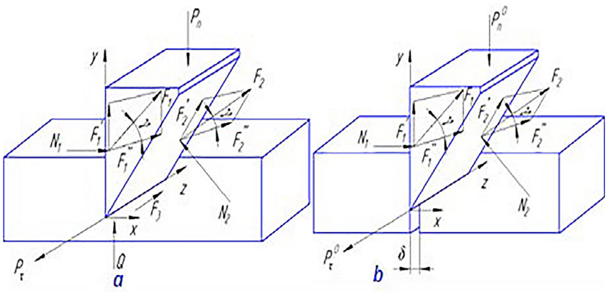

Figure 5. Diagram of the forces acting on the knife when cutting with sliding
Note: *a* – full diagram; *b* – simplified diagram
Source: developed by the author

Since the movement of the knife is uniform, the equilibrium equations of these forces in the projections Ox, Oy, and Oz will have the following form:

$$\begin{cases} -P\sin\alpha + Q + F_2\sin\gamma\cos\beta + F_1\sin\gamma + N_2\sin\beta = 0; \\ N_1 - F_2\sin\beta\sin\alpha - N_2\cos\beta = 0; \\ P\cos\alpha - F_3 - F_1\cos\alpha - F_2\cos\alpha = 0. \end{cases} \tag{5}$$

In the case of normal cutting, the scheme is simplified (Fig. 5b). Therefore $Q = 0$, $F_3 = 0$, and $P = P_0$:

$$\begin{cases} -P\sin\alpha + fN_2\sin\gamma\cos\beta + fN_1\sin\gamma + N_2\sin\beta = 0; \\ N_1 - fN_2\sin\beta\sin\alpha - N_2\cos\beta = 0; \\ P_0\cos\alpha - fN_1\cos\gamma - fN_2\cos\gamma = 0. \end{cases} \quad (6)$$

$$N_1 = \frac{P_0\sin\alpha(\cos\beta - f\sin\gamma\sin\beta)}{2f\sin\gamma\cos\beta + (1-f^2\sin^2\gamma)\sin\beta}.$$

$$N_1 = \frac{(P_0\sin\alpha)}{(2f\sin\gamma\cos\beta + (1-f^2\sin^2\gamma)\sin\beta)}. \quad (7)$$

Substituting the values N_2 and N_2 into the equation, the ratio between the angles α and γ is obtained:

$$tg\alpha = \frac{2f\sin\gamma\cos\beta + (1-f^2\sin^2\gamma)\sin\beta}{(1+\cos\beta - f\sin\gamma\sin\beta)\cos\gamma}. \quad (8)$$

The method is simple and allows solving approximate problems. Its disadvantage is that to determine the angle γ, it is necessary to experimentally determine the angle α, which is not a constant value. In addition, the method does not consider the cutting speed and mechanical and technological properties of the shredded material. Furthermore, the cutting resistance force cannot be mathematically modelled at all.

The cutting force can be determined using the following expression:

$$P_p = 2EFtg\alpha\sin^2\left(\frac{\alpha}{2}\right), \quad (9)$$

where E – Young's modulus, MPa, and F – cross-sectional area of plant material, mm². The disadvantage of this expression is that all the mechanical and technological characteristics of the material that is subjected to shredding are actually represented in it by only one parameter, namely, the modulus of elasticity. When developing theoretical models of the cutting process, the design cutting angle α_1, which characterises the geometric features of the interaction between the cutting element and the material, is additionally taken into consideration (Fig. 6).

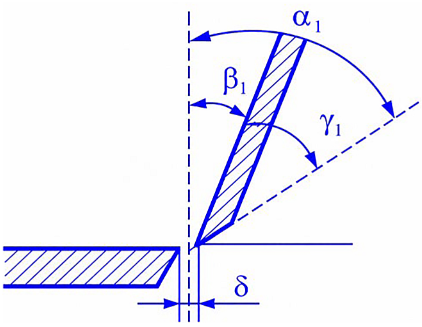

Figure 6. Cutting pair

Source: developed by the author

It is defined as:

$$\alpha_1 = \gamma_1 + \beta_1, \quad (10)$$

where γ_1 – knife sharpening angle; β_1 – knife setting angle.

For cutting mechanisms used in roughage shredders, the optimum knife sharpening angle γ_1 is in the range of 12-22°. The minimum value of this parameter is determined by the requirements for the strength and stability of the cutting edge, while the maximum value is limited by the conditions for ensuring the energy efficiency of the cutting process. Analysis of the features of the interaction of the blade with plant material shows that during the operation of coarse feed shredders, the determining factors are the value of the normal pressure of the knife on the material and the presence of a lateral component of the movement of the cutting element. Quantitative assessment of the relationship between these parameters is carried out using the sliding coefficient and the cutting coefficient with sliding. The size of the gap δ between the cutting edge of the knife and the anti-cutting plate is an important design parameter and should be provided in the range of 0.5-4.6 mm, which allows maintaining the required cutting quality and efficiency of the cutting equipment.

The analysis showed that conventional theoretical provisions regarding the cutting process do not cover all the important factors that affect the cutting of plant raw materials. One of the most significant disadvantages is insufficient consideration of the heterogeneity of the internal structure of the stem materials to be cut. In addition, many studies do not sufficiently consider the dynamic features of the stem destruction process, in particular, the effect of the impact interaction of the cutting body with the material. Thus, there is no single consistent approach to describing the theory of coarse stem feed cutting among scientists.

A characteristic feature of drum cutting mechanisms is the equality of the angle α of inclination of the knife relative to the anti-cutting plate and the angle χ of pinching the material. In this regard, the study of the scheme of a cylindrical cutting machine in a plane perpendicular to the cutting plane provides for the analysis of the main structural and kinematic parameters: the thickness of the layer of material h to be cut, the height of the drum axis above the anti-cutting plate a, the diameter of the drum D, and the establishment of dependencies between these parameters, the feed rate of the material v_{sl}, and the circumferential speed of rotation of the drum V_b. The movement of the knives of the drum cutting machine relative to the material layer is formed due to the simultaneous rotation of the knives around the axis of the drum with an angular velocity ω and the translational movement of the feed mass layer to the drum with a velocity v_{sl}. As a result of such a complex movement, the trajectory of the end point of the knife is described by a trochoid, the equation of which in the fixed coordinate system Ox and Oy has the following form:

$$x = v_{sl}t + \frac{D}{2}\cos(\omega t); \quad (11)$$

$$y = \frac{D}{2}\left(1 - \sin(\omega t)\right), \quad (12)$$

where t – time it took for the drum to rotate by the angle ωt. In this approach, it is assumed that not the feed mass layer moves in the direction of the drum, but on the contrary, the drum performs translational motion relative to the stationary layer of material at a speed corresponding to the feed rate of this layer. When constructing consecutive knife positions, the ratio between the circumferential speed of the vb drum and the feed rate of the v_{sl} material was assumed to be close to unity, as a result of which the trajectory of the knife acquired an elongated trochoidal shape. However, this assumption is a significant limitation of the above theoretical model, since in real operating conditions the speed of movement of the material layer is significantly lower compared to the speed of rotation of the drum.

The distance between the corresponding points of the same name of neighbouring turns of the trochoid remains constant and determines the calculated cutting length lp. To determine it, the difference between the abscissa coordinates x and x_b of two successive knife positions must be found, provided that their ordinates coincide, i.e., $y = y_b$. Thus, the calculated cutting length is determined by the corresponding ratio:

$$l_p = x_b - x, \tag{13}$$

where z – number of knives on the drum. $\theta = 2\pi/z$ can be written as:

$$\sin \omega t = \frac{R-y}{R}, \tag{14}$$

where:

$$R = \frac{D}{2}, \tag{15}$$

from where:

$$\cos \omega t = \sqrt{1 - \left(\frac{R-y}{R}\right)^2}. \tag{16}$$

Substituting the value of cos ωt into the equation:

$$x = v_{sl}t + R\sqrt{1 - \left(\frac{R-y}{R}\right)^2}. \tag{17}$$

Thus, knife b will reach the position α in the layer with a delay of the time Δt required to rotate the drum by the angle θ, i.e.:

$$t = \frac{\theta}{\omega}. \tag{18}$$

Therefore, the abscissa for the resulting position of knife b will have the form:

$$x_b = v_{sl}(t + \Delta t) + R\sqrt{1 - \left(\frac{R-y_b}{R}\right)^2}. \tag{19}$$

Given the value of δt and given that $y_b = y$ according to the expression, obtain:

$$l_p = x_b - x = v_{sl}\left(t + \frac{\theta}{\omega}\right) + R \times \sqrt{1 - \left(\frac{R-y}{R}\right)^2} - v_{sl}t - R\sqrt{1 - \left(\frac{R-y}{R}\right)^2};$$

$$l_p = v_{sl}\frac{2\pi}{2\pi nz} = \frac{v_{sl}}{nz}. \tag{20}$$

Given the values of θ and ω, obtain:

$$P_{zag} = \sum_{i=1}^{n} P_1 + \sum_{j=1}^{m} P_2, \text{ H}. \tag{21}$$

The analysis of the obtained theoretical provisions shows that at the present stage of development of equipment and technologies, the study of the processes of shredding plant raw materials remains relevant and requires further development both from theoretical and experimental standpoints. Special attention should be paid to the theoretical substantiation of the structural and technological parameters of the working bodies of shredding machines, which provide a complex effect on the stem material, in particular, the combination of its splitting processes with the destruction of the internal structure and subsequent sliding cutting of the resulting fragments.

The rational design and operating parameters of such working elements, considering the results of previous scientific studies, should be determined through mathematical modelling of the process, with minimal reliance on empirical correction coefficients. This is explained by the fact that most of the existing coefficients used in the theory of stem feed shredding depend on a significant number of interrelated factors, the determination of the impact of which requires comprehensive experimental studies. The results of the analysis show that the existing theoretical base is still insufficient for the full creation of new highly efficient shredder structures. Therefore, further development of this industry requires systematisation of existing scientific approaches, clarification of theoretical models, and improvement of methods for substantiating the parameters of working bodies.

DISCUSSION

The analysis of the process of cutting plant stem materials has shown that the key factor in the efficiency of shredding is the ratio of normal and tangent component forces, as well as the transition between normal and sliding cutting modes. The obtained generalisations allow considering the process as a multi-factor system in which the geometric parameters of the knife, speed modes, and the structure of the material interact in a complex way. The study by M. Yiğit *et al*. (2024) found that the humidity of the material and the speed of rotation of the working bodies significantly affect the energy consumption of the shredding process. On the one hand, these results are consistent with the conclusions obtained in this paper regarding the dominant role of speed modes in cutting forces. However, the above analysis showed a different picture: the authors of this paper did not consider the transition modes between normal and sliding cutting, which limits the physical interpretation of the obtained empirical dependencies.

Technical solutions proposed by L. Lin *et al*. (2026) related to the construction of anisotropic models of biomass destruction are quite appropriate, since they consider the heterogeneity of the structure of plant fibres. This is consistent with the results of this study on the influence of strain direction and structural anisotropy of stems. The main emphasis was placed on the material model of destruction, while the design and technological parameters of the cutting machine remain outside the scope of analysis. The study by L. Kandlbauer *et al*. (2021) on shredding process control systems confirmed the importance of rapid regulation of the load and feed rate of the material. The conclusions made by the researcher are quite appropriate, since they contribute to the stabilisation of the technological process. However, the current study showed that effective control should be based not only on sensor data, but also on analytical prediction of cutting modes. Additionally, O. Andersen & N.E.L. Haugen (2026) showed that classical pyrolysis models (in particular, the CPD approach) have limitations associated with a violation of the mass balance and simplification of the internal structure of biomass. This is fundamentally important, since such simplifications lead to errors in predicting the yield of products and the energy characteristics of the process. Thus, the conclusions made by the researchers are partially limited, since they do not consider the multiphase and structural heterogeneity of real plant raw materials, which is consistent with the problems identified in this study regarding the description of stem destruction processes.

Some studies integrated CFDs with machine learning. Y. Shi *et al*. (2025) showed that hybrid models allow adaptive updating of kinetic parameters in real time, which significantly improves the accuracy of modelling. However, such approaches require significant amounts of high-quality data and cannot always be applied to new materials without first training the model. The technical solutions of these researchers, based on the results of this study, can be considered in a different plane, since their application is more appropriate for thermochemical processes than for the problems of engineering design of cutting mechanisms. Another important area is the modelling of reactor processes using CFD-DEM platforms, which allows considering the interaction of particles and the gas phase. In particular, M. Hadian *et al*. (2024) proved that such integration is critical for describing agricultural and energy processes, including shredding, gasification, and pyrolysis. The above analysis shows a different picture: the excessive detail of contact processes inherent in CFD-DEM models makes it difficult to use them in the engineering practice of designing shredders, where simplified but physically substantiated analytical dependencies are required.

Thus, the comparative analysis showed that the existing approaches to modelling the shredding process can be divided into empirical, numerical, and analytical. Technical solutions of foreign researchers were mainly focused on empirical or simulation description of processes, while the results of this study were aimed at generalising the physical patterns of cutting and highlighting critical parameters of the transition between deformation modes. It was established that the most promising area is the combination of analytical models with elements of digital modelling, which will ensure sufficient accuracy of forecasting without excessive complication of calculation procedures. The results obtained create the basis for improving the design parameters of cutting machines and optimising the operating modes of shredders, considering the energy and power efficiency criteria. Thus, the proposed approach complements existing studies of mechanical processing of biomass, providing a transition from the description of individual experimental dependencies to the development of physically based models for controlling the shredding process.

CONCLUSIONS

As a result of the analysis of the process of cutting plant materials, it was found that the transition between cutting modes occurs in the range of the interaction angle τ from 0 to 39°, while the most stable transition mode is observed in the range of 10-25°. This confirms that this particular interval is critical for the establishment of a mixed (normally tangent) cutting mode. It was established that the resultant cutting force R remains practically constant as the ratio of the normal P_n and tangential P_τ components changes, in accordance with the analytical relationship: $R = \sqrt{P_n^2 + P_\tau^2}$. Simultaneously, the redistribution of forces leads to a decrease in the specific energy intensity of the process up to 45% in the sliding cutting mode compared to the normal mode, which confirms its energy efficiency.

Analysis of the design parameters showed that the optimal knife sharpening angle is $\gamma_1 = 12\text{-}22°$, where the minimum energy losses are achieved at a value of about 18-0°. Going beyond this range leads to an increase in the cutting force by 15-25%, which negatively affects the overall efficiency of the process. It was also found that the gap of the cutting pair δ in the range of 0.5-0 mm provides maximum cutting quality (up to 90-95% efficiency of destruction of the stem structure), while its increase to 4.6 mm reduces the quality of the process to about 55%, which is accompanied by the appearance of ragged sections. Comparative analysis showed that sliding cutting was the most energy-efficient mode, reducing specific energy consumption by 40-45% compared with normal cutting while maintaining a stable resultant force .

Further development of research should be directed to experimental verification of the proposed dependencies for different types of plant raw materials, since its structural heterogeneity significantly affects the characteristics of the destruction process.

ACKNOWLEDGEMENTS

None.

FUNDING

None.

CONFLICT OF INTEREST

None.

REFERENCES

[1] Andersen, O., & Haugen, N.E.L. (2026). Revisiting the biomass pyrolysis chemical percolation devolatilization model. *Energy Fuels*, 40(7), 3637-3646. doi: 10.1021/acs.energyfuels.5c05760.

[2] Ayamga, M., Tekinerdogan, B., & Annosi, M. (2025). Strategizing ecological sustainability in agricultural ecosystems: A systematic literature review on actor-specific practices and technologies. *Journal of Rural Studies*, 120, article number 103893. doi: 10.1016/j.jrurstud.2025.103893.

[3] Babii, A., & Vovk, I. (2025). Mathematical model of contact interaction between a rotating working body and plant stems for their shredding. *Engineering Energy Transport*, 14(45), 77-86. doi: 10.37128/2520-6168-2025-3-11.

[4] Curtis, A., & Sarc, R. (2021). Real-time monitoring of volume flow, mass flow and shredder power consumption in mixed solid waste processing. *Waste Management*, 210, 93-104. doi: 10.1016/j.wasman.2021.05.024.

[5] Hadian, M., Munck, M., & Buist, K. (2024) Modeling of a catalytic fluidized bed reactor via coupled CFD-DEM with MGM: From intra-particle scale to reactor scale. *Chemical Engineering Science*, 284, article number 119473. doi: 10.1016/j.ces.2023.119473.

[6] Hernandez-Escobedo, Q., Muñoz-Rodríguez, D., & Vargas-Casillas, A. (2025). Renewable energies in the agricultural sector: A bibliometric perspective analysis. *Energies*, 16(1), article number 345. doi: 10.3390/en16010345.

[7] Kandlbauer, L., Khodier, K., Ninevski, D., & Sarc, R. (2021). Sensor-based particle size determination of shredded mixed commercial waste based on two-dimensional images. *Waste Management*, 120, 784-794. doi: 10.1016/j.wasman.2020.11.003

[8] Kishore, K., Sinha, M., Singh, A., Archana, A., Gupta, K., & Korkmaz, M. (2022). A comprehensive review on the grinding process: advancements, applications and challenges. *Journal of Mechanical Engineering Sci*ence, 236(22), 10923-10952. doi: 10.1177/09544062221110782.

[9] Kordoghli, S., Settar, A., Belaati, O., & Alkhatib, M. (2025). Hydrogen production from blended waste biomass: Pyrolysis and AI-based modelling. *Hydrogen*, 7(1), article number 43. doi: 10.3390/hydrogen7010043.

[10] Lasch, T., Khodier, K., Feyerer, C., Lehner, M., & Sarc, R. (2025). Influence of material-material interactions and wear on coarse waste shredders. *Waste Management*, 43(8), 1234-1244. doi: 10.1177/0734242X241306602.

[11] Ligarda-Samanez, C.A., *et al*. (2025). Technological innovations and circular economy in the valorization of agri-food by-products: Advances, challenges and perspectives. *Foods*, 14, article number 1950. doi: 10.3390/foods14111950.

[12] Lin, L., Lacey, J.A., & Qu, J. (2026). An anisotropic yield and damage material model to improve contact pressure analysis in a biomass shredding system. *Journal of Materials Engineering and Performance*, 35, 28442-28453. doi: 10.1007/s11665-026-13755-9.

[13] Pérez del Rio, R., Hidalgo Reyes, M., Caballero Caballero, M., & Hernández Gómez, L.H. (2022). Multi-objective optimization through artificial intelligence for designing of an *Agave angustifolia* leaf shredder. *Scientia Agropecuaria*, 13(3), 291-299. doi: 10.17268/sci.agropecu.2022.026.

[14] Rahman, M.M., & Thill, J.-C. (2024). A comprehensive survey of the key determinants of electric vehicle adoption: Challenges and opportunities in the smart city context. *World Electric Vehicle Journal*, 15, article number 588. doi: 10.3390/wevj15120588.

[15] Rodino, S., Voicilă, D.N., & Sterie, C.M. (2024). The use of forestry and agricultural biomass in the production of pellets: Current state and trends. *Proceedings of Business Excellence*, 18(1), 957-965. doi: 10.2478/picbe-2024-0083.

[16] Sheichenko, V., Volskyi, V., Kotsiubanskyi, R., Dnes, V., Shevchuk, M., Bilovod, O., & Drozhchana, O. (2021). Design of a roll crusher for sunflower stems and substantiation of rational modes of its operation. *Eastern-European Journal of Enterprise Technologies*, 6(1(114)), 28-37. doi: 10.15587/1729-4061.2021.244903.

[17] Shi, Y., *et al*. (2025). Deep learning meets process-based models: A hybrid approach to agricultural challenges. *arXiv*. doi: 10.48550/arXiv.2504.16141.

[18] Sileshi, G.W., Barrios, E., Lehmann, J., & Tubiello, F.N. (2025). Consolidating global residue data from agriculture and livestock systems. *Earth System Science Data*, 17(2), 369-391. doi: 10.5194/essd-17-369-2025.

[19] Yiğit, M., Çanakcı, M., & Karayel, D. (2024). Empirical modelling of power requirements in olive pruning residue shredding: Effects of moisture content and rotary speed. *Agronomy*, 14(7), article number 1455. doi: 10.3390/agronomy14071455.

[20] Zastempowski, M., Bochat, A., & Walentyn, B. (2023). Shredder design effect on the material circulation rate and loadof the shredding chamber. *Advances in Science and Technology Research Journal*, 17(5), 89-103. doi: 10.12913/22998624/171504

Вадим Грицюк
Аспірант
Національний університет біоресурсів і природокористування України
03041, вул. Героїв Оборони, 15, м. Київ, Україна
https://orcid.org/0009-0001-8943-6307

Аналітичність машиновикористання подрібнювача рослинних матеріалів

Анотація. Проблема ефективного подрібнення рослинних матеріалів є актуальною для сільськогосподарського машинобудування, оскільки визначає енергоефективність та якість підготовки кормів. Метою роботи було обґрунтування необхідності удосконалення математичного опису процесу машиновикористання подрібнювача рослинних матеріалів. У дослідженні використано аналітичний огляд наукових джерел, методи теоретичної механіки різання, порівняльний аналіз моделей нормального та ковзального різання, а також елементи математичного моделювання силових взаємодій у зоні різу. Встановлено, що існуючі теоретичні моделі різання рослинних стебел не забезпечують достатньої точності прогнозування сил опору та не враховують повною мірою неоднорідність структури матеріалу і динаміку процесу руйнування. Виявлено, що зміна кута взаємодії τ та співвідношення нормальної і дотичної складових зусилля істотно впливає на перехід між режимами нормального та ковзального різання, що визначає характер деформацій у стеблах. Показано, що режим ковзального різання є більш енергоефективним порівняно з нормальним різанням, оскільки забезпечує раціональний розподіл навантажень і зменшення питомої енергоємності процесу. Узагальнено, що підвищення ефективності подрібнення можливе за рахунок врахування конструктивно-технологічних параметрів робочого органу, зокрема кута заточування ножів, зазору різальної пари та швидкісних режимів роботи. Встановлено, що на ефективність різання істотно впливають кут заточування ножа, зазор між елементами різальної пари, швидкість руху ножа та фізико-механічні властивості сировини. Обґрунтовано доцільність комплексного врахування зазначених параметрів у математичній моделі. Практична цінність роботи полягає у можливості використання отриманих результатів при проєктуванні та удосконаленні барабанних подрібнювачів рослинних матеріалів у сільськогосподарському та переробному машинобудуванні

Ключові слова: процес подрібнення; рослинна сировина; енергетичні витрати; математичне моделювання; різальні механізми; структура стебел; технологічні параметри

MACHINERY & ENERGETICS

Scientific Journal

Volume 17, No. 2. 2026

Founded in 2010. Published four times per year

Managing editor:
N. Shevchenko

Signed for print of May 21, 2026.
Format 60*84/8
Conventional printed pages 15.3
Circulation 100 copies

Publisher's address:
National University of Life and Environmental Sciences of Ukraine
03041, 15 Heroiv Oborony Str., Kyiv, Ukraine
Tel.: +38(044)-258-42-63
E-mail: me@technicalscience.com.ua
https://technicalscience.com.ua/en

ТЕХНІКА ТА ЕНЕРГЕТИКА

Науковий журнал

Том 17, № 2, 2026

Заснований у 2010 р. Виходить чотири рази на рік

Відповідальний редактор:
Н. Шевченко

Підписано до друку 21 травня 2026 р.
Формат 60*84/8
Умов. друк. арк. 15,3
Наклад 100 прим.

Адреса видавництва:
Національний університет біоресурсів і природокористування України
03041, вул. Героїв Оборони, 15, м. Київ, Україна
Тел.: +38(044)-258-42-63
E-mail: me@technicalscience.com.ua
https://technicalscience.com.ua/uk